Title	High Precision Proper Motions in Globular Star Clusters using Parallel Deconvolution of Hubble Space Telescope Images
Author(s)	Saini, Navtej Singh
Publication Date	2013-05-24
Item record	http://hdl.handle.net/10379/3815

High Precision Proper Motions in Globular Star Clusters using Parallel Deconvolution of Hubble Space Telescope Images

A DISSERTATION SUBMITTED IN ACCORDANCE WITH THE
REQUIREMENTS FOR THE DEGREE OF DOCTOR OF PHILOSOPHY IN
THE COLLEGE OF SCIENCE

by

Navtej Singh Saini

Supervisor: Dr. Ray Butler

Centre for Astronomy

School Of Physics

National University of Ireland, Galway

May 2013

This thesis is dedicated to my loving father and mother who
encouraged me to pursue knowledge for its own sake.

Acknowledgements

This thesis is based on three years of research funded by the Science Foundation Ireland (SFI) under award number 08/RFP/PHY1236, titled “Do Black Holes Exist in Globular Star Clusters?”. During the course of the research I have been helped by many individuals.

First of all I would like to thank my supervisor Ray Butler, who took me as a PhD student and was the main driving force behind the project. Thanks for all the help and support throughout the four years. I learned a lot about astronomical data processing, and astronomy in general from you. Thanks also for encouraging and supporting my trip to various conferences and the exchange program to the US. Thanks for giving constructive and valuable feedback on the thesis.

Thanks to Andy Shearer for the continued support and encouragement, first as the director of the Centre for Astronomy, and later as head of the School of Physics at NUIG. Thanks for giving me the responsibility of operate the 3D visualisation suite, and the university telescope as part of the astronomy public outreach activities.

A big thanks to all my colleagues in the astronomy corridor - Gillian, Paul, Mike, Susan, Lisa-Marie, Brandon, Aonghus, Mags, Ronan, Niall, Diarmaid, and Gordon. Thanks also to the old gang of office 135 and 136 - Paddy, Bob, Rory, Leon, Andrea, James, John, and Gregg. Thanks to Mike for many stimulating discussions about image deconvolution and computers in general. Thanks to Lisa-Marie for the tasty baked goodies and encouraging words! Thanks also to my office colleagues Gillian and Paul for discussing interesting technical and scientific problems.

I would also take this opportunity to thank School of Physics technical staff, especially Conor McBrierty, James Nallen, Oliver Ryan, and Stuart Harries for their technical support and help. A special thanks to Tess Mahoney for helping me out with admin stuff.

During my work I had the pleasure of spending six months at the University of California - Santa Cruz (UCSC) in the US. I would like to thank Prof. Jean Brodie for hosting me at UCSC and for the social gatherings at her place. A special thanks to Aaron Romanowsky for mentoring me during the stay in Santa Cruz and for the excellent scientific discussions. A big thanks to Jacob Arnold for technical, scientific, and philosophical discussions. Thanks also for training me on the Keck II telescope, during the March 2011 observation run. A sincere thanks to Ruth McGurk for making my stay in Santa Cruz pleasant and enjoyable. You made it feel like home! Also, the wonderful friends that I have had around me during my stay in US have made my experience there a pleasure.

I would like to thank my friends Benarji, Saravanan, Mani, Gomathy, Bala, Naresh, Ignacio, Andrea, Marco, Luis, and all those who made my stay in Galway pleasant.

A big thanks to my parents for motivating me throughout these four years to keep going. I would not have done without you two. I would take this opportunity to thank my sister and brother-in-law Tarsem for making my frequent trips to Cambridge enjoyable. Finally, and not the least, I would like to give a huge thanks to my wife Manjyot, whose patience, understanding, and support was monumental in making this happen.

Abstract

It has been suggested that globular star clusters may host a black hole with intermediate mass ($\sim$ a few $\times$ 1000 $M_\odot$) or a collection of low mass ($\sim 10\ M_\odot$) black holes at their centre. High velocity dispersion in the cluster core and the presence of the ultra-luminous X-ray sources at the cluster's centre are thought to be signatures of black holes. However, only indirect and/or inconclusive evidences exists for the presence of black hole in the core of globular clusters.

Stars passing very close to the black hole in a cluster can, under certain circumstances, be accelerated to a much higher velocity than the cluster dispersion. Such high proper motion of the stars in the sphere of influence of the black hole can be detected using multi-epoch images of globular cluster separated by reasonable baseline. The variation in proper motion dispersion with radial distance from the cluster centre can give an indication of the presence (or absence) of a central black hole.

To resolve the stars in the crowded core of globular clusters, and thus to determine precise proper motions, a sub-sampled deconvolution technique was developed. An automated simulation pipeline was also developed to generate realistic, multi-epoch, simulated globular star cluster images for the Hubble Space Telescope WFPC2 and ACS instruments. Simulations showed that the technique, which takes account of the point-spread function spatial variation, can provide better star detection and recovers the resolution lost to aberrations and poor sampling.

To speed up the data processing pipeline, a parallel version of the sub-sampled deconvolution was implemented. In addition, World Coordi-

nate transformation, and Monte Carlo completeness testing routines, were also parallelized. We used the Python programming language and PyRAF tasks for the implementation. The cross-platform nature of Python makes the code portable on multiple computer platforms.

Proper motion measurements and internal proper motion dispersion determination was carried out for three Galactic globular clusters - M71, NGC 6293, and M15. For globular cluster M71, the central proper motion dispersion profile is almost flat from $3''$ to $18''$ from the cluster centre. This could be interpreted as the absence of a central black hole in M71. Similar results were also reached for the southern hemisphere cluster NGC 6293, which showed flat central proper motion dispersion profile from $0.8''$ to $18''$ from the cluster centre. For both these clusters, multi-epoch images from the Hubble Space Telescope WFPC2 detector were used. Multi-epoch images from two different detectors (WFPC2 and ACS WFC) were used to determine the stellar proper motions in the core collapsed globular cluster M15, on a 12 year baseline. M15 did show a gradual increase in proper motion dispersion towards the inner cluster core.

Declaration

The work in this thesis is based on research carried out at the Centre for Astronomy, School of Physics, National University of Ireland, Galway. No part of this thesis has been submitted elsewhere for any other degree or qualification and it is all my own work unless referenced to the contrary in the text.

Abbreviations and Acronyms

ACS	Advanced Camera for Surveys
CCD	Charge Coupled Device
CMD	Colour Magnitude Diagram
CPU	Central Processing Unit
CTE	Charge Transfer Efficiency
DAOPHOT	Dominion Astrophysical Observatory Photometry
ESO	European Southern Observatory
FITS	Flexible Image Transport System
GC	Globular Cluster
GPU	Graphical Processing Unit
HRC	High Resolution Camera
HST	Hubble Space Telescope
IMBH	Intermediate Mass Black Hole
IRAF	Image Reduction and Analysis Facility
LMBH	Low Mass Black Hole
LMC	Large Magellanic Cloud

LY	Light Year
M$_\odot$	1 Solar Mass
MEM	Maximum Entropy Method
MPI	Message Passing Interface
MSTO	Main Sequence Turnoff
NGC	New General Catalogue
PSF	Point Spread Function
SMBH	Super Massive Black Hole
SMC	Small Magellanic Cloud
VLT	Very Large Telescope
WCS	World Coordinate System
WFC	Wide Field Camera
WFPC2	Wide Field Planetary Camera 2

Contents

Acknowledgements ii

Abstract iv

Declaration vi

Abbreviations and Acronyms vii

Contents ix

List of Figures xiv

List of Tables xviii

1 Introduction and Motivation 1

2 Globular Clusters: Evolution and Dynamics 4

2.1 Galactic Globular Cluster System 4
2.2 Globular Cluster Properties 6
  2.2.1 Colour Magnitude Diagram and Stellar Life Cycle 6
  2.2.2 Globular Cluster Ages 11
  2.2.3 Metallicity 12
  2.2.4 Globular cluster radii 12
  2.2.5 Evolutionary Time Scales 13
2.3 Star Cluster Life Cycle 17
  2.3.1 Formation and Early Evolution 17
  2.3.2 Long Term Evolution 19

2.4 Globular Cluster Dynamics 20
2.4.1 King Empirical Model 20
2.4.2 Dynamical Models 20
2.4.3 N-Body Models 25
2.4.4 Hardware and Software 26

3 Detection Techniques: Black Holes in Globular Clusters 28
3.1 Black Holes 28
3.1.1 Black Hole Classification by Mass 30
3.2 Black Holes in Globular Clusters 30
3.2.1 Low Mass Black Holes 31
3.2.2 Intermediate Mass Black Holes 31
3.3 Signatures of Black Holes in GCs 33
3.3.1 Surface Brightness Profile 34
3.3.2 Ultra-luminous X-Ray Sources 35
3.3.3 Central Radial Velocity Dispersion 37
3.3.4 Gravitational Wave 38
3.3.5 Radio Sources 38
3.3.6 Kinematics of Individual Cluster Stars 39

4 High Angular Resolution Imaging of GCs 42
4.1 Digital Imagers 42
4.1.1 CCD Characteristics 43
4.1.1.1 Quantum efficiency 43
4.1.1.2 Charge Transfer Efficiency 44
4.1.1.3 Dark Current 45
4.1.1.4 Gain, Noise and Dynamic Range 46
4.1.2 Digital Image Characteristics 47
4.1.2.1 Field of View and Pixel Scale 47
4.1.2.2 Signal-to-Noise Ratio 48
4.1.2.3 Point Spread Function 48
4.1.2.4 Blooming 49
4.2 Hubble Space Telescope 49

4.2.1 Wide Field Planetary Camera 2 52
4.2.1.1 Instrument Characteristics 52
4.2.1.2 Filter Set 54
4.2.1.3 Cosmic Rays, Hot Pixels and CTE 55
4.2.1.4 Optical Distortions 57
4.2.1.5 Point Spread Function 59
4.2.2 Advanced Camera for Surveys 60
4.2.2.1 Instrument Characteristics 61
4.2.2.2 Filter Set 62
4.2.2.3 Cosmic Rays, Hot Pixels and CTE 63
4.2.2.4 Optical Distortions 65
4.2.2.5 Point Spread Function 66

5 HST Data Reduction, Deconvolution, and Astrometry 69
5.1 Image Restoration 69
5.1.1 Maximum Entropy Method Deconvolution 71
5.1.1.1 Entropy in Information Theory 71
5.1.1.2 Bayes’ Theorem 73
5.1.1.3 Putting it all together 73
5.2 Sub-sampled Deconvolution 74
5.3 Data Reduction and Analysis Pipeline 75
5.3.1 Image Reduction and Registration 77
5.3.1.1 WFPC2 Image Registration 77
5.3.1.2 ACS WFC Image Registration 79
5.3.1.3 Dithering 79
5.3.1.4 Drizzling 80
5.3.2 Modelling the Analytical Point Spread Function 83
5.3.3 Image Deconvolution 83
5.3.4 Star Detection 86
5.3.5 Aperture Photometry 87
5.3.5.1 Aperture Correction 88
5.3.5.2 CTE correction 88
5.3.6 Empirical Point Spread Function 89

5.3.7 Proper Motion 89
5.3.8 Internal Proper Motion Dispersion 94
5.4 Conclusions 94

6 Speed up: Parallel Processing 95
6.1 Introduction 95
6.2 Parallel Data Processing 97
6.3 Python Multiprocessing 99
6.4 Benchmarking 101
6.4.1 PIX2SKY and SKY2PIX 102
6.4.2 Completeness Test 104
6.4.3 Parallel Sub-Sampled Deconvolution 106
6.5 Discussion 107
6.5.1 Ease of Implementation 107
6.5.2 Load Balancing 109
6.5.3 Multiprocessing Method Performance 111
6.5.4 Scalability and Portability 112
6.6 Conclusions 114

7 Stellar Proper Motions I: Simulated Cluster Images 116
7.1 Simulated Globular Cluster Images 116
7.1.1 Padova Isochrones 117
7.1.2 Surface Brightness Profile 119
7.1.3 Instrument Characteristics 120
7.1.4 Stellar Proper Motion 121
7.1.5 Pipeline 121
7.2 Sub-sampled Deconvolution Benchmarks 124
7.2.1 WFPC2 Detector 125
7.2.2 ACS WFC Detector 131

8 Stellar Proper Motion II: Real Cluster Images 148
8.1 Globular Cluster M71 (NGC 6838) 149
8.1.1 Data 149

8.1.2 Image Reduction, Star Detection, and PSF-Fitting Photometry . . . 151
8.1.3 Starlist Merging and Proper Motion Determination 152
8.1.4 Internal Proper Motion Dispersion 157
8.2 Globular Cluster NGC 6293 162
8.2.1 Data 162
8.2.2 Image Reduction, Star Detection, and PSF-Fitting Photometry . . . 164
8.2.3 Starlist Merging and Proper Motion Determination 166
8.2.4 Internal Proper Motion Dispersion 169
8.3 Globular Cluster M15 (NGC 7078) 175
8.3.1 Data 176
8.3.2 Image Reduction, Star Detection, and PSF-Fitting Photometry . . . 176
8.3.3 Starlist Merging and Proper Motion Determination 180
8.3.4 Internal Proper Motion Dispersion 185

9 Conclusions and Future Work **191**
9.1 Conclusions 191
9.1.1 Cluster Simulation Pipeline and Data Processing Pipeline . 191
9.1.2 Sub-sampled Spatially-varying Deconvolution Technique . 192
9.1.3 Parallel Processing 192
9.1.4 Measurement of Proper Motions and Determination of Internal Proper Motion Dispersion 193
9.2 Future Work 193

Appendix A **196**

Appendix B **199**

Appendix C **206**

References **212**

List of Figures

2.1 Distribution of globular clusters in the Milky Way galaxy 5
2.2 Metallicity and luminosity of milky way globular clusters 6
2.3 Colour magnitude diagram of globular cluster M3 8
2.4 Hertzsprung-Russell (HR) diagram for stars in the Solar neighbourhood 9
2.5 Evolution of star clusters in the Large Magellanic Cloud 18

3.1 Schematic of a rotating black hole 29
3.2 Black Hole mass - galaxy velocity dispersion relation for elliptical galaxies and bulges 32
3.3 Surface brightness profile of globular cluster NGC 6388 35
3.4 Core of the G1 globular cluster in the Andromeda galaxy 36
3.5 The central velocity dispersion profile of globular cluster ω Centauri 37
3.6 Proper motion of stars in the cluster NGC 6266 40

4.1 Quantum Efficiency of the back and front-illuminated CCDs . . . 44
4.2 Charge transfer efficiency in CCDs 45
4.3 CCD dark current-temperature plot 46
4.4 Bleeding and diffraction spikes in an HST WFPC2 PC1 image . . 50
4.5 Hubble Space Telescope schematic 51
4.6 The position of different instruments in the HST focal plane . . . 52
4.7 WFPC2 field of view on the sky and WFPC2 optical assembly . . 53
4.8 WFPC2 CCDs' quantum efficiency variation with wavelength . . 55
4.9 WFPC2 broad band filter response curves 56
4.10 HST WFPC2 TinyTIM point spread functions 60

4.11 HST ACS optical configuration 62
4.12 ACS WFC and HRC quantum efficiency curves 63
4.13 ACS broad band filter throughput with wavelength 64
4.14 Hot pixel growth rate for the the ACS HRC detector 65
4.15 ACS WFC TinyTIM point spread functions 67
4.16 ACS HRC TinyTIM point spread functions 68

5.1 Variation of the entropy function with probability distribution function 72
5.2 Flowchart of our sub-sampled deconvolution technique 76
5.3 HST WFPC2 image reduction and registration flowchart 78
5.4 Hubble Space Telescope Dither Patterns 81
5.5 Linear image reconstruction method Drizzling 82
5.6 Artificial star grid images for the WFPC2 and ACS detectors . . . 84
5.7 Absolute percentage residual of the TinyTIM fitted image 85
5.8 NGC 6293 WFPC2 point spread function 90

6.1 Coordinate transformation benchmark 104
6.2 HST WFPC2 co-added image of the globular cluster M71 105
6.3 Detection completeness plots 106
6.4 Parallel sub-sampled deconvolution plot 108
6.5 Parallel computing load balancing plots 111
6.6 Performance of different multiprocessing methods 113
6.7 Scalability of our parallel routine 114

7.1 Flowchart of the simulated image generation pipeline 118
7.2 Padova isochrone curves for galactic globular clusters 119
7.3 Surface brightness profile of four galactic globular clusters 120
7.4 Simulated proper motion vector plot 122
7.5 Simulated images of clusters M15 and M5 123
7.6 Simulated tricolor images of cluster M15 124
7.7 NGC 6293 colour magnitude diagram and luminosity function . . 126
7.8 Simulated NGC 6293 image and nearest neighbour distance histogram 127

7.9 Simulated NGC 6293: Star detection as a function of star magnitude 127
7.10 Simulated NGC 6293: Star detection efficiency plots 128
7.11 Simulated NGC 6293: Stellar positional error plots - I 129
7.12 Simulated NGC 6293: Stellar positional error plots - II 130
7.13 Simulated NGC 6293: Proper motion plot 132
7.14 Simulated NGC 6293: Internal proper motion error plots - I . . . 133
7.15 Simulated NGC 6293: Internal proper motion error plots - II . . . 134
7.16 Simulated M5 colour magnitude diagram and luminosity function 135
7.17 Simulated M5 image and nearest neighbour distance histogram . . 135
7.18 Simulated M5: Star detection as a function of star magnitude . . 136
7.19 Simulated M5: Star detection efficiency plots 137
7.20 Simulated M5: Positional error plots for the TinyTIM point spread function - I 139
7.21 Simulated M5: Positional error plots for the TinyTIM point spread function - II 140
7.22 Simulated M5: Positional error plots for the empirical point spread function - I 141
7.23 Simulated M5: Positional error plots for the empirical point spread function - II 142
7.24 Simulated M5: Proper motion scatter plots 143
7.25 Simulated M5: Proper motion errors for the TinyTIM PSF - I . . 144
7.26 Simulated M5: Proper motion errors for the TinyTIM PSF - II . . 145
7.27 Simulated M5: Proper motion errors for the empirical PSF - I . . 146
7.28 Simulated M5: Proper motion errors for the empirical PSF - II . . 147

8.1 Multi epoch HST WFPC2 pointings on the core of M71 core . . . 151
8.2 M71 deconvolved images 153
8.3 M71: Location of the stars whose proper motion was measured in the 2006 epoch image 155
8.4 M71 stellar proper motion 156
8.5 M71: Proper motion, and proper motion error, as a function of star magnitude 157
8.6 M71 colour magnitude diagram 158

8.7 Proper motion histogram of M71 cluster stars 159
8.8 Internal proper motion dispersion of M71 as a function of radial distance from the cluster centre 161
8.9 Multi epoch HST WFPC2 pointings on the core of NGC 6293 . . 164
8.10 Hubble Space Telescope pointing jitter 165
8.11 NGC 6293 deconvolved image 167
8.12 NGC 6293: Location of stars whose proper motion was measured in the 2009 epoch images 168
8.13 NGC 6293 stellar proper motion 170
8.14 NGC 6293: Proper motion, and proper motion error, as a function of star magnitude 171
8.15 NGC 6293 colour magnitude diagram 172
8.16 Proper motion histogram of NGC 6293 cluster stars 173
8.17 Internal proper motion dispersion of NGC 6293 as a function of radial distance from cluster centre 175
8.18 Multi epoch HST WFPC2 and ACS WFC pointings on the core of M15 178
8.19 The HST ACS WFC TinyTIM point spread function 179
8.20 Globular cluster M15 image sections 180
8.21 M15: Location of stars whose proper motion was measured in the 1994 epoch image 182
8.22 M15 proper motion scatter plots 183
8.23 M15: Proper motion, and proper motion error, as a function of star magnitude 184
8.24 Colour magnitude diagram of M15 185
8.25 Proper motion histograms of M15 globular cluster stars 187
8.26 Internal proper motion dispersion of M15 as a function of radial distance from the cluster centre 189
8.27 Internal proper motion dispersion of M15 using Noyola & Gebhardt [2006] cluster centre estimate 190

A-1 Flowchart of steps involved in the Multidrizzle task 197

List of Tables

4.1 HST WFPC2 instrument characteristics 54
4.2 HST ACS detector characteristics 61

6.1 Hardware and software configuration for parallel code benchmarking 101

8.1 Globular cluster M71 properties 149
8.2 HST WFPC2 observations of M71 150
8.3 Internal proper motion dispersion of globular cluster M71 160
8.4 Globular cluster NGC 6293 properties 162
8.5 HST WFPC2 observations of NGC 6293 163
8.6 Internal proper motion dispersion of globular cluster NGC 6293 . 174
8.7 Globular cluster M15 properties 176
8.8 HST observations of M15 177
8.9 Internal proper motion dispersion of globular cluster M15 188

Chapter 1

Introduction and Motivation

Our Galaxy is surrounded by $\sim$150 spherical star clusters, consisting of thousands to millions of old stars orbiting around the centre of mass of the cluster. These are known as *globular star clusters*. These old clusters are held together by their gravitational pull within a region of 10 to 200 light years (ly) across. Apart from the Milky Way galaxy, these cluster systems are also found in most bright and dwarf galaxies. They are very simple systems as all their constituent stars were formed at the same time, with the same starting material, and in the same region of space. However, this simple picture of globular star clusters has changed recently. It has been suggested that second and maybe third generation stars may also exist in the globular star clusters [Bedin *et al.*, 2004; D'Ercole *et al.*, 2008; Kalirai & Richer, 2010; Milone *et al.*, 2012].

Globular clusters are excellent labs for studying stellar evolution and dynamics as well as estimating the age of the universe. Stellar densities in the cores of the globular clusters may exceed the density of stars in the solar neighbourhood by a factor of a million or more. This suggests that a wide range of dynamical encounters are occurring between the stars in the cluster core.

A Black hole is a region in space-time from which nothing can escape - not even light. Two types of black holes are known to exist - Low Mass Black Holes (LMBH) and Super Massive Black Holes (SMBH). Stellar black holes or LMBHs are formed by the collapse of massive stars and are several times the mass of the Sun. SMBHs are millions to billions of Solar mass ($M_\odot = 1$ Solar mass) and they exist in elliptical galaxies and galaxy bulges.

Formation of LMBHs in a globular star cluster is expected, but their retention is divisive because of the theoretical possibility of them being thrown out of the cluster during the supernova explosions which creates them. However if these LMBHs are formed without significant velocity kick then the retention fraction is expected to be high, and may constitute a dynamically important cluster sub-population [Kulkarni *et al.*, 1993]. Recently, Strader *et al.* [2012] detected two stellar mass black holes in globular cluster M22, using radio data from the Karl G. Jansky Very Large Array (VLA). Black holes with intermediate masses ($\sim$ a few x 1000 $M_\odot$) are also suggested to exist in the cores of globular clusters [Gebhardt *et al.*, 2002].

However to date, only indirect and/or inconclusive evidences exist for the presence of such Intermediate Mass Black Holes (IMBHs) or populations of LMBHs in the globular clusters. High velocity dispersion in the cluster core and ultra luminous X-ray sources at the cluster's centre are thought to be the signatures of IMBHs. Although these phenomena could also be explained using other compact stellar remnants.

The only way to establish beyond doubt the presence of an IMBH (or compact LMBH core) at the centre of a globular cluster, and to accurately measure its mass, is through the direct dynamical analysis of stars lying within the black hole's sphere of influence.

This thesis deals with developing an image processing technique to resolve stars in the inner core of the globular clusters and determining the internal proper motion dispersion. The proper motion dispersion profile can then be used with existing theoretical models to predict the presence (or absence) of black holes in the cluster. We developed a parallel sub-sampled deconvolution technique to determine the proper motion of stars in the crowded cores of the globular clusters. The technique was benchmarked using Hubble Space Telescope (HST) simulated images. Finally, stellar proper motion and internal proper motion dispersion was determined for three test case globular clusters - M71, NGC 6293, and M15. Demonstrating the advantages of sub-sampled deconvolution with spatially varying PSFs was a strong motivation in this thesis. To speed up the computationally demanding data processing, developing a parallel computing approach was also a major goal. Having achieved this goal, we were then motivated to demonstrate the generic usefulness of parallel code implementations to other astronomers.

Globular cluster evolution and dynamics is described in **Chapter** 2. This chapter introduces the time scales and the distance measurement terms most frequently used in the context of globular cluster dynamics. Various theoretical models used to describe the evolution of star clusters are also presented.

The globular cluster-black hole connection is described in **Chapter** 3. The various indirect and direct "signatures" used to detect black holes in globular star clusters are presented in the chapter. This chapter concludes with a description of the internal proper motion dispersion "signature", which this thesis deals with.

We have used high angular resolution images from the Hubble Space Telescope (HST) for our work. The HST instruments and detectors are described in **Chapter** 4. Data processing issues, and calibrating photometry and astrometry, are also discussed in this chapter.

We introduce our sub-sampled deconvolution technique in **Chapter** 5. An in-depth description of the reduction pipeline developed for HST data processing, and for proper motion determination and analysis, is also given.

The results and discussion are divided into three chapters. **Chapter** 6 deals with our implementation of parallel sub-sampled deconvolution, and discusses the techniques that can be used to parallelize astronomical routines using the *Python* programming language. For benchmarking our sub-sampled deconvolution technique, we developed an automated pipeline to generate realistic multi-epoch simulated globular cluster images. This simulation pipeline and the benchmarking results are described in **Chapter** 7. The stellar proper motions and internal velocity dispersion analysis of the three Galactic globular clusters is described in **Chapter** 8.

We conclude the thesis by summarising the main results in **Chapter** 9. The future work is also outlined in this chapter.

Chapter 2

Globular Clusters: Evolution and Dynamics

To understand the existence of low mass black holes (LMBHs) or Intermediate mass black holes (IMBHs) in globular clusters, knowledge of dynamical processes and time scales in self-gravitating systems, consisting of a large number of stars, is required. In the sections below, we discuss the current theory about globular cluster formation and its dynamical evolution. The influence of the Galaxy's tidal field on the evolution is also discussed. Analytical, empirical, and numerical models of stars clusters are discussed in brief. The chapter ends with a discussion about system of N-body simulations.

2.1 Galactic Globular Cluster System

As mentioned in the introduction, our Milky Way galaxy has approximately 150 known globular clusters, mostly in the halo. Their mass varies from a few thousand $M_\odot$ to a few Million $M_\odot$ [Zwart *et al.*, 2010]. A simplified picture of the globular cluster distribution in the Milky Way galaxy is show in Figure 2.1. The data for all the plots in this section is taken from the galactic globular cluster catalogue originally published by Harris [1996] and updated on his website[1].

As can be seen from Figure 2.1, a large percentage of the Milky Way globular

---

[1] http://physwww.mcmaster.ca/ harris/mwgc.dat

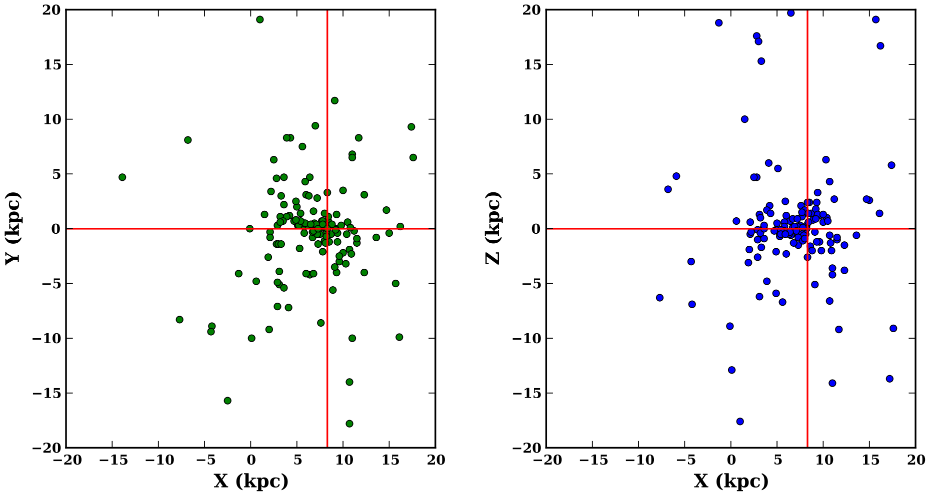

Figure 2.1: Distribution of globular clusters in the Milky way galaxy. X, Y and Z are Sun-centric galactic coordinates. The intersection of the horizontal and the vertical line corresponds to the galactic centre. Data from updated version of the Harris [1996] Galactic globular cluster catalogue.

clusters are within the 5 kpc distance of the Galactic centre. Like that of most galaxies, the Milky Way globular cluster system display metallicity bimodality i.e. a collection of metal rich and metal poor clusters[1] (see Figure 2.2(a)). Metal rich clusters are predominately found in the disk of the galaxy whereas the metal poor are predominately found in the halo. Although, Cote [1999] suggested that metal rich clusters may be part of the Galaxy bulge, rather than the thick disk. The thick disk or bulge globulars are also rotating at higher speed compared to the halo globular clusters [Harris, 2001].

The Milky Way globular cluster system luminosity function[2] has been fitted as a Gaussian distribution with mean absolute visual magnitude -7.33 [Ashman & Zepf, 1998] (see Figure 2.2(b)).

---

[1] According to Archinal & Hynes [2003], a metal rich globular cluster has [Fe/H] > -0.8 whereas a metal poor globular cluster has [Fe/H] < -0.8

[2] number of globular clusters per unit magnitude bins

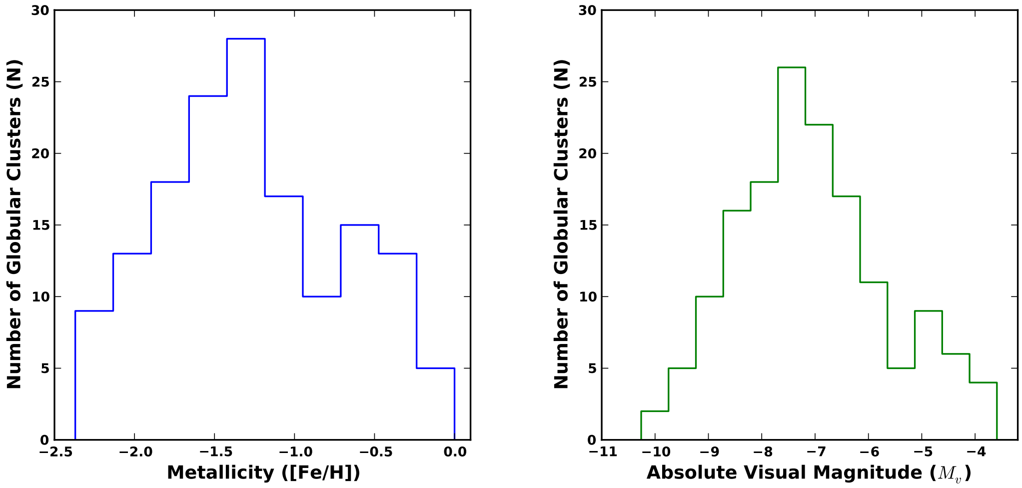

(a)

(b)

Figure 2.2: (a) Bimodality of the Milky Way globular cluster system metallicity. Similar bimodality is also seen in extra-galactic globular cluster systems. (b) The luminosity function of the Milky Way globular clusters can be fitted by a Gaussian distribution with mean absolute visual magnitude -7.33. Data from updated version of the Harris [1996] galactic globular cluster catalogue.

2.2 Globular Cluster Properties

Some of the common concepts used in connection with star cluster evolution and dynamics are introduced below.

2.2.1 Colour Magnitude Diagram and Stellar Life Cycle

Stellar photometry of globular star clusters involves measuring the luminosity of the constituent stars. Luminosity is the energy emitted per unit time by a source. Stellar luminosity and temperature can be represented graphically on a plot known as a Colour magnitude diagram (CMD). Observationally, luminosity corresponds to the absolute magnitude of the star in a particular filter and temperature corresponds to the colour i.e. the difference of magnitude between two different filters or bands. Stellar luminosity is dependent on the size and the temperature of the star. For stars, luminosity and mass is connected by the following relation [Prialnik, 2000]:

$$\frac{L}{L_\odot} \propto \left(\frac{M}{M_\odot}\right)^{\alpha}, \tag{2.1}$$

where $L_\odot$ and $M_\odot$ are solar luminosity and solar mass, respectively. This relationship is only valid for the main sequence stars. The value of α varies between 3 and 5, depending on the mass range of the star.

Colour magnitude diagrams of globular clusters are different from the CMD of the stars in the solar neighbourhood (see Figures 2.3 and 2.4). A typical CMD of a globular cluster, NGC 5272 (M3), is shown in Figure 2.3.

Some of the important information about a cluster can be deduced from the CMD. Different stellar evolutionary phases are visible and are clearly marked on the CMD in Figure 2.3. Stars spend most of their life time in the main sequence (MS) phase. In this phase, hydrogen fuses into helium at the core and the energy is transmitted to the surface by radiation and convection. The low mass stars burn hydrogen via proton-proton chain reaction, whereas high-mass stars do it via carbon-nitrogen-oxygen (CNO) cycle. The core temperature for a MS star can reach ~15 million Kelvin (K). The main difference between stars in the solar neighbourhood compared to those in a globular cluster is that in a GC, the MS phase does not reach the horizontal branch (as is the case with solar neighbourhood stars) [Binney & Merrifield, 1998]. This signifies that the globular clusters are made up of old stars, as only their faint, low-mass stars remain in the MS. The main sequence turnoff (MSTO) gives the age of the cluster (see Section 2.2.2).

At the end of the MS phase, hydrogen is exhausted in the core, creating an inert helium core. The inner core keeps on contracting with hydrogen burning in the shell surrounding the core. The cooler envelope beyond the shell expands and luminosity increase by a small amount. This phase is known as the *sub-giant branch* (SBG) and it lies past the MSTO. The narrow sub-giant branch in globular clusters constrains the age range of the member stars to $\sim$ 2% of the cluster age [Binney & Merrifield, 1998]. The slope of the SGB is dependent on the metallicity of the cluster - it is flatter for metal poor clusters.

For the low mass stars (M $<$ 4 $M_\odot$), the star climbs the giant branch as it

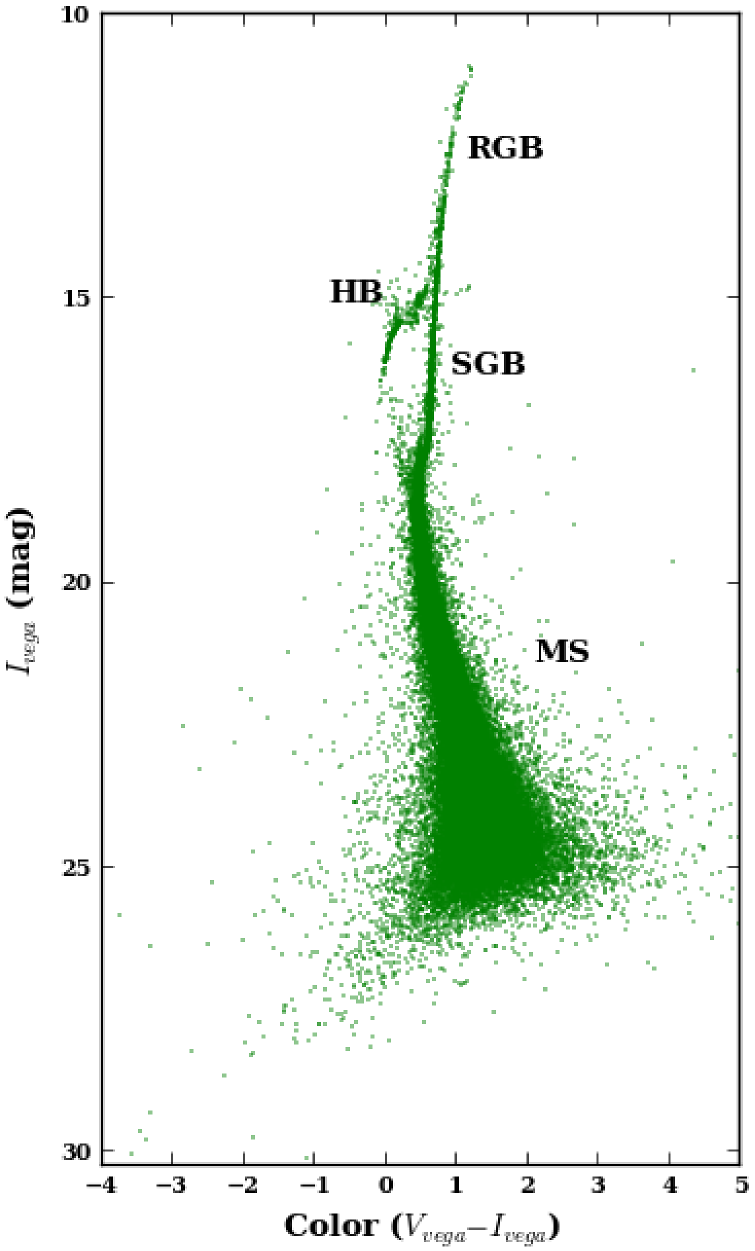

Figure 2.3: Colour magnitude diagram of the globular cluster M3. Data from the ACS survey of galactic globular clusters [Sarajedini *et al.*, 2007]. MS: main sequence, SGB: Sub-giant branch, RGB: Red Giant Branch and HB: Horizontal Branch.

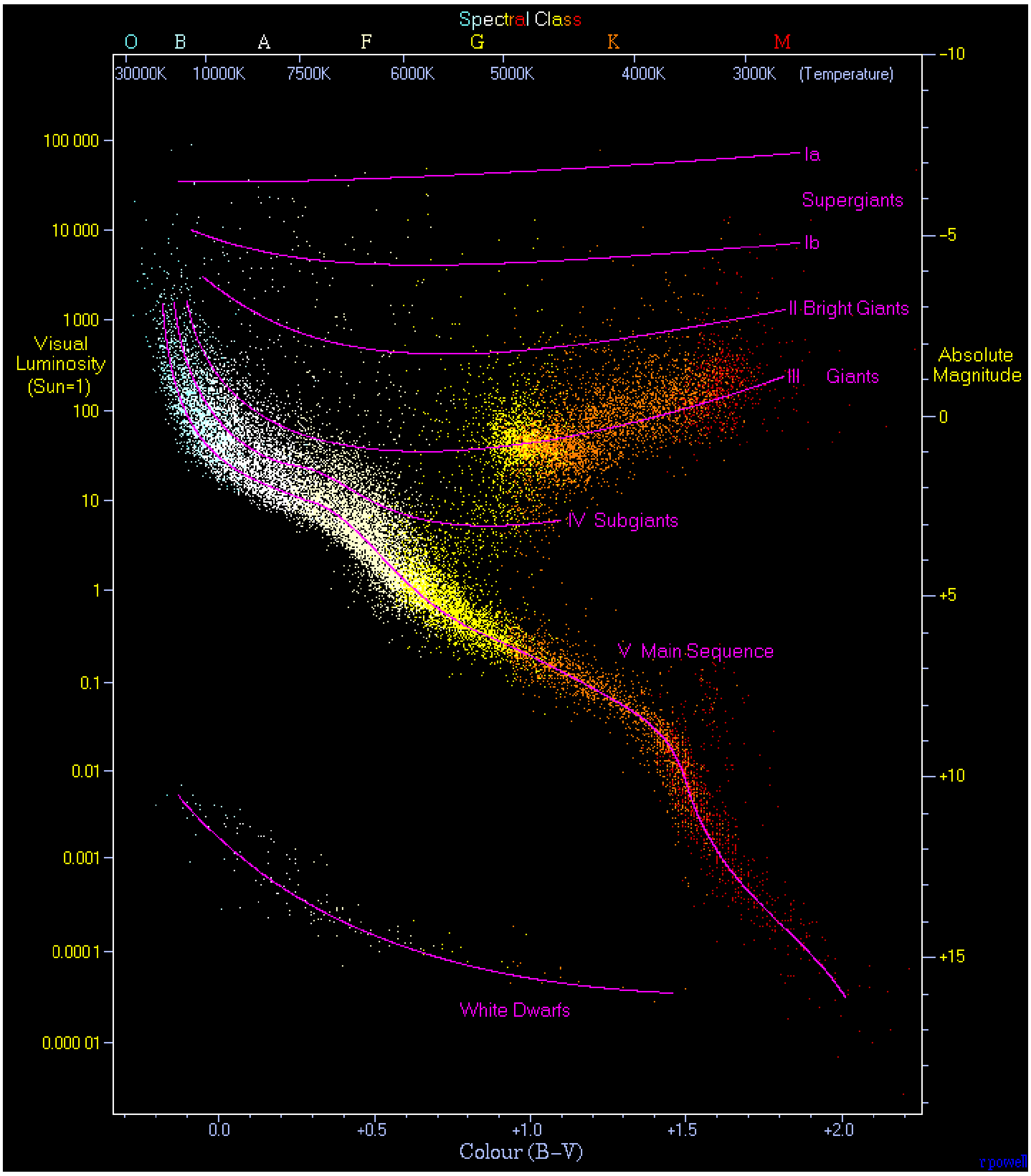

Figure 2.4: Hertzsprung-Russell diagram of 23,000 stars in the Solar neighbourhood. Data from Hipparcos and Gliese catalogues. Figure taken from atlasoftheuniverse website (http://www.atlasoftheuniverse.com/hr.html).

gets brighter and redder. This is the *Red Giant Branch* (RGB). It takes ~1 Gyr for the star to reach the tip of the red giant branch. The core temperature rises to ~100 million K at the tip of the giant branch, leading to helium fusion (via triple-alpha process) into carbon and oxygen. This is known as the *Helium flash*. The energy provided by helium burning in the core, and hydrogen burning in the thin shell around the core leads to star shrinking and moving along the *Horizontal Branch* (HB). The star becomes hotter and bluer. Composition of the Horizontal branch is dependent on metallicity of the cluster, with metal poor clusters having bluer stars compared to metal rich clusters. RR lyrae variable stars lie on the instability gap between the red and the blue horizontal branch stars. The HB phase lasts for ~100 million years and forms a carbon-oxygen (C-O) inert core. After 100 Myr, the C-O core collapses and heat up with a helium and hydrogen burning shell around it. The star moves into the *Asymptotic Giant Branch* (AGB) phase. This giant branch is at higher effective temperature than the original giant branch and situated left of the original giant branch on the Hertzsprung-Russell (HR) diagram. The star grows rapidly and cools. Thermal instabilities causes the outer envelope to slowly get ejected and the inner C-O core to contract. This leads to the formation of planetary nebula and a central white dwarf star.

The high mass stars ($M > 4\ M_\odot$) enter the Red Supergiant phase after MS phase. This involves an inert He core with hydrogen burning shell around it, and a much cooler outer envelope. After 1 Myr on the supergiant branch, the star reaches a core temperature of ~170 million K and undergoes Helium flash. This causes helium burning to carbon and oxygen in the core. The star becomes a blue supergiant. The core runs out of He and results in formation of an inert C-O core surrounded by a He and H burning shells. The star again enters the red supergiant phase. The C-O core contracts with core temperature reaching to ~600 million K. This causes carbon-carbon fusing in the core of the star, resulting in an inert oxygen-neon-magnesium (O-Ne-Mg) core. This last for ~1000 years before the star runs out of carbon in its core. The inert O-Ne-Mg core contract and heats up in the case of the high mass stars with $M < 8\ M_\odot$ with carbon, helium, and hydrogen burning shells. Thermal instabilities causes ejection of the outer envelope with a central O-Ne-Mg white dwarf remnant.

For massive stars ($M > 8\ M_\odot$), neon burning leads to contraction of O-Ne-

Mg core with core temperatures reaching ∼1.5 billion K. This leads to Neon burning in the core, building a O-Mg core with Ne burning shell around it. When Ne runs out, the core contracts and heat up until the core temperature reaches ∼2.1 billion K. This causes oxygen burning in the core and forming silicon in the core. Exhaustion of oxygen leads to contraction of the Si core and increasing the core temperature to ∼3.5 billion K. This causes formation of an inert nickel-iron (Ni/Fe) core. At the end of silicon burning, the star has an onion like "layered" structure - with an inert Ni/Fe core and a Si, O, Ne, C, He, and H burning shells around it. As Fe burning is endothermic, it signals the end of fusion reactions in the star. The end of life for a massive star is a Type II supernova explosion to form a neutron star or a black hole.

2.2.2 Globular Cluster Ages

Globular clusters are among the oldest objects in the Milky Way. Best estimates have dated them between 10 Gyr and 16 Gyr [Krauss & Chaboyer, 2003]. Observational CMDs are fitted with theoretical isochrones of a specific metallicity and age. The best-fitting isochrone at the main sequence turn-off is then used to determine the age of the globular cluster. The age of the globular clusters sets a lower limit to the age of the universe. In the past, there have been discrepancies between the age predicted using globular clusters and that using cosmological parameters [Binney & Merrifield, 1998]. In part, this arose because the absolute age of the globular clusters was not precisely known, because of the uncertainties in the stellar evolutionary models. Some uncertainties remain, but there is no longer a conflict between the estimated ages of GCs (< 13 Gyr) and the Universe (13.772 ± 0.059 Gyr) [Bennett *et al.*, 2012]. But the relative ages of the clusters are much more accurately known. In general, metal rich clusters in the galaxy disk are found to be a few billion years younger than the metal poor halo clusters [Binney & Merrifield, 1998]. Marín-Franch *et al.* [2009] suggested the presence of two groups of globular clusters - older clusters with no age-metallicity relation and younger clusters, following an age-metallicity relation:

$$Age = -0.38\ [M/H] + 0.45. \tag{2.2}$$

2.2.3 Metallicity

Any element heavier than helium is considered a metal in astronomy, because together they comprise only 1% of the elemental matter in the universe [Karttunen *et al.*, 2000]. Because iron is one of the most abundant elements found in stellar spectra, the abundance of iron is the most quoted metallicity parameter [Binney & Merrifield, 1998]. It is given as:

$$[Fe/H] = log_{10} \frac{Fe/H}{(Fe/H)_{\odot}}, \tag{2.3}$$

where $(Fe/H)_{\odot}$ is the iron to hydrogen ratio for the Sun. This single parameter [Fe/H] does not fully trace the chemical composition of the globular clusters. The abundance of oxygen relative to iron ([O/Fe]) is another parameter used by astronomers [Binney & Merrifield, 1998].

2.2.4 Globular cluster radii

Different types of star cluster radii have been used in the literature for different purposes. Below, we define the radii most commonly used in connection with globular cluster dynamics.

1. **Virial Radius**. For a system in virial equilibrium, the virial radius is defined as [Spitzer, 1987]

   $$r_{virial} \approx \frac{GM^2}{2U}, \tag{2.4}$$

   where G is the gravitational constant, M is the star cluster mass and U is the total gravitational potential energy.

2. **Core Radius**. The core radius is defined as the distance from the centre of the star cluster, to where the surface brightness is half the central value. For the King model [King, 1966], it can be expressed in terms of cluster velocity dispersion as:

   $$r_c = \sqrt{\frac{9 < \sigma >_0^2}{4\pi G\rho_0}}, \tag{2.5}$$

where $< \sigma >_0$ is the mean cluster velocity dispersion and ρ_0 is the central density. According to Spitzer [1987], core radius for most of the galactic globular clusters lies between 0.3 and 10 pc.

3. **Half Mass Radius**. Half mass radius (r_{hm}) is the radius from the star cluster center of the spherical volume which contains half of the cluster mass. Another term used by astronomers instead, is the half-light radius (r_h), as it is easy to measure. It is defined as the distance from the cluster center which contains half the total luminosity received from the star cluster Spitzer [1987]. It is comparable to the virial radius.

4. **Tidal Radius**. The full extent of the globular cluster is defined by the tidal radius r_t. A star which moves outside this radius is no longer gravitationally bound and will escape the cluster. Observationally, it is the distance from the center of the cluster to where the surface brightness approaches zero.

Another term that is constantly used in the literature is the concentration parameter c. It is defined as the ratio of the tidal and the core radius:

$$c = log_{10} \left(\frac{r_t}{r_c} \right) \tag{2.6}$$

For galactic globular clusters, its value lies between 0.5 and 3 (based on the current Harris [1996] globular cluster catalogue). A high value of c corresponds to a cluster with a small and highly concentrated core.

2.2.5 Evolutionary Time Scales

Different dynamical processes in the star clusters (as well as in galaxies) occur on different time scales. Stars in a cluster can either interact with other stars in what are known as *strong encounters*, or with the combined gravitational potential from the rest of the stars, known as *weak encounters*. Many weak encounters are more important than a few strong encounters in changing the state (position and velocity) of the stars [Sparke & Gallagher, 2007]. Different time scales involved in star cluster evolution are defined below.

1. **Hubble Time Scale**. The inverse of the Hubble constant, H, is known as the *Hubble time*. It has units of time and can be expressed as

$$t_H = \frac{1}{H_0}, \tag{2.7}$$

where H_0 is the present epoch value of the Hubble constant, as the value of H varies with time. Hubble time provides an estimate of the age of the universe. Value of H_0 have been estimated using different techniques, including microwave background fluctuations [Coles, 2008], Cepheid-calibrated indicators [Freedman *et al.*, 2001; Riess *et al.*, 2011], and gravitational lensing [Koopmans & Fassnacht, 1999]. At present the value stands in the vicinity of 73 km/sec/Mpc[1], and thus Hubble time is $\sim$ 13.7 $\times 10^9$ years.

2. **Crossing Time**. The crossing time is the time required for a star to cross the cluster once. It is also known as the Dynamical Time. Mathematically, it can simply be expressed as

$$t_{cross} = \frac{R}{V} \ \ years, \tag{2.8}$$

where R is the size of the cluster and V is the average velocity of the star. For an old galactic globular cluster with R $\sim$ 5 pc and V $\sim$ 10 km/sec, crossing time would be $t_{cross} \sim 0.5 \times 10^6$ years. For a spherical symmetric and isotropic cluster in virial equilibrium, with N number of stars and each with mass m, the average velocity can be written as

$$V = \sqrt{\frac{GNm}{R}}, \tag{2.9}$$

where G is the gravitational constant. Substituting equation 2.9 in equation 2.8, crossing time can be expressed as

$$t_{cross} = \left(\frac{R^3}{GNm}\right)^{\frac{1}{2}} \ \ years \tag{2.10}$$

---

[1] Mega Parsecs

3. **Strong Encounters Time**. Close encounters between two stars are rare, but there could be 1 or 2 per star in the lifetime of the star cluster [Sparke & Gallagher, 2007]. The strong encounter cross section r_s (distance of closest approach) and strong encounter time scale t_s are defined as follows [Sparke & Gallagher, 2007]:

$$r_s \equiv \frac{2Gm}{V^2} \tag{2.11}$$

$$t_s \approx 4 \times 10^{12} \left(\frac{V}{10\, kms^{-1}}\right)^3 \left(\frac{m}{M_\odot}\right)^{-2} \left(\frac{n}{1\, pc^{-3}}\right)^{-1} \; years, \tag{2.12}$$

where $M_\odot$ is the solar mass and n is the number of stars per unit volume. For a globular cluster with V $\sim$ 10 kms^{-1} and n $\sim$ 1000 pc^{-3}, the two body strong interaction time would be $\sim 10^9$ years.

4. **Two Body Relaxation Time**. When a stable system is perturbed by a disturbance (internal or external), it tries to return back to its previous stable equilibrium state. This is known as relaxation. Relaxation time is the time elapsed between the two stable equilibrium states.

   An interaction between two stars in the cluster is known as *two body relaxation*. Two body relaxation time is dependent on the masses of the stars involved and can lead to an exchange of energy and momentum between the stars. It can be expressed as [Spitzer, 1987]

$$t_{twobody} = \frac{v_{rel}^3}{8\pi\, G^2\, (m_1 + m_2)^2\, ln(0.5N)}, \tag{2.13}$$

   where v_{rel} is the relative velocity between the two stars, m_1 and m_2 are the masses of the two stars, and N is the total number of stars in the cluster. Two body relaxation time in globular clusters is $\sim 10^9$ years.

5. **Half Mass Relaxation Time**. As the two body relaxation time varies throughout the cluster, a more practical relaxation time is the *half-mass relaxation time*. It is the two-body relaxation time calculated inside the half-mass radius. Spitzer [1987] defined it as:

$$t_{rh} = 0.138 \frac{N^{1/2}\, r_h^{3/2}}{m^{1/2}\, G^{1/2}\, ln(\gamma N)}, \tag{2.14}$$

where N is the total number of stars in the cluster, r_h is the half-mass radius, m is the mean mass, and γ is the Coulomb logarithm. Half mass relaxation time in globular clusters is $\sim 10^9$ years. As the half-mass relaxation time is greater than the crossing time, a star in the globular cluster could cross the cluster many times without being involved in a two-body encounter.

6. **Violent Relaxation Time**. Young star clusters (and elliptical galaxies) show smooth surface brightness profiles, even long before two body relaxation can make much impact. This has been attributed to *violent relaxation*, which is relaxation in the presence of a fluctuating gravitational potential [Elson, 1999]. Mathematically, it can be written as [Elson, 1999]

$$t_{vr} \approx \begin{cases} 4.5 \times 10^6 \rho_m^{-1/2} \;\; years \\ 0.2 \; t_{cross} \end{cases} \tag{2.15}$$

where ρ_m is the mean density of the cluster. As the violent relaxation time scale is much shorter than the crossing time, even young star clusters ($\sim 10^7$ years) have gone through the violent relaxation phase. Violent relaxation time does not depend on the mass of the cluster or its stars.

7. **Evaporation Time**. Two body relaxation allows energy and momentum exchange between the stars. If the star gains enough energy and becomes unbound - with velocity greater than the escape velocity - it will escape the cluster. This process is accelerated if the cluster travels through the galaxy bulge or the thick disk. The whole cluster may evaporate on a longer time scale and it has been estimated that the cluster evaporation time can be $\sim 136\; t_{twobody}$ [Sparke & Gallagher, 2007]. This is greater than the age of the universe for the old globular clusters, but its just a few billion years for young clusters. Although open clusters are comparable in size to globular clusters, the star density and stellar speeds are much lower. An open cluster with star density ~ 10 pc^{-3}, velocity dispersion ~ 1 km/sec, and average

stellar mass of 0.5 $M_\odot$ would have $t_{relax} \sim 50$ Myr [Sparke & Gallagher, 2007]. Such an open cluster would have an evaporation time of ~ 6.8 Gyr. Therefore many of the young clusters evaporate much earlier in their life cycle.

2.3 Star Cluster Life Cycle

Almost all of the globular clusters in the Milky Way galaxy are older than 1 Gyr. Zwart *et al.* [2010] have suggested that young massive clusters (YMC) are logical predecessors to the old globular clusters. Therefore investigation of the YMCs in the local group of galaxies (LMC, SMC and M31) could give us an idea about the formation and early evolution of the globular clusters [Caldwell *et al.*, 2009; Goodwin, 1997; Goodwin & Bastian, 2006]. The Large Magellanic Cloud (LMC) has a globular cluster system with star clusters at different evolutionary stages - from 10^6 to 10^{10} year - which gives us an excellent picture of the formation of a globular cluster. A qualitative picture of the star cluster evolution is shown in Figure 2.5. The figure shows age progression in a selection of LMC star clusters - the youngest cluster in the figure is R136 at $\sim$ 1-2 Myears old [Massey & Hunter, 1998]. NGC 1850 is $\sim$ 50 Myears old [Gilmozzi *et al.*, 1994], whereas the intermediate age cluster NGC 2108 is $\sim$ 1 Gyears old [Goudfrooij *et al.*, 2011]. The oldest one is NGC 2121, estimated to be $\sim$ 3.2 Gyears old [Rich *et al.*, 2001].

A simplified timeline of the star cluster formation and evolution is presented in the sub-sections below. A more detailed theoretical treatment of their dynamics is given in Section 2.4.

2.3.1 Formation and Early Evolution

Theoretically, a star cluster is formed when a giant molecular cloud (GMC), under the right conditions of density, pressure, turbulence, internally collapses

---

[1] The Digitized Sky Survey was produced at the Space Telescope Science Institute under U.S. Government grant NAG W-2166. The images of these surveys are based on photographic data obtained using the Oschin Schmidt Telescope on Palomar Mountain and the UK Schmidt Telescope. The plates were processed into the present compressed digital form with the permission of these institutions.

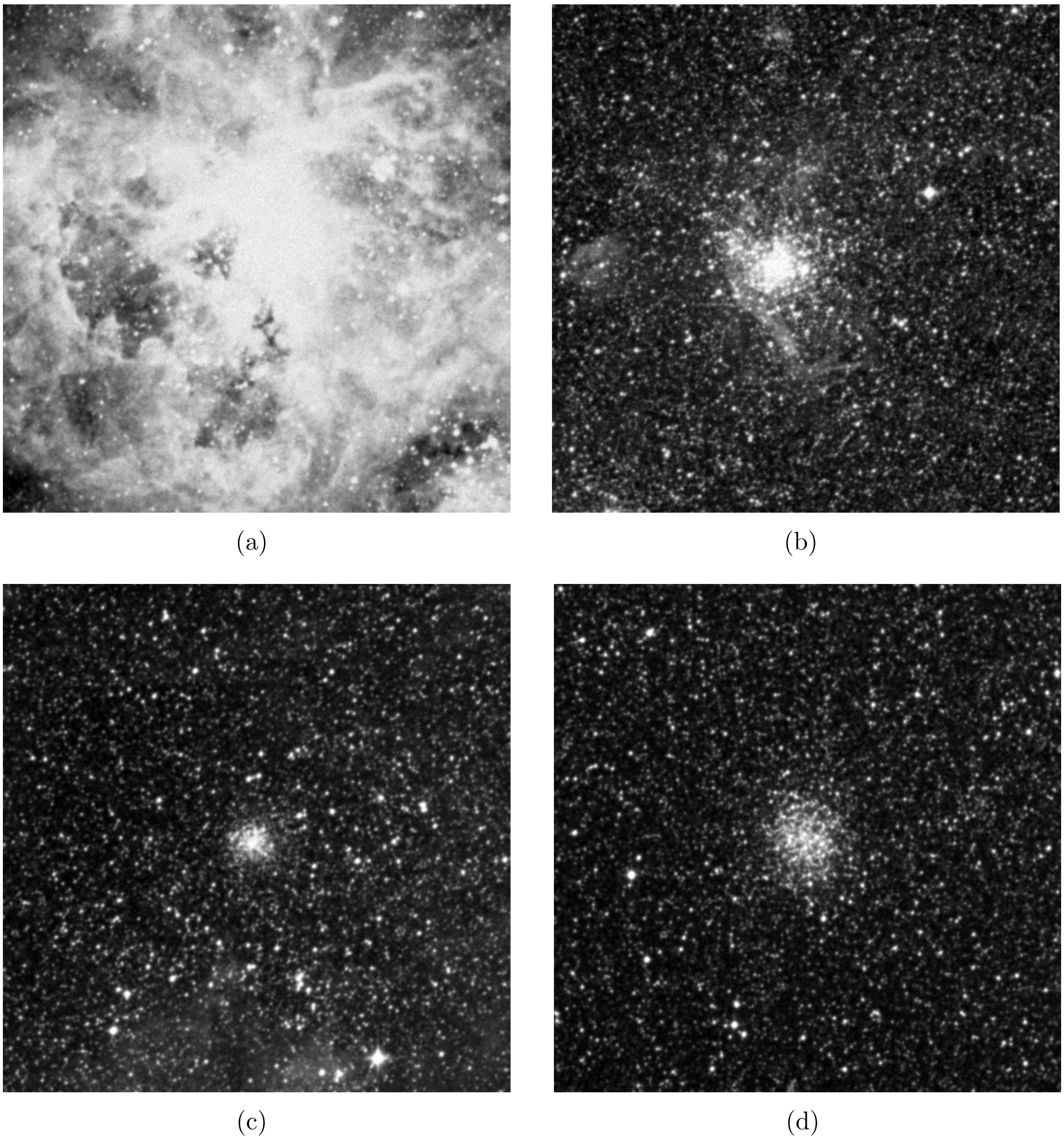

(a) (b) (c) (d)

Figure 2.5: Evolution of star clusters in the LMC. (a) R136 cluster (b) NGC 1850 cluster (c) NGC 2108 cluster (d) NGC 2121 star cluster. Images from the STScI Digitized Sky Survey website[1].

on several lengths and time scales to produce a large number of stars. It has been suggested that the young massive clusters with age less than 5 Myears are still embedded in the primordial gas cloud (see Figure 2.5(a)) and have not gone through the two body relaxation process [Zwart *et al.*, 2010]. Kroupa & Boily [2002] have suggested that these protoclusters or embedded clusters show power law mass functions with exponent between 0.9 and 2.6. By the time the cluster is 10^7 years old, it relaxes *violently*, leading to little or no trace of the primordial gas (see Figure 2.5(b)). Stellar winds from the massive stars and the supernova explosions disperse the primordial gas clouds. This causes a few of the stars to escape the cluster (because of its shallower gravitational potential), or the whole embedded cluster may be disrupted [Zwart *et al.*, 2010]. Therefore, Parmentier *et al.* [2008] concluded that the initial mass that can be inferred for the molecular gas cloud is not only dependent on the star formation efficiency (SFE) but also on the mass fraction of the cloud that remains bound to the cluster.

2.3.2 Long Term Evolution

On a shorter time scale, the gravitational attraction between the stars would result in a collapsing system, but the star-star interactions will prevent the radial infall and the system will stabilise after a few contractions and some shrinking. On a longer time scale, the interaction of two stars in different orbits will result in the less massive star gaining kinetic energy at the expense of the more massive star (see Section 2.2.5, Two Body Relaxation). The less massive star will move to a higher orbit whereas the massive star's orbit will shrink. Over time, this will lead to *mass segregation*, with an over abundance of massive stars in the cluster core. The stars in the outer orbits of the cluster, close to the tidal radius, are stripped over time by the galaxy's tidal force. Meanwhile, the centre will gain density by many orders of magnitude and the inner region will contract. This process is known as *core collapse*. Binary stars formed after the core collapse, provide dynamical energy until the whole cluster evaporates. Between core collapse and evaporation, the system undergoes so called *gravothermal oscillations* - a swing in central density (contraction and expansion of the system) because of a shorter relaxation time for core compared to the rest of the system [Heggie & Hut, 2003].

Ultimately the stars in the outer part of the cluster will be stripped, reconfiguring the gravitational potential, radii and timescales, and the cluster will dissolve on a much longer time scale (see Section 2.2.5, Evaporation Time).

2.4 Globular Cluster Dynamics

Various models - analytical, empirical, and numerical - have been proposed to describe the properties of the globular clusters. These properties include surface brightness profile, central velocity dispersion as well as kinematics and dynamics of the cluster. These models are briefly discussed in the following sub-sections. More details can be found in the references mentioned within.

2.4.1 King Empirical Model

The first model developed specifically for globular clusters was proposed by King [1962], using the surface brightness profiles of the galactic globular clusters. The empirical function is different for the core and the outer regions of the cluster. The combined function, which is valid for both the core and the outer regions was defined by King [1962] as

$$f = k\left[\frac{1}{(1+(\frac{r}{r_c})^2)^{1/2}} - \frac{1}{(1+(\frac{r_t}{r_c})^2)^{1/2}}\right]^2, \tag{2.16}$$

where r_c is the core radius, r_t is the tidal radius, and k is a constant.

2.4.2 Dynamical Models

Although the King empirical models were able to fit well with surface brightness profiles of many globular clusters, they were not realistic models. Later, King [1966] proposed more realistic dynamical models based on the *collisionless Boltzmann equation*. These were based on the assumption that a globular clusters is a spherically symmetric, isotropic, and self gravitating system with stars having the same mass. A brief description of the equations and various solutions is given below.

Understanding the dynamics of a star cluster involves solving the equations of motion to determine the force acting between all the stars. One way to look at it is as a cluster having N number of particles (or stars) in 6 dimensional phase space (r,v), where r comprises 3 vectors for position in 3 dimensions, and v comprises 3 velocity vectors. A star can interact with the collective field of distant stars, called *collisionless encounters*, or it can interact with another star in a *two-body encounter*.

Collisionless System

In a collisionless system, one only takes into consideration the interaction of each star with the collective field of other stars, and excludes the close encounters. Collisionless or collective interactions have been used to explain violent relaxation in young clusters, internal mass loss in clusters due to stellar evolution and interaction, and external mass loss due to tidal fields, bulge and disk shocking. For systems with a large number of particles, a continuous distribution of mass (rather than a discrete distribution) is better suited for analysis. A probability density or density of stars in the phase space function $f(\boldsymbol{r},\ \boldsymbol{v},\ \boldsymbol{t})$ can then define the dynamics of the cluster, such that

$$\int f(\boldsymbol{r},\ \boldsymbol{v},\ \boldsymbol{t})\ d^3\mathbf{v} = N, \tag{2.17}$$

where N is total number of stars in the cluster and bold characters signify vectors. f can then be used to determine the space density of the stars (each with mass m)

$$\rho(\mathbf{r}, t) = m \int f(\boldsymbol{r},\ \boldsymbol{v},\ \boldsymbol{t})\ d^3\mathbf{v} \tag{2.18}$$

This in turn can be used to determine the gravitational potential of the cluster using Poisson's equation

$$\bigtriangledown^2 \phi(\mathbf{r}, t) = 4\pi G\rho, \tag{2.19}$$

where G is the gravitational constant. The equation of motion of a star in the $\phi(\mathbf{r}, t)$ potential can be solved using the following equation

$$\ddot{r} = - \bigtriangledown \phi \tag{2.20}$$

It is evident that the motion of the star is independent of its mass and the motion of the neighbouring stars will be identical. The evolution of function f can be expressed in terms of the fundamental *Collisionless Boltzmann Equation* [Heggie & Hut, 2003]

$$\frac{\partial f}{\partial t} + \mathbf{v}.\bigtriangledown_r f - \bigtriangledown\phi.\bigtriangledown_v f = 0, \tag{2.21}$$

where $\mathbf{v}$ and $\mathbf{r}$ are independent and ϕ does not depend on $\mathbf{v}$.

According to Jean's theorem, function f is an equilibrium solution if it depends on energy E. A few of the equilibrium models used to explain star clusters are defined below.

1. **Isothermal Sphere**. This is the simplest distribution function, although it does not give a realistic picture of a star cluster. The distribution function and density function are defined as [Heggie & Hut, 2003]

$$f = f_0 \; e^{\frac{-E}{\sigma^2}}, \tag{2.22}$$

$$\rho = \rho_0 \; e^{-\sigma^2(\phi-\phi_0)}, \tag{2.23}$$

   where E is the energy, f_0 is a constant, σ is the velocity dispersion, and ρ_0 and ϕ_0 are density and potential at a particular point in the cluster. The velocity dispersion (σ) and central potential (ϕ_0) are the two free parameters in the isothermal model.

2. **Plummer Model**. The distribution function and mass density for the Plummer model is given as [Heggie & Hut, 2003]

$$f = \frac{3.2^{7/2} a^2 (-E)^{7/2}}{7\pi^3 G^5 M^4 m} \tag{2.24}$$

$$\rho = \frac{3M}{4\pi a^3}(1 + \frac{r^2}{a^2})^{-5/2}, \tag{2.25}$$

where scale radius a and system mass M are the free parameters of the model and E is the total energy. The Plummer model has been used for simple spherical star clusters and round galaxies.

3. **King Model**. This is a modified form of the isothermal model and given as [King, 1966]

$$f(E) = \begin{cases} f_0\,[e^{\frac{-E}{\sigma^2}} - e^{\frac{-E_0}{\sigma^2}}] & if E < E_0, \\ 0 \quad if E > E_0 \end{cases} \tag{2.26}$$

where E_0 is the cluster escape energy. In addition to the two free parameters for an isothermal model (σ and ρ_0), the King model has a third parameter known as the scaled potential (W_0) [Heggie & Hut, 2003]

$$W_0 = \frac{(E_0 - E_c)}{\sigma^2}, \tag{2.27}$$

where E_c is the energy of the star at rest at the center of the cluster. The central region of the cluster in the King model is characterised by the core radius (see Section 2.2.4). Compared to the isothermal model, the King model has finite mass and radius.

Modified versions of the King model with velocity anisotropy, varied mass, and an external tidal field have also been proposed. Observationally, to model a cluster with velocity anisotropy would require kinematic data i.e. either radial velocity or proper motion of the stars.

Collisional System

The above discussion did not take into account the two-body interaction between the stars. During a two-body encounter, one neglects the effect due to the rest of the cluster for the time being. According to Newton's gravitational law, the equation of motion for two stars of masses m_1 and m_2 is given by

$$\ddot{\mathbf{r}} = \frac{G(m_1 + m_2)}{r^3}\mathbf{r} \tag{2.28}$$

The Gravitational potential energy of the cluster is defined as the work done to move a mass from a reference point (infinity or a point where potential energy is zero) to a distance, say r, from the cluster centre. Gravitational potential is the gravitational potential energy required to do the work on a unit mass. Again, acceleration is related to the central potential as

$$\ddot{\mathbf{r}} = - \bigtriangledown \phi(r); \qquad\qquad r = |\mathbf{r}| \tag{2.29}$$

Solving Equations 2.28 and 2.29

$$\phi(r) = \frac{G(m_1 + m_2)}{r} \tag{2.30}$$

For the time independent central potential, both angular momentum and energy are conserved or invariant:

$$\frac{E}{m} = \frac{\dot{\mathbf{r}}^2}{2} + \phi(r) \tag{2.31}$$

$$\frac{\mathbf{J}}{m} = \mathbf{r}.\dot{\mathbf{r}} \tag{2.32}$$

If the potential is time dependent, angular momentum is still invariant but energy will vary with time. This is the case when a central black hole is present in a cluster and during two body relaxation [Heggie & Hut, 2003].

Mass segregation results from two-body relaxation. Equipartition of kinetic energy i.e. $m_1 < v_1 >^2 = m_2 < v_2 >^2$ results in massive stars dropping to lower levels in the cluster potential well and less massive stars moving up and eventually escaping. This leads to segregation of masses by energy (and spatially), with the central core having massive stars. Mass segregation is a runaway process and would lead to a dense core. This is known as core collapse. In the three body encounters between a single star and binary at the core, the energy is transferred to the single star and as a result the binary stars come closer. Depending on the number of binaries present in the cluster core, the energy provided by the binaries could lead to expansion of the core. As mentioned earlier, this cyclic contraction and expansion of the cluster core is known as gravo-thermal oscillations.

Fokker-Planck Equation

A realistic star cluster displays both the collective collisionless interactions and strong two-body interactions. Therefore a complete dynamical model should include both of these encounters. The Collisionless Boltzmann equation can be extended to include the two body relaxation, giving either the Boltzmann equation or the Fokker-Planck equation.

In stellar dynamics, clusters are in quasi-equilibrium as stars keep on escaping [Heggie & Hut, 2003]. The Fokker-Planck equation for a quasi-equilibrium system with isotropic velocity distribution is given as [Heggie & Hut, 2003]

$$\frac{\partial f}{\partial t}.\frac{\partial s}{\partial E} - \frac{\partial f}{\partial E}.\frac{\partial s}{\partial t} = -\frac{\partial (D_E f)}{\partial t} + \frac{1}{2}\frac{\partial^2 (D_{EE} f)}{\partial E^2}, \tag{2.33}$$

where f is the probability density function, s is volume in phase space, D_E and D_{EE} are diffusion coefficients. Numerically, Monte-Carlo and Finite difference methods have been used to solve the Fokker-Planck equations for star clusters.

2.4.3 N-Body Models

The King models and the Plummer model are of the type known as *Static models* as they do not evolve with time. Whereas Fokker-Planck and N-Body models are known as *Evolutionary models*. For a more precise modelling of the globular clusters, numerical N-Body models have been proposed. These models take the mass and time-dependent positions of all the stars. Mathematically, it would involve solving the force equations for all the N stars [Heggie & Hut, 2003]

$$\ddot{\mathbf{r}} = -\sum_{j \neq i} \frac{G m_j (\mathbf{r}_i - \mathbf{r}_j)}{|\mathbf{r}_i - \mathbf{r}_j|^3} \tag{2.34}$$

Ideally, one would like to integrate all the individual force equations for the N number of stars in the cluster. But as the number of stars in the cluster could be quite large, a few short cuts and approximations have been suggested. These include - integrating different stars over different time frames, a more frequent force calculation between neighbouring stars than distant ones. Equation 2.34 can be reduced to the collisionless Boltzmann equation (Equation 2.20; 2.21) by approximating the right hand side of the equation as a gradient of a continuous gravitational potential.

Present N-Body models have incorporated the following [Aarseth, 1999]:

1. Stellar evolution
2. Hard binary formation
3. Binary interaction with single stars and with other binaries (Neutron star binaries are possible)
4. Primordial binaries and black holes
5. Triple encounters
6. External tidal fields
7. Two body relaxation

This has resulted in more realistic cluster models that are comparable to observed star clusters, both in terms of properties and the number of member stars.

2.4.4 Hardware and Software

Numerical simulation of star cluster dynamics is among the most computationally intensive problems in astrophysics. This is because of the substantial length and time scales involved in modelling the systems. For example - typical stars are smaller than the star clusters by a factor of 10^9 (varied length scale) [Heggie & Hut, 2003]. While the time scales of the cluster evolution can be the same as the age of the universe, a normal star-star interaction may last for only a few hours (varied time scale) [Heggie & Hut, 2003]. The sheer number of stars N is the other factor and direct N-body calculations scales as N^3 [Heggie & Hut, 2003].

Therefore special purpose hardware, rather than general purpose supercomputers are used to model these massive star clusters. The first dedicated special purpose hardware was developed by Makino *et al.* [1997] in Japan, known as GRAPE-4. GRAPE (**GRA**vity **P**ip**E**) systems are used in conjunction with a general-purpose host computer. The host computer sends the information about all the particles (or stars) in the system to the GRAPE hardware, which in turn calculates the acceleration for each particle. This speeds up the execution as each force calculation between the particles takes 3 clock cycles (instead of many cycles in the case of conventional machines). The initial GRAPE-4 hardware was able to clock around 1.08 TFlops [Makino *et al.*, 1997] peak performance. The newer version, GRAPE-6, is able to peak around 64 TFlops, a big improvement from the GRAPE-4 machines [Makino *et al.*, 2003]. With the advent of GPGPU[1], for example Nvidia Tesla graphic cards, the N-Body simulation codes have been ported to them. But most of the current N-body simulation is still being carried out on the existing GRAPE machines.

Two software packages are mainly used for modelling star clusters - Starlab and NBODY4 (or the improved NBODY6). Starlab [Hut, 2003] is a software package consisting of loosely coupled programs to simulate the evolution of dense stellar clusters. NBODY4, developed by Aarseth [1999], is based on a Hermite individual time step with Kustaanheimo-Stiefel (KS) regularization. A Hermite time step is a fourth order force polynomial used to calculate force and its first derivative on dedicated hardware like GRAPE [Aarseth, 2003]. Regularization is used for the treatment of close encounters between two stars or the perturbed two body problem. It has been extended to chain regularization, to deal with up to six body interaction. Single star interaction with a binary, binary-binary interactions, and triple and quadruple body interaction leading to binary formation are also included in the code. Unlike the older N-Body codes, NBODY4 includes single and binary star evolution as part of the full cluster evolution.

More recently the trend is to move from GRAPE machines to GPUs. The new version of NBODY4, NBODY6, has been ported to the graphical processing units [Nitadori & Aarseth, 2012]. This is cost effective and GPUs are much more readily available compared to a custom built GRAPE. A version for supercomputers - NBODY6++ - is also available[2].

---

[1] General Purpose Graphical Processing Units

[2] More details on http://www.gac-grid.de/project-products/Applications/nbody6.html

Chapter 3

Detection Techniques: Black Holes in Globular Clusters

3.1 Black Holes

A massive star, at the end of its life, collapses under the influence of high density (and thus gravity) into an entity known as a *black hole*. Mathematically, a black hole is a volume surrounding a singularity in spacetime, where the escape velocity reaches the speed of light. The intense gravitational field can be produced by crushing the matter beyond nuclear densities. Black holes are highly dense bodies with a strong gravitational pull, but the sphere of influence is not big. They can be produced in a supernova explosion, when a massive star's exterior explodes and interior implodes. A massive star with mass between 8 $M_\odot$ and 40-50 $M_\odot$, at the end of life, fuses heavier elements till an iron-nickel inert core is left. If the inert core has mass greater than the Chandrasekhar limit ($1.4 \times M_\odot$), electron degeneracy can not keep it intact and an explosion takes place, causing the outer stellar material to detach and the interior to implode. This is known as the *Type II Supernova*. Neutron degeneracy halts the collapse of the star. If the mass of the progenitor star is less than 20 $M_\odot$, the degenerate remnant is a neutron star. For progenitor stars having mass greater than 20 $M_\odot$, but less than 40-50 $M_\odot$, the compact remnant would be a black hole. Stars having mass greater than 50 $M_\odot$ would collapse directly into a black hole. [Prialnik, 2000].

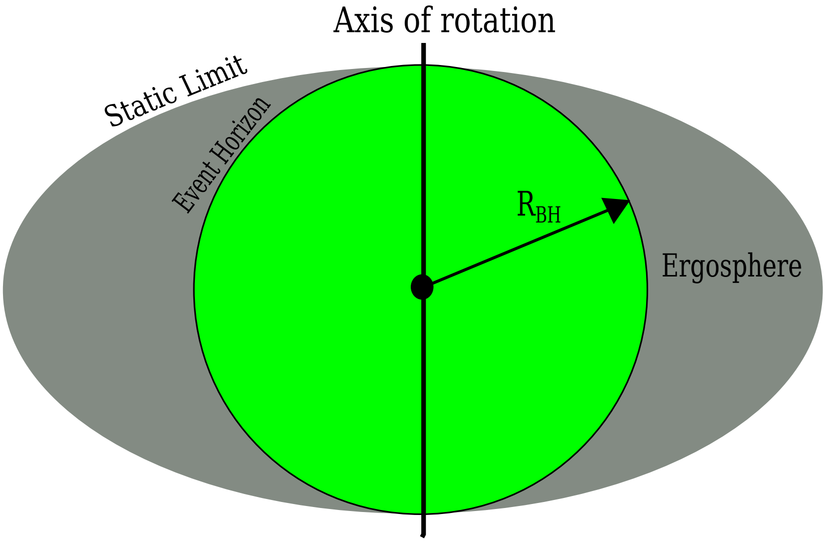

Figure 3.1: Schematic of a rotating black hole. For a Schwarzschild black hole, ergosphere and static limit does not exist. Re-drawn from the image in Karttunen *et al.* [2000].

For a non-rotating black hole, the sphere of influence is defined as

$$R_{BH} = \frac{2GM_{BH}}{c^2}, \tag{3.1}$$

where R_{BH} is known as the Schwarzschild radius, M_{BH} is the mass of the black hole, and c is the speed of light. The sphere of influence around the black hole with radius R_{BH} is known as the *event horizon*. If the Sun were to end as a black hole, it would have a 3 km Schwarzschild radius (although it will end its life as a white dwarf). Rotating black holes have another feature known as the *static limit*. The region between event horizon and static limit is known as the *ergosphere*. The rotating black hole ‘drags’ the space-time along with it in the ergosphere, a phenomenon known as *frame-dragging*. It is also known as *Lense-Thirring* effect, named after the physicists who derived the frame-dragging effect using general relativity. Any object in the ergosphere has an unstable orbit and a small change in the kinetic energy of the object can either take it to a stable orbit around the black hole or plunge it into the black hole. A schematic of such a black hole is shown in Figure 3.1.

Black holes are characterised by their *mass*, *spin*, and *electric charge*. *Schwarzschild* black holes have mass but are not charged and are not spinning. Another class of black holes known as Reissner-Nordström have mass and are electrically charged (although not spinning). The *Kerr-Newman* black holes have mass, are spinning, and are electrically charged. Black holes cannot divide into smaller black holes, but can merge with other black holes to produce a bigger black hole.

3.1.1 Black Hole Classification by Mass

The class of black holes mentioned above are known as stellar or low mass black holes (LMBHs). They weigh a few times the solar mass. At the other extreme there are black holes with masses a million or more times that of Sun (M $\sim 10^6 - 10^9$ $M_\odot$). They are known as super-massive black holes (SMBHs). A super-massive black hole, Sagittarius A (Sgr A^*), has been detected at the centre of our Milky Way galaxy [Ghez *et al.*, 1998]. They have also been suggested to exist at the centre of the elliptical galaxies and galaxy bulges [Fabbiano, 2005; Gebhardt *et al.*, 2011; Richstone *et al.*, 1998].

Black holes with intermediate mass ($\sim 10^3$ $M_\odot$) i.e. mass lying between that of LMBHs and SMBHs have also been suggested to exist [Farrell *et al.*, 2009; Gebhardt *et al.*, 2005; Gerssen *et al.*, 2002; Gultekin *et al.*, 2004]. These are known as the intermediate mass black holes (IMBHs). It has been suggested that another class of black holes, called quantum black holes or micro black holes, exists in nature. These primordial black holes were formed during the initial moments of the Big Bang, when the high density environment would have been conducive [Carr & Hawking, 1974]. Micro black holes with small mass ($\sim 10^{12}$ kg) will evaporate in a short time ($\sim 10^9$ years) by losing mass via Hawking radiation [Hawking, 1974].

3.2 Black Holes in Globular Clusters

N-body modelling of the globular star clusters have sometimes suggested the presence of either an IMBH or a collection of LMBHs at the cluster centre [Baumgardt *et al.*, 2005; Gerssen *et al.*, 2002; Mackey *et al.*, 2008; Noyola & Gebhardt, 2008]. We will look at these in turn.

3.2.1 Low Mass Black Holes

Formation of LMBHs in the star clusters is expected, as a natural consequence of the death of supermassive stars in the life of the cluster but their retention is a divisive matter. The LMBH may be ejected from the star cluster because of asymmetries in the supernova explosion. Although, if the velocity kick from the explosion is not sufficient to eject these black holes then they would constitute a sizeable dynamic sub-population in the globular star clusters [Kulkarni *et al.*, 1993; Sigurdsson & Hernquist, 1993].

LMBHs are suggested to play a vital role in globular cluster dynamical processes (see Chapter 2 for details about star cluster dynamics). Merritt *et al.* [2004] suggested that the massive stars and the stellar black holes are responsible for the formation of the cores in all globular clusters. N-body modelling by Mackey & Gilmore [2003a,b] predicts that the LMBH population could be at least partly responsible for the *core radius-age trend*[1] observed for Magellanic Cloud clusters. The trend in the Magellanic Cloud clusters is relevant to the Galactic globulars because both possess an extensive system of star clusters with comparable masses [Merritt *et al.*, 2004].

3.2.2 Intermediate Mass Black Holes

Gebhardt *et al.* [2000] and Ferrarese & Merritt [2000] suggested a fundamental relationship between black hole mass and galaxy bulge velocity dispersion known as the $M_{BH} - \sigma$ relation. A relationship also exists between the black hole mass and the galaxy luminosity, but it is not as strong. Based on this relationship, it was suggested by Gebhardt *et al.* [2002] that globular clusters may contain a central black hole with intermediate mass ($10^3 - 10^6$ $M_\odot$) (see Figure 3.2).

As a black hole with a mass of several ×1000 $M_\odot$ in a globular cluster will be considerably more massive than any other member, it is extremely unlikely to be ejected via dynamical interactions. Therefore it is quite reasonable to conclude that if a globular cluster possessed an IMBH at some stage of its evolution, it should still retain it during the present epoch. However, recently Holley-Bockelmann *et al.* [2008] suggested that even 1000 $M_\odot$ black holes can be ejected

---

[1] the core radius range (or spread) increases with increasing cluster age.

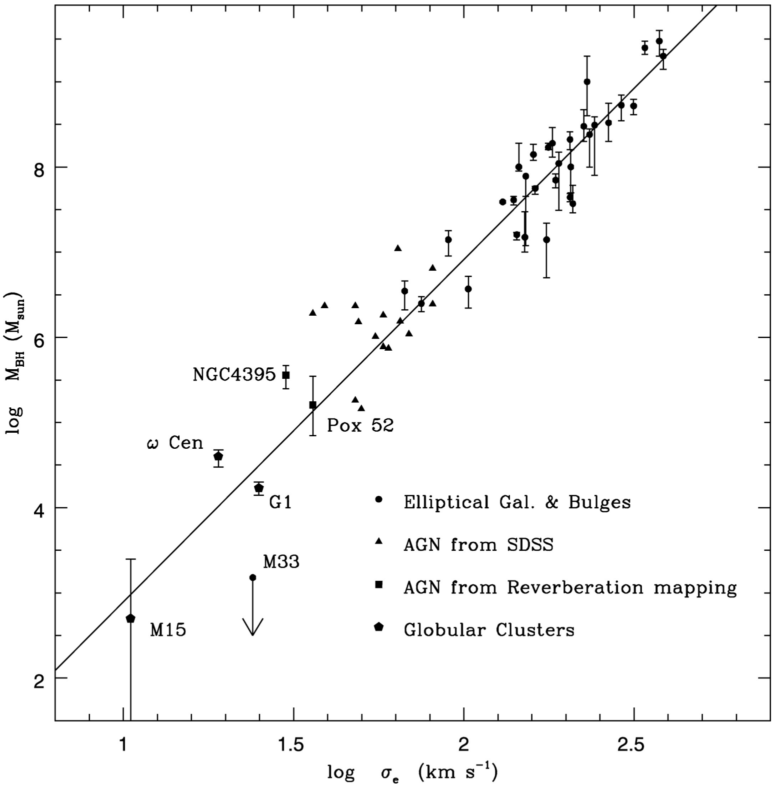

Figure 3.2: Black Hole mass - galaxy velocity dispersion relation for elliptical galaxies and bulges. Three globular clusters - M15, ω Centauri and G1 - are also shown. The extrapolation of black hole mass-velocity dispersion relation for galaxies is used to predict the BH mass for these three globular clusters. These globular cluster's black hole mass is consistent with the linear regression scatter for large masses. Figure taken from Noyola & Gebhardt [2008].

from the globular clusters by the gravitational recoil process during IMBH-LMBH interactions.

Several possible mechanisms are suggested for the formation of IMBHs in globular clusters. One possibility is through *runaway merging* [Zwart *et al.*, 2004]. This only occurs in very dense and young clusters. For clusters with shorter mass segregation time-scale for massive stars, the core collapse time scale is shorter than their main sequence lifetimes. During core collapse, the density is sufficient to initiate direct collisions between the massive stars. The massive merged object formed by the first collision has the possibility of undergoing further collisions with massive stars. This can lead to a runaway process, resulting in the production of an object (possibly an IMBH) with a mass up to 0.1% of that of the cluster mass [Zwart & McMillan, 2002]. Another mechanism for IMBH formation was put forward by Miller & Hamilton [2002]. They suggested a slow process for IMBH formation in dense clusters by the accretion of cluster stars by a black hole binary on Hubble timescale. A third formation mechanism was proposed by Madau & Rees [2001]. They suggested that IMBHs are the stellar remnants from the very first stars in the universe (Population III stars).

An altogether new mechanism was proposed by Vesperini *et al.* [2010]. It is based on the idea of multiple stellar populations in globular clusters. They suggested that seed black holes[1] can accrete the dense gas in the centre of the globular cluster during the formation of the second generation stars in the cluster. This could lead to the formation of black holes with intermediate mass.

N-body simulations [Baumgardt *et al.*, 2005] have shown that the radius of the black hole sphere of influence (R_i) within a cluster can be given as:

$$\frac{R_i}{R_h} \sim 2.5 \frac{M_{BH}}{M_C}, \tag{3.2}$$

where R_h is the cluster half-mass radius, M_{BH} is the IMBH mass, and M_C is the cluster mass. For a Galactic globular cluster with typical $R_h \sim 0.5$ parsec (pc) and $M_C \sim 2 \times 10^5$ $\mathrm{M}_\odot$, the sphere of influence should be ~ 0.1 pc. Even for the closest Galactic globular cluster, this region is only ~ 20 arcseconds in diameter.

3.3 Signatures of Black Holes in GCs

To date only indirect and/or inconclusive evidence exists for the presence of IMBHs or a population of LMBHs in globular clusters. The various “signatures” of black holes in the globular star clusters are discussed below.

---

[1] existing before the formation of second generation stars

3.3.1 Surface Brightness Profile

Initially it was thought that the core-collapsed globular clusters are the best candidates to harbour an intermediate mass black hole. This could be because of the higher densities in the core, that can lead to the formation of large black holes. N-body simulations predict that clusters with an IMBH at the centre have the appearance of normal King model clusters (see Chapter 2 for more details) with the central region having power-law profiles with ~ -0.25 slope [Baumgardt *et al.*, 2005]. Out of the 37 globular clusters mentioned by Noyola & Gebhardt [2006][1], Baumgardt *et al.* [2005] suggested that only 9 clusters are candidates with a central IMBH. N-body simulations done by Baumgardt *et al.* [2005] suggested that the formation of an IMBH by runaway merging would lead to a *larger* core than what is observed for core-collapsed clusters. They suggested that the most probable candidates to have an IMBH at the centre would have a shallow central cusp, rather than the steep central profile expected for a core-collapsed cluster. This was expected because of the Bachall-Wolf density cusp in the sphere of influence of the black hole [Bahcall & Wolf, 1976]. The cluster follows a dynamic King model profile in the outer regions.

Lanzoni *et al.* [2007] reported the presence of an IMBH surface brightness "signatures" in NGC 6388 (see Figure 3.3). Similar results were also obtained by Noyola & Baumgardt [2011]. They constructed synthetic HST images using data from realistic N-body simulations. Models with and without a central black hole were used. They concluded that a globular cluster with a central black hole would have a logarithmic slope between -0.1 and -0.4 in the central region and a core to half-light radius (r_c/r_h), that is characteristic of a cluster which has not undergone core-collapse. A globular cluster harbouring an IMBH would have a high r_c/r_h ratio but it alone is not a reliable signature for the presence of an IMBH [Hurley, 2007]. However, this predicted shallow central density profile "signature" for intermediate mass black holes has been challenged by Vesperini & Trenti [2010]. They showed that the presence of compact remnants (and absence of IMBH) can also lead to shallow central cusps, and therefore cannot be used as a reliable IMBH signature.

---

[1] Submitted in July 2004, published in June 2006

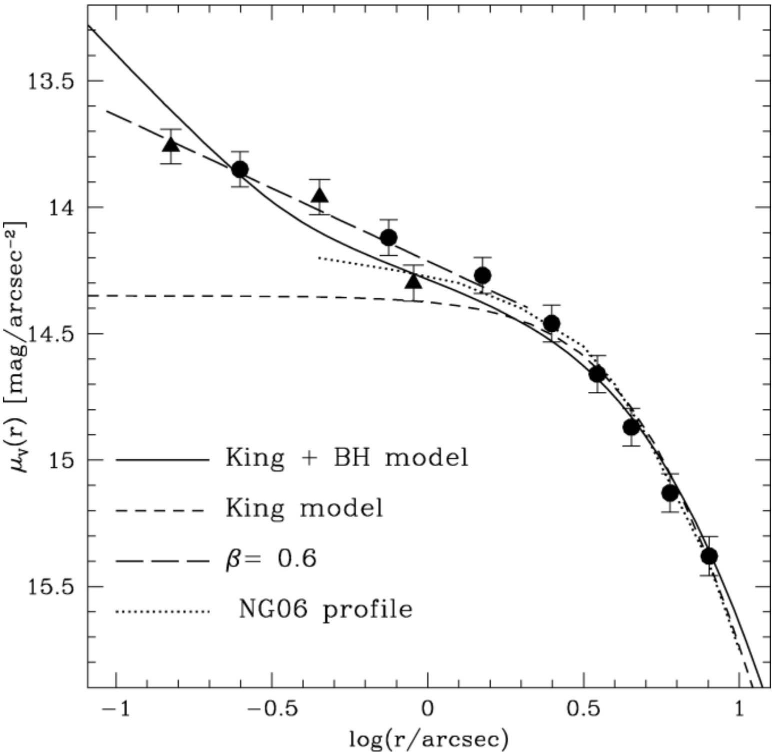

Figure 3.3: Surface brightness profile of globular cluster NGC 6388. The observational data is from the HST ACS/HRC detector. According to Lanzoni *et al.* [2007], the profile demonstrates a “signatures” of an IMBH in the core of NGC 6388. Figure taken from Lanzoni *et al.* [2007].

3.3.2 Ultra-luminous X-Ray Sources

The Eddington limit is the maximum luminosity a star can emit in hydrostatic equilibrium[1]. Mathematically, it is given as [Bradt, 2008]

$$L_{edd} = 1.2 \times 10^{38} \frac{M}{M_\odot} \qquad erg/sec, \tag{3.3}$$

where M is the object mass, and $M_\odot$ is the solar mass. For a stellar mass black hole binary, the Eddington luminosity limit is estimated to be $\sim 10^{39}$ ergs/sec. The exact value depends on the black hole mass and which elements (hydrogen or heavy elements) are accreted from the companion star [Maccarone *et al.*, 2007].

---

[1] A star is in hydrostatic equilibrium when the force due to radiation pressure is balanced by the force due to gravity

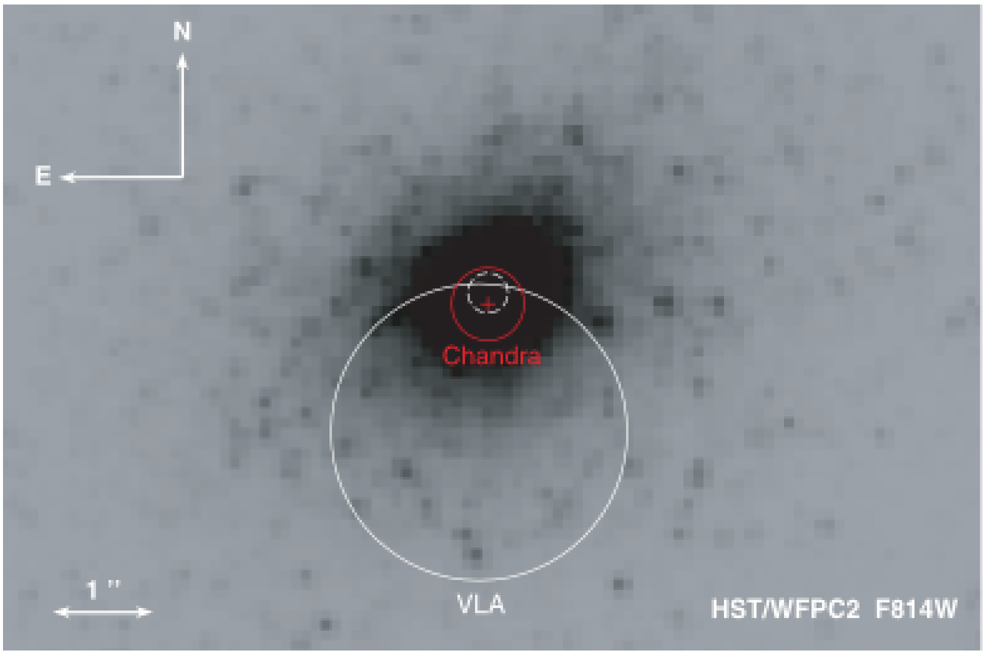

Figure 3.4: The G1 globular cluster in the Andromeda galaxy is suspected to host an intermediate mass black hole. An ultra luminous X-ray source (marked Chandra in the figure) and radio source (marked VLA) have been detected at positions which are consistent with the core of G1. Image taken from Kong *et al.* [2010].

One of the key observational evidences for the existence of IMBHs is the detection of ultra-luminous X-rays sources (ULXs) at the centre of globular clusters [Ulvestad *et al.*, 2007; Zwart *et al.*, 2004]. An example ULX detection is shown in Figure 3.4. The X-ray data has been obtained by the Chandra and XMM-Newton X-ray space telescopes. ULXs have super-Eddington luminosity i.e. luminosity greater than the Eddington luminosity limit. These are attributed to a single black hole (IMBH binary) accreting cluster stars or ionised cluster gas [Maccarone *et al.*, 2007; Pooley & Rappaport, 2006]. However, Fabbiano [2005] suggested that super-Eddington luminosity can be explained by a collection of stellar mass black holes binaries, if either the emission is anisotropic or the accretion disk is not homogeneous. A similar conclusion was also put forward by Maccarone *et al.* [2007] for ULX emission from an extragalactic globular cluster in Virgo cluster galaxy NGC 4472. Signatures of IMBH have also been seen in an extragalactic globular cluster in the Fornax cluster galaxy NGC 1399 [Irwin *et al.*, 2010]. Intermediate mass black holes have also been suggested to exist outside of the globular clusters [Farrell *et al.*, 2009; Miller *et al.*, 2003]. The exact origins of ULXs is still in dispute [Sutton *et al.*, 2012].

3.3.3 Central Radial Velocity Dispersion

Another indirect evidence or signature is the size of the central velocity dispersion (the spread in stellar velocities), measured by spectroscopy. For some globular clusters, an extremely crowded core and an unusually high velocity dispersion has been interpreted as the gravitational signature of an IMBH or a core of LMBHs. Stars passing very close to the IMBH in a cluster can, under certain circumstances, be accelerated to a much higher velocity than the cluster dispersion. Thus causing increase in the central velocity dispersion. Hubble Space Telescope measurements suggest the presence of an $\sim 2300\ \mathrm{M}_\odot$ IMBH in the Milky Way globular cluster M15 [Gerssen *et al.*, 2002], and a $\sim 1.7 \times 10^4\ \mathrm{M}_\odot$ IMBH in the Andromeda galaxy cluster G1 [Gebhardt *et al.*, 2005]. Recently, Noyola & Gebhardt [2008] suggested the presence of a $\sim 4.0 \times 10^4\ \mathrm{M}_\odot$ IMBH in the Galactic globular cluster ω Centauri (see Figure 3.5).

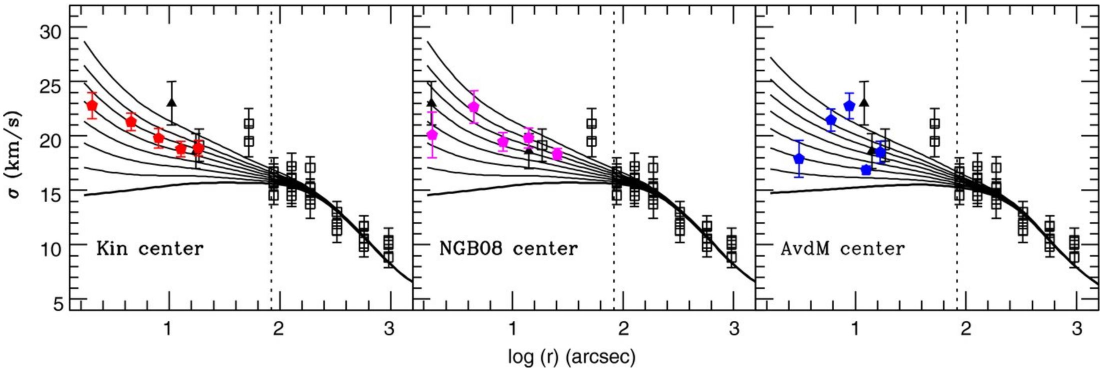

Figure 3.5: The central velocity dispersion profile of globular cluster ω Centauri. The solid red pentagons in the left hand panel are from the observed data, and various lines correspond to different black hole masses ($0,1,2,3,4,5,6,7,8 \times 10^4\ \mathrm{M}_\odot$, from bottom to top). The middle and right panels are fitting the same data with different cluster centres. Image taken from Noyola *et al.* [2010].

However, detailed N-body simulations suggest that neither of these detections require the presence of black holes; they can be explained using other stellar remnants such as neutron stars and white dwarfs [Baumgardt *et al.*, 2003a,b]. Using HST ACS images and ground based VLT/FLAMES spectroscopy, Lützgendorf *et al.* [2011] proposed a $\sim 17 \times 10^3$ $M_\odot$ IMBH at the centre of globular cluster NGC 6388. A lower estimate ($\sim 5.7 \times 10^3$ $M_\odot$) has been obtained by Lanzoni *et al.* [2007] using the surface brightness density profile method.

3.3.4 Gravitational Wave

It has been predicted that gravitational waves or "ripples" are produced during black hole mergers [Hils & Bender, 1995; Thorne & Braginskii, 1976]. Gravitational waves or radiation are produced when a mass is accelerated, which happens in the case of black hole merger with other compact objects (neutron star or black hole). The power emitted by gravitational waves may only be significant, and thus detectable, when a massive object is accelerated with velocities close to the speed of light. These gravitational waves could be detected by sensitive detectors, both in space and on the ground. According to Miller [2002], the upcoming Laser Interferometer Space Antenna (LISA) mission is one such detector, which can be used to confirm the presence of an IMBH (or collection of LMBHs) in globular clusters. Advanced LIGO (Laser Interferometer Gravitational-Wave Observatory) and the upcoming Einstein Telescope (ET) could also be used to detect IMBH-BH and IMBH-NS mergers and thus confirm the presence of IMBHs in dense star clusters [Mapelli *et al.*, 2010].

3.3.5 Radio Sources

Maccarone [2004] suggested that the ratio of radio to X-ray power can be used as a signature for the presence of an IMBH. The ratio increases with black hole mass but decreases with accretion rate. Ulvestad *et al.* [2007] used radio data from the VLA (Very Large Array) and reported the presence of an $\sim 2 \times 10^4$ $M_\odot$ accreting IMBH in the G1 globular cluster in galaxy M31, on the basis of its radio to X-ray power ratio. G1 is one of the leading candidates to host an IMBH, based on radio, X-ray and optical observations. But, analysing the latest radio observations from the VLA, Miller-Jones *et al.* [2012] were not able to find any radio source in the core of G1. They have suggested that the radio source found by Ulvestad *et al.* [2007] may be a variable source, attributed to LMXBs[1]. Similarly, no central radio source was detected by Maccarone & Servillate [2008] in NGC 2808, which was previously thought to harbour an IMBH. Strader *et al.* [2012b] used the Jansky Very Large Array (JVLA) in an attempt to detect radio sources in the cores of globular clusters M15, M19, and M22. They did not find any radio signature of an intermediate mass black hole in these globular clusters. Similarly, Cseh *et al.* [2010] did not find any radio source in globular cluster NGC 6388, which has an ULX in the core. They concluded that this may be due to a low IMBH accretion rate and thus constrained the upper limit to be a 1500 $M_\odot$ black hole (at 3σ confidence interval). A search for an IMBH at the centre of M15 using VLBI (Very Large Baseline Interferometry) has also given negative results [Kirsten & Vlemmings, 2012].

3.3.6 Kinematics of Individual Cluster Stars

The final “signature” is the one that this thesis work concentrates on. At present, the only way to establish beyond doubt the presence of an IMBH (or an LMBH population) in the cluster core, is through direct dynamical analysis of stars lying in the sphere of influence of the black hole.

Stars passing very close to an IMBH in a cluster can, under certain circumstances, be accelerated to a much higher velocity than the cluster dispersion. Drukier & Bailyn [2003] suggested that radial velocity and/or proper-motion studies of these high velocity stars could provide the evidence for the existence of a black hole in the cluster core. But the measurement of the stellar proper motions and radial velocities is hampered by the crowded cluster core as well as the small sphere of influence (see Section 3.2.2). The radial velocity approach for detection of black holes in the cluster cores will not be suitable, as we may be measuring the spectra of only the brightest stars or the integrated spectra of overlapping stars. However, it is possible to detect the proper motions of these high velocity stars using high resolution imaging facilities. In a star cluster at 7 kiloparsecs from Earth, a high velocity star with transverse velocity ~100 km/sec would have a proper motion of 3 mas/year across the sky. Such a rapid motion

---

[1] Low Mass X-Ray Binaries

would be detectable by centroiding each star's position in images taken over a baseline of a few years.

Images from HST are already being used to determine the internal proper-motion of the stars in Galactic globular clusters. The three most studied clusters (for the presence of black holes) are 47 Tuc, M15, and Omega Centauri. The proper motion studies in the central cores of these clusters have only returned negative results (see Anderson & van der Marel [2010]; McLaughlin *et al.* [2006]; McNamara *et al.* [2003] for more details). McNamara *et al.* [2012] determined the proper motions of the stars in globular cluster NGC 6266, another cluster candidate suggested by Baumgardt *et al.* [2005] to harbour an IMBH. Again, they did not find any signature of a central IMBH (see Figure 3.6).

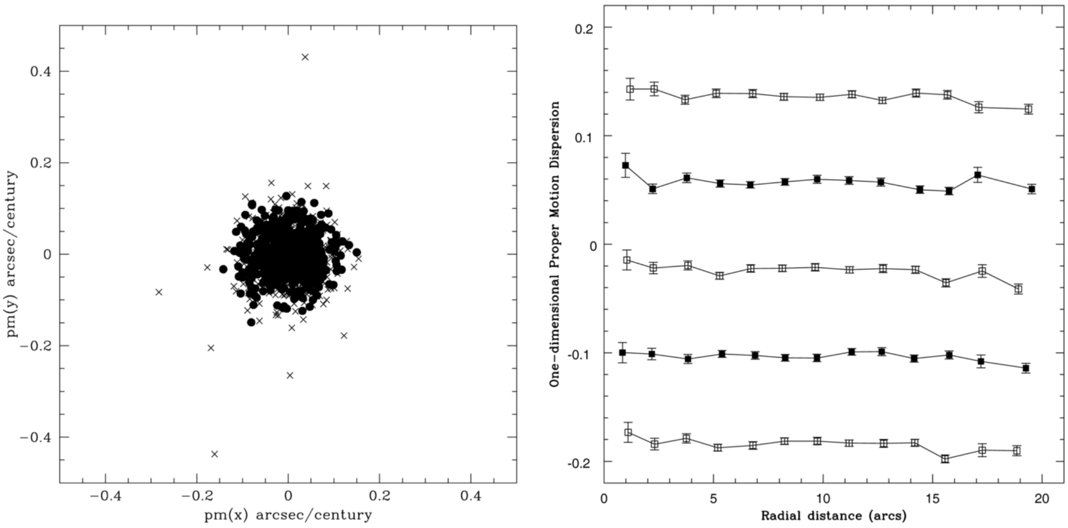

(a) (b)

Figure 3.6: Proper motion of stars in the cluster NGC 6266. (a) Proper motion per century in the RA and DEC directions; (b) The proper motion dispersion is flat from the core to the radius of 18″, leading McNamara *et al.* [2012] to conclude that NGC 6266 does not host an IMBH. Figures taken from McNamara *et al.* [2012].

Ground based telescopes have also been used for proper motion detection. Samra *et al.* [2012] used the Gemini North telescope with a 3.8 year baseline to determine the internal proper motion of stars in the core of M71 (NGC 6838). The MPG/ESO 2.2 meter telescope was used by Sariya & Yadav [2012] to determine the relative proper motion of stars in NGC 6809. Absolute proper motions of Galactic globular clusters have also been determined using both HST [Kalirai *et al.*, 2007] and ground based telescopes [Zloczewski *et al.*, 2011]. Combined with absolute radial velocity information, this gives the cluster's velocity vector through space. Proper motion dispersion measurements are complimentary to the central radial velocity dispersion using spectroscopy as proper motion of fainter and blended stars can be determined.

Chapter 4

High Angular Resolution Imaging of GCs

High angular resolution images for the present study were taken from the Hubble Space Telescope (HST) archive. Multi epoch images from the second generation Wide Field Planetary Camera 2 (WFPC2), and third generation Advanced Camera for Surveys (ACS), were used to determine the proper motion of the stars in our selected galactic globular clusters. This chapter gives a brief introduction to digital imaging (Section 4.1). Section 4.2 discusses the HST instrumentation, issues and solutions related to processing the images, and calibrating photometry and astrometry.

4.1 Digital Imagers

Before digital sensors for electronic imaging cameras were invented, photographic plates were routinely used in astronomy. Many of the solar system objects and minor planets were discovered using photographic plates. But in the past few decades, digital imagers have almost completely replaced the photographic plates because of their better efficiency and simple image acquisition and processing. Two main types of digital imaging detectors exist - Charge-Coupled Devices (CCD) and Complementary Metal Oxide Semiconductor (CMOS). In astronomy, CCDs have traditionally been preferred because of their higher dynamic range, uniformity and lower cost [Howell, 2006]. Therefore, only CCD detectors are considered in the following sections.

Charge coupled devices work on the principle of the photoelectric effect. The photo active silicon substrate of the CCD is divided into smaller units called pixels[1] and each of these pixels acts like a charge collector. Incident light on the CCD is converted into photoelectrons and stored in the depletion layer of the MIS (metal-insulator-semiconductor) interface. At the end of the exposure, these electrons are collected by the readout electronics and the analog voltage for each pixel is converted to digital units and stored in the memory. The digitised values are known as ADU (analog-to-digital units) or simply counts. Silicon is opaque to electromagnetic radiation between 1.1 and 10 eV (electron volts) but it can absorb light from the near infra-red to the soft X-ray regime. This defines the spectral response function of the CCD detector.

4.1.1 CCD Characteristics

The main characteristics of a CCD are discussed briefly in the following subsections. The emphasis is on the properties that will be frequently cited in the rest of the thesis.

4.1.1.1 Quantum efficiency

The quantum efficiency (QE) of a CCD is the measure of its efficiency to convert incoming photons into electrons. It is the ratio of the number of photons detected to the number of photons hitting the device. The QE for a CCD varies with the incoming photon wavelength. Old photographic plates had a maximum QE of $\sim 10\%$ but present day CCDs are able to achieve $\sim 90\%$ QE in some wavelength bands [Howell, 2006]. Back-illuminated CCDs have better QE compared to the front-illuminated CCDs, especially in bluer light because polysilicon based metallic gates absorb the bluer light and thus reduce the QE in front-illuminated CCDs (see Figure 4.1). QE is also sensitive to the temperature and it decreases as the CCD is cooled because the photon absorption length increases with silicon bandgap increase.

---

[1] can be a square or rectangle in shape

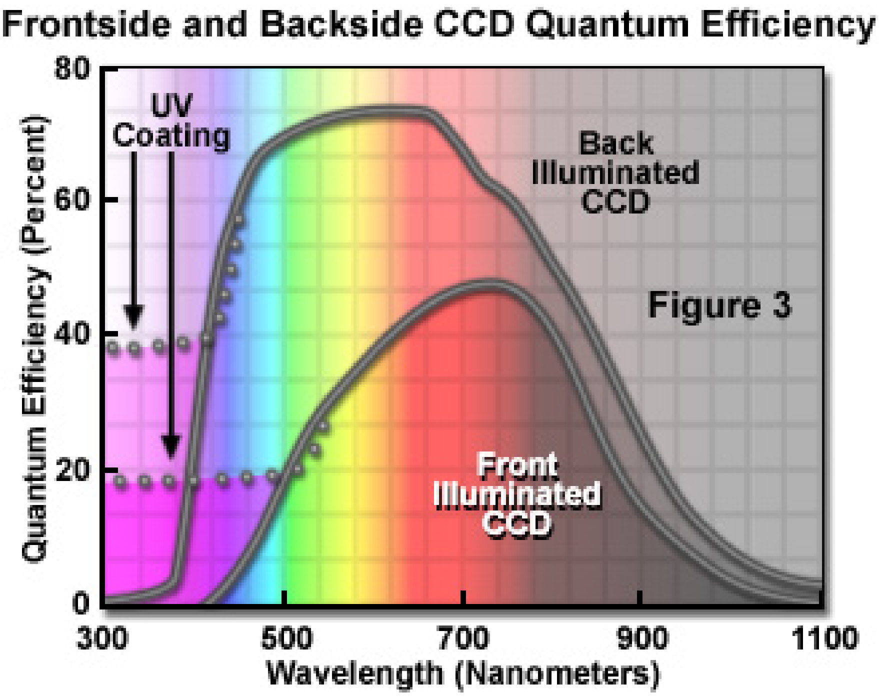

Figure 4.1: Quantum Efficiency of the back and front-illuminated CCDs. Image taken from Hamamatsu Photonics online article titled "*Quantum Efficiency*" (http://learn.hamamatsu.com/articles/quantumefficiency.html).

4.1.1.2 Charge Transfer Efficiency

Charge transfer efficiency (CTE) is the fraction of the photo-electrons that are moved from each pixel during the sensor readout. Most modern CCDs have CTE of 0.999995 or more [Howell, 2006], where 1.0 is perfect efficiency. The second generation HST WFPC2 instrument had some CTE issues, which are discussed briefly in Section 4.2.1.3. The readout from a CCD uses three clock cycles - one for parallel transfer, one for serial transfer, and the last one to signal out to the read-out amplifier (see Figure 4.2). The pixels values in the rows are read in parallel and transferred to the serial shift-register. The accumulated value in the columns of the serial shift-registers is transferred to the output node serially. Thus, the pixel closest to the amplifier would require the least number of transfers whereas the pixel furthest would require the most number of transfers. Therefore, charge transfer inefficiency would be more significant with increased number of charge transfer and prominent towards the chip edges and corners.

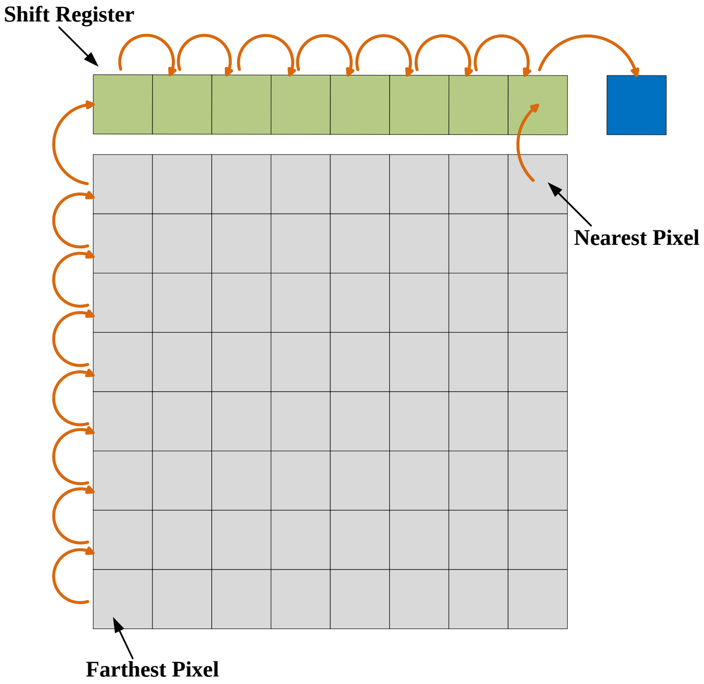

Figure 4.2: Charge transfer efficiency in CCDs. Pixel values are moved in parallel transfer to the serial shift register and then serially transferred to the output node. Image re-drawn from the Hamamatsu Photonics online article titled "*Electronic Imaging Detectors*" (http://learn.hamamatsu.com/articles/digitalimagingdetectors.html).

4.1.1.3 Dark Current

Even when the camera shutter is closed, electrons are generated in the silicon substrate. This is because of thermal noise and is known as the *dark current*. As the thermally generated electrons are indistinguishable from the photoelectrons, they become part of the signal. Dark current can be easily quantified and subtracted from the images. As dark current is dependent on the temperature of the CCD, doubling with every 6 - 9 °C rise in temperature (see Figure 4.3), most astronomical detectors are cooled to very low temperatures[1] to reduce the thermally generated electrons.

---

[1] CCDs for astronomy purposes are either cooled by liquid nitrogen or using the Peltier effect.

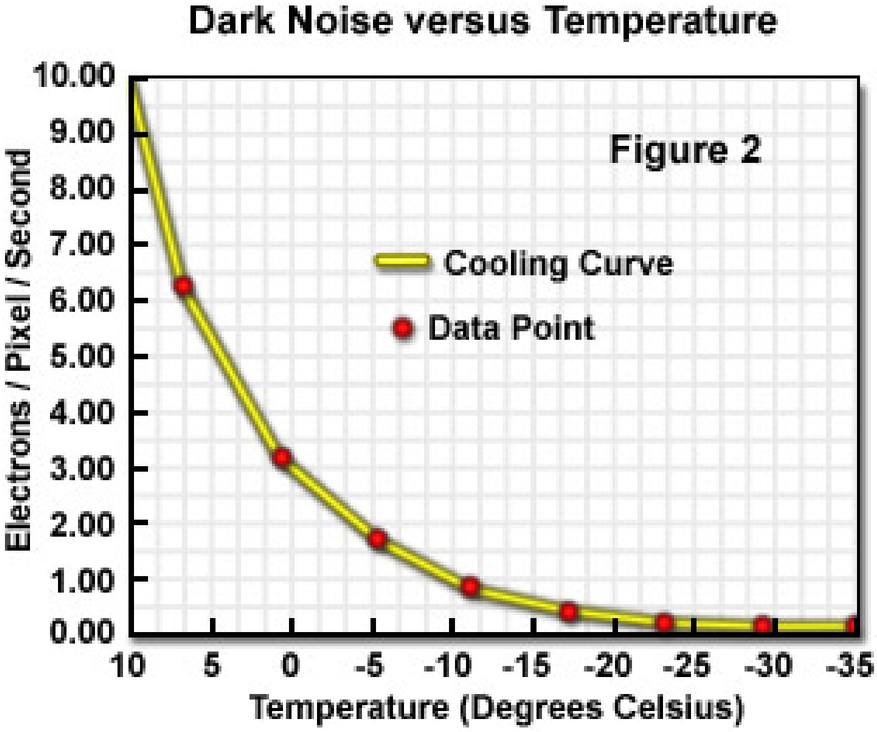

Figure 4.3: CCD dark current-temperature plot. Dark current doubles every $6 - 9$ °C rise in temperature. Image taken from Hamamatsu Photonics online article titled "*CCD Noise Sources and Signal-to-Noise Ratio*" (http://learn.hamamatsu.com/articles/ccdsnr.html).

4.1.1.4 Gain, Noise and Dynamic Range

Gain is the conversion factor between the number of photo electrons in each pixel and its value in ADU. If gain is 1.0 then the instrument outputs values which correspond directly to the photon count. Most of the HST instruments have different gain settings for different observing requirements.

The output digitised value from a CCD depends on the A/D converter. A 16-bit A/D converter can output values varying from 0 to 65535 ADU. This defines the intensity resolution of the CCD. The full well capacity of a CCD pixel is the maximum electron count a pixel can hold. We can also calculate the gain required to cover the full dynamic range if we know the full well capacity of the CCD and the choice of A/D converter. For example, for a device with a pixel well depth of 295,000 electrons, and a 16-bit A/D converter, a gain setting of 4.5 e^{-}/ADU would be optimal.

CCDs have three main noise sources - photon noise, dark noise, and the readout noise. Photon noise is the statistical variation in arrival of the photons incident on the CCD. It is Poisson in nature and therefore varies as square-root of the total number of photons i.e. $\sqrt{N}$. Dark noise arises because of the statistical variation in thermally generated electrons in the silicon substrate. Similar to photon noise, dark noise also follows Poisson distribution. Readout noise is result of conversion of charge carriers to voltage and analog to digital conversion of the signal and is Gaussian in nature. Readout noise is the most dominant of these three for low signal-to-noise (SNR) exposures, whereas photon noise starts to dominate for high illumination pixels (see the next section for more details).

Dynamic range of a CCD is the ratio of CCD full well depth and the read noise

Dynamic Range = Full Well Depth (electrons) / Read Noise (electrons)

A CCD with full well capacity of 18,000 electrons per pixel and read noise of 4 electrons would have dynamic range of 4500. Dynamic range is interrelated to the bit depth of the CDD's analog-to-digital converter. In order to utilise the full depth capacity of the above mentioned example CCD, a 12-bit ADC would be sufficient[1].

4.1.2 Digital Image Characteristics

The characteristics of digital images acquired by CCDs are briefly discussed in the following subsections.

4.1.2.1 Field of View and Pixel Scale

In astronomy, the field of view (FOV) of an imager is the area it covers in the sky. It is generally given in arcminutes or in arcseconds. The CCD pixel scale is the sky covered per pixel (in the units of arcsecond/pixel). For example - the FOV of the WFPC2 PC1 detector is $34'' \times 34''$ and the pixel scale is $0.046''$/pixel.

---

[1] A 12-bit ADC would detect $2^{12} - 1 = 4095$ gray levels.

The pixel scale is connected to the telescope's focal length f (in mm) and CCD pixel size μ (in micrometer) by the following relation [Howell, 2006]:

$$P = \frac{206,265\ \mu}{1000\ f} \tag{4.1}$$

4.1.2.2 Signal-to-Noise Ratio

As mentioned in the last section, digital images also have noise in addition to the signal. The quality of the digital image can be quantified using the Signal-to-Noise ratio (SNR). Mathematically, SNR can be defined as [Howell, 2006]

$$SNR = \frac{N}{\sqrt{N + n_{pix}(N_s + N_D + N_R^2)}}, \tag{4.2}$$

where signal is equal to the total number of photons (N) received on n_{pix} number of pixels, and noise is the sum of the intrinsic photon noise ($\sqrt{N}$), and product of n_{pix} with the sky background per pixel (N_s), the dark current in electrons per pixel (N_D) and the square of the readout noise (N_R). For a bright source, photon noise dominates and Equation 4.2 is reduced to

$$SNR = \sqrt{N} \tag{4.3}$$

But for faint sources, other terms are equally important and may be more significant than the intrinsic photon noise.

4.1.2.3 Point Spread Function

No optical system is ideal and therefore the image is degraded as it passes through the system. Degradation of the image by the optical system is quantified by looking at the response of the system to a point light source. The output in the spatial domain is known as the *Point Spread Function* (PSF). Its counterpart in the frequency domain is called the Optical Transfer Function (OTF), which is nothing but the Fourier transform of the point spread function. In mathematical terms, an image can be thought of as the convolution of an object and the point spread function of the system

$$IMAGE = OBJECT \;\otimes\; PSF, \tag{4.4}$$

where, $\otimes$ is the convolution symbol. The convolution of an object and the PSF can be re-written in integral form as

$$I(u, v) = \int\int O(x, y)\; PSF(u - x, v - y)\; dx\; dy \tag{4.5}$$

For a distortion and aberration free system, the PSF can be represented by an Airy function. As convolution of functions in real space is equivalent to multiplication in Fourier or frequency space, Equation 4.5 can be re-written in the Fourier domain as:

$$\tilde{f}(I) = \tilde{f}(O \otimes PSF) = \tilde{f}(O) \;*\; \tilde{f}(PSF) \tag{4.6}$$

We will be using this equation later on when discussing image deconvolution.

4.1.2.4 Blooming

In Section 4.1.1.4, we defined the pixel well full depth for a CCD. In long exposures of bright objects, the pixel well can overflow or saturate with photoelectrons and these electrons will then transfer to the adjacent pixels (up and down the same column of pixels). The pattern resulting from this is known as bleeding or blooming. An example of a bleeding pattern, created by a bright star on the HST WFPC2 detector is shown in Fig 4.4. The 45 degree crossed lines are the diffraction spikes, arising at the thin metal vanes which support the secondary mirror - known as the *spider*.

4.2 Hubble Space Telescope

Astronomical data for this thesis was taken from the Hubble Space Telescope archive, hosted by the European Southern Observatories[1] (ESO). Images from two HST instruments - WFPC2 and ACS - were used to study the proper motion of the stars in the selected galactic globular clusters.

---

[1] http://archives.esac.esa.int/hst/

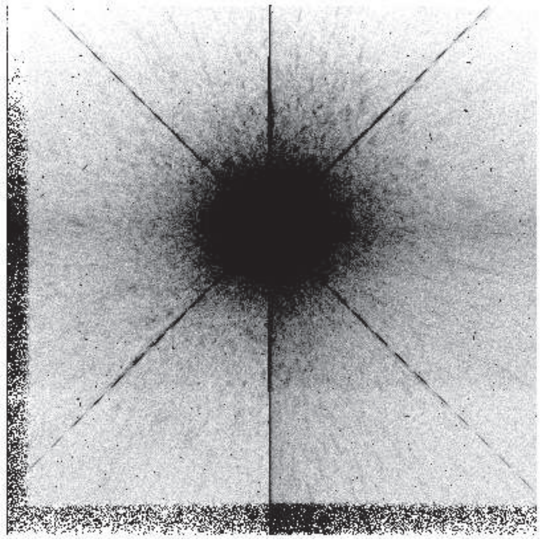

Figure 4.4: Bleeding and diffraction spikes in an HST WFPC2 PC1 image of an overexposed bright source, in an inverted colour image. Image taken from the WFPC2 instrument handbook [McMaster & Biretta, 2008].

Space telescopes have the benefit of observing above the Earth's atmosphere and are thus not affected by the atmospheric turbulence and attenuation as well as able to observe in wavelengths which are blocked by Earth's atmosphere. The Hubble Space Telescope with a 2.4 meter aperture and a Ritchey Chretien optical design, was launched in 1990 on the Space Shuttle Discovery. It orbits in the low earth orbit (LEO) at an altitude of $\sim$ 600 km and takes about 97 minutes to orbit earth once. HST observes in the electromagnetic region between 110 nm to 3 μm.

Since the time HST was launched, four servicing missions (SM) have taken place. In addition to installing the optical correction unit (COSTAR) to compensate for the primary mirror spherical aberrations, the original wide field camera WF/PC was replaced with the second generation Wide Field Planetary Camera 2 in servicing mission 1 (SM1; December 1993). The Advanced Camera for Surveys was installed in servicing mission 3 (SM3B; March 2002). Schematics of the HST and the location of the different instruments after servicing mission 3 are shown in Figure 4.5 and Figure 4.6 respectively. The WFPC2 was placed on the centre of the focal plane of the telescope whereas ACS is off axis. For telescope guiding, fine guidance sensors (FGS) are used. After SM3B, HST also had the Near Infrared Camera and Multi-Object Spectrometer (NICMOS). The WFPC2 was replaced with the Wide Field Camera 3 (WFC3) in the last servicing mission (SM4; May 2009).

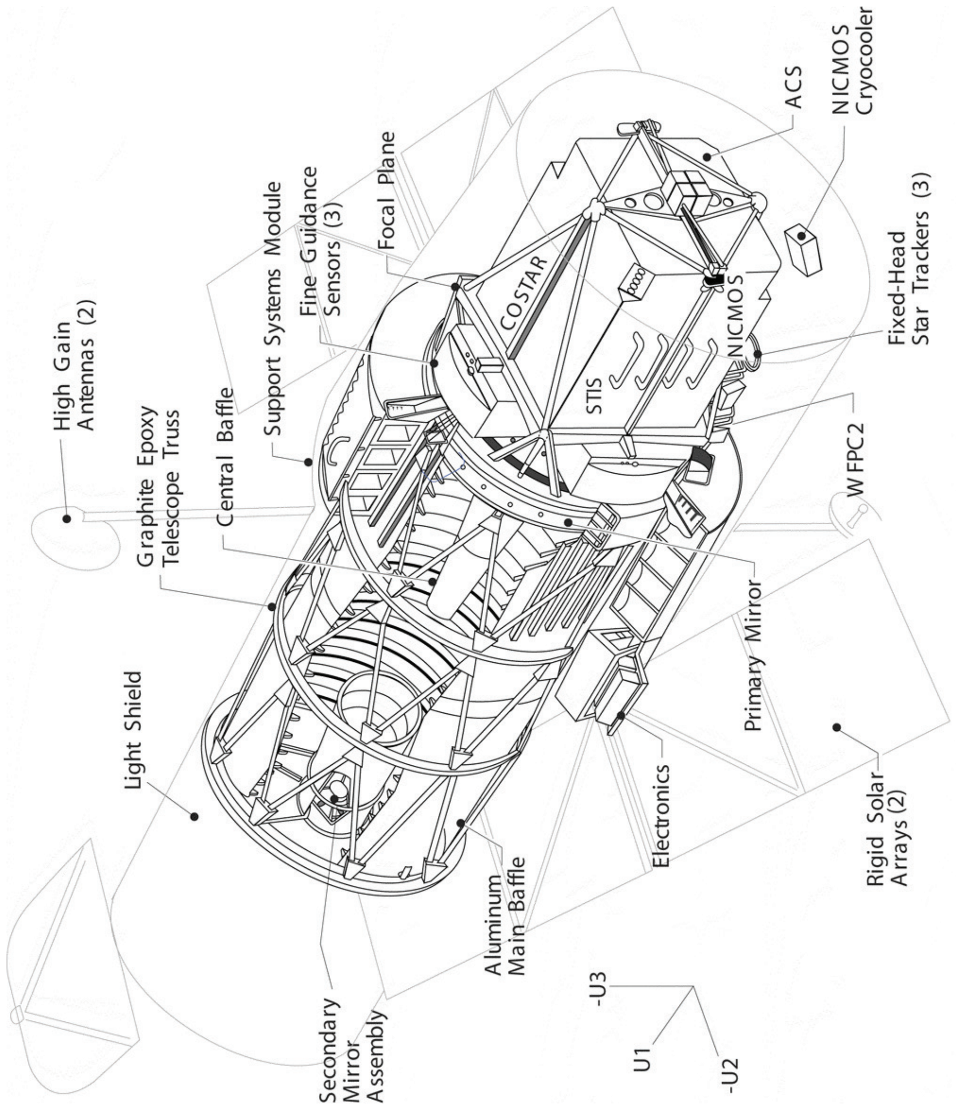

Figure 4.5: Hubble Space Telescope schematic showing the position of the instruments and spacecraft modules. Image taken from the HST Primer for Cycle 16 [Karakla & Rose, 2010].

The following sub-sections deals with the WFPC2 and ACS instrument characteristics.

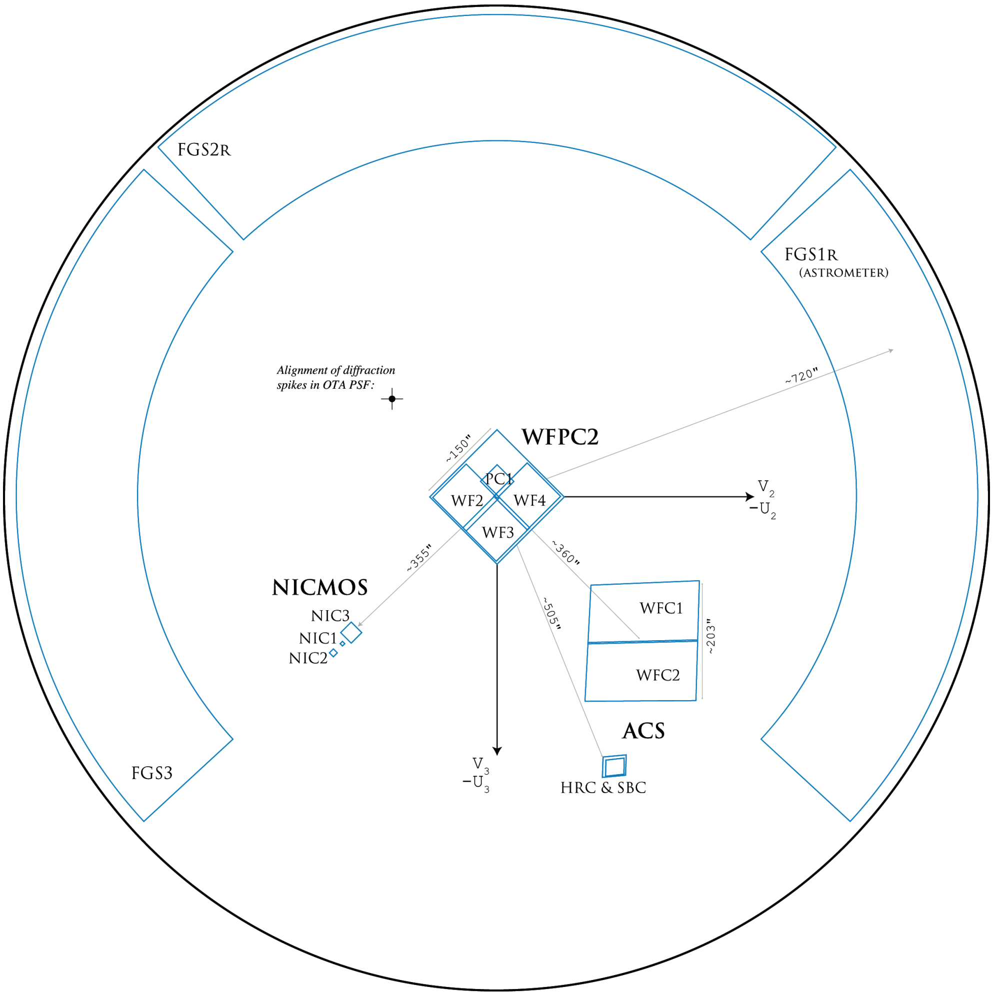

Figure 4.6: The position of different instruments in the HST focal plane. Image taken from the HST Primer for Cycle 16 [Karakla & Rose, 2010].

4.2.1 Wide Field Planetary Camera 2

4.2.1.1 Instrument Characteristics

The WFPC2 was a two dimensional photometer with three “wide field” CCDs and one high resolution “planetary camera” CCD. All the three CCDs have 800×800 pixel resolution. The three Wide field CCDs (pixel scale $\sim 0.1''$) make an “L” shaped region which covers a $150'' \times 150''$ sky area. The planetary camera (pixel scale $\sim 0.046''$) covers $34'' \times 34''$ of sky (see Figure 4.7(a)). The optical configuration of the instrument is shown in Figure 4.7(b).

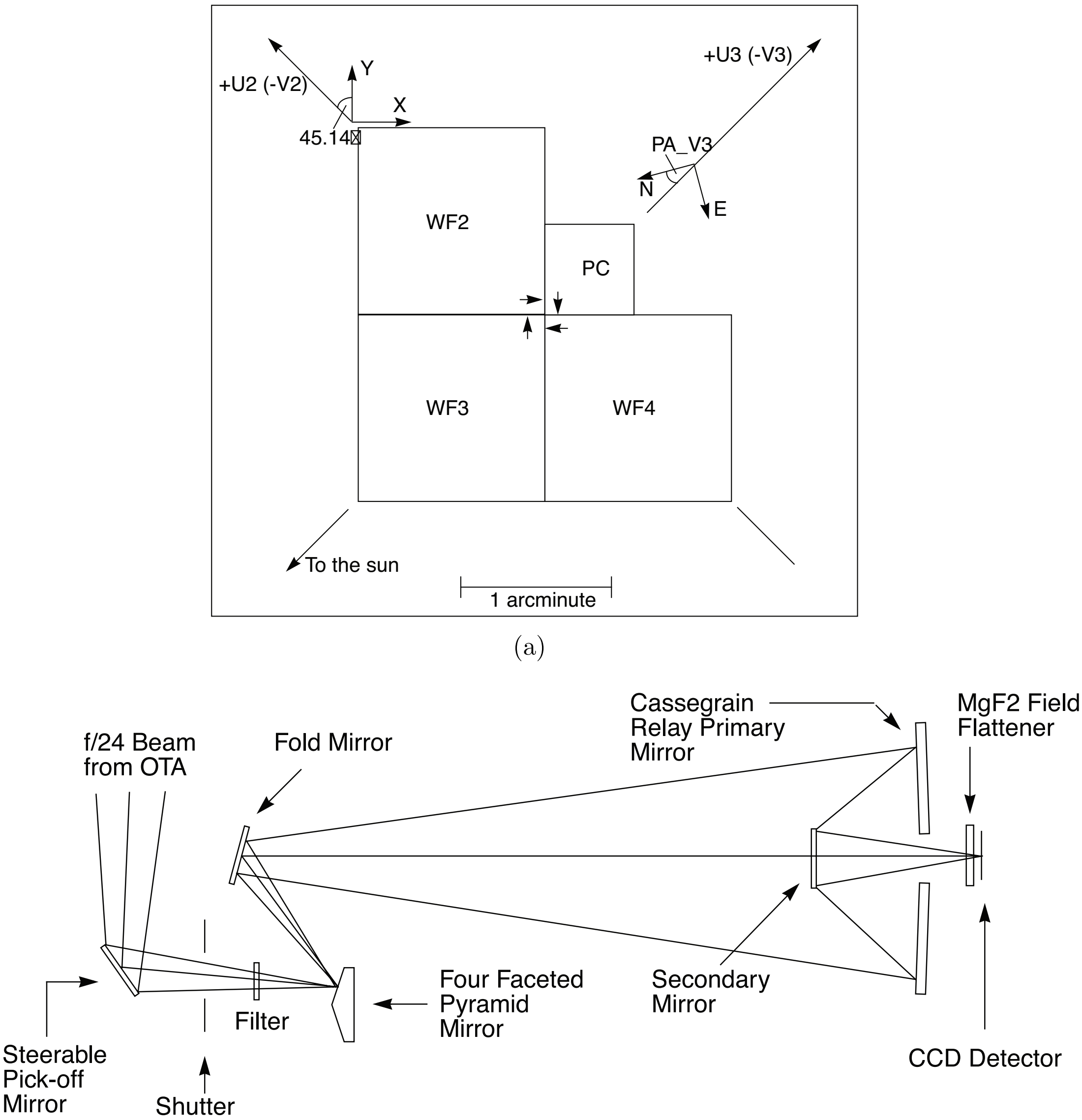

(a)

(b)

Figure 4.7: (a) WFPC2 field of view (FOV) on the sky and (b) WFPC2 Optical assembly. Images taken from the WFPC2 instrument handbook [McMaster & Biretta, 2008].

Basic WFPC2 instrument characteristics are listed in Table 4.1 (see [McMaster & Biretta, 2008] for more details). The WFPC2 CCDs had peak quantum efficiency of only 40% although it drops to 10% in the UV region. The variation of the QE with wavelength for the WFPC2 is shown in Figure 4.8. These plots

Parameter	**Value**
CCD type	Loral front-side illuminated
Pixel and CCD format	800 × 800 × 3 CCDs (WFC) / 800 × 800 × 1 CCD (PC)
Pixel size	$15^2 \mu m$
F-number	F/12.9 @WF F/28.3 @PC
Spatial Resolution	$0.0996''$ @WFC / $0.0455''$ @PC
Field of View	$150'' \times 150''$ @ $0.1''$/pix $34'' \times 34''$ @ $0.046''$/pix
Wavelength range	1150Å - 11,000Å
Gain	7.0 e^-/DN 14.0 e^-/DN
Read Noise	5 e^- (Gain = 7.0) / 7 e^- (Gain = 14.0)
Digital Saturation	27,000 e^- (Gain = 7.0) / 53,000 e^- (Gain = 14.0)

Table 4.1: HST WFPC2 instrument characteristics

are generated using data from STSDAS synphot[1] tables [Laidler *et al.*, 2008]. All four CCD peaks in QE at around 700 nm.

As shown in Figure 4.4, WFPC2 saturated images show vertical bleeding, horizontal smearing, 45° diffraction spikes and “ghosts” images (internal reflection). These artefacts have to be taken care of while reducing the images and performing photometry.

4.2.1.2 Filter Set

The WFPC2 has 48 filters - on 12 filter wheels with 4 filters each. The filter set includes long-pass (LP), wide (W), medium (M) and narrow (N) band filters. It covers the electromagnetic spectrum from the infra-red to ultraviolet. Apart from the broad band Johnson-Cousins UBVRI [Bessell, 2005] filters[3], WFPC2 also includes two Wood’s Sun blind filters and the Strömgren filter set. The transmission throughput of the broad band WFPC2 filters is shown in Fig 4.9.

---

[1] STScI’s synthetic photometry package in IRAF STSDAS package

[2] Downloaded from STScI Calibration Database (CDBS) website: http://www.stsci.edu/hst/observatory/cdbs/cdbs_throughput.html

[3] The broad band filters are not the exact Johnson-Cousins filters

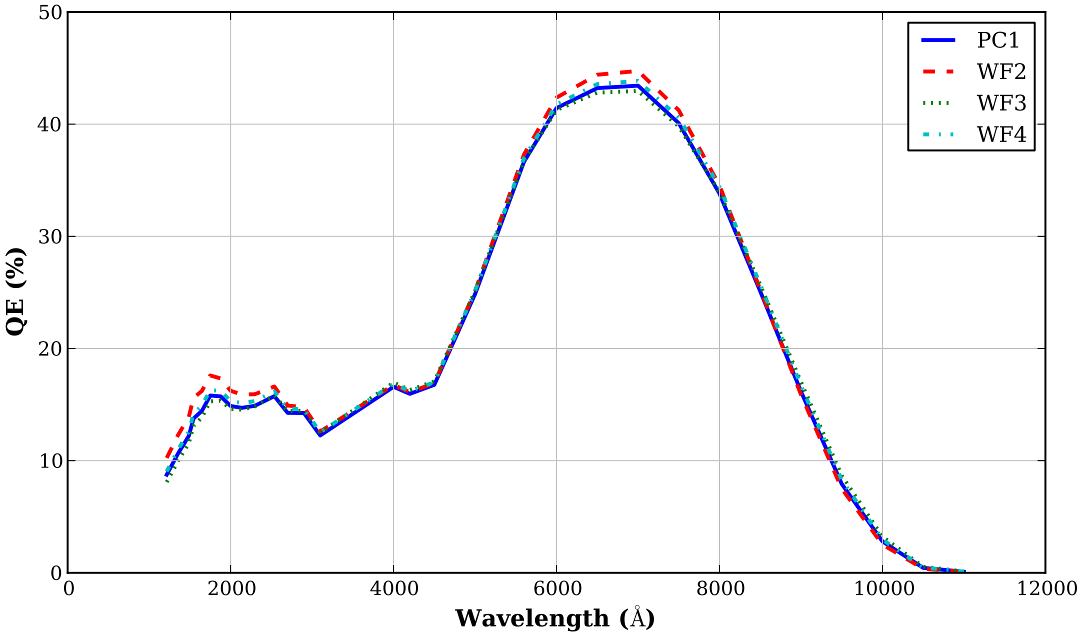

Figure 4.8: WFPC2 CCDs' quantum efficiency variation with wavelength. Data from the STSDAS *Synphot* component throughput tables[2].

4.2.1.3 Cosmic Rays, Hot Pixels and CTE

Galactic cosmic rays and protons in Earth's radiation belt interact with HST CCDs and can create high pixel values in the digital images. Flux due to the cosmic rays is dependent on the length it travels in the silicon substrate and not on the energy of the cosmic ray. Because of this, for the under-sampled WFPC2 CCDS, sometimes cosmic rays may be detected as stellar objects on a single exposure. The standard way to remove these high pixel value cosmic rays is to co-add multiple frames of the same scene and statistically reject any pixel with a big flux difference. The IRAF[1] task *crrej* is commonly used for this purpose.

Hot (or warm) pixels are pixels with elevated dark current, often due to radiation damage. For WFPC2 at -88°C, hot pixels can have dark current anywhere between 0.02 $e^{-}sec^{-1}$ and several $e^{-}sec^{-1}$ [Gonzaga & Birreta, 2010]. Warm pixels can affect aperture photometry of faint objects in crowded fields as well as aperture photometry with large apertures. Decontamination maps provided by

---

[1] Image Reduction and Analysis Facility

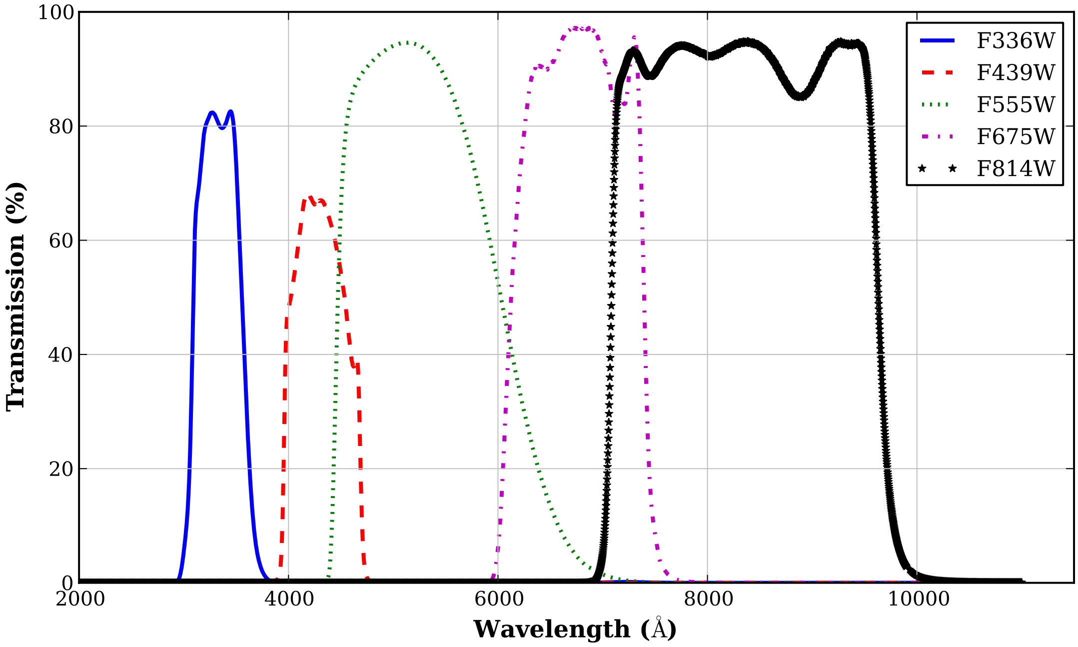

Figure 4.9: WFPC2 broad band filter response curves - they are analogous to the UBVRI filter set. Data from the STSDAS *Synphot* component throughput tables.

STScI[1] are used in the STSDAS[2] task *warmpix* to repair these pixels. Hot pixels have already been repaired in the flat-fielded reduced images in the HST archive.

As mentioned in Section 4.1.1.2, charge transfer efficiency is the fraction of photoelectrons that are read out from the CCD. WFPC2 CCDs have imperfect CTE and as a result, objects located further away from the readout amplifiers appear fainter [Gonzaga & Birreta, 2010]. This can result in incorrect stellar magnitudes for stars which are situated away from the amplifier. Dolphin [2009] proposed corrections to quantify this magnitude loss. This is briefly discussed below.

Magnitude loss is calculated in both x and y directions (of the image). For a star with brightness FLUX, sky background BG, position (X, Y) and observation date OBS, CTE corrections in the X and Y direction (XCTE and YCTE respectively) are given as:

---

[1] Space Telescope Science Institute

[2] Space Telescope Science Institutes' IRAF package

$$XCTE = 0.0077\ e^{-0.050\ lbg}\ (1 + 0.10\ yr)\ \frac{X}{800} \tag{4.7}$$

$$YCTE = 2.41\ ln[(1+c)\ e^{0.02239\ max(1.0-0.201\ lbg+0.039\ lbg\ lct+0.002\ lct,0.15)\ (\frac{Y}{800})} - c], \tag{4.8}$$

where

$$\begin{aligned} lbg &= \frac{1}{2}(BG^2+1) - 1 \\ yr &= \frac{OBS - 49461.9}{365.25} \\ lct &= ln(FLUX) + 0.921\ XCTE - 7 \\ c &= 0.958\ (yr - 0.0255\ yr^2)\ e^{-0.450\ lct} \end{aligned} \tag{4.9}$$

The instrumental magnitude of a point source with CTE corrections can then be written as

$$m = -2.5\ (counts/sec) + ZP - XCTE - YCTE, \tag{4.10}$$

where ZP is the photometric zeropoint. For our work, stellar photometry of globular star clusters has been corrected for the CTE imperfections using the above formula.

4.2.1.4 Optical Distortions

Optical distortion in the WFPC2 images is a combination of distortion due to the corrective optics for each CCD chip, as well as the global distortion arising from the optical telescope assembly. The original distortion correction proposed by Holtzman *et al.* [1995] were inadequate to take care of the linear skew terms. Anderson & King [2003] proposed a third order polynomial solution for distortion correction, which is calculated separately for each WFPC2 chip.

The basic idea behind the corrections is to normalise the raw object positions; X_{raw} and Y_{raw}, to the centre of the usable chip area

$$\begin{aligned} X &= \frac{X_{raw} - 425}{375} \\ Y &= \frac{Y_{raw} - 425}{375} \end{aligned} \tag{4.11}$$

and then apply the third order polynomial distortion corrections

$$\begin{aligned} \delta x &= a_1 + a_2 X + a_3 Y + a_4 X^2 + a_5 XY + a_6 Y^2 + a_7 X^3 + a_8 X^2 Y + a_9 XY^2 + a_{10} Y^3 \\ \delta y &= b_1 + b_2 X + b_3 Y + b_4 X^2 + b_5 XY + b_6 Y^2 + b_7 X^3 + b_8 X^2 Y + b_9 XY^2 + b_{10} Y^3, \end{aligned} \tag{4.12}$$

where filter dependent coefficients (a_1, b_1 etc.) are tabulated in the Anderson & King [2003] paper. Distortion corrected coordinates for the object are then given as

$$\begin{aligned} X_{corr} &= X_{raw} + \delta x \\ Y_{corr} &= Y_{raw} + \delta y \end{aligned} \tag{4.13}$$

Optical distortion not only affects astrometry, but also photometry of the objects. Optical distortion causes sky covered by the pixels to differ, especially at the edges and the corners of the CCD. Flat-fielding overcorrect flux for ‘smaller’ pixels because it corrects the surface brightness. But the integrated object flux for a point source in a fixed aperture is still affected by 1% to 5% [Gonzaga & Birreta, 2010]. Pixel Area Maps (PAM) (available on the STScI website) are used to correct photometric errors arising because of the geometric distortions.

Apart from the geometric distortion mentioned above, WFPC2 chips also suffer from a manufacturing defect known as the *34th row defect*. This caused every 34th row on the CCDs to be narrower than the other rows. This leads to both photometric and astrometric errors. Anderson & King [1999] modelled the residual of the defect as a saw-tooth wave and provided the following astrometric and photometric corrections

Astrometric Correction

$$y - y_{raw} = \begin{cases} 0.06\,(0.25 - p) & \text{if } p \leq 0.5 \\ 0.0008920\,(p - 17.3167) & \textit{otherwise} \;, \end{cases} \tag{4.14}$$

where y_{raw} is the observed y coordinate value and

$$p = (y + 3.70)\ mod\ 34.1333 \tag{4.15}$$

Photometric Correction

Photometric correction involves multiplying the image by a factor of 0.97 to de-correct the flat fields

$$P(i,j) = \begin{cases} 0.97\,P(i,j) & \text{if } (j + 3.95)\,mod\,34.1333 \leq 1.0 \\ P(i,j) & otherwise \end{cases} \tag{4.16}$$

4.2.1.5 Point Spread Function

The WFPC2 point spread function is under-sampled, spatially varying, and has high frequency structure in the "wing" [McMaster & Biretta, 2008]. Before the corrective optics were installed, the fraction of the incident light was reduced by a factor of 5 in the central 0.1$''$ because of optical telescope assembly (OTA) spherical aberrations [McMaster & Biretta, 2008]. The residual spherical aberrations were reduced after the installation of the corrective secondary mirrors. Residual spherical aberrations still makes measurement of faint objects in crowded fields problematic, and reduces the accuracy of astrometric measurements.

The WFPC2 detectors are affected by the charge diffusion of electrons to adjacent pixels, causing blurring of the image. As the temporal variation of HST PSFs is minimal, a tool was developed by Krist *et al.* [2011] to model the analytical PSF for the HST detectors. The software package is known as TinyTIM and is freely available from the STScI website[1]. TinyTIM allows to take into account pointing jitter and the small temporal focus variations.

Analytical point spread functions generated for different filters and chip positions of the WFPC2 detector are shown in Figure 4.10. Figures 4.10(a) and 4.10(b) show the difference between the PSF for two different filters at the same chip position. The spatial variation of PSF is depicted in Figures 4.10(c) and 4.10(d), which are generated for the same filter but at different chip positions.

---

[1] http://www.stsci.edu/hst/observatory/focus/TinyTim

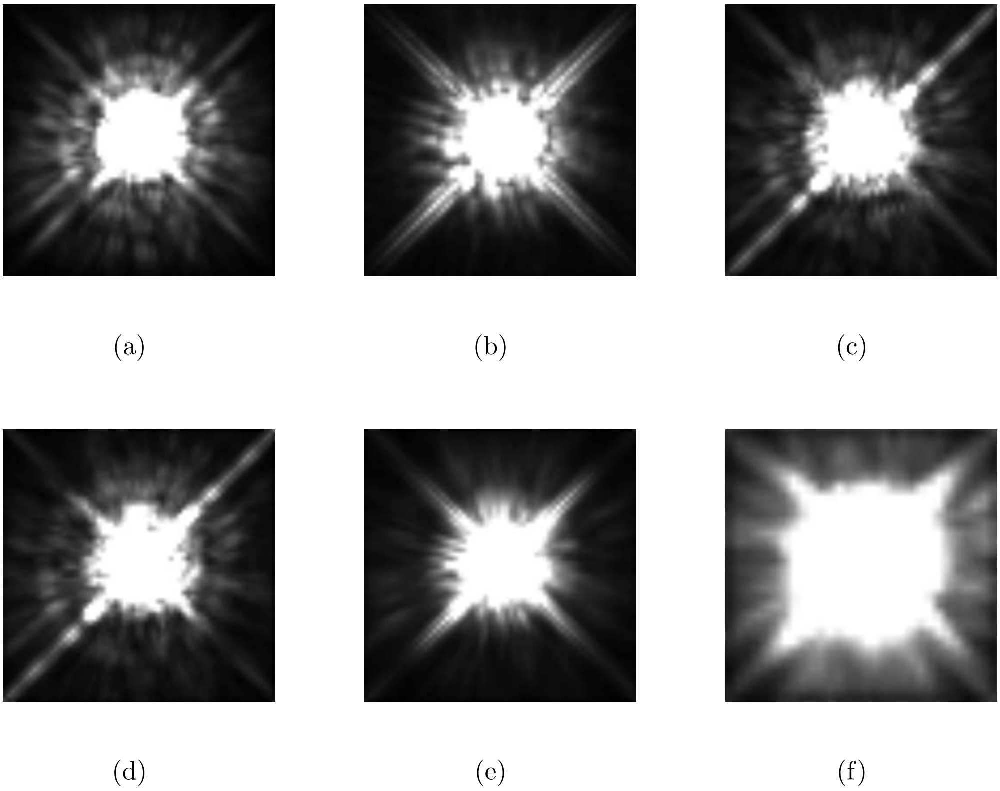

(a) (b) (c)

(d) (e) (f)

Figure 4.10: HST WFPC2 TinyTIM point spread functions. (a) F336W filter at PC chip position (400,400); (b) F814W at PC chip position (400,400) (c) F439W at PC chip position (100,100) (d) F439W at PC chip position (700,700) (e) F555W on PC chip (f) F555W on WF3 chip. These are generated for a PSF radius of 1.5″.

The difference in PSF for chips PC1 and WF3 is shown in Figures 4.10(e) and 4.10(f). High frequency "wings" structure are also evident in all the point spread functions.

In this thesis, TinyTIM PSFs were used as the "first guess" point spread functions for deconvolving the globular cluster images.

4.2.2 Advanced Camera for Surveys

The Hubble Space Telescope's ACS instrument is the third generation wide field imaging camera with deep survey capability. It was commissioned during the

2002 servicing mission (SM3B). Section 4.2.2.1 describes the basic instrument characteristics, including its optical design, filter set, distortion, and point spread function.

4.2.2.1 Instrument Characteristics

The HST ACS consists of a Wide field camera (WFC), covering the visible to near-IR spectral region, a high resolution camera (HRC) with imaging capability between far-UV to near-IR, and a solar blink imaging camera (SBC). Basic instrument detector characteristics are listed in Table 4.2. The WFC and HRC use CCD sensors, while the SBC uses a Multi-Anode Microchannel (MAMA) imaging photon-counting detector.

Parameter	**Value**
CCD type [WFC & HRC]	Scientific Imaging Technologies (SITe), back illuminated
Pixel and CCD format	Mosaic of 2 4096 × 2048 CCDs (WFC) / 1024 × 1024 (HRC) / 1024 × 1024 (SBC)
Pixel size	15μm @WFC 21μm @HRC 25μm @SBC
F-number	F/12.9 @WFC F/28.3 @HRC
Spatial Resolution	$0.05''$ @WFC / 0.028 × $0.025''$ @HRC / 0.034 × $0.030''$ @ SBC
Field of View	$202''$ × $202''$ @WFC / $29''$ × $26''$ @HRC / $34.6''$ × $30.8''$ @SBC
Wavelength range	3500Å - 11,000Å @WFC / 1700Å - 11,000Å @HRC / 1150Å - 1700Å @SBC
Gain	0.5, 1.0, 1.4, 2.0 e^-/DN @WFC / 1, 2, 4, 8 e^-/DN @HRC
Read Noise	4.2 e^- @WFC / 4.7 e^- @HRC
Full Well Depth	84,700 e^- @WFC / 155,000 e^- @HRC

Table 4.2: HST ACS detector characteristics. The HRC and SBC cameras have different spatial resolution along with two axis because of the 25° tilt to the principal optical axis, causing smaller scale along the radial direction of the field of view than along the tangential direction [Maybhate, 2010].

The optical designs of the WFC, HRC, and SBC detectors are shown in Figure 4.11. All the detectors have separate corrective optics to compensate for the primary mirror aberrations.

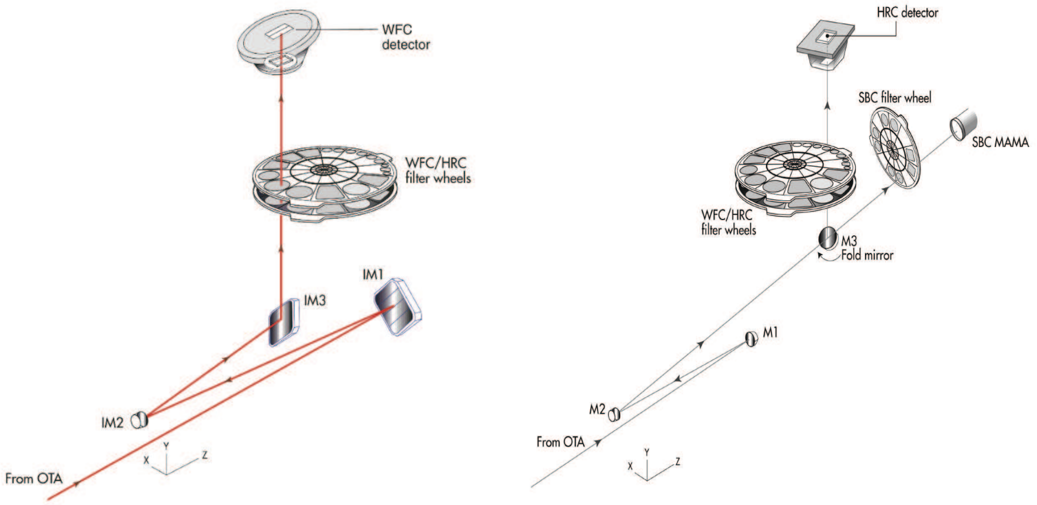

(a) (b)

Figure 4.11: (a) ACS optical configuration for the WFC detector and (b) for the SBC and HRC detectors. Images taken from the HST ACS Instrument Handbook [Maybhate, 2010].

The Quantum efficiency of the WFC and the HRC detectors is shown in Figure 4.12. Responsive quantum efficiency (RQE) of the CCD sensor includes corrections related to the instrument sensitivity in orbit.

The wide field camera comprises of two chips; WFC1 and WFC2, separated by an inter-chip gap of ~ 50 pixels. The HRC has a fixed occulting finger at the upper left of the chip, which casts a shadow on every image. ‘Dithering’ the telescope pointing by $\sim 2''$ between exposures allows the ‘lost’ data to be recovered. Images from the WFC detector were used for the present work.

4.2.2.2 Filter Set

The ACS includes three filter wheels - two for the WFC/HRC detectors and one for the SBC detector. The two filter wheels for WFC/HRC have 40 filters in total, plus 1 CLEAR[1] filter each. Filters include broadband ACS & SDSS filter

---

[1] CLEAR aperture centred at 6200Å with 5200Å width

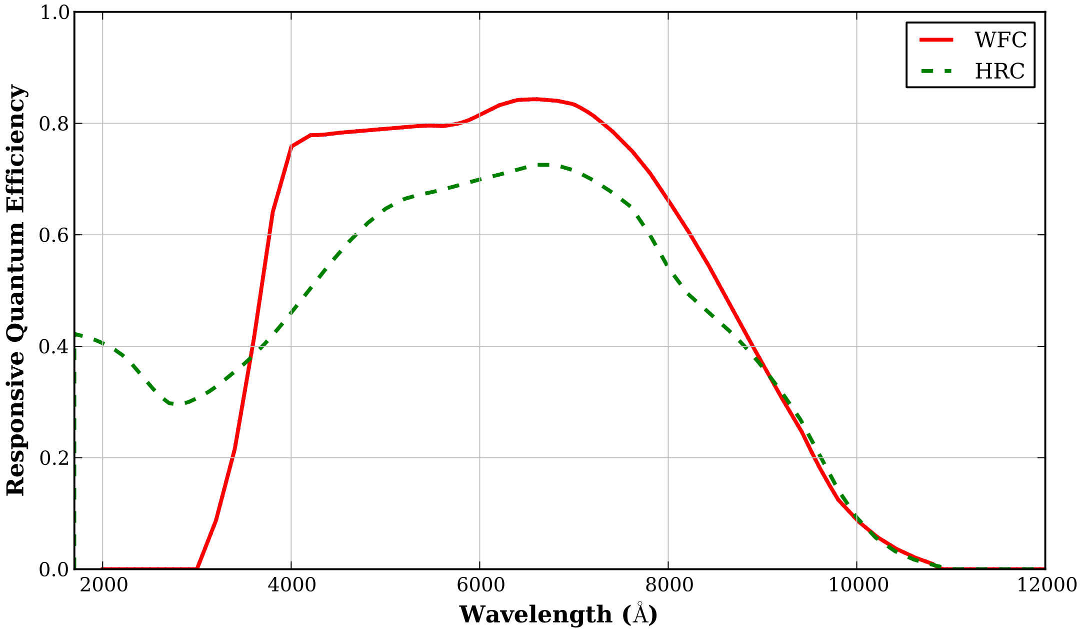

Figure 4.12: Quantum efficiency variation with wavelength for the ACS WFC and HRC detectors. Data from the STSDAS *Synphot* component throughput tables.

sets, narrow band filters, spectroscopic dispersers, and polariser filters. The SBS filter wheel has 8 filters. The optical throughput of the ACS broadband filters is shown in Figure 4.13. Compared to that of the WFPC2 filters in Figure 4.9, the ACS bandpasses are generally broader and higher in efficiency.

4.2.2.3 Cosmic Rays, Hot Pixels and CTE

Like all the HST instruments, ACS detectors are also affected by the cosmic rays. As described in Section 4.2.1.3, co-adding images in the same filter and pointing can remove most of these cosmic rays. In the case of the ACS detectors, cosmic ray removal algorithm is built into the IRAF *Multidrizzle* and *pyDrizzle* tasks.

Radiation damaged pixels in detectors can lead to elevated dark current. For the ACS detectors, any pixel with dark current between 0.02 $e^{-}sec^{-1}$ and 0.08 $e^{-}sec^{-1}$ are tagged as warm pixels and pixel with dark current above 0.08 $e^{-}sec^{-1}$ are tagged as hot pixels in DQ (Data Quality) masks [Maybhate, 2010]. Approximately every month, the CCD chips are annealed (raising the temperature of the chip) to repair these hot pixels. Overall the hot pixel increase trend is linear,

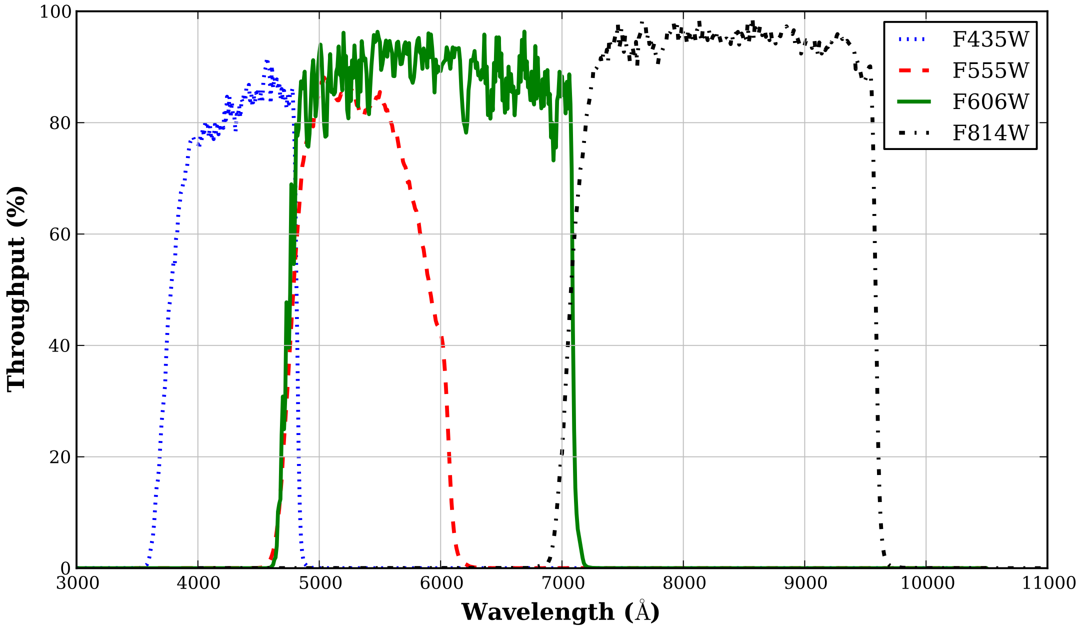

Figure 4.13: ACS broad band filter throughput with wavelength. Data from the STSDAS *Synphot* component throughput tables.

with almost 1200 new hot pixels (with dark current $> 0.04\, e^{-}\ sec^{-1}$) added every day on the WFC CCD [Pavlovsky *et al.*, 2006]. A similar trend is also seen on the HRC detector, with a small drop every time the chip is annealed (see Figure 4.14).

Because of the harsh radiation environment, the ACS detector's CTE is not perfect. As noted in Section 4.1.1.2, CTE degradation can lead to incorrect integrated counts in aperture photometry and thus reduced brightness of the source. This will obviously lead to errors in the photometric magnitude of the objects. Analytical solutions have been devised to rectify for this loss for both the parallel and the serial transfers. Although, for both the WFC and HRC detectors, the charge loss as due to CTE are insignificant. Riess & Mack [2004] suggested the following corrections for the time dependent WFC CTE errors:

$$YCTE = 10^{A}\ \ SKY^{B}\ \ FLUX^{C}\ \frac{Y}{2048}\ \frac{MJD - 52333}{365}, \tag{4.17}$$

where FLUX is the total flux enclosed in an aperture and SKY is the sky value measured adjacent to the star (in units of electrons), Y is y pixel value, MJD is

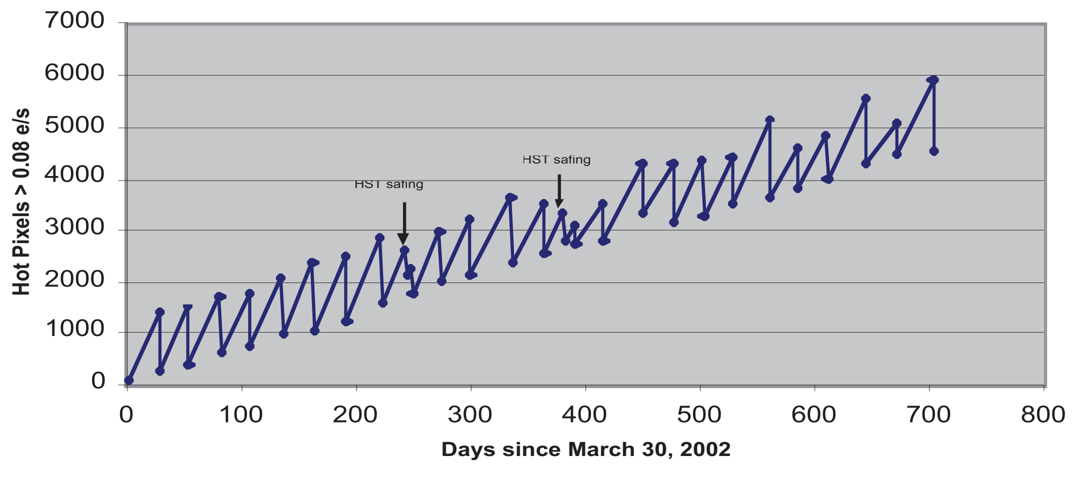

Figure 4.14: Hot pixel growth rate for the ACS HRC detector. Taken from ACS Data Handbook [Pavlovsky *et al.*, 2006].

modified Julian date, and A, B & C are fit parameters. Values of A, B and C are given in Table 2 in Riess & Mack [2004]. Similarly, for the HRC detector, the parallel CTE correction can be parameterized as follows -

$$YCTE = 10^{A}\ SKY^{B}\ FLUX^{C}\ \frac{Y}{1024}\ \frac{MJD - 52333}{52714 - 52333} \tag{4.18}$$

Symbols in Equation 4.18 have the same meaning as in Equation 4.17. Values of the A, B and C best fit parameters are given in Table 6.2 in Pavlovsky *et al.* [2006].

4.2.2.4 Optical Distortions

The HST ACS is situated at an off-axis position in the focal plane - see Figure 4.6. This causes the projected sky coverage of the pixels to be elongated in one direction (tangential direction) compared to the radial direction, and pixel area is not the same across the detector. STScI provides geometric distortion correction polynomial coefficients for ACS images in *IDCTAB* FITS tables. The PyRAF module *Multidrizzle* can be used apply this distortion correction to the images. The corrected positions (x_c, y_c) in arcseconds are given as [Hack & Cox, 2000]:

$$
\begin{aligned}
x_c &= \sum_{i=0}^{k} \sum_{j=0}^{i} a_{ij} \; (x - x_r)^j \; (y - y_r)^{i-j} \\
y_c &= \sum_{i=0}^{k} \sum_{j=0}^{i} b_{ij} \; (x - x_r)^j \; (y - y_r)^{i-j}
\end{aligned}
\tag{4.19}
$$

where (x, y) are image pixel values, (x_r, y_r) are reference pixel coordinates, k is order of the polynomial fit, and a_{ij} & b_{ij} are polynomial coefficients (provided in the *IDCTAB* tables). The inverse transformation, from corrected positions in arcseconds to uncorrected pixel values, can be determined using the following complementary equations [Hack & Cox, 2000]

$$
\begin{aligned}
x &= x_r + \sum_{i=0}^{k} \sum_{j=0}^{i} c_{ij} \; x_c^j \; y_c^{i-j} \\
y &= y_r + \sum_{i=0}^{k} \sum_{j=0}^{i} d_{ij} \; x_c^j \; y_c^{i-j}
\end{aligned}
\tag{4.20}
$$

where, again c_{ij} and d_{ij} are polynomial coefficients for the inverse transformation and are included in the *IDCTAB* table. The above solution only provides correction up to 0.1 pixel accuracy. For distortion correction better than 0.01 pixels, one can use STScI's *DGEOXY* FITS files [Anderson & King, 2004].

4.2.2.5 Point Spread Function

Comparing Tables 4.1 and 4.2, it can be seen that the sampling of the ACS WFC/HRC point spread function is $\sim 2\times$ better than the WFPC2 detector. The PSFs are also spatially varying, although not to the extent of WFPC2. This is because the ACS uses the off-axis optics whereas the WFPC2 uses Cassegrain repeater optics, which causes field dependent obscuration pattern [Krist, 2003]. Like the WFPC2, the ACS chips are also affected by the charge diffusion of electrons to adjacent pixels. Charge diffusion in the ACS can be modelled using a pixel response function (PRF). Like the WFPC2, analytical PSF models of ACS PSFs can be modelled using TinyTIM, which also takes into account the PRF of the CCD. ACS WFC point spread functions generated by TinyTIM are shown in

Figure 4.15. Off-axis geometric distortion is clearly evident in the images.

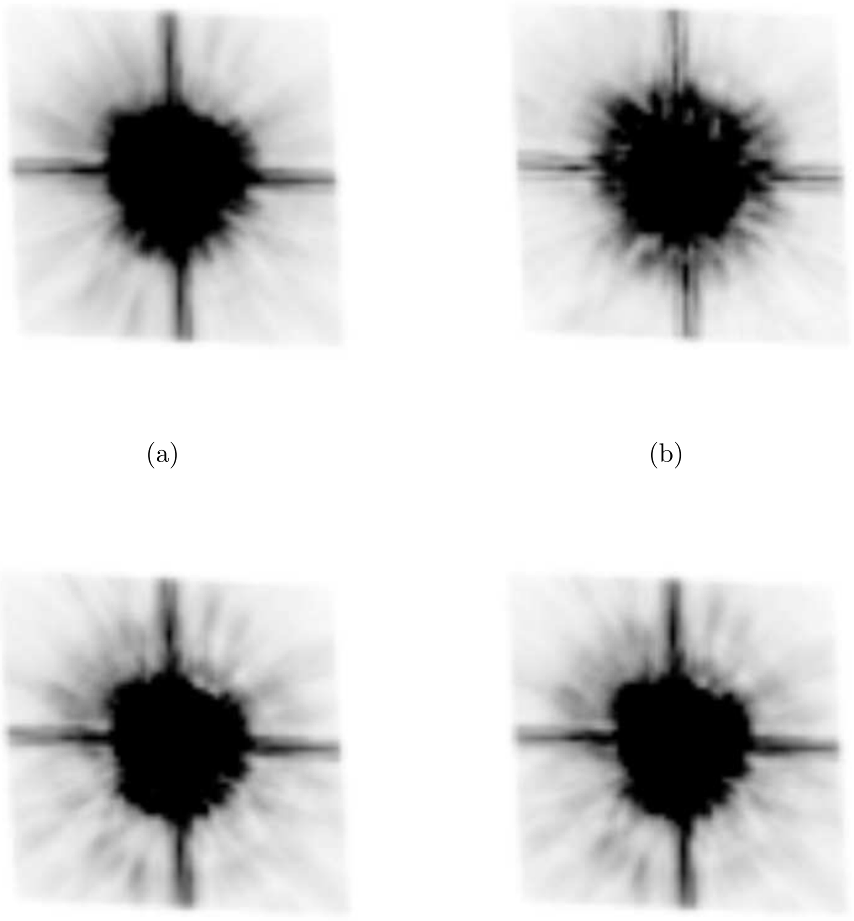

(a) (b)

(c) (d)

Figure 4.15: Inverted colour ACS WFC TinyTIM PSFs for different filters and positions within the CCD chip. (a) F606W (b) F814W at the same WFC1 chip position (c) F555W at WFC1 chip position (500,500) (d) F555W at WFC1 chip position (2000,1000).

Similarly, HRC point spread functions for different filters and chip positions are shown in Figure 4.16.

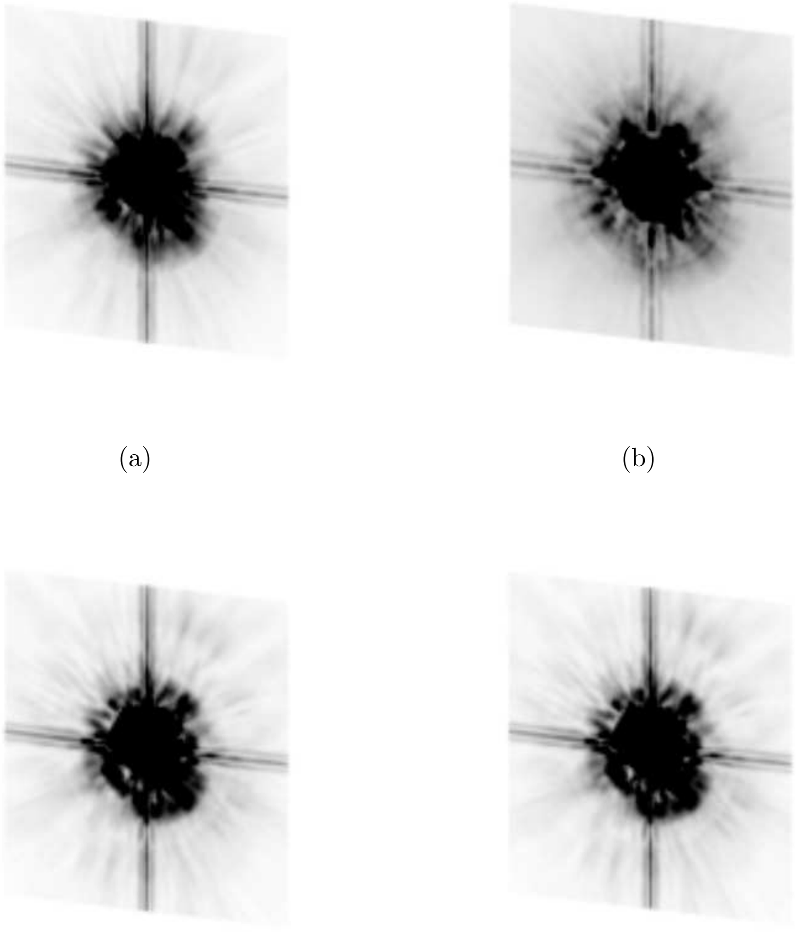

(a) (b)

(c) (d)

Figure 4.16: Inverted colour ACS HRC TinyTim PSFs for different filters and positions within the CCD chip. (a) F606W (b) F814W at the same chip position (c) F555W at chip position (100,100) (d) F555W at chip position (800,800).

Chapter 5

HST Data Reduction, Deconvolution, and Astrometry

For the proper motion determination of stars in globular clusters, positional accuracy of the stellar positions is of paramount importance. As the technique we developed for accurate star detection and position determination is based on image deconvolution, the restoration of degraded images is introduced in Section 5.1, with emphasis on the Maximum Entropy Method (MEM) of deconvolution. Our sub-sampled deconvolution technique, which is the method developed to do sub-pixel astrometry, is described in Section 5.2. A detailed account of the astronomical pipeline developed for star detection and differential proper motion determination is given in Section 5.3.

5.1 Image Restoration

Image restoration refers to the reconstruction or recovery of the image that has been degraded by noise or instrumental aberrations. Mathematically, in the spatial domain, the degraded image can be represented as (similar to Equation 4.4)

$$g(x, y) = f(x, y) \otimes h(x, y) + \eta(x, y), \tag{5.1}$$

where $\otimes$ is the convolution symbol, f(x,y) is the object, h(x,y) is the degradation function, and $\eta(x, y)$ is the noise. Alternatively, in the frequency or Fourier domain,

$$G(x,y) = F(x,y) \times H(x,y) + N(x,y), \tag{5.2}$$

where G(x,y), F(x,y), H(x,y) and N(x,y) are the Fourier transforms of g(x,y), f(x,y), h(x,y) and $\eta(x,y)$, respectively. We have used the fact that the convolution of the functions in the spatial domain is equivalent to multiplication in the Fourier domain. Theoretically, the original image F(x,y) can be determined if G(x,y) and H(x,y) are known and we are able to model the image noise N(x,y). This means finding the inverse solution of Equation 5.2.

In astronomy, one is interested in the instrument degradation function called the Point Spread Function (see Section 4.1.2.3 for more details). A ground based telescope's PSF is mainly affected by the atmospheric seeing, whereas a space telescope's PSF is diffraction limited. Therefore image restoration in astronomy basically involves deconvolving the PSF from the degraded image. Theoretically, we can find an exact solution to Equation 5.2 for images without noise and with an accurate PSF. But for most of the "real" images, there is no unique or stable solution [Starck *et al.*, 2002]. The reasons for this are two fold. Firstly, deconvolution would involve dividing the Fourier transform of the PSF into that of the image. Some of the spatial frequencies may have undefined values. Secondly, noise complicates the restoration as it is a statistically random process and there is no unique probabilistic solution.

As mentioned in Section 4.1.1.4, digital images have Poisson noise and random Gaussian readout noise. Therefore, both linear and non-linear deconvolution (restoration) techniques are dependent on the image signal-to-noise ratio. For astronomical images, the object type in the image (point source or extended) as well as the sky background affects the technique to be chosen. As mentioned in the last chapter, the WFPC2 PSF is undersampled (by a factor of 1 to 2 for the PC chip or 2 to 4 for the WF chips), spatially varying, and has high frequency structure in the extended "wings" [Butler, 2000]. Deconvolution with an accurate empirical PSF can suppress these "wings" and can boost the point sources in the image [Starck *et al.*, 2002].

Both linear and non-linear image deconvolution methods have been proposed.

Linear methods include the least square solution and Tikhonov regularization. The non-linear method CLEAN is primarily used in radio astronomy research for deconvolving point sources. The restored image is a convolution of δ functions and an ideal PSF with residuals. Other non-linear methods include Lucy-Richardson, Maximum Entropy Method (MEM), and the Jansson-Van Cittert method. Please refer to the review by Starck *et al.* [2002] for more in-depth description of deconvolution techniques used in astronomy.

We chose MEM deconvolution method as it is readily available as part of the IRAF package with option to sub-sample the input image or image section. Lucy-Richardson non-linear deconvolution task is also available in IRAF, although the image sections have to be sub-sampled afterwards. Another interesting idea is to suppress noise during deconvolution iterations, which can prevent "breaking down" of low signal-to-noise images. Starck & Murtagh [1994] proposed one such technique using Lucy-Richardson deconvolution with wavelet denoising.

5.1.1 Maximum Entropy Method Deconvolution

The Maximum entropy method uses the concept of entropy, which can be explained both from the point of view of thermodynamics and of information theory. The concept of entropy in information theory is explained in the next section, before venturing into the MEM deconvolution technique itself.

5.1.1.1 Entropy in Information Theory

Let us define a sample space of N outcomes as S = $(s_1, s_2, ..., s_N)$ with probability distribution function P, such that

$$\sum_{i=1}^{N} P(s_i) = 1, \tag{5.3}$$

where $P(s_i)$ is the probability of getting the s_i outcome.

In thermodynamics, entropy is defined as the measure of disorder and according to the second law of thermodynamics, systems tend to move towards higher entropy. From the information theory point of view, entropy is a measure of uncertainty or lack of correlation. For the sample space S and probability distribution P (as defined in Equation 5.3), entropy can be defined as [Togneri & deSilva, 2002]

$$E(P) = -\sum_{i=1}^{N} P(s_i)\ ln(P(s_i)) \tag{5.4}$$

The reason for choosing logarithm of probability distribution function is two fold - firstly the entropy will be 0 when we are certain about the outcome (for example when P$(s_i) = 0$ or 1), and secondly it makes entropy additive. The base of the logarithm does not specifically have to be **e**.

The functional form of entropy E = - p ln(p) is plotted in Fig. 5.1, for 0 < p ≤ 1 [Togneri & deSilva, 2002].

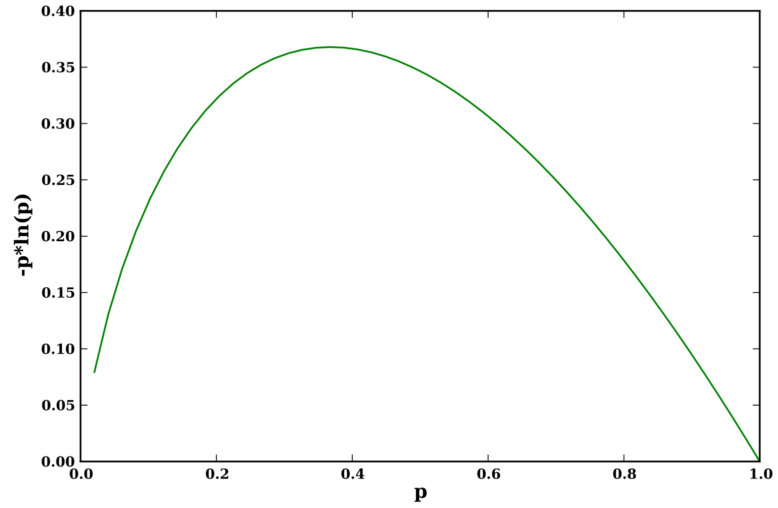

Figure 5.1: Variation of the entropy function [E = - p ln(p)] with the probability distribution function

The slope of the function is infinite at p = 0, leading to positive values (one of the constraints in deconvolution). The curve shows a very basic trend about probability and entropy - p = 0 and p = 1 do not contribute to entropy whereas p = 0.4 contributes most strongly towards it. Entropy approaches 0 for p = 0 and p = 1, because we are certain about the outcomes for both of these scenarios.

5.1.1.2 Bayes' Theorem

Non-linear deconvolution techniques like MEM can be easily understood using Bayesian methods. The conditional probability of two events A and B is related mathematically by Bayes' theorem; which states that

$$P(A \mid B) = \frac{P(B \mid A)P(A)}{P(B)} \tag{5.5}$$

i.e. the probability of A, given B is equal to product of probability of B, give A and probability of A, divided by probability of B.

Image restoration can be expressed in terms of Bayes' theorem as follows [Starck *et al.*, 2002]

$$P(O \mid I, M) = \frac{P(I \mid O, M)P(O \mid M)}{P(I \mid M)}, \tag{5.6}$$

where $P(O \mid I, M)$ is the conditional probability of obtaining the object (O) given degraded image (I), $P(I \mid O, M)$ is the likelihood of obtaining the degraded image I given object O, $P(O \mid M)$ and $P(I \mid M)$ are the individual probabilities of the object and the image respectively. Maximum likelihood and maximum entropy restoration techniques involve maximising the term on the left hand side of Equation 5.6 i.e. $P(O \mid I, M)$. Lucy-Richardson deconvolution is an example of maximum likelihood whereas MEM is of maximum entropy restoration technique.

5.1.1.3 Putting it all together

In the case of image restoration, we can redefine Equation 5.3 and Equation 5.4 as constraints

$$\sum_{i=1}^{N} p_i = 1 \tag{5.7}$$

$$I = \sum_{i=1}^{N} p_i \, PSF_i, \tag{5.8}$$

where p_i is the fraction of total image brightness in the i^{th} pixel.

The term $P(O \mid M)$ in Equation 5.6 is the prior probability of the object and is independent of the input data for deconvolution. For the maximum likelihood method, this term is constant whereas in the case of MEM, it is represented in terms of entropy (as defined in Equation 5.4) as:

$$P(O \,|\, M) = e^{\alpha\, E}, \tag{5.9}$$

where α is a weighting factor, E is entropy, and $P(O \,|\, M)$ is the probability distribution function for obtaining object O given degraded image I. According to Narayan & Nityananda [1986], for the image with Gaussian noise **n** and variance σ

$$P(O \,|\, M) \propto exp(-n^2/2\sigma^2), \tag{5.10}$$

$P(I \,|\, M)$ is the prior probability of the degraded image and is independent of the object O.

So, MEM deconvolution involves maximising the product of the entropy term and the probability density function $P(O \,|\, M)$, using the constraints (Equation 5.7 and Equation 5.8). As there is no exact solution, MEM is an iterative technique to minimise the solution. In the deconvolution of the globular cluster images, the STSDAS task *mem* was used.

5.2 Sub-sampled Deconvolution

As mentioned in the last chapter, the point spread function of HST WFPC2, and to a lesser extent ACS WFC/HRC suffer from the following:

1. It is under-sampled by a factor of 2 to 4
2. it has extended "wings" with considerable high-frequency structure
3. it is spatially varying because of optical aberrations etc.

According to Butler [2000], under-sampling limits the accuracy of the PSF fitting and the extended "wings" cause spurious star detections or missed faint stars in the neighbourhood of the bright stars. This can in turn limit the accuracy of both aperture photometry and star detection efficiency. HST WFPC2 and ACS images also suffer from optical aberrations and geometric distortions. For proper motion study of the stars in the crowded fields of globular clusters, positional accuracy of stars is of utmost importance.

To overcome these issues, Butler [2000] proposed an innovative sub-sampled deconvolution technique to recover the resolution lost to aberrations and poor sampling. This technique involves iterating to generate an exact point spread function in a crowded stellar field and using this spatially varying PSF to deconvolve overlapping sub-images. The sub-image positions determined on the sub-sampled deconvolved image are mapped back to the reference frame of the normal sampled images and used to calculate the proper motion between different time epochs. A simplified flowchart of the method is shown in Figure 5.2.

A detailed account of the sub-sampled deconvolution technique is given in Sections 5.3.2 to 5.3.4.

5.3 Data Reduction and Analysis Pipeline

PyRAF[1] is a python wrapper for the IRAF data reduction software suite. A semi-automated python pipeline was developed to process multi-epoch globular cluster images for proper motion determination. For realistic error analysis, we also developed a fully automated pipeline to generate simulated WFPC2 and ACS WFC/HRC globular star cluster images, for multiple epochs. This simulation pipeline is described in detail in the Chapter 6.

The reduction and analysis pipeline is written in the Python programming language and uses PyRAF tasks extensively. Python was chosen for pipeline development as it is an open source, cross-platform programming language, and can directly involve PyRAF tasks.

The Stetson [1987] package for crowded field photometry, DAOPHOT, was used for star detection, aperture photometry, PSF modelling, and PSF fitting.

Most of the pipeline tasks are automated, although a couple of them require some user interaction. The pipeline tasks are discussed in detail in the following sub-sections.

---

[1] STSDAS, TABLES, PyRAF and PyFITS are products of the Space Telescope Science Institute, which is operated by AURA for NASA

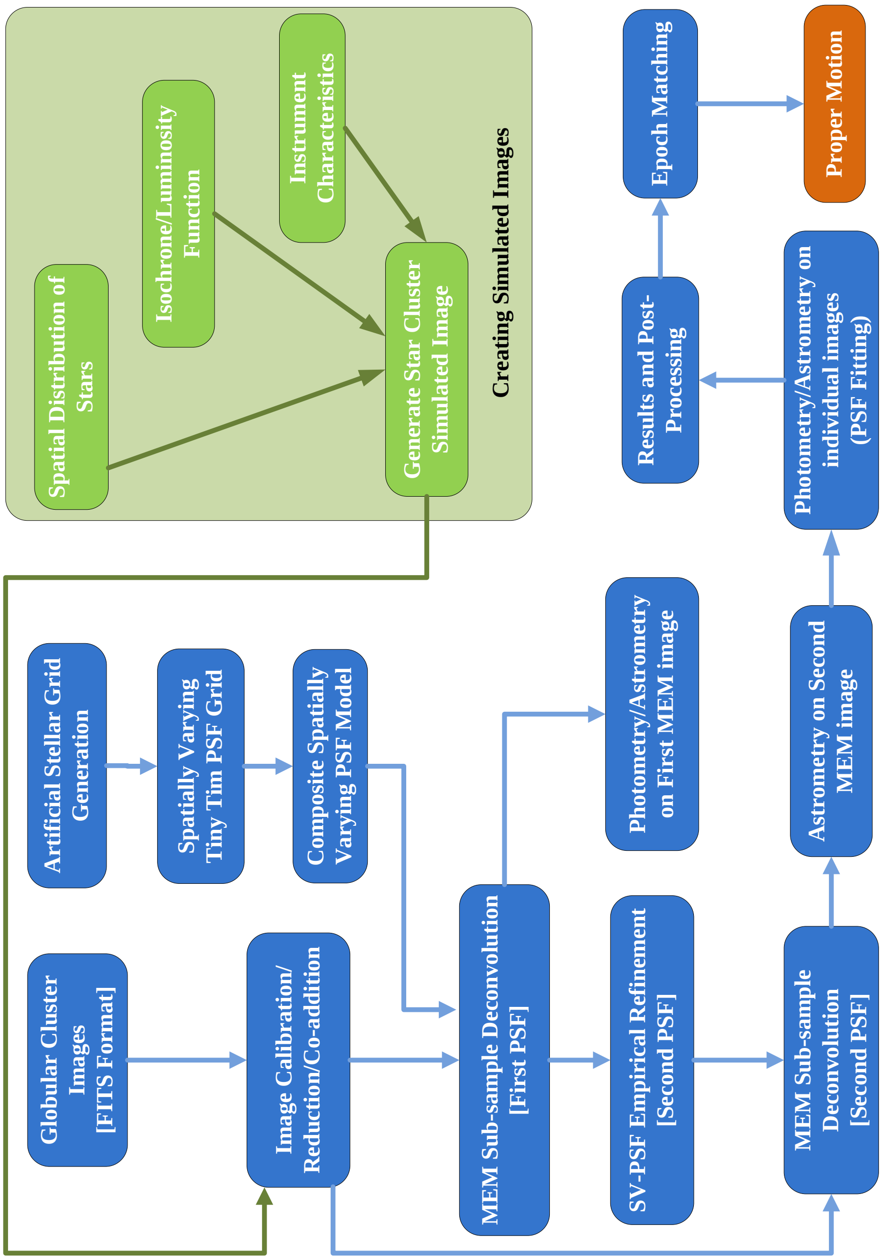

Figure 5.2: Flowchart of our sub-sampled deconvolution technique. Although it has been used for HST images, it can also be used with ground based telescope images (albeit with the modification that the first PSF must usually be determined empirically). The empirical PSF is generated iteratively.

5.3.1 Image Reduction and Registration

De-biased and flat-fielded cluster images were downloaded from the ESO HST archive website[1]. Different image registration routes were taken for WFPC2 and ACS images.

5.3.1.1 WFPC2 Image Registration

Raw images from the detector are processed through the OPUS pipeline at STScI. This involves: flagging the bad pixels in the science frames, calculating and subtracting the bias frame, subtracting the dark frame, flat fielding, and updating the header keywords. The final product is a reduced science image and its corresponding data quality (DQ) mask. For our work, we downloaded the calibrated images directly from the HST archive.

For each epoch and filter, a combined high SNR image was generated. We followed the steps in Gonzaga [2002] for image reduction and registration. A simplified flowchart of the WFPC2 image calibration and registration is show in Figure 5.3.

Geometric corrections and the 34th row photometric corrections were performed using the equations in Section 4.2.1.4. Corrections for the charge transfer efficiency imperfection and the hot pixels was done using the prescriptions in Section 4.2.1.3. For the images in the same epoch, misalignment was calculated using the IRAF task *wregister*, and *imcombine* task was used to remove any misalignment and to coadd the images. Based on the exposure time of the frames involved, the images were either summed (if the exposure times differed) or averaged (if all the frames had the same exposure time) to generate the final combined registered image. Combining images not only removes cosmic rays but also increases the signal to noise ratio of the final combined image.

Photometry, star detection, and deconvolution was carried out on the combined images. However for the error analysis, individual frames were also used. The 34th row and the geometric corrections mentioned above only reduce the photometric errors, not positional errors. Positional error corrections arising because of geometric distortion and manufacturing defects were performed on the

---

[1] http://archives.esac.esa.int/hst/

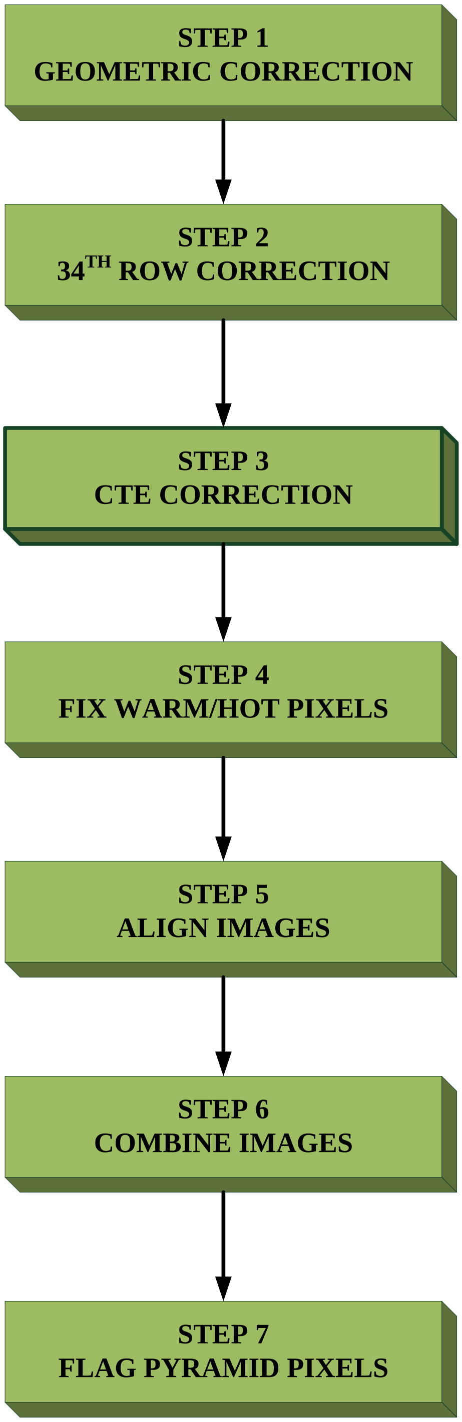

Figure 5.3: HST WFPC2 image reduction and registration flowchart.

the final catalogue of stars, for each filter and epoch image.

5.3.1.2 ACS WFC Image Registration

Similar to the WFPC2, flat fielded ACS WFC images were downloaded from the ESO HST archive. The raw frames had been processed using the OPUS pipeline at STScI, to generate the calibrated images. Raw images can also be re-processed locally using the *CALACS* software, which is part of the STSDAS package [Pavlovsky *et al.*, 2006].

Most of the ACS observations are taken using the so called *dither* patterns. Dithering is described, and the procedure to combine the dithered images to generate the final registered image is given, in the following sub-section.

5.3.1.3 Dithering

Dithering involves taking a series of exposures with small or large shifts. Depending on the amount of shift, dithering can achieve the following [Fruchter & Sosey, 2009]:

1. A sub pixel shift for improving the PSF sampling
2. A few pixel shift for flagging the bad pixels, hot pixels etc.
3. A few arcseconds shift to cover the ACS WFC inter-chip gap and the HRC occulting finger
4. A shift comparable to the detector dimensions for creating image mosaics

Both the ACS HRC and the WFC point spread functions are critically sampled towards the red end of the spectrum (1160 nm for the WFC and 630 nm for the HRC) but undersampled by a factor of 3 towards the blue end [Maybhate, 2010]. Combining sub-pixel dithered WFC images not only increases the sampling but also removes image artefacts from the final combined image. Dithering also helps in robustly removing comic rays and hot pixels, in addition to increasing the signal-to-noise ratio of the combined image.

The Hubble team have proposed three main dither patterns - *2 point*, *3 point* and *4 point* [Fruchter & Sosey, 2009]. The two point dither pattern can involve only one axis or both axes. The simplest two point sub-pixel dither pattern involves a shift in only one direction. For example - if the first image is taken at (0, 0) pixel offset, the dithered image can be obtained at (0, n + $\frac{1}{2}$) pixels, where n is an integer pixel shift. A two point dither in both directions involves taking a sub-pixel offset in both directions. Again, if the first image is taken at (0, 0) pixel value, the shifted image can be taken at (n + $\frac{1}{2}$, m + $\frac{1}{2}$), where n and m are integer pixel shifts (see Figure 5.4(b)).

The four point dither pattern involves taking four exposures at (0, 0), (0, $\frac{1}{2}$), ($\frac{1}{2}$, $\frac{1}{2}$), ($\frac{1}{2}$, 0) pixel positions (see Figure 5.4(d)). This can recover most of the resolution lost to under-sampling of the point spread function. If the observation time does not allow four dither points, three point dither pattern (see Figure 5.4(c)) can also be used. This involves taking at least three exposures at (0, 0), ($\frac{1}{3}$, $\frac{1}{3}$) and ($\frac{2}{3}$, $\frac{2}{3}$) pixel positions. For multiple orbit exposures, these three dither patterns can be combined to get 6 and 8 points dither patterns.

5.3.1.4 Drizzling

Fruchter & Hook [1997] proposed a variable pixel linear reconstruction technique to combine dithered images. The technique is now known as *Drizzle*. Drizzling is a linear reconstruction technique which tries to recreate the instrumental point spread function convolved image. This is different from image restoration, where the effect of the point spread function is removed from the image (see Section 5.1 for more details about image restoration).

Conceptually, drizzle falls in between the *interlacing* and *shift-and-add* linear reconstruction methods [Fruchter & Sosey, 2009]. Because of the telescope pointing errors and optical aberrations, input image pixels cannot be interlaced to the output pixels. In drizzle, input image pixels are mapped to sub-sampled output pixels, taking into account image translation and rotation as well as the telescope optical aberrations. A simplified schematic of the drizzling technique is shown in Figure 5.5. *Pixfrac* is the fraction of the input pixel contributing to the output pixel. Its value varies from 0 to 1, where 1 means having the same pixel sampling as the input images. To improve the sampling of the under-sampled ACS images, *pixfrac* of 0.5 is recommended [Pavlovsky *et al.*, 2006]. *Scale* is the pixel scale in

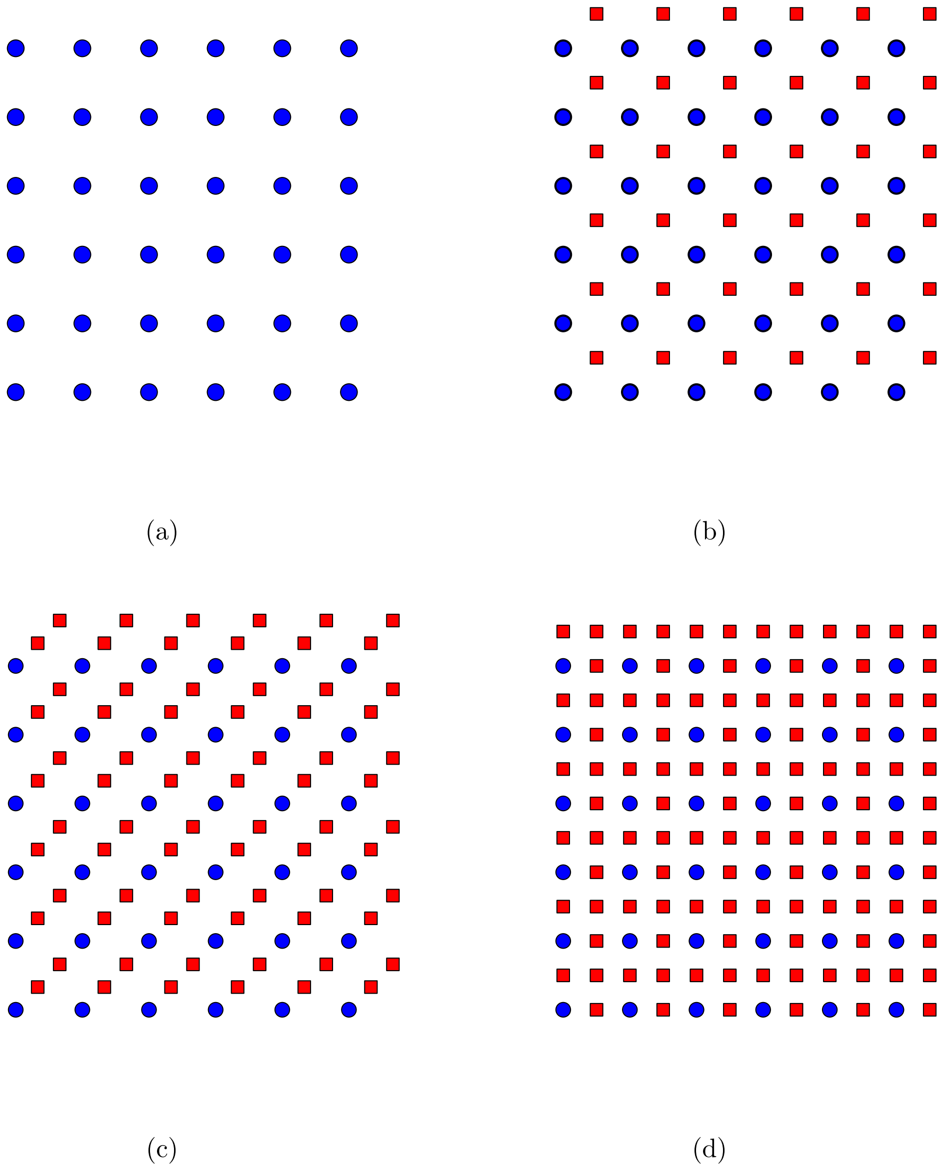

(a) (b) (c) (d)

Figure 5.4: HST Dither Patterns (a) Normal sampling (b) Two point dither pattern (c) Three point dither pattern (d) Four point dither pattern. The blue dots depicts the original sampling whereas the red squares are the dither points. Re-drawn from figures 2.1, 2.2, 2.3 and 2.4 in *The Multidrizzle Handbook* [Fruchter & Sosey, 2009]

arcseconds/pixel. It is also given as fraction of the input pixel scale and varies from 0 to 1.

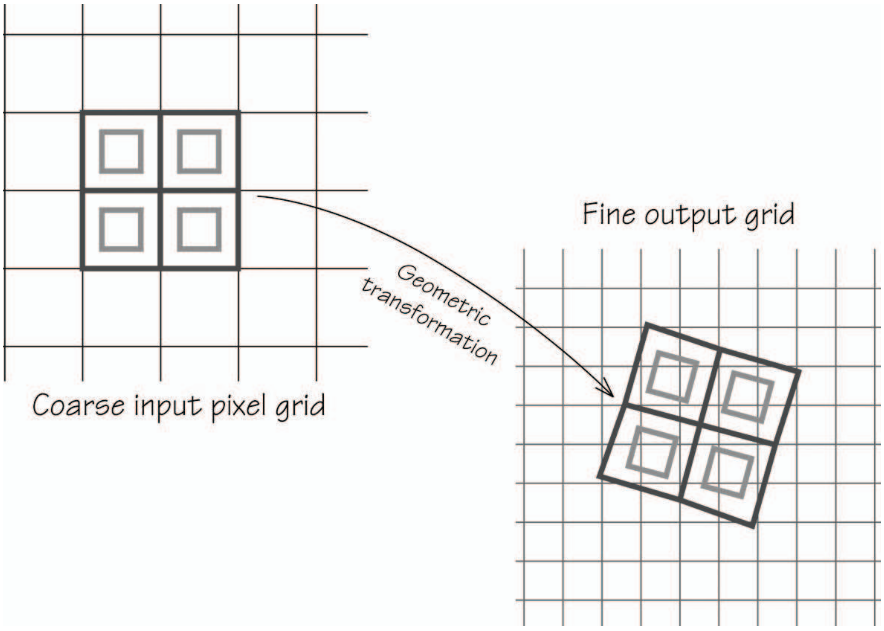

Figure 5.5: Linear image reconstruction method Drizzling. Mapping from a coarse input grid to a sub-sampled finer grid is evident. Image taken from *The Multidrizzle Handbook* [Fruchter & Sosey, 2009]

In their paper, Fruchter & Hook [1997] have shown that the sub-sampled point spread function of the drizzled images is much smoother, with photometric errors < 0.015 mags and astrometric accuracy of ~ 0.018 pixels.

The IRAF STSDAS *dither* package include three main tasks to drizzle the HST dithered images - *Drizzle*, *PyDrizzle* and *Multidrizzle*. As the *Multidrizzle* task is more extensive than the other two, we have used it for processing the ACS WFC images. The main benefit of using *Multidrizzle* is that it takes care of the cosmic ray rejection and automatically determines the shifts and rotations between the images (using WCS[1] information in the image header).

A brief description of the *Multidrizzle* task is given in Appendix A.

---

[1] World Coordinate System

5.3.2 Modelling the Analytical Point Spread Function

The next step in the pipeline is to generate the first guess point spread function. TinyTIM software [Krist *et al.*, 2011] from STScI was used to model the analytical PSF for both the WFPC2 and ACS detectors. The TinyTIM generates a positional dependent, noise-less PSF for each filter bandpass, and each detector chip, of the HST instruments. As the PSFs for WFPC2, and to a lesser extent the ACS WFC and HRC, are spatially varying, we generated an image with a grid of artificial stars (PSFs). For each of the four WFPC2 chips, a 6×6 artificial star grid (each PSF radius = 63 pixels) was formed (see Figure 5.6(a)). Whereas for the ACS WFC, one grid each for WFC1 and WFC2 of 32×16 stars was created (see Figure 5.6(c)). For the ACS HRC, the image was formed with a 16x16 artificial star grid (see Figure 5.6(b)).

The PSFs generated by TinyTIM are normal sampled, dependent on the position of the star on the chip, the filter used, and the spectrum type (we adopted G2V star spectrum, considering that brighter globular cluster stars can be of type A to M). ACS WFC and HRC PSFs are on a distorted grid. The IRAF/-DAOPHOT task *psf* was used to generate a composite spatially varying PSF model from each artificial star grid. The VARORDER parameter in the *psf* task was set to 2, to generate six LUTs (Look Up Tables) accounting for the mean fitting residuals, their 1^{st} derivatives and their 2^{nd} derivatives, as a function of position within the chip. The accuracy of the composite model point spread function was tested by fitting it to all the artificial stars in the image. The DAOPHOT task *allstar* was used for this. Although the cores of the artificial stars were quite cleanly subtracted, the extended “wings” were not completely fitted (see Figure 5.7). This indicates a limitation of the quadratic composite PSF model. The first guess analytical PSFs were then used to deconvolve the reduced and combined HST images in the first iteration of deconvolution.

5.3.3 Image Deconvolution

The STSDAS task *mem* (Maximum Entropy Method) was used to deconvolve the registered and combined images. The *mem* task deconvolves only with a spatially invariant point spread function. Therefore spatially invariant instances of the

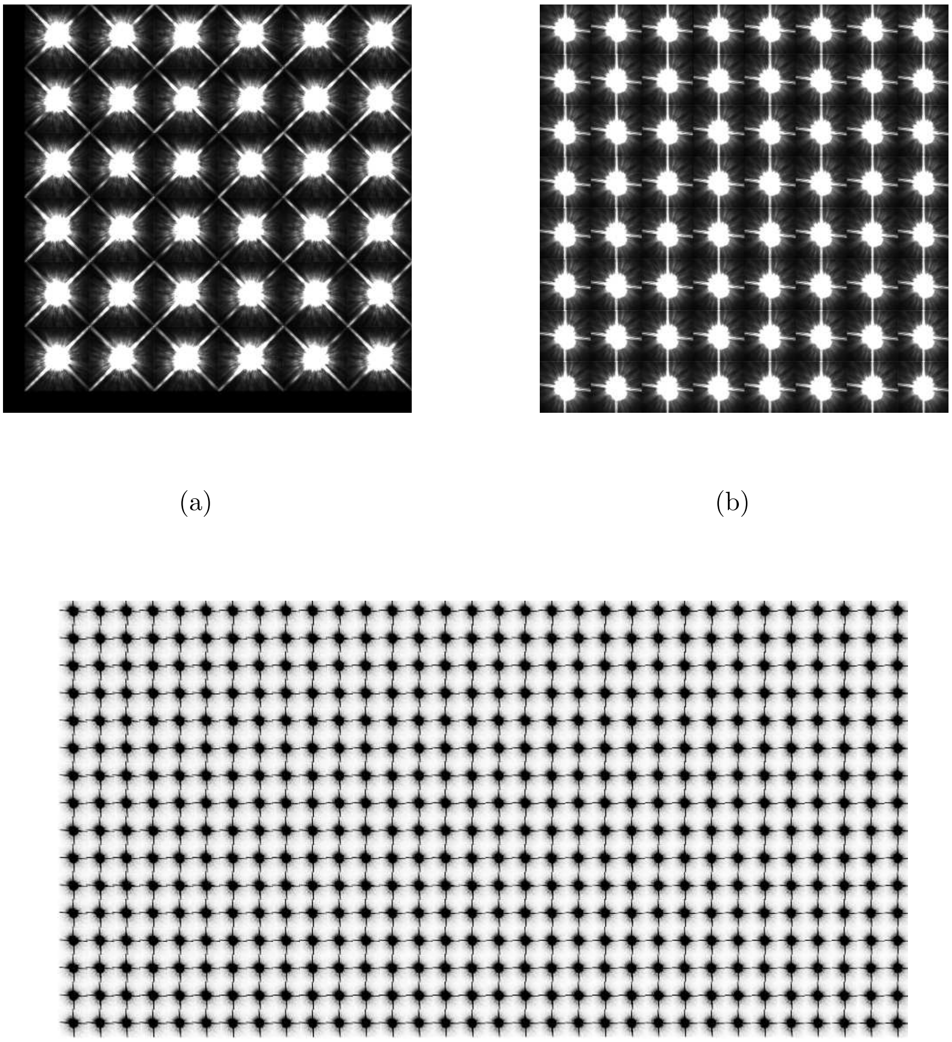

(a)

(b)

(c)

Figure 5.6: Artificial star grid image for (a) WFPC2; (b) ACS HRC; (c) ACS WFC1 (inverted colour). Individual position dependent point spread functions were generated using TinyTIM and added on to a blank image such that they abut in these grids. The WFPC2 PSF grid was generated at positions which exclude the vignetting/pyramid region (the block strips on the left and bottom of the image).

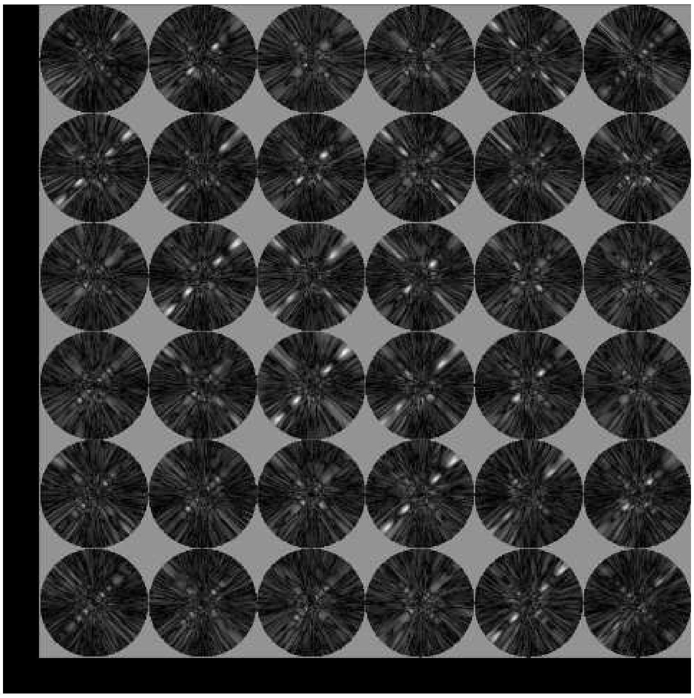

Figure 5.7: Absolute percentage residual of the TinyTIM fitted image. The absolute residual percentage value varies from 0 to 300%. Higher residuals in the PSF "wings" are clearly visible.

point spread functions at specific chip positions were generated from the analytical PSF. The *seepsf* task was used for this purpose. If the mem task is supplied with a sub-sampled PSF, it will generate a sub-sampled deconvolved output. This is vital for WFPC2 images, which actually loses sub-pixel centroiding information, if virtually all the flux of a star is drawn into a single pixel. Since DAOPHOT combines essentially dithered stars images to form its composite PSF model, it stores the model at 2×2 sub-sample. The *seepsf* task is able to extract instances of that model at its native 2×2 sub-sampling (or interpolated higher degrees of sub-sampling). These PSFs were then used to deconvolve image sub-sections or tiles, which overlapped by a width equal to or exceeding the PSF radius on all sides; this allowed the entire 'tile' perimeter with its deconvolution edge effects to be discarded.

As deconvolution is an iterative process, which may require a minimum of

1024 tiles (for ACS WFC detector), the execution time can be long. This is true for the larger FOV ACS WFC images. To speed up the processing, a parallel deconvolution routine was implemented. It is discussed in detail in the next chapter on parallel computing.

The overlapping deconvolved sub-images were then trimmed of their boundary overlaps and combined to generate the final sub-sampled deconvolved image.

Sub-sampled deconvolution provides better star detection (refer to Section 7.2 for more details) compared to the detection on the normal sampled images, especially for the faint stars. This was quantified by running tests on simulated star cluster images (more details in Chapter 7). Therefore, the star list generated from the sub-sampled deconvolved images were used for proper motion determination.

5.3.4 Star Detection

As both the ACS and WFPC2 detectors are under-sampled, star detection by direct detection techniques may not be accurate. This is because, the exact centre of the object is unlikely to be at the centre of a pixel. Sub-pixel accuracy of star detection requires precise determination, of the object position in the image. This is the most critical step in proper motion determination as the inaccuracies in position will propagate into proper motion inaccuracies.

The two most common tools used for object detection are the DAOPHOT task DAOFIND and the SExtractor software by Bertin & Arnouts [1996]. We found that SExtractor works better for moderately crowded fields (for example - the globular cluster M71) but misses most of the detections in the inner crowded cores (for example - the globular cluster M15). Therefore, for moderately crowded fields, we use SExtractor for star detection whereas for the crowded cores, we used the DAOFIND task.

To compare the detection efficiency, resilience to false detections, and positional accuracy of the stars detected on the sub-sampled deconvolved image with other methods, we used simulated cluster images (more details in Chapter 7). Deconvolved star detection efficiency and accuracy were compared to positions generated by *daofind* on the normal sampled image and the positions determined by fitting the point spread function. Star detection efficiency from PSF fitting was better compared to direct detection on normal sampled images (refer to Section 7.2 for more details).

As shown in 5.3.6, modelling the point spread function is not a trivial task, especially for an under-sampled image. Anderson & King [2000] proposed the idea of an *effective point spread function* (ePSF) for WFPC2, which has been used by many authors ([Bedin *et al.*, 2001; Gerssen *et al.*, 2002; McLaughlin *et al.*, 2006; Piatek *et al.*, 2008]) to determine accurate star positions. They were able to achieve positional accuracy of ~ 0.02 pixel for an uncrowded bright star. In our case, we have derived the empirical PSF directly from the image, using bright stars (away from the influence of neighbouring stars' light) in the image. We then deconvolved the cluster images with this PSF and did star detection on the deconvolved image. The star positions from the deconvolved images were re-mapped to the normal sampled images to get the final star positions.

5.3.5 Aperture Photometry

Photometry is the determination of flux (counts) and the magnitude of an astronomical object. Aperture photometry involves defining a circular aperture around a star and measuring the value of the star's flux in it. Flux is converted to magnitude using the following formula -

$$mag = -2.5 * log_{10}\left(\frac{flux}{exptime}\right) + ZP, \tag{5.11}$$

where log_{10} is logarithm to base 10, exptime is image exposure time, and ZP is the photometric zeropoint.

We used the DAOPHOT *phot* task to determine the magnitude of the globular cluster stars. Flux is calculated by subtracting the sky background from the total count in the aperture. Magnitude errors are calculated as [Stetson, 1987]

$$error_{mag} = 1.0857\,\frac{\sqrt{(\frac{flux}{epadu} + area\ \times\ stdev^2 + \frac{area^2 \times stdev^2}{nsky})}}{flux}, \tag{5.12}$$

where epadu is the CCD gain in e^-/ADU, *area* is the aperture area in pixel squared, *stdev* is the standard deviation of the sky value, and *nsky* is the number of pixels contributing to the sky background value.

Photometric recipes by Holtzman *et al.* [1995] were used for WFPC2 instrument images, whereas Sirianni *et al.* [2005] techniques were used for ACS images.

5.3.5.1 Aperture Correction

Changing the aperture size samples a different proportion of the PSF, leading to slightly different flux, and thus different magnitude values. Therefore a magnitude calculated using aperture photometry has to be corrected. This is known as *aperture correction*. For the WFPC2 instrument, Holtzman *et al.* [1995] suggested correcting the magnitude to a $0.5''$ aperture first and then for infinity aperture. To correct for the $0.5''$ aperture, a few bright stars (unsaturated and not crowded) are selected in the field of view and their magnitude determined for both the original and $0.5''$ aperture (~ 11 pixels for the PC1 chip and ~ 5 pixels for the WF chips). The median difference between the two magnitudes is added to correct for the aperture difference (this is done for all the detected stars). Finally, 0.1 mag is subtracted from the $0.5''$ aperture corrected magnitude to implement the $0.5''$ to infinity aperture correction.

For the ACS WFC and HRC detectors, the $0.5''$ to nominal infinity aperture correction is dependent on the filter and does not have a constant value like the WFPC2. These corrections are given in Table 5 in Sirianni *et al.* [2005]. The aperture correction from the original aperture to $0.5''$ is performed in the same way as for WFPC2 images mentioned above. The approximate $0.5''$ to infinity aperture correction is then subtracted from this magnitude to get the aperture corrected instrumental magnitude.

5.3.5.2 CTE correction

As mentioned in the last chapter, both the WFPC2 and ACS detectors suffer from charge transfer errors. For the WFPC2 chips, Dolphin [2009] modelled the CTE errors and these are described in Section 4.2.1.3. The Riess & Mack [2004] formula was used to correct ACS CTE errors (see Section 4.2.2.3 for details).

5.3.6 Empirical Point Spread Function

As mentioned in the previous section, the analytical TinyTIM PSF does not fully represent the actual or "real" PSF of the HST images. In the second iteration, we generate an empirical point spread function directly from the combined image. Because of crowding in the cores of the globular clusters, modelling the empirical PSF is not trivial. One of the ways to overcome this is to subtract the fitted stars (from the first *allstar* iteration with the analytical PSF). Then the stars away from the scattered light of the bright stars can be used to model the spatially varying empirical PSF. As before, the DAOPHOT task *psf* was used to model the point spread function and again, a quadratically varying model was constructed, from a large number of star (~ 80 on WFPC2 and ~ 200 on ACS WFC). In our semi-automated pipeline, the user has the option to control the magnitude and position of the PSF stars. This allows the user to exclude saturated and faint stars as well as stars that are lying close to the edge of the image.

Analytical and empirical point spread functions for a WFPC2 image of globular cluster NGC 6293 are shown in Figure 5.8. How well the empirical point spread function represents the image was again tested using the *allstar* task. A better fitting was achieved compared to the analytical point spread function (see Figure 5.8). However, perfect fitting throughout the chip is hard to achieve for an under-sampled PSF.

5.3.7 Proper Motion

The space velocity of an astronomical object include two components - *radial velocity* and *proper motion*. Radial velocity is directed along the line of sight (with respect to the Earth). The tangential component of the space velocity results in the proper motion of the object. Proper motion gives the rate of angular change in the position of the object in the sky. Mathematically, space motion can be written as

$$v = \sqrt{v_r^2 + v_t^2}, \tag{5.13}$$

where v_r is the radial velocity and v_t is the tangential velocity of the object.

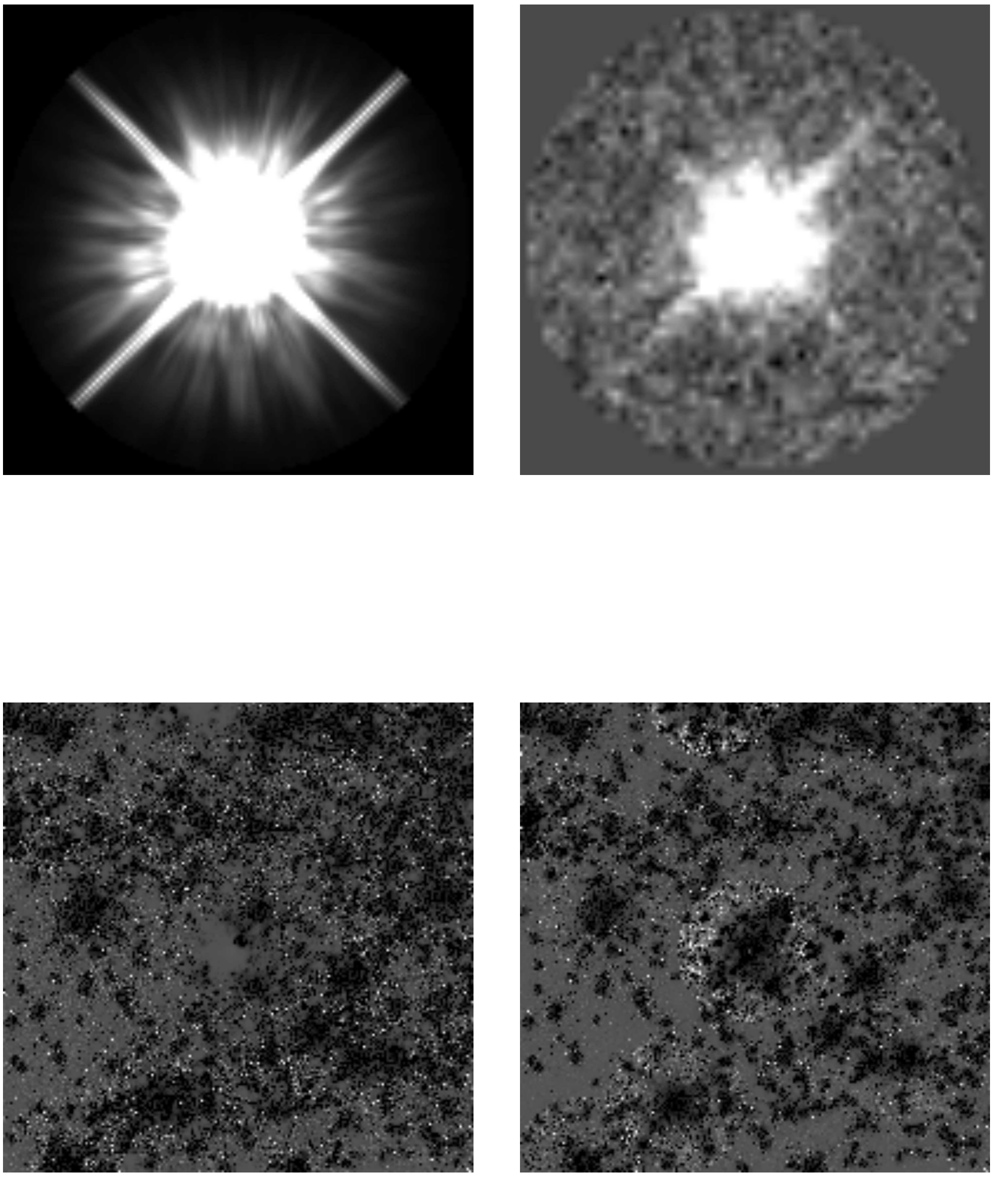

Figure 5.8: NGC 6838 WFPC2 point spread function. The analytical TinyTIM PSF is on the upper left hand side and an empirical PSF is on the upper right hand side. The PSF is for the F555W filter and PC1 chip. The PSF radius for the TinyTIM PSF is 63 pixels and 30 for the empirical PSF. The empirical PSF has sufficient signal to noise to exhibit the subtle outer image structure's of the analytical PSF, but it nevertheless results in better deconvolution and PSF-fitting photometry. The PSF fitted subtracted images are shown below their respective PSFs.

The tangential velocity and proper motion are connected by the following formula:

$$v_t = \mu \; r, \tag{5.14}$$

where μ is the proper motion and r is the distance of the object from the Sun. If the distance to the object (d) is known, tangential velocity in km/sec can be given as:

$$v_t = 4.74 \; \mu \; d, \tag{5.15}$$

where proper motion is in arcsec/year and distance d is in parsecs.

The Proper motion of an object in turn can be represented mathematically as

$$\mu = \sqrt{\mu_\alpha^2 \, cos\delta + \mu_\delta^2}, \tag{5.16}$$

where $\mu_\alpha \; cos\delta$ and μ_δ are the proper motion components giving change in right ascension and declination, respectively.

The proper motion of an object is measured by calculating the object's shift between two or more images[1], normally taken a few years apart. The average proper motion of the stars in globular star clusters is $\sim$ 0.2 mas/yr [Binney & Merrifield, 1998]. Therefore, to measure an appreciable proper motion of stars in the Galactic globular clusters requires images to be separated by a few tens of years.

The proper motion can be measured with respect to a fixed frame of reference (for example - a Quasar). This is known as the *absolute proper motion* of the object. As pointed out by McLaughlin *et al.* [2006], absolute HST pointing is good to about $0.1''$. For a short baseline of 10 years or so, we need to resolve the stellar motion of $0.002''$or better. Therefore we cannot obtain the absolute proper motion of the globular clusters stars using only HST images[2].

Another way to measure the proper motion of the globular cluster member stars is to determine the *relative proper motion.* The epoch with the high signal-to-noise ratio image is taken as the "reference" and all the matched stars between

---

[1] can be old photographic plate, although their positional accuracy is poor, they do provide a very long baseline

[2] For most globular clusters, HST images are available for a 2 - 10 years baseline

the epochs are iteratively mapped to the reference frame. This can be done either by a *global* or a *local* transformation. In a global transformation, the geometric transformation of the star at any CCD location is determined by all the other matched stars in the frame. This may not be the most accurate method, as the geometric distortions and other aberrations may differ from the edge to the centre of the chip.

Anderson *et al.* [2006] proposed the local transformation method to overcome this problem. Instead of using all the matched stars to transform the position of a particular star, only a few stars (~ 50) in the neighbourhood of the star are used to calculate the geometric transformation. As we expect the mean proper motion of the cluster stars to be centred around zero, the choice of the stars for the transformation is important. Ideally, we would like to include only the cluster member stars in calculating the transformation. This can be achieved by choosing the stars from their loci in the colour magnitude diagram (CMD). If a CMD is not available, the transformation can be performed iteratively to sift out the field stars. Thus, proper motion determination is also used to test globular cluster membership. The final reference coordinate frame then allows for high velocity stars to be easily identified.

The IRAF task *geomap* was used iteratively to calculate both the intra and inter epoch transformations between the matched stars. *Geomap* determines the geometric transformation (with the option to include higher order distortion terms) between the reference and the input coordinate system. It solves the equation of the following type:

$$\begin{aligned} x_{in} &= f(x_{ref}, y_{ref}) \\ y_{in} &= f(x_{ref}, y_{ref}) \end{aligned} \tag{5.17}$$

to map the coordinate transformation. x_{ref}, y_{ref}, x_{in} and y_{in} are the reference and input coordinates respectively. For example, a quadratic polynomial solution would require solving the following two equations:

$$
\begin{aligned}
x_{in} = a_{11} + a_{21} * x_{ref} + a_{31} * x_{ref}^2 + a_{12} * y_{ref} + \\
a_{22} * x_{ref} * y_{ref} + a_{32} * x_{ref}^2 * y_{ref} + a_{13} * y_{ref}^2 + \\
a_{23} * x_{ref} * y_{ref}^2 + a_{33} * x_{ref}^2 * y_{ref}^2 \\
y_{in} = a^{'}_{11} + a_{21}{}' * x_{ref} + a^{'}_{31} * x_{ref}^2 + a^{'}_{12} * y_{ref} + \\
a^{'}_{22} * x_{ref} * y_{ref} + a^{'}_{32} * x_{ref}^2 * y_{ref} + a^{'}_{13} * y_{ref}^2 + \\
a^{'}_{23} * x_{ref} * y_{ref}^2 + a^{'}_{33} * x_{ref}^2 * y_{ref}^2
\end{aligned}
\tag{5.18}
$$

For the ‘general’ fitting geometry in *geomap*, the problem involves solving the following equation (only linear term):

$$
\begin{aligned}
x_{in} &= a + b * x_{ref} + c * y_{ref} \\
y_{in} &= d + e * x_{ref} + f * y_{ref},
\end{aligned}
\tag{5.19}
$$

Solving for unknown coefficients a, b, c, d, e and f provides values of shift, rotation, skew and scale changes between the two coordinate systems. Higher order polynomial terms provide distortion solution in addition to the linear solution.

We followed Anderson *et al.* [2006] recipe to calculate the errors associated with proper motion determination. As mentioned before, the accuracy of the proper motion is dependent on the accuracy of the star position in the images. The rms of the displacement in intra-epoch positions[1] gives an indication of the positional accuracy in each epoch. If the rms for epoch 1 and 2 are (σ_{x1}, σ_{y1}) and (σ_{x2}, σ_{y2}) respectively, then the proper motion errors in the x and y pixel directions can be given as [Anderson *et al.*, 2006]:

$$
\begin{aligned}
\sigma_{\delta x}^2 &= \sqrt{\frac{\sigma_{x1}^2}{N_1} + \frac{\sigma_{x2}^2}{N_2}} \\
\sigma_{\delta y}^2 &= \sqrt{\frac{\sigma_{y1}^2}{N_1} + \frac{\sigma_{y2}^2}{N_2}},
\end{aligned}
\tag{5.20}
$$

where N_1 and N_2 are number of images in epoch 1 and 2 respectively.

---

[1] Repeatedly measuring the star’s position in identical images taken at the same epoch

5.3.8 Internal Proper Motion Dispersion

The observed internal proper motion dispersion in the x and y pixel directions can be defined as [Jones, 1970]:

$$\begin{aligned} \sigma_{x0}^2 &= \frac{1}{n-1}\sum_{i=1}^{n}\mu_{xi}^2 \\ \sigma_{y0}^2 &= \frac{1}{n-1}\sum_{i=1}^{n}\mu_{yi}^2, \end{aligned} \tag{5.21}$$

where μ_{xi} and μ_{yi} are the proper motions of the i^{th} star in the x and y directions respectively, and n is the total number of stars in the sample. The actual proper motion dispersion includes observational errors, therefore the real proper motion dispersion can be given as (assuming both proper motion and errors fit a Gaussian profile) [Jones, 1970]:

$$\begin{aligned} \sigma_x^2 &= \sigma_{x0}^2 - \frac{1}{n}\sum_{i=1}^{n}\zeta_{xi}^2 \\ \sigma_y^2 &= \sigma_{y0}^2 - \frac{1}{n}\sum_{i=1}^{n}\zeta_{yi}^2, \end{aligned} \tag{5.22}$$

where ζ_{xi} and ζ_{yi} are the standard errors in the x and y proper motions of the i^{th} star. Error in the terms σ_x, and σ_y can be expressed as [Meylan & Mayor, 1991]:

$$\sigma_{\sigma_x} = \sigma_x\sqrt{\frac{1}{2n}} \qquad \sigma_{\sigma_y} = \sigma_y\sqrt{\frac{1}{2n}} \tag{5.23}$$

5.4 Conclusions

A detailed account of processing the Hubble Space Telescope images from WFPC2 and ACS WFC detectors was presented in the chapter. We introduced our sub-sampled deconvolution pipeline and gave an in-depth account of data reduction, deconvolution, photometry, and astrometry. Relative proper motions and internal proper motion dispersion in globular cluster, along with associated errors were also described in the chapter.

Chapter 6

Speed up: Parallel Processing

6.1 Introduction

In 1965, Gordon Moore predicted that the number of transistors in integrated circuits would double every two years [Moore, 1965]. This prediction has proved true until now, although semiconductor experts[1] expect it to slow down by the end of 2013 (doubling every 3 years instead of 2). The initial emphasis was on producing single core processors with higher processing power. But with increasing heat dissipation problems and higher power consumption, the focus in the last decade has shifted to multicore processors - where each core acts as a separate processor. Each core may have lower processing power compared to a high end single core processor, but it provides better performance by allowing multiple threads to run simultaneously, known as thread-level parallelism (TLP). At present, dual and quad core processors are common place in desktop and laptop machines and even in the current generation of high end smart phones. With both Intel [Garver & Crepps, 2009] and AMD[2] working on next generation multicore processors, the potential for utilizing processing power in desktop machines is massive. However, traditional software for scientific applications (e.g. image processing) is written for single-core Central Processing Units (CPU) and is not harnessing the full computational potential of the multicore machines.

---

[1] From the 2011 executive summary of International Technology Roadmap for Semiconductor (http://www.itrs.net/links/2011itrs/2011Chapters/2011ExecSum.pdf)

[2] Advanced Micro Devices

Traditionally, high performance computing (HPC) is done on supercomputers with a multitude of processors (and large memory). Computer clusters using commercial off the shelf (COTS) hardware and open source software are also being utilised [Szalay, 2011]. And recently graphical processing unit (GPU) based clusters have been put to use for general purpose computing [Belleman *et al.*, 2008; Strzodka *et al.*, 2005]. The advent of multicore processors provides a unique opportunity to move parallel computing to desktops and laptops, at least for simple tasks. In addition to hardware, one also needs unique software protocols and tools for parallel processing. The two most popular parallel processing protocols are Message Passing Interface (MPI) and OpenMP. MPI is used on machines with distributed memory (for example - clusters) whereas OpenMP is geared towards shared memory systems.

Parallel computing has been used in different sub-fields of astrophysical research. Physical modelling and computationally intensive simulation code have been ported to supercomputers. Examples include N-Body simulation of massive star and galaxy clusters [Makino *et al.*, 1997], radiative transfer [Robitaille, 2011], plasma simulation around pulsars, galaxy formation and mergers, cosmology etc. But most of the astronomical image processing and general time consuming data processing and analysis tasks are still run in serial mode. One of the reasons for this is the intrinsic and perceived complexity connected with writing and executing parallel code. Another reason may be that day to day astronomical data processing tasks do not take an extremely long time to execute. Irrespective of this, one can find a few parallel modules developed for astronomical image processing. The cosmic ray removal module CRBLASTER [Mighell, 2010] is written in C and based on the MPI protocol, and can be executed on supercomputers or cluster computers (as well as on single multicore machines). For co-addition of images, Wiley *et al.* [2011] proposed software based on the MapReduce[1] algorithm, which is geared towards processing terabytes of data (for example - data generated by big sky surveys like the SDSS[2]) using massively parallel systems.

In this chapter, we are exploring a few recipes for utilizing multicore machines for parallel computation, to perform faster execution of astronomical tasks. These

---

[1] Model to process large data sets on a distributed cluster of computers

[2] SDSS: Sloan Digital Sky Survey [http://www.sdss.org/]

recipes are written in the Python scripting language and use PyRAF or IRAF tasks for image/data processing and analysis. Instead of rewriting the existing optimised serial tasks, we have utilised the Python multiprocessing modules to parallelize iterative processes.

In Section 6.2, we introduce the concept of parallel data processing and the various options available. Python multiprocessing in discussed in Section 6.3 with emphasis on native parallel processing implementation. Three different data processing examples are benchmarked in Section 6.4. In Section 6.5, we discuss load balancing, scalability, and portability of the parallel Python code.

6.2 Parallel Data Processing

Processors execute instructions sequentially and therefore, from the initial days of computers to the present, most of the applications have been written as serial code. Generally coding and debugging of serial code is much simpler than parallel code. However, debugging is an issue only for parallel programs where many processes depend on results from other processes - whereas it is not an issue while processing large datasets in parallel. Moving to parallel coding not only requires new hardware and software tools, but also a new way of tackling the problem in hand. To run a program in parallel, one needs multiple processors/cores or computing nodes[1]. The first question one asks is how to divide the problem so as to run each sub-task in parallel.

Generally speaking, parallelization can be achieved using either *task parallelization* or *data parallelization*. In task parallelism, each computing node runs the same or different code in parallel. Whereas, in data parallelism, the input data is divided across the computing nodes and the same code processes the data elements in parallel. Data parallelism is simpler to implement, as well as being the more appropriate approach in most astronomical data processing applications, and we only deal with it.

Considering a system with N processors or computing nodes, the speedup that can be achieved (compared to 1 processor) can be given as:

---

[1] The terms processors and computing nodes will be used interchangeably in the rest of the chapter.

$$S = \frac{T_1}{T_N}, \tag{6.1}$$

where T_1 and T_N are the code runtime for one and N processors respectively. T_N depends not only on the number of computing nodes but also on the fraction of code that is serial. The total runtime of the parallel code using N processors can be expressed using Amdahl's law [Amdahl, 1967]:

$$T_N = T_S + \frac{T_P}{N} + T_{sync} \tag{6.2}$$

where T_S is the execution time of the serial fraction of the code, T_P is the runtime of code that can be parallelized, and T_{sync} is the time for synchronisation (I/O operations etc.). The efficiency of the parallel code execution depends a lot on how optimised the code is, i.e. the lower the fraction of serial code, the better. If we ignore synchronisation time, theoretically unlimited speedup can be achieved as $N \to \infty$ by converting the serial code to completely parallel code. More realistically, T_{sync} can be modelled as $K * ln(N)$, where N is the number of processors and K is a synchronisation constant [Gove, 2010]. This means that at a particular process count, the performance gain over serial code will start decreasing. Minimisation of Equation (6.2) gives:

$$N = \frac{T_P}{K} \tag{6.3}$$

This means that the value of N for which the parallel code scales is directly proportional to the fraction of code that is parallel and inversely proportional to synchronisation. In other words, by keeping N constant, one can achieve better performance by either increasing the fraction of parallel code or decreasing the synchronisation time, or both.

We have used multiprocessing instead of multithreading to achieve parallelism. There is a very basic difference between threads and processes. *Threads* are code segments that can be scheduled by the operating system. On single processor machines, the operating system gives the illusion of running multiple threads in parallel, but in actuality it switches between the threads quickly (time division multiplexing). But in the case of multicore machines, threads run simultaneously on separate cores. Multiple processes are different from multiple threads in the sense that they have separate memory and state from the master process that invokes them (multiple threads use the same state and memory).

The most popular languages for parallel computing are C, C++ and FORTRAN. MPI as well as OpenMP protocols have been developed for these three languages. But wrappers or software implementations do exist to support interpreted languages like Python, Perl, Java etc. The speed gain with compiled code comes at the cost of longer development time. Therefore we have used the Python scripting language and integrated PyRAF tasks in parallel mode. The secondary objective is *code reuse* i.e. using the existing Python code and/or IRAF tasks to parallelize the problem (wherever it is feasible).

6.3 Python Multiprocessing

Python supports both multi-threading and multi-processing programming. The threads in Python are managed by the host operating system i.e. scheduling and switching of the threads is done by the operating system and not by the Python interpreter. Python has a mechanism called the Global Interpreter Lock (GIL) that generally prevents more than one thread running simultaneously, even if multiple cores or processors are available [Foundation, 2012]. This results in only one thread having exclusive access to the interpreter resources, or in other words resources are "locked" by the executing thread. The running thread releases the GIL for either I/O operations or during interpreter periodic checks (by default after every 100 interpreter ticks or bytecode instructions) [Beazley, 2006]. The waiting threads can run briefly during this period. This unfortunately affects the performance of multi-threaded applications and for CPU bound tasks, the execution time may be actually higher than serial execution. The performance deteriorates further on the multicore machines as the Python interpreter wants to run a single thread at a time whereas the operating system will schedule the threads simultaneously on all the available processor cores.

This is only true for the CPython implementation; PyPy[1], Jython[2], and Iron-

---

[1] Just-in-time (JIT) compilation implementation

[2] Python implementation for Java virtual machine

Python[1] do not prevent running multiple threads simultaneous on multiple processor cores. Jython and IronPython use an underlying threading model implemented in their virtual machines. But the default Python implementation on most operating systems is CPython and therefore the rest of this chapter assumes the CPython implementation.

A better option to get parallel concurrency is to use Python's native *multiprocessing* module. Other standalone modules for parallelising on shared memory machines include Parallel Python, pyLinda, and pyPastSet. Python multiprocessing and Parallel Python can also be used on a cluster of machines.

Another parallelising option for distributed memory machines is message passing. A Python MPI implementation or wrappers (e.g.. PyCSP [Vinter *et al.*, 2009], mpi4py [Dalcin *et al.*, 2008], pupyMPI [Bromer *et al.*, 2011], and Pypar [Nielsen, 2003]) can be used for this purpose. Parallelization can also be achieved by vectorizing the tasks using NumPy. Vectorization is an efficient and optimised way of replacing explicit iterative loops from the Python code. However, not all the operations can be parallelized in Numpy/SciPy [2].

We have used the native *multiprocessing* module and the standalone *Parallel Python* module to achieve parallelization. For comparison purposes, we have implemented parallel code for four astronomy routines.

The *multiprocessing* module is part of Python 2.6 and onwards, and backports exist for versions 2.4 and 2.5[3]. *Multiprocessing* can also be used with a cluster of computers (using the multiprocessing *Manager* object), although the implementation is not trivial. We are only interested in shared memory or symmetric multiprocessing (SMP) machines, although detailed information about computer clusters for astronomical data processing can be found elsewhere[4].

A few approaches exist in the Python *multiprocessing* library to distribute the workload in parallel. In the present work we will be considering two main approaches - a pool of processes created by the *Pool* class, and individual processes spawned by the *Process* class. The *Parallel Python* module uses inter-process communication (IPC) and dynamic load balancing to execute processes in paral-

---

[1] Python implementation for .NET framework

[2] Refer to http://www.scipy.org/ParallelProgramming for more details

[3] More details on http://pypi.python.org/pypi/multiprocessing

[4] One such document can be found on our website - http://astro.nuigalway.ie/staff/navtejs

lel. Code implementation using these three approaches is discussed in detail in Appendix B.

6.4 Benchmarking

To benchmark the parallel processing approaches described in the previous section, three different kinds of astronomical problems, of varied complexity, were parallelized. Three machines of different configuration were used to benchmark the code. The hardware and software configuration of the test machines is listed in Table 6.1.

Machine	**Processor**	**Memory**	**Operating System**
Homebuilt	AMD Phenom II X4 B60 quad core processor @3.4GHz	4 GB @1066 MHz	Ubuntu 11.10 32-bit. Linux Kernel 3.0.0-16-generic-pae
Dell Studio XPS	Intel Core i7 920 quad core processor (8 threads) @2.67GHz	6 GB @1066 MHz	Ubuntu 12.10 32-bit. Linux Kernel 3.5.0-22-generic
iMac 21.5 inch	Intel Core i5 I5-2400S quad core processor @2.5GHz	4 GB @1333 MHz	Mac OS X 10.8.1 64-bit. Darwin 12.1.0

Table 6.1: Hardware and software configuration of the SMP machines used for benchmarking the parallel code.

The homebuilt machine was over-clocked to 3.51 GHz and was running the Ubuntu 11.10 operating system (OS). The Dell Studio XPS was running the same OS but as a guest OS in a VirtualBox[1] virtual machine on a Windows 7 host. Out of the 6 GB of RAM on the Dell machine, 2 GB was allocated to the guest OS. The iMac was running Mac OS X Mountain Lion. For astronomical data and image processing, existing routines from the ESO Scisoft 7.6[2] software

---

[1] VirtualBox is open source virtualization software. More details on https://www.virtualbox.org/

[2] ESO Scisoft software package is a collection of astronomical utilities distributed by European Southern Observatory

package were used. This version of Scisoft is using Python 2.5 and therefore the python *multiprocessing* backport was separately installed. The latest version of Scisoft (version 7.7 released in March 2012) has been upgraded to Python 2.7 and therefore does not require separate installation of the *multiprocessing* module. The iMac machine was using the latest version of Scisoft.

All of our benchmarking examples concern a class of parallel work flow known as *Embarrassingly Parallel* problems. In simple terms this means that the problem can be easily broken down into components to be run in parallel. The first astronomy routine is a parallel implementation of coordinate transformation of the charge-coupled device (CCD) pixel to sky coordinates (RA and DEC), and vice-versa, for Hubble Space Telescope (HST) images, for a large number of input values. The second routine parallelized a Monte Carlo completeness test. The third routine is parallel implementation of sub-sampled deconvolution of HST images with a spatially varying point spread function (PSF). These routines are described in the following sub-sections. They are freely available and can be downloaded from our website[1]. All three routines helped accelerate the data analysis described in this thesis.

6.4.1 PIX2SKY and SKY2PIX

The STSDAS package for IRAF includes the routines *xy2rd* and *rd2xy* to transform HST CCD image pixel coordinates to sky coordinates, and vice-versa. These tasks can only process one coordinate transformation at a time. Running them serially, or even in parallel, to process hundreds to thousands of transformations (e.g. star coordinate transformations in massive star clusters) is not efficient, as it will be performing the same expensive FITS header keyword reads on each call. Non-IRAF routines to transform lists of coordinates do exist, but they default to serial processing. Two such routines (*xy2sky* and *sky2xy*, implemented in C) are part of the WCSTools[2] software. A pure Python implementation exists in the *pywcs* module, which is part of the *astropy* package[3].

As these IRAF routines are not lengthy, they can easily be re-written for

---

[1] http://astro.nuigalway.ie/staff/navtejs

[2] More details on http://tdc-www.harvard.edu/wcstools/

[3] Refer to http://www.astropy.org/ for more details

multicore machines to process a large input dataset in parallel. We have implemented two tasks - PIX2SKY (based on *xy2rd*) and SKY2PIX (based on *rd2xy*) - in Python, using both the *multiprocessing* and *Parallel Python* modules. These routines read input files with either [X,Y] pixel coordinates (PIX2SKY routine) or [RA, DEC] values (SKY2PIX routine), and output transformed coordinates. We have used the PyFITS[1] module from the Space Telescope Science Institute (STScI) for handling FITS images.

The speedup factor (as defined in Section 6.2) for PIX2SKY and SKY2PIX is plotted against the number of processes in Figure 6.1. For this benchmarking, one million input coordinates were fed into the *Parallel Python* based transformation modules with guided scheduling.

Best performance was achieved when the number of processes was equal to the number of physical cores on the machine. The Intel Core i7 based machine showed better speedup than the AMD Phenom based machine. This is because Intel Core i7 processors use hyper-threading technology[2] and have 2 threads per core. Theoretically, we would have expected close to eight-fold speedup on the Intel Core i7 quad-core processor (with hyper-threading), but bottlenecks like I/O operations restrict higher performance gains (keeping the fraction of code running in parallel constant). As the number of processes increases beyond the number of cores, the speedup factor is almost flat. This is a result of dynamic load balancing in Parallel Python, which is not the case for the Process/Queue approach (as we will see in Section 6.5.3).

Another interesting point regarding Figure 6.1 is the somewhat inferior performance of the Core i5 processor compared to the other two quad core processors. We could not do a direct comparison between the Core i5 processor and other two processors as by default *Turbo Boost*[3] and *Speed Step*[4] are turned on in the iMac machine (and cannot be switched off). For the other two processors - *Speed Step technology* was turned off on the Core i7 processor and *Cool'n'Quiet*[5] was

---

[1] STScI's python module for working with FITS files

[2] Proprietary technology of Intel Corporation to allow multiple threads to run on each core

[3] Proprietary technology of Intel Corporation to run processors above their base frequency

[4] Refer to http://en.wikipedia.org/wiki/SpeedStep for more details

[5] Refer to http://www.amd.com/us/products/technologies/cool-n-quiet/Pages/cool-n-quiet.aspx for more details.

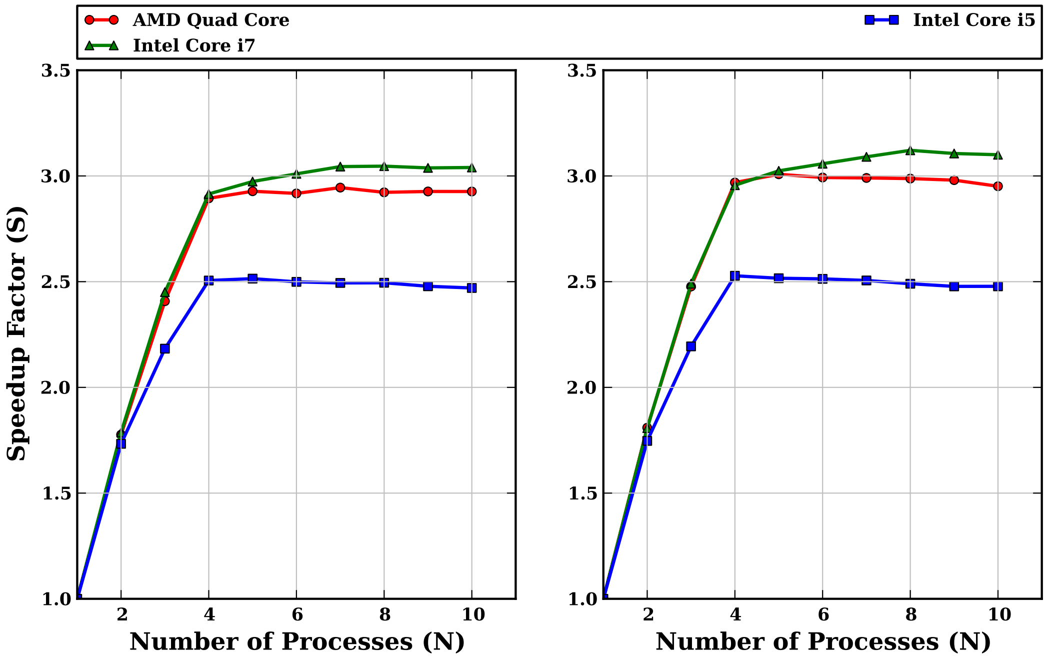

(a) (b)

Figure 6.1: Coordinate transformation benchmark, using the Parallel Python approach with a guided scheduler. (a) PIX2SKY and (b) SKY2PIX speedup on the three test machines. Data points are the average of 50 runs. As expected, maximum speedup occurs when the number of processes is equal to the number of physical cores on the machine. Of course, load balancing and the serial to parallel code fraction also influence the speedup.

switched off on the AMD machine to prevent CPU throttling.

6.4.2 Completeness Test

In more complex or lengthy problems, it makes much more sense to reuse the existing tasks or optimised serial codes, rather than re-writing code as we did in Section 6.4.1. A good example is a completeness test - the method to determine the detection efficiency of different magnitude stars in images. It is a Monte Carlo class of algorithm, i.e. it involves repeated random execution. The basic idea behind the method is to add artificial stars of varied magnitudes to random positions within the image, and then determine their recovery rate as a function of magnitude. For the test to be statistically relevant, an average of a few hundred random iterations of modified images is taken.

To reuse the existing code, the *addstar* task in the DAOPHOT package of IRAF was used to add artificial stars to the image under question and the *daofind* and *phot* tasks in DAOPHOT were used to detect and match the added stars. One way to achieve parallelism in this case is to run multiple iterations in parallel on the available computing nodes, where each node gets a complete image.

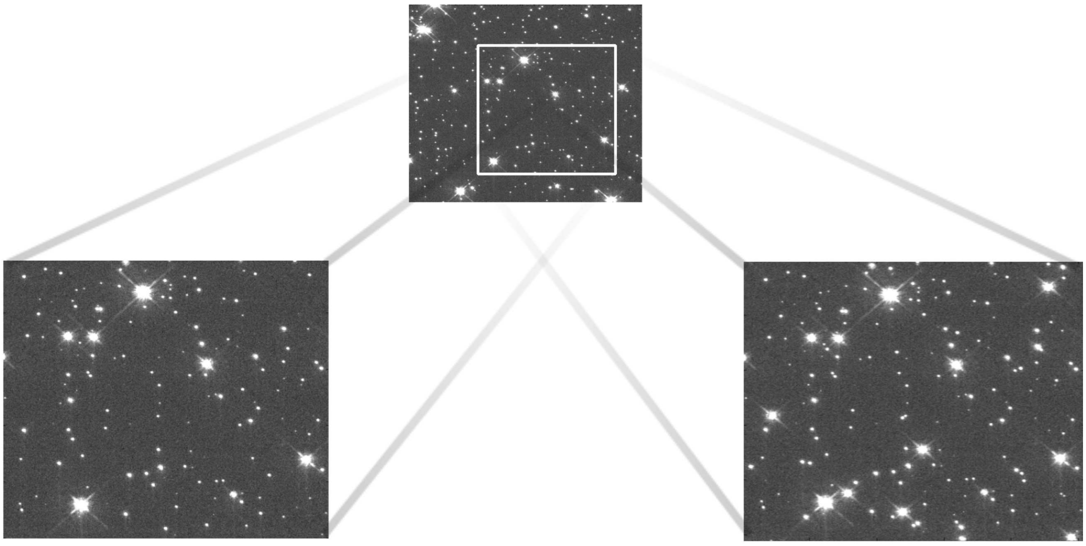

Figure 6.2: HST WFPC2 co-added image of the globular cluster M71 (NGC 6838) in the F555W filter, used for benchmarking the completeness routine. The test was performed on a 512×512 image section (lower left). This image plus 50 artificial stars between 14^{th} and 28^{th} magnitude, generated in one of the Monte Carlo iterations, is shown in the lower right.

For the benchmark, we used the reduced and co-added HST WFPC2 (chip PC1) image of galactic globular star cluster M71 (NGC 6838) in the F555W filter (shown in Figure 6.2). The completeness test was performed on a 512×512 pixel uncrowded section of the image with $14^{th} - 28^{th}$ magnitude stars in each iteration. Fifty stars (a sufficiently small number to avoid changing the star density appreciably) were added randomly to the image section (shown in Figure 6.2), and 100 iterations per magnitude interval were run. As in the previous benchmark, we used the Parallel Python approach with guided scheduler.

In Figure 6.3(a), we plot the completeness test results, computed by averaging

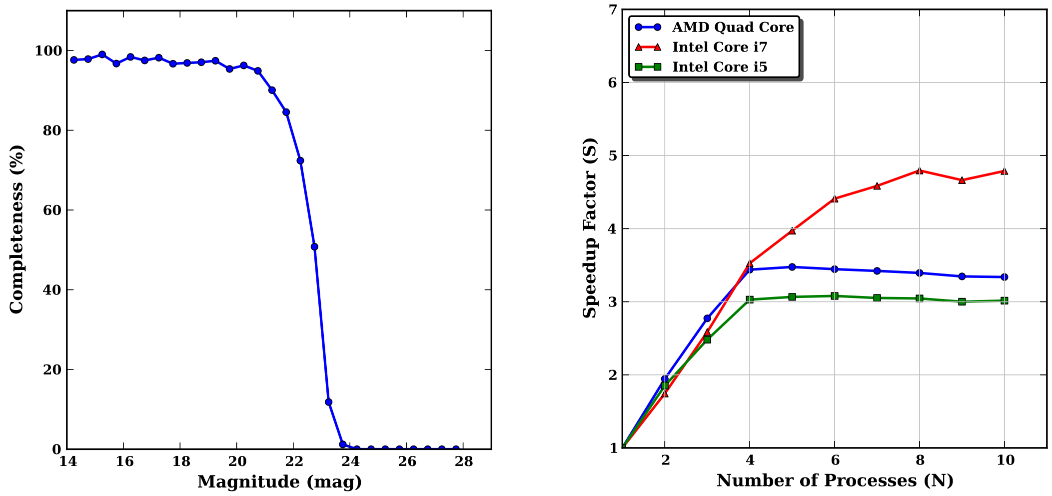

(a) (b)

Figure 6.3: (a) Detection completeness plot for the images in Figure 6.2 with artificial star magnitudes varying from 14.0 to 28.0 mag within 0.5 mag intervals; (b) Speedup achieved on the test machines as a function of the number of parallel processes. The Parallel Python approach with guided scheduler was used for benchmarking.

results from all the iterations, with a 0.5 magnitude bin interval. Figure 6.3(b) shows that maximum speedup is achieved when the number of processes is equal to the number of physical cores, or the total number of threads (in the case of the Intel Core i7 machine). All three processors show close to 2× speedup with 2 spawned processes. After four processes, speedup flattens out for the AMD and Core i5 processors whereas it keeps on increasing for the Core i7 machine (although not as steeply as from 1 to 4 processes). This is explained by Equation 6.3 - the number of processes is scaled on the parallel code fraction and synchronisation time.

6.4.3 Parallel Sub-Sampled Deconvolution

Image deconvolution is an embarrassingly parallel problem, as image sections can be deconvolved in parallel and combined at the end. In addition to being under-sampled, HST detector point spread functions are spatially varying. To recover resolution lost to aberration and poor sampling in HST images, Butler [2000] proposed an innovative sub-sampled deconvolution technique. We have implemented a parallel version of this technique.

To deconvolve HST images with a spatially varying PSF, we wrote a parallelized version of the sub-sampled image deconvolution algorithm. The Maximum entropy method (MEM) implementation in the STSDAS package was used for deconvolution. As it only uses a spatially invariant PSF, highly overlapping 256×256 sub-images were deconvolved with the appropriate PSF for that position on the CCD. Deconvolved sub-images were reassembled to generate the final sub-sampled deconvolved image.

For benchmarking, we used a coadded HST WFPC2 PC1 chip image of the globular cluster NGC 6293. A spatially varying analytical PSF model was generated from the TinyTim PSF grid. The Parallel Python module with guided scheduler was used for benchmarking. The central region of NGC 6293, along with a high resolution section of the normal sampled image and sub-sampled deconvolved image, are shown in Figure 6.4(a). The speedup factor levels out close to 4 for the AMD machine, whereas it levels out at 5 for the Intel Core i7 machine (see Figure 6.4(b)). In general, embarrassingly parallel problems provide the best speedup as a higher fraction of code is running in parallel.

6.5 Discussion

6.5.1 Ease of Implementation

As shown in Section 6.3, parallelising existing python serial code can be pretty straightforward for problems that can be easily broken down into smaller parts. This is especially true if the *multiprocessing* Pool/Map approach is used in existing functional python code. Python includes excellent code profilers - *cProfile* and *Profile*. These, along with the *pstats* module, can be used to optimise the parallel code as well as the serial code.

Astronomers using IRAF scripts now have another reason to move to PyRAF, and the python scripting language in general. The PyRAF command line interface allows execution of IRAF CL scripts, and also gives full flexibility and the

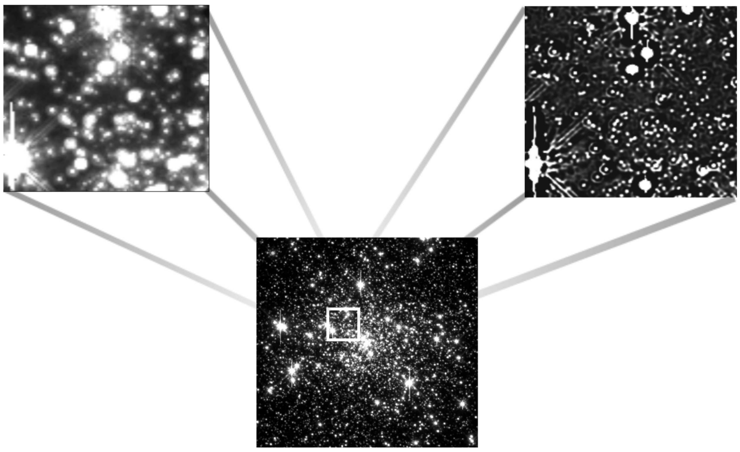

(a)

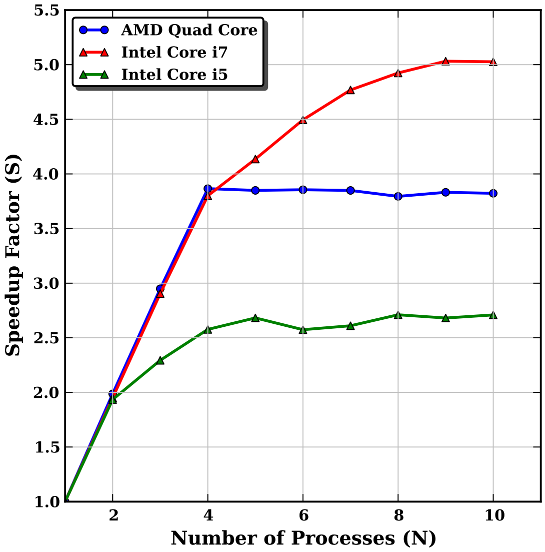

(b)

Figure 6.4: (a) HST WFPC2 PC1 coadded image of globular cluster NGC 6293 in the F814W filter. A normal sampled $4.6'' \times 4.6''$ image section is shown in the upper left hand corner, and the 2× sub-sampled deconvolved section in the upper right hand corner; (b) Sub-sampled deconvolution benchmark. The AMD quad core performance levels out after four processes, whereas the Intel quad core achieves a speedup factor of almost 5 for eight processes. The Parallel Python approach with guided scheduler was used for benchmarking.

power of the python language. STScI has a very useful PyRAF introductory tutorial[1] on their website. Another reason for using python is that it is an open source language, supported by community development, with most of the modules available for free. Python modules NumPy and SciPy comprise an extensive collection of numerical and scientific functions[2].

IRAF saves the task parameter values in global parameter files. This could lead to deadlock if same two tasks try to gain write access to the parameter file. This can be avoided in PyRAF by explicitly specifying all the parameters in the task, thus avoiding accessing the global parameter file.

6.5.2 Load Balancing

Load balancing in parallel computing is the distribution of the workload on computing nodes to optimise performance. It is an important issue to deal with while designing a parallel application. On multicore machines, all the cores will not perform identically as other activities and tasks are running concurrently. A parallel program will run as fast as the slowest core. Thus, the performance of a parallel program will be dictated by the slowest processor core. Therefore, efficient load balancing of the workload on the processor cores is very important. On shared memory machines, the OpenMP protocol has implemented four types of schedulers or load balancing routines - *static*, *guided*, *dynamic* and *runtime* [Chandra *et al.*, 2001]. On the same lines, we have implemented *static* and *guided* scheduler routines to slice large input datasets into smaller chunks and distribute them on the computing nodes. In the static scheduler, equal chunks of data are distributed on each computing node. In the guided scheduler, instead of distributing equal chunks in one go, the dataset is divided in much smaller chunks to provide better performance. These two schedulers were used in both the PIX2SKY and SKY2PIX routines. For more efficient load balancing, dynamic or runtime routines can be implemented.

In normal usage of both PIX2SKY and SKY2PIX, we read hundreds to thousands of input records. Sending large chunks of file data to computing nodes

---

[1] http://stsdas.stsci.edu/pyraf/doc.old/pyraf_tutorial/

[2] Numerical Python (NumPy) and Scientific Python (SciPy) are non-standard Python modules

would result in a longer synchronisation time. Instead, we send the starting and ending byte values of the file chunks, and actual file reading is done inside the worker process at each node. Example scheduler implementation code is shown below:

Listing 6.1: Scheduler implementation code

```
def getchunks( infile, ncpus, scheduler = ‘guided‘ ):
  # Based on scheduler, divide the input data element
  if scheduler == ‘static‘:
    size = getsize( infile ) / ncpus
  else:
    size = getsize( infile ) / (ncpus * 20)

  # Open the input file. Display error and
  # exit if open fails
  try:
    ifile = open( infile )
  except:
    print >> sys.stderr, ‘Error : Not able to open ‘, infile, ‘. Exiting.‘
    sys.exit( -1 )

  # Get starting and ending byte values for each chunk,
  # taking care to read the full line
  while 1:
    start = ifile.tell()
    ifile.seek(size, 1)
    s = ifile.readline()
    yield start, ifile.tell() - start
    if not s:
      break

  # Close the input file
  ifile.close()
```

In the case of the *guided* scheduler, the number of records is divided into a large number (20 times the number of processes) of smaller chunks. The performance of the PIX2SKY routine with one million input records on our AMD quad core machine, with both the *static* and *guided* scheduler, is shown in Figure 6.5. The

Parallel Python approach was used, but we get the same results with the other two approaches also.

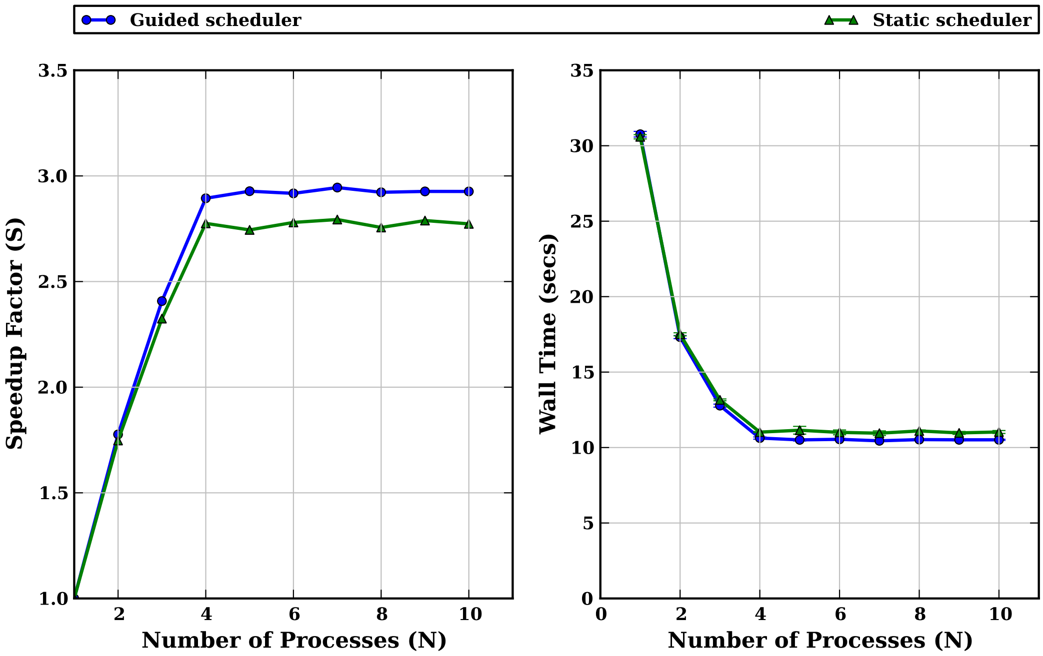

(a)

(b)

Figure 6.5: (a) Speedup and (b) Wall time for the PIX2SKY routine with different schedulers. The guided scheduler shows better performance than the static. Wall time is the total execution time for the routine. Data points are averaged over 100 runs. Program wall time on COTS machines depends on the other jobs and programs running. Error bars depict 1 standard deviation. The Parallel Python approach on AMD processor was used.

The graph clearly shows a better performance for the guided scheduler. Therefore dividing work into smaller fragments is better for optimum performance of parallel programs.

6.5.3 Multiprocessing Method Performance

To compare the performance of the different multiprocessing methods introduced in Section 6.3, we again took the PIX2SKY and SKY2PIX routines with one million input coordinates to be transformed. Our plots of run time (wall time) versus number of processes for the AMD quad core machine are shown in Figure 6.6(a) and Figure 6.6(b).

For both PIX2SKY and SKY2PIX, the Process/Queue approach performs better than both the Pool/Map and Parallel Python approaches. However, Parallel Python scales nicely when the number of processes are more than number of physical cores. Although the Process/Queue performs better, implementing the Pool/Map method is much more straightforward.

For our routines using existing IRAF tasks - the completeness test and sub-sampled deconvolution - all three approaches have comparable performance. This is because the execution time of these routines is dictated by the performance of the underlying IRAF tasks (see Figure 6.6(c) and Figure 6.6(d)).

6.5.4 Scalability and Portability

Data parallelism using Python multiprocessing scales nicely with the number of processor cores, as shown in Section 6.4. Our coordinate transformation code also scales nicely with the number of input data elements. As depicted in Figure 6.7, the PIX2SKY routine scales linearly with the number of input data elements. It was benchmarked on an AMD quad core machine for 4 processes, using the Process/Queue multiprocessing method and varying the input data elements from 500 to 1 million. Similar scalability is also achieved for the SKY2PIX routine. These routines can also be executed on multi-processor supercomputers with Python support.

As Python is a platform-independent interpreted language, the parallel code implementation is portable, i.e. it can be implemented on any of the Python-supported OS. In two of our examples, we have used IRAF tasks which can only be executed on Linux or Unix-like OS (e.g. Mac OS X), as IRAF is only available for these platforms. But astronomical data analysis tasks not requiring IRAF can be run on other supported platforms.

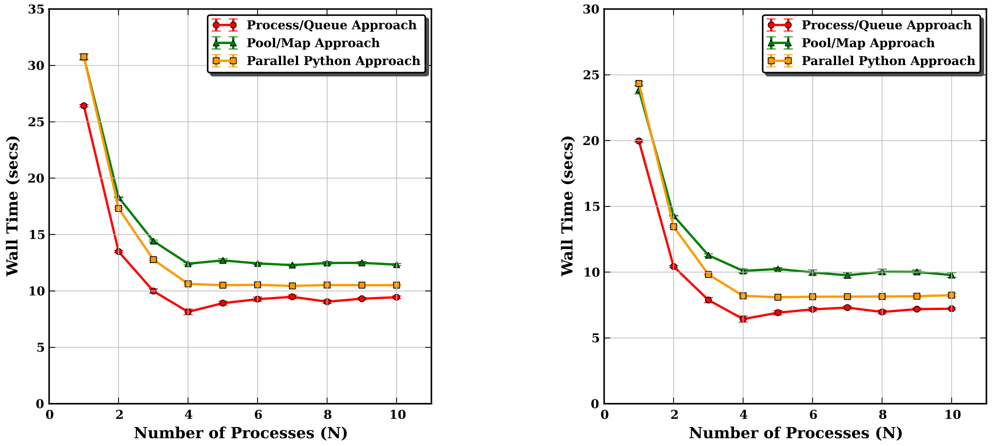

(a) PIX2SKY (b) SKY2PIX

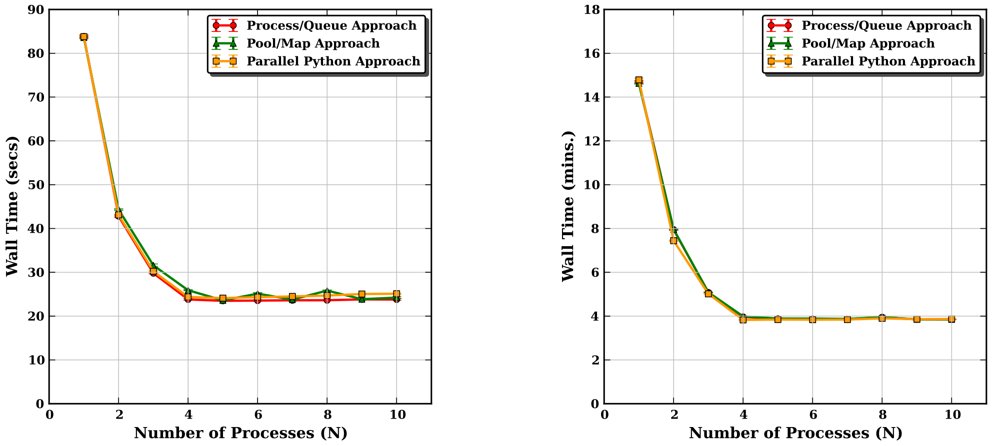

(c) Completeness Test (d) Sub-sampled Deconvolution

Figure 6.6: Performance of different multiprocessing methods. Panels (a) and (b) depict the performance of our PIX2SKY and SKY2PIX routines on our AMD quad core machine respectively. Panel (c) depicts the performance of our completeness test and panel (d) that of our parallel sub-sampled deconvolution. Data points are the average of 50 iterations for the PIX2SKY benchmark and 10 iterations for the completeness test and deconvolution. The Parallel Python, Pool and Process approaches show comparable performance for our completeness and sub-sampled deconvolution routines, whereas the Process/Queue approach performs better than both the Parallel Python and Pool/Map approaches for the PIX2SKY and SKY2PIX routines.

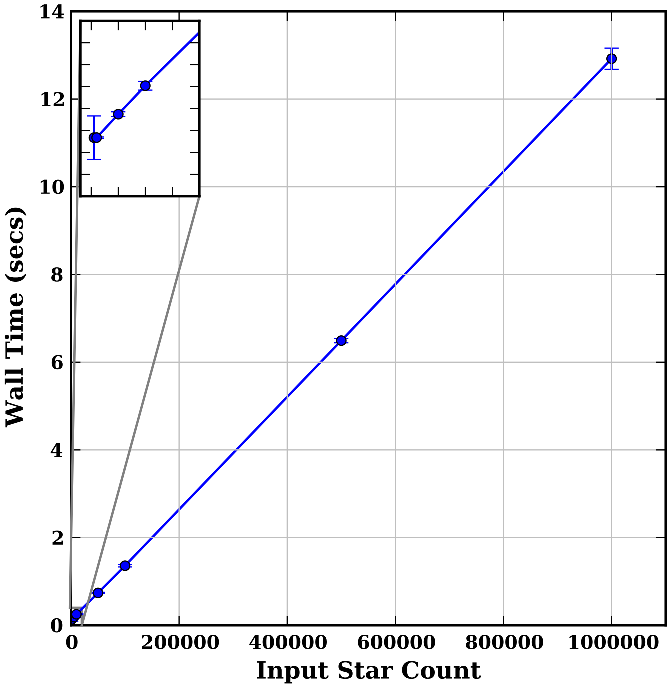

Figure 6.7: Scalability of our PIX2SKY routine with the number of input elements, for a fixed number of processes. The number of input coordinates was varied from 500 to 1 million. The benchmark was carried out on an AMD quad core machine with 4 parallel processes. The data points are the average of 50 iterations, with error bars corresponding to 1σ. The inset box is a close-up of the area near the origin. The Process/Queue approach was used with guided scheduler.

6.6 Conclusions

We have shown that moving to parallel astronomical data processing is not as daunting as most astronomers perceive. The open source Python programming language provides the necessary tools to implement parallel code on multicore machines. We used three different hardware configurations, three different parallelising schemes or approaches, two different load balancing routines, and three different applications of varied complexity to demonstrate the ease of implementation and benefits of parallelising data processing tasks. Although the emphasis was on the Python *multiprocessing* module, results from the Parallel Python module were also presented. The Process/Queue approach performed better as a parallelising scheme than both the Pool/Map and Parallel Python approaches. Parallel performance can be optimised by carefully load balancing the workload. Where there is no possibility of re-writing the code for parallel processing because of complexity or any other factor, the existing serial code can still be used to parallelize the problem (as shown in the completeness test and sub-sampled deconvolution tasks). While these are not the only or the most optimised methods to parallelize the code, the computational time savings are still very significant, even with these straightforward approaches. The cross-platform nature of Python makes the code portable on multiple computer platforms.

Chapter 7

Stellar Proper Motions I: Simulated Cluster Images

Our sub-sampled deconvolution technique was benchmarked for astrometric and proper motion accuracy using simulated images of the globular clusters. The photometric accuracy of the technique was already addressed by Butler [2000]. An automated pipeline was developed in the *Python* programming language to generate realistic multi-epoch cluster images. It was implemented for the HST instruments WFPC2, ACS WFC, and ACS HRC, with the possibility of extending it for other space and ground based instruments.

The pipeline for generating simulated cluster images is described in Section 7.1. Section 7.2 details the benchmarking routine and results of the sub-sample deconvolution technique for HST WFCP2 and ACS WFC detectors.

7.1 Simulated Globular Cluster Images

An automated pipeline was developed to generate realistic multi-epoch globular cluster simulated images. It uses a combination of isochrone data, surface brightness profiles of the globular clusters, instrument characteristics, and estimated internal proper motion dispersion to generate the images. A simplified flowchart of the pipeline is shown in Figure 7.1. The pipeline was developed in *python* using the existing back end PyRAF tasks. The pipeline can generate multi-epoch simulated galactic globular cluster images in different optical bands for WFPC2, ACS WFC, and ACS HRC detectors.

The following sub-sections describe the isochrone model, surface brightness profile, instrument characteristics, and proper motion data used as input to the pipeline. Example images are also presented below.

7.1.1 Padova Isochrones

Isochrones depict the properties of the cluster stellar population at a particular time in the evolution of the cluster. Theoretical isochrones are used to determine the current age of the star clusters by fitting the observed properties to the theoretical calculated values. This is mostly done by fitting theoretical isochrones to the observed colour magnitude diagram. We used Padova isochrones to generate a set of cluster stellar population CMDs based on the cluster age and metallicity. Theoretical isochrone tables were downloaded from Padova's online tool - *CMD* version 2.3[1]. We only considered the Padova isochrones as they go deep enough for our simulated cluster images and are freely available publicly in easy to use format.

For most of the input parameters, default values were used. The evolutionary track was based on Marigo *et al.* [2008] and Girardi *et al.* [2010] and Chabrier's lognormal initial mass function was used. The Padova isochrone web interface allows data to be exported in various photometric systems. We used the default absolute Vega mag zeropoints for both the WFPC2 and the ACS WFC/HRC detectors [Holtzman *et al.*, 1995; Sirianni *et al.*, 2005]. Values for interstellar extinction/reddening, age and metallicity for the cluster were taken from Harris [1996]. Theoretical isochrone curves for four galactic globular clusters, using this approach, are plotted in Figure 7.2.

Our simulated images require the correct number of stars for each magnitude and colour interval (bin), so luminosity function tables were calculated from the isochrone data.

---

[1] We used the older version 2.3, the current version is 2.5. It can be accessed from http://stev.oapd.inaf.it/cgi-bin/cmd

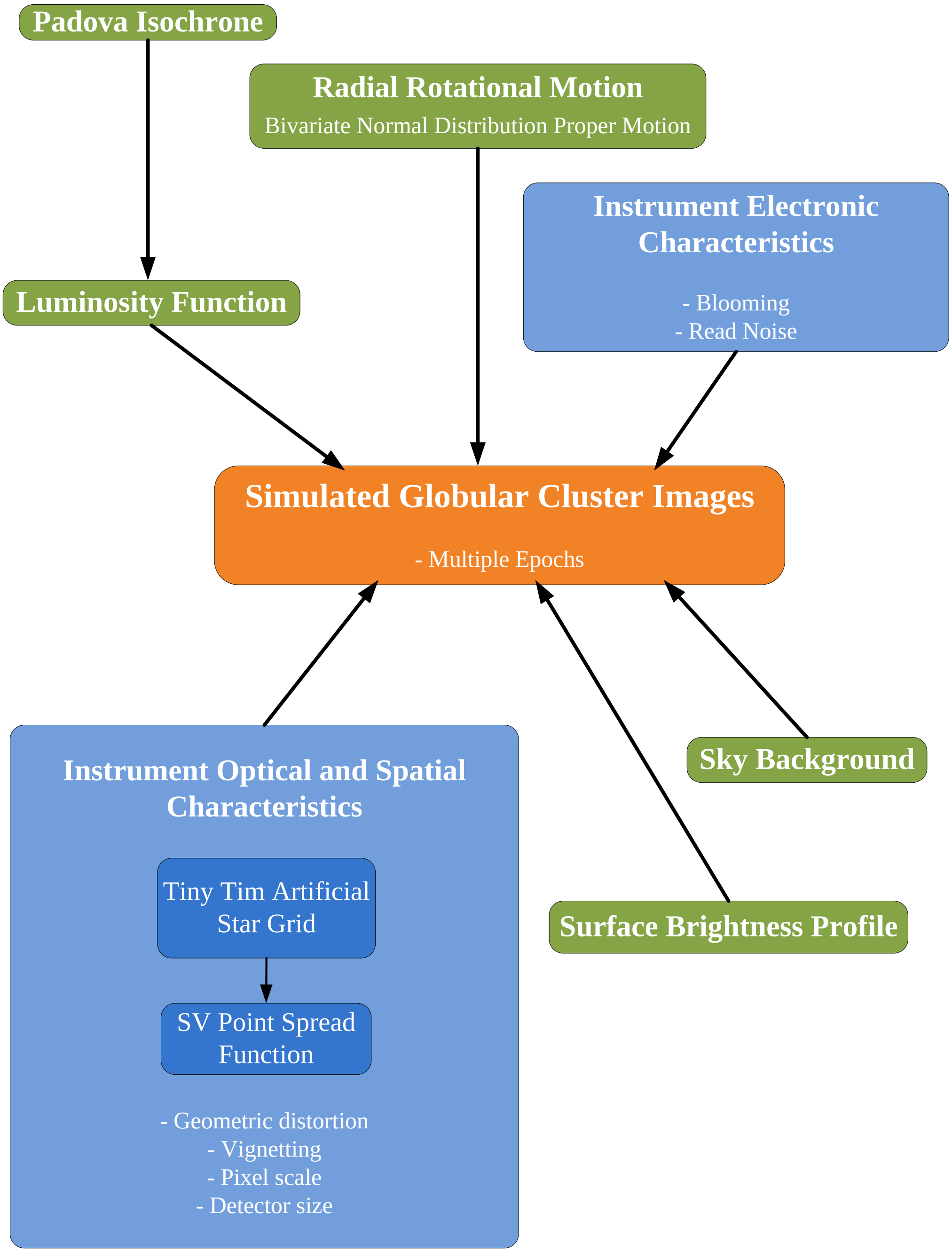

Figure 7.1: Flowchart of the simulated image generation pipeline. The isochrone data was taken from the Padova website and the surface brightness profile is based on Noyola & Gebhardt [2006].

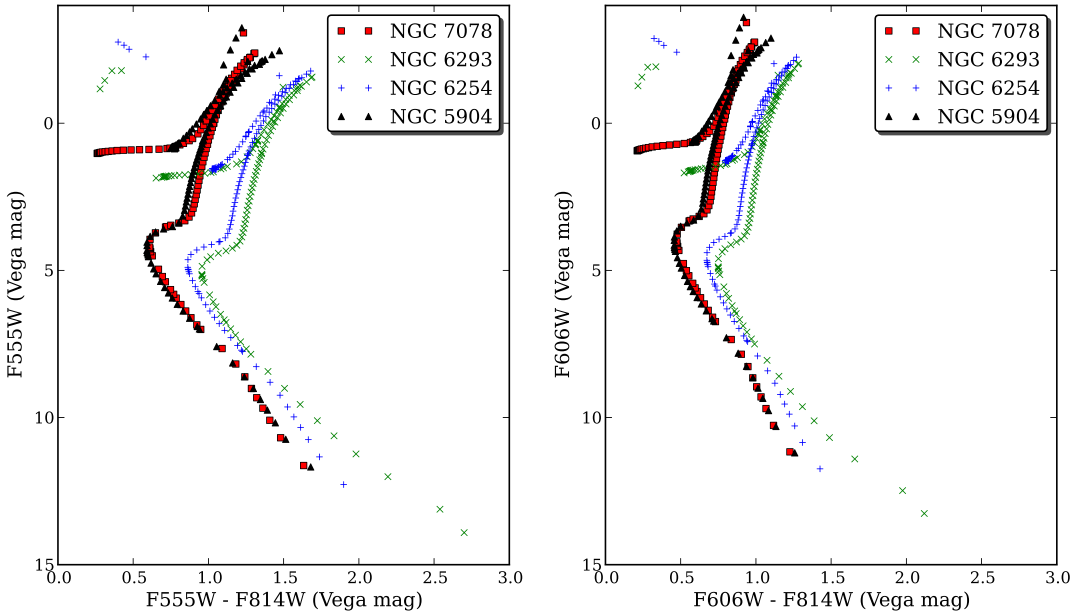

Figure 7.2: Padova isochrone curves for galactic globular clusters based on Harris [1996] parameters. The same curves are plotted for the WFPC2 (on left) and ACS WFC (on right) detectors in the absolute Vega magnitude system. A small offset between F555W and F606W magnitudes can be observed.

7.1.2 Surface Brightness Profile

The spatial distribution of light (and thus stars) in a star cluster or a galaxy can be depicted by its surface brightness profile. This is the variation of surface brightness with radial distance from the centre of the astronomical object. We used the surface brightness profiles of the selected galactic globular clusters from Noyola & Gebhardt [2006]. These were downloaded from the CDS Strasbourg VizieR catalogue service (http://vizier.u-strasbg.fr/viz-bin/VizieR). Noyola & Gebhardt [2006] used the Hubble Space Telescope images to generate the surface brightness profiles of 38 galactic globular clusters. They were the most appropriate surface brightness profiles to use as they were constructed using the high resolution data from the Hubble Space Telescope and was an improvement over the profiles generated using ground based telescope by Trager *et al.* [1995]. The surface brightness profile of four globular clusters is plotted in Figure 7.3. The surface brightness tables give the radial distance (in log base 10 unit) and the surface brightness in V band (in units of $mag/arcsec^2$). There is an offset between the V band zeropoint and the WFPC2 F555W and ACS WFC F606W zeropoints. As the offset is small, we did not transform the V band magnitude to F555W or F606W magnitudes. This should have little or no affect on the proper motion benchmarking. Surface brightness profile was solely used for distribution of stars in the field of view and stellar magnitudes were based on the isochrone models.

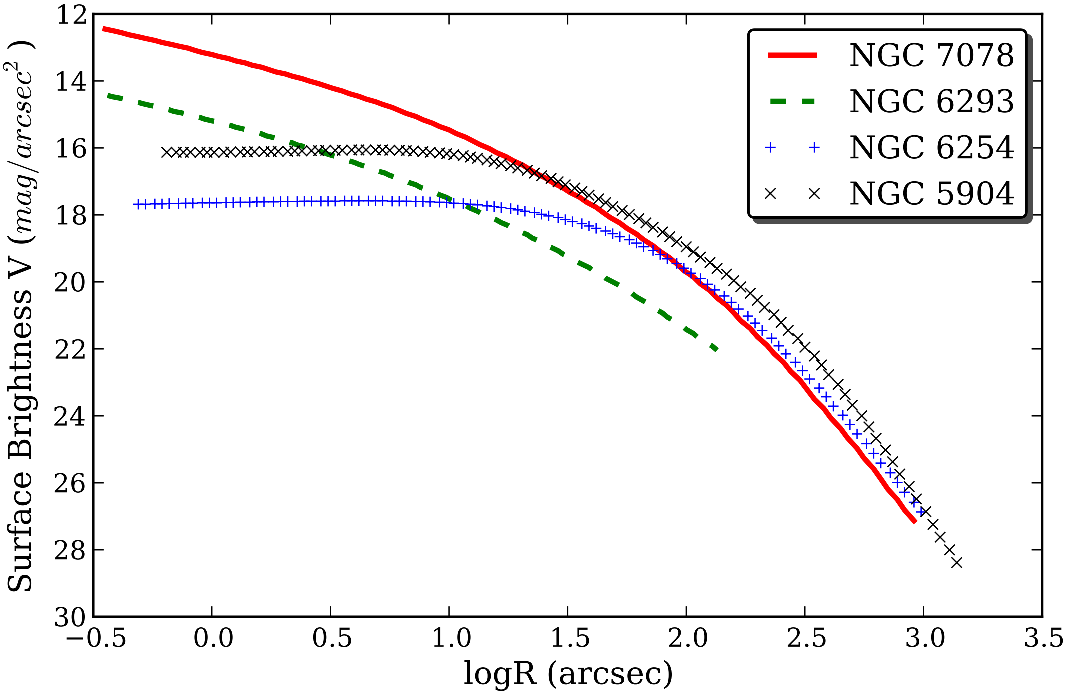

Figure 7.3: Surface brightness profile of four galactic globular clusters. M15 (NGC 7078) and NGC 6293 show a gradual increase in surface brightness towards the core. Both are core collapsed clusters and were once thought to harbour an intermediate mass black hole.

7.1.3 Instrument Characteristics

To add stars to a simulated globular cluster image, we need an analytical or an empirical point spread function. For HST instruments, our pipeline automatically generates a spatially varying point spread function using an analytical TinyTIM PSF (see Section 5.3.2). For other instruments, a PSF can be passed to the pipeline through the configuration file. In addition to the point spread function, the pipeline also requires the detector gain, read noise, and saturation value. The user can either provide a constant mean sky value for the image or the pipeline can determine it using an existing real image. Similarly, it can copy the reference sky and pixel coordinates from the header of a real cluster image or the user can enter those in the configuration file. The pipeline can also generate artificial bleeding or blooming using the saturation value for the detector.

7.1.4 Stellar Proper Motion

To create multiple epoch images, stellar proper motion is superimposed on all the stars. With the assumption that the proper motion of the stars in a cluster follows a Gaussian distribution (as observed in many globular clusters studied; e.g. McLaughlin *et al.* [2006]), we generate random proper motion vectors equal to the number of simulated stars in the [x, y] detector plane, using the *MASS* package in **R** statistical software. The mean value and dispersion for the Gaussian distribution can be changed by the user. For the present study, central radial velocity dispersion values from Harris [1996] were used and mean proper motion value set close to 0. At present our code randomly assign proper motion vectors to the cluster stars and does not take variation with radial distance from the cluster centre into consideration. In a realistic globular star cluster, the presence of an intermediate mass black hole or collection of LMBHs or neutron stars at the centre would lead to variation in the internal proper motion dispersion with the radial distance from the centre of the cluster. A simulated proper motion vector plot (for $\sim$ 16000 stars) with 0.0 mas/year mean and 0.3 mas/year dispersion is shown in Figure 7.4.

7.1.5 Pipeline

The luminosity tables are used in conjunction with the globular cluster surface brightness profile and detector spatial characteristics to generate the star list with pixel coordinates and two filter magnitudes. The IRAF task *starlist* is used for this purpose.

The second step in the pipeline is to use the above star list to generate the

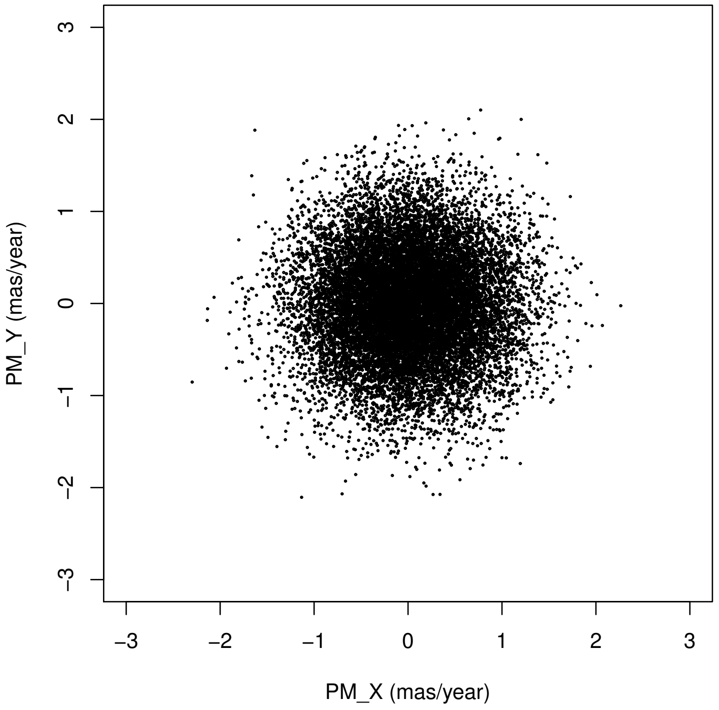

Figure 7.4: Simulated proper motion vector plot. A Gaussian motion distribution was used with 0.0 mas/year mean and 0.3 mas/year dispersion.

simulated cluster image. The spatially varying point spread function is used in the IRAF task *addstar* to add stars to a blank image. The blank image is created using the task *mkpattern* with constant sky value (either entered by the user or taken from a real cluster image in the same filter and exposure time). The reference pixel and sky values (spatial world coordinate system) are updated in the image header with user supplied values in the configuration file or copied from another image[1]. Gaussian noise is added to the image using the IRAF task *mknoise* per the read noise value for the detector. As mentioned earlier, any pixel with flux above the saturation value has its access flux redistributed iteratively into adjacent pixels in the same CCD column.

---

[1] CRPIX1 and CRPIX2 are reference pixel header keywords and CRVAL1 and CRVAL2 are reference sky value header keywords. CD1_1, CD1_2, CD2_1, and CD2_2 are the CD matrix coefficients scale and orientation information in the image header.

The above step generates a single epoch image. The pipeline has the provision to generate multi-epoch images separated by any desired interval of years. For example - it can generate 10 images separated by 10 years on a 100 year baseline. The position of the stars on the detector in different epochs is calculated using the proper motion vector assigned to them. We are assuming that the star's proper motion remains the same between the intervals. This is reasonable for intervals of the order of decades, considering that the typical time between dynamical interactions is 10^6 years [Heggie & Hut, 2003].

Simulated images of globular clusters M15 and M5 are shown in Fig 7.5. The M15 image generated for the WFPC2 detector has 50,000 stars in an 800×800 pixel area, whereas the ACS WFC M5 image has 100,000 stars in an 4096×4096 pixel area. The WFPC2 image is in the F555W filter and ACS WFC image is in the F606W filter.

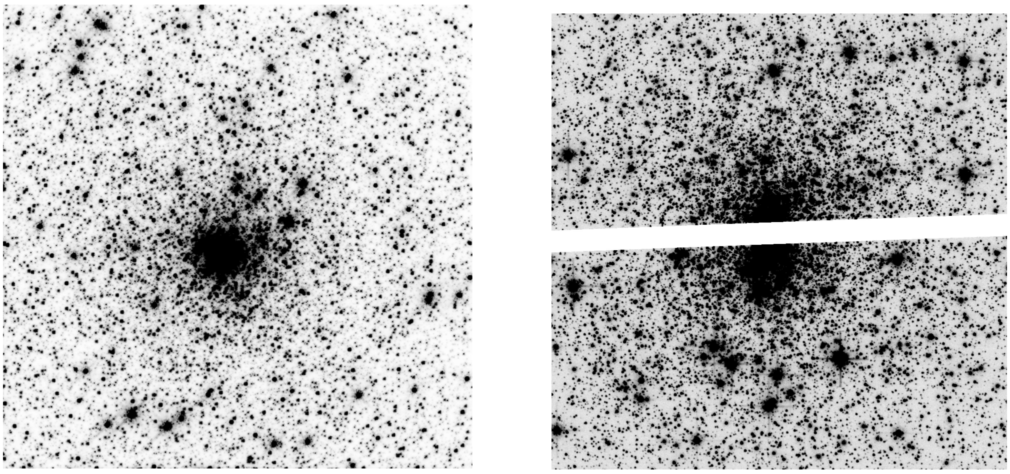

Figure 7.5: Simulated images of clusters M15 (left) and M5 (right). The M15 image is in the F555W filter, having 50,000 stars, whereas the M5 image has 100,000 stars in the F606W WFC filter. Both images are represented in negative color space. Severe crowding is evident at the centre of the clusters.

Tricolor simulated images of cluster M15 (WFPC2 camera with 10,000 stars), created with three multi-epoch images in the F814W filter are shown in Figure 7.6. The first epoch image was assigned to the red channel, second epoch image to green, and last epoch image to the blue channel. Results are shown for two different baselines: 100 years (50 year intervals) and 1000 years (500 year intervals). As expected, appreciable motion of the stars is more clearly visible for the 1000 year baseline. This allows us to visualise dynamical motion in clusters, but it must be noted that the minimum epoch gap for visual perception of motion is far greater than that required for software detection and quantification of stellar motion.

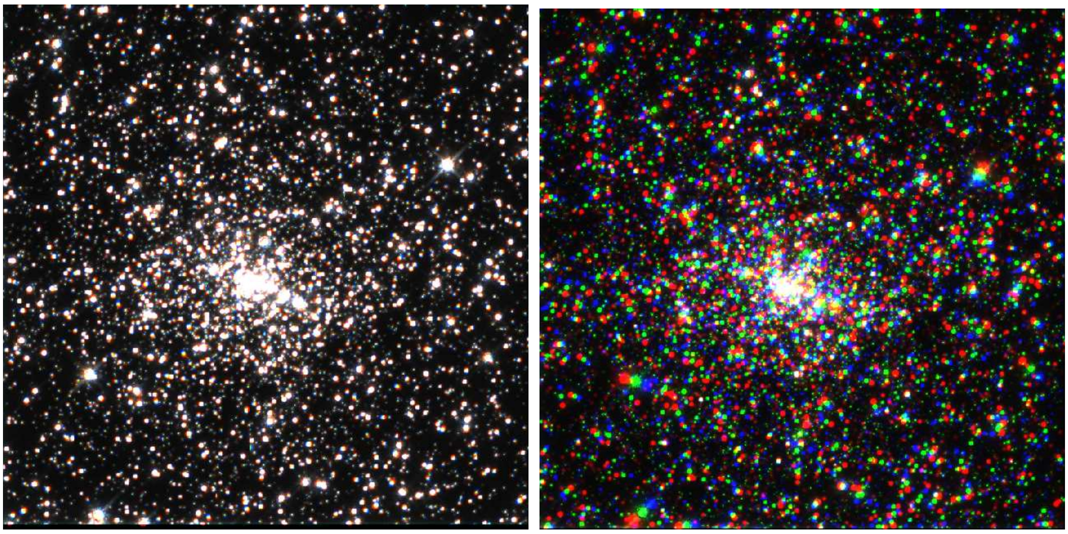

Figure 7.6: Simulated tricolor images of cluster M15 created by combining three multi-epoch, same-filter images, separated by 50 year interv als (left) and 500 year intervals (right). The red channel displays the first epoch image, green for the second epoch, and blue for the last epoch.

At present the pipeline is single threaded and therefore generates the images serially. In future we will convert the application to multi-threaded, so as to generate multiple images in parallel.

7.2 Sub-sampled Deconvolution Benchmarks

To benchmark the sub-sampled deconvolution technique, multi-epoch simulated images were tested for astrometric, and proper motion accuracy. Proper motion accuracy is dependent on the stellar positional measurement errors in each epoch and the geometric transformation errors. Realistic cluster images were generated using the pipeline described in the previous section. We only considered the simplest case - where the cluster stars were situated at approximately the same position on the detector. This is not the case for most of the real multi-epoch datasets because of different telescope pointing/orientation between the epochs. As mentioned earlier, both WFPC2 and ACS WFC suffer from geometric distortions. Therefore, change in telescope pointing and orientation (and thus inconsistent cluster positioning) from one epoch to another affects the positional accuracy of the stars between the epochs. Statistical errors were considered from the proper motion study of the real cluster images.

For the case of the WFPC2 instrument, NGC 6293 simulated images were used for benchmarking. Benchmarking of M15 ACS WFC simulated images is described in Section 7.2.2. ACS HRC detector images were not benchmarked but when analysing real HRC images, we get similar results to WFC detector.

7.2.1 WFPC2 Detector

The automated pipeline was used to generate simulated images of NGC 6293. A Padova isochrone of age 13×10^9 years and metallicity Z=0.0003 [Lee & Carney, 2006] was used. Two sets of WFPC2 (PC chip only) images in the F555W and F814W bands were generated (separated by 14 years and having 20,000 stars). Exposure times and mean sky values were taken from the real NGC 6293 cluster images from a 1994 epoch. The input color magnitude diagram and luminosity function is shown in Figure 7.7.

One of the simulated image is shown in Figure 7.8. Crowding is evident in the cluster center. The mean distance between any stars and its nearest neighbour is around 2 pixels, as shown in Figure 7.8.

We processed the simulated images through the sub-sampled deconvolution technique, similar to real cluster images. The simulated images in both the epochs were deconvolved with the spatially varying TinyTIM point spread function. The F555W and F814W filter deconvolved images were combined with cosmic ray rejection and smothered with a Gaussian kernel. Star detection was performed on the combined smoothened image. Both aperture photometry and PSF fitting photometry was performed on the detected stars. The first guess PSF was improved upon by modelling a new PSF it directly from $\sim 60-70$ bright stars in

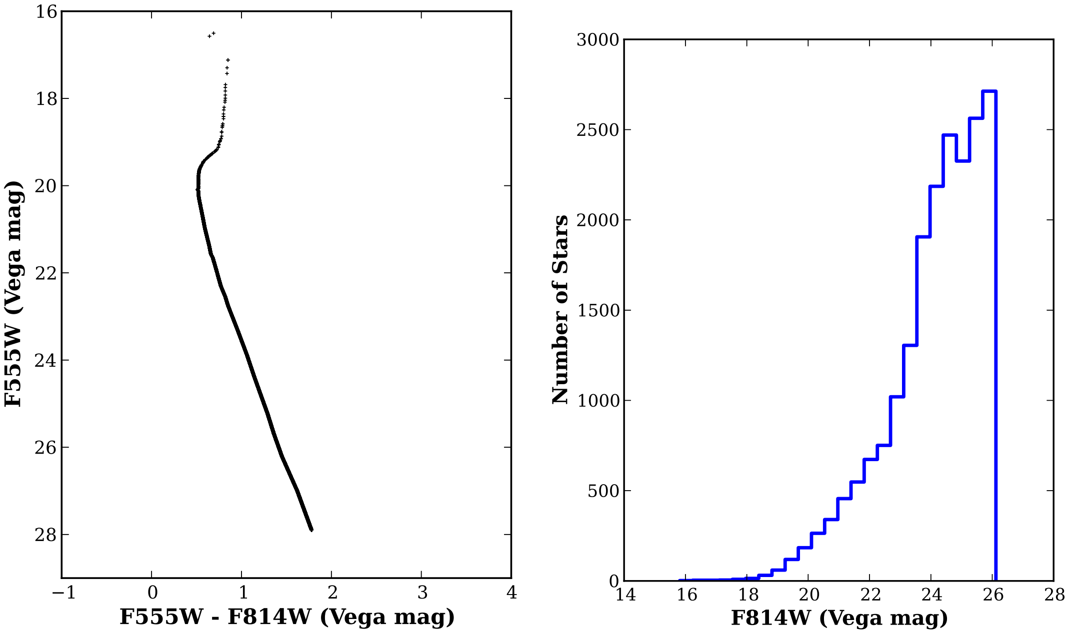

Figure 7.7: Input color magnitude diagram (left) and luminosity function (right) used to simulate the NGC 6293 WFPC2 images. The Padova isochrone is 26^{th} magnitude deep in F814W filter and therefore the abrupt cutoff in the luminosity function.

the image. All the stars fitted by the first PSF (except for stars used for PSF modelling) were subtracted from the image and the *psf* task used to model the empirical point spread function. The second refined point spread function was then used to fit the stars again to give us both stellar position and magnitude.

The output star lists were matched to the input star lists and only stars within ±0.5 pixel and ±0.5 magnitude of the input star coordinate were kept in the final matched list. The total number of stars and the matched stars, are plotted as a function of star magnitude in Figure 7.9. As expected, the detection efficiency decreases for low magnitude stars.

However, our sub-sampled deconvolution technique shows better detection efficiency for high magnitude stars as well as in the inner crowded core of the cluster, compared to direct detection on the science images (see Figure 7.10).

For proper motion studies, low positional errors are important. A histogram of the positional difference between input and detected stellar positions is shown

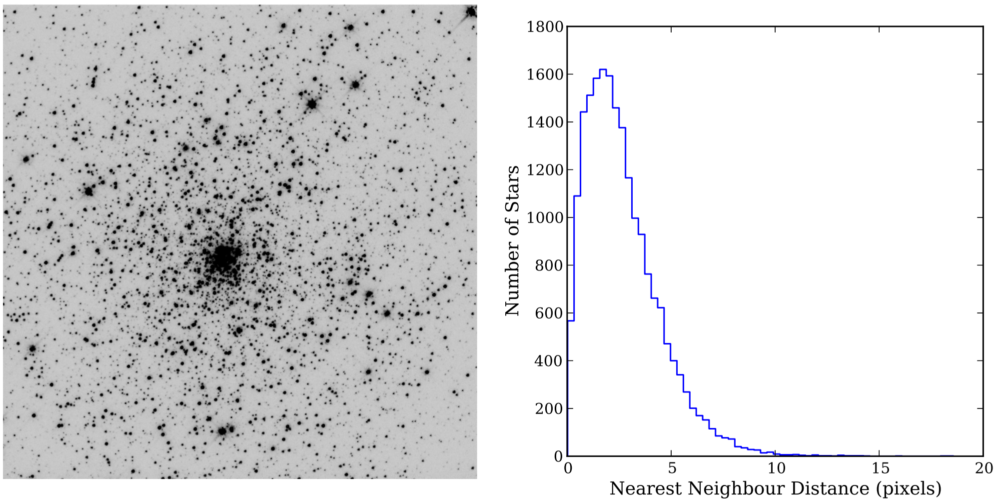

Figure 7.8: Left: One of the simulated NGC 6293 images in the F555W filter. Right: histogram of the nearest neighbour separation, in pixels. The mean minimum separation between the stars is around 2 pixels.

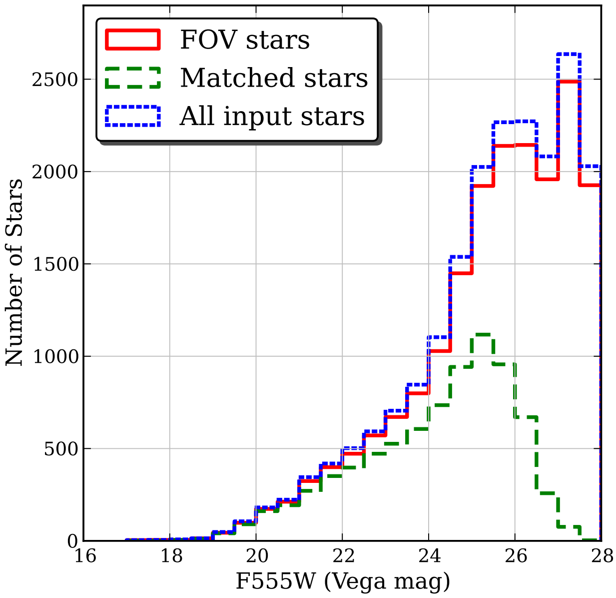

Figure 7.9: The total number of input stars and matched stars as a function of star magnitude. The field of view (FOV) of WFPC2 excludes the vignetting regions. As expected, detection efficiency is poor for high magnitude stars.

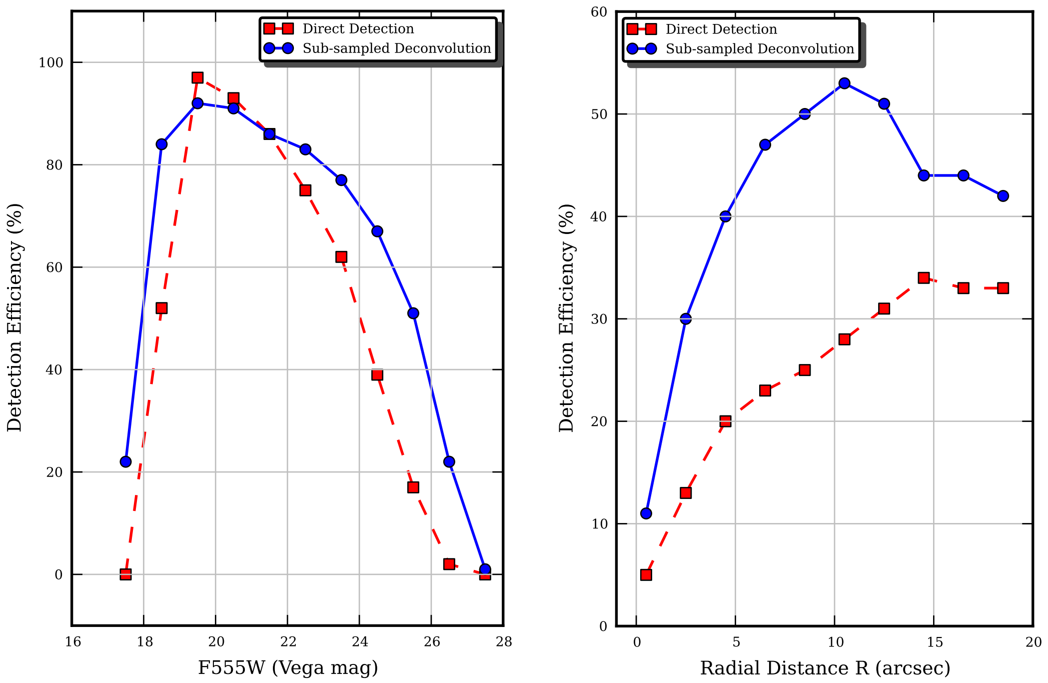

Figure 7.10: Comparison of star detection efficiency of the direct method and our sub-sampled deconvolution method. Left: detection efficiency as a function of stellar magnitude. Right: as a function of radial distance from the cluster centre. Our sub-sampled technique shows better detection efficiency, especially for the high magnitude stars and stars in the inner crowded core of the cluster. Overall, detection efficiency is lower in the core because of crowding.

in Figure 7.11. These are the PSF fitted values obtained with the second, refined point spread function. Although many of the cluster stars have absolute positional errors greater than 0.2 pixels, mean positional error for bright stars ($<=$ 21 mag) is $\sim$ 0.03 pixels. These are the stars that are used for internal proper motion dispersion calculation.

To test if there are systematic positional errors, the x and y pixel errors were re-binned within 0.1 pixel bin increment. The scaled positional errors are shown in Figure 7.11. The plot does not indicate any systematic error introduced by the technique. The positional errors do increase for high magnitude stars, but the errors are not higher near the cluster center compared to the outer regions (see Figure 7.12).

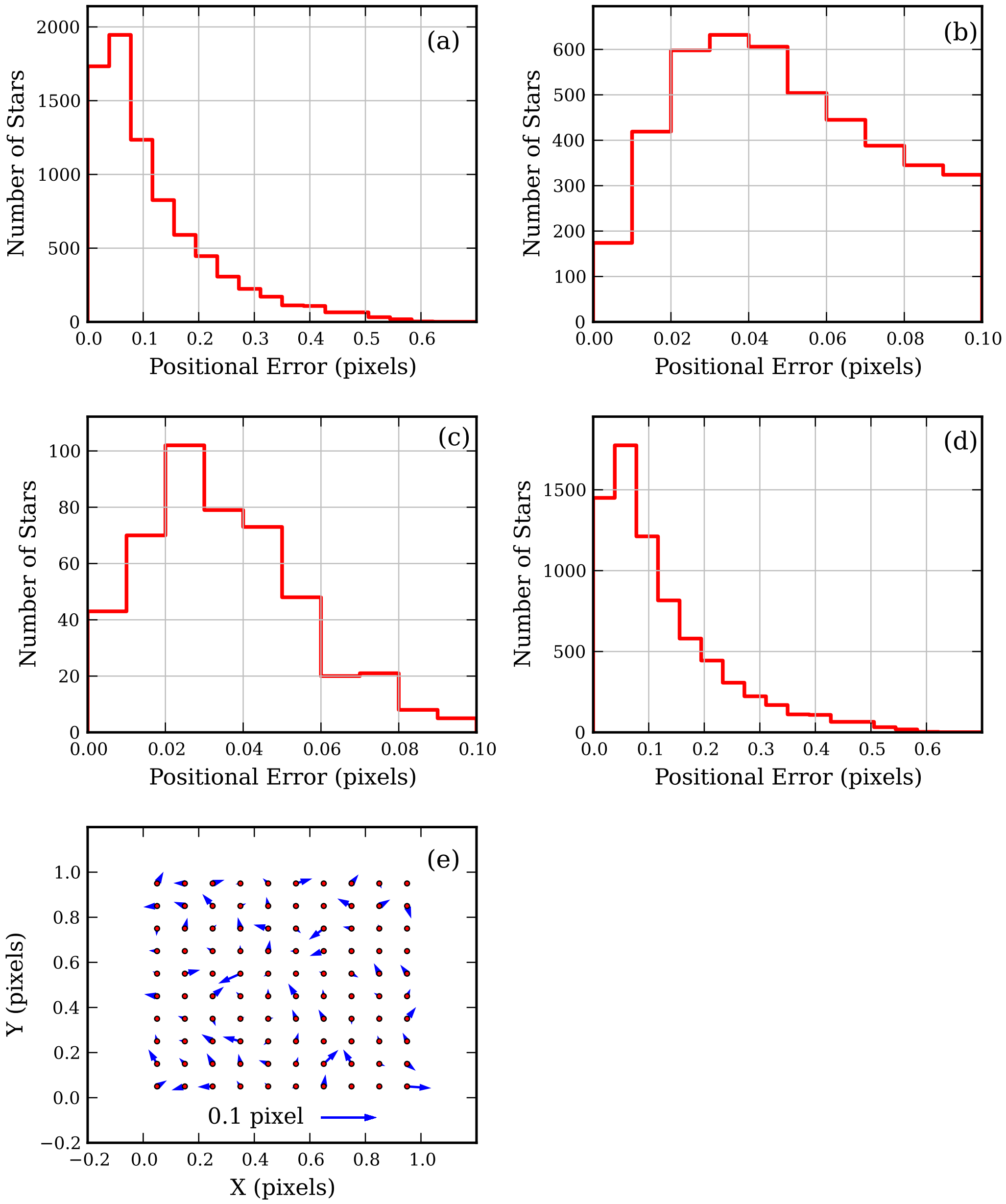

Figure 7.11: (a) & (b) Histogram of the positional difference between input and detected stellar positions with different binning. (c) Histogram of the absolute positional difference for only bright stars (<= 21 mag) (d) Histogram of the absolute positional difference for only faint stars (> 21 mag) (e) Vector plot of the stellar positional errors. The vectors are 2× scaled and do not show systematic errors.

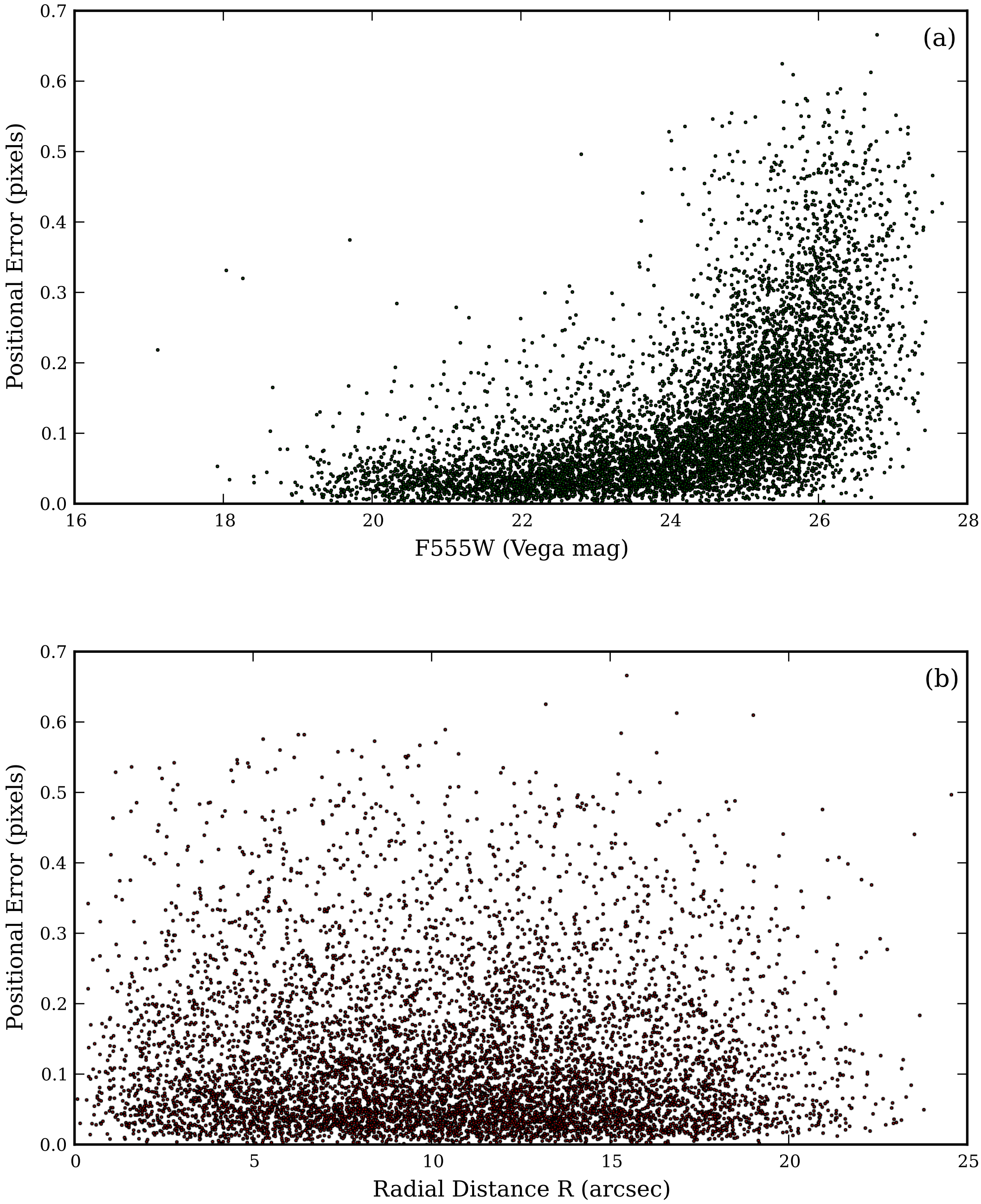

Figure 7.12: Absolute positional error as a function of magnitude (a) and as a function of radial distance from the cluster centre (b). High magnitude stars show higher positional errors. Higher positional error stars are uniformly distributed around the FOV.

After getting the final star lists in both the epochs, the lists were matched between the two epochs based on the star ID (the same star IDs were used in both epochs). The proper motion was simply calculated by subtracting the stellar position in one epoch from another. The vector plot of the input and output proper motions is shown in Figure 7.13. As was the case with stellar positional errors, absolute proper motion errors are mostly introduced by faint cluster stars (> 21 mag).

A histogram of the proper motion errors is plotted in Figure 7.14. Almost 92% of the matched stars have errors below 0.2 pixel in both x and y directions. $\sim$ 95% of bright stars ($<= 21$ mag) have absolute proper motion errors below 0.04 pixels. As proper motion errors are related to positional accuracy in the measurement of stars in each epoch, higher proper motion errors are primarily because of the stars with poorer signal to noise (see Figures 7.14 and 7.15).

7.2.2 ACS WFC Detector

Our automated pipeline was used to generate simulated images of M5. Although real ACS WFC images were used to determine proper motions in M15 (instead of M5), the benchmarking results would still be valid. The geometric distortion corrected point spread function was used to create the simulated image with 100,000 stars. A Padova isochrone of age 13×10^9 years and metallicity Z=0.0009 [Harris, 1996] was used. Two sets of ACS WFC images, separated by 12 years, were generated in the F606W and F814W bands. Exposure time and mean sky values were taken from the real cluster images. The input color magnitude diagram and luminosity function is shown in Figure 7.16.

One of the simulated images is shown in Figure 7.17. Crowding is evident at the cluster center. The mean distance between the nearest neighbour is around 6 pixels (see Figure 7.17), although the smallest minimum separation between the stars in the core is below 0.1 pixel.

We processed the simulated images through the sub-sampled deconvolution technique, similar to real cluster images. The simulated images in both the epochs were deconvolved with the spatially-varying distortion-corrected TinyTIM point spread function (generated from a drizzled geometric distorted grid of PSFs).

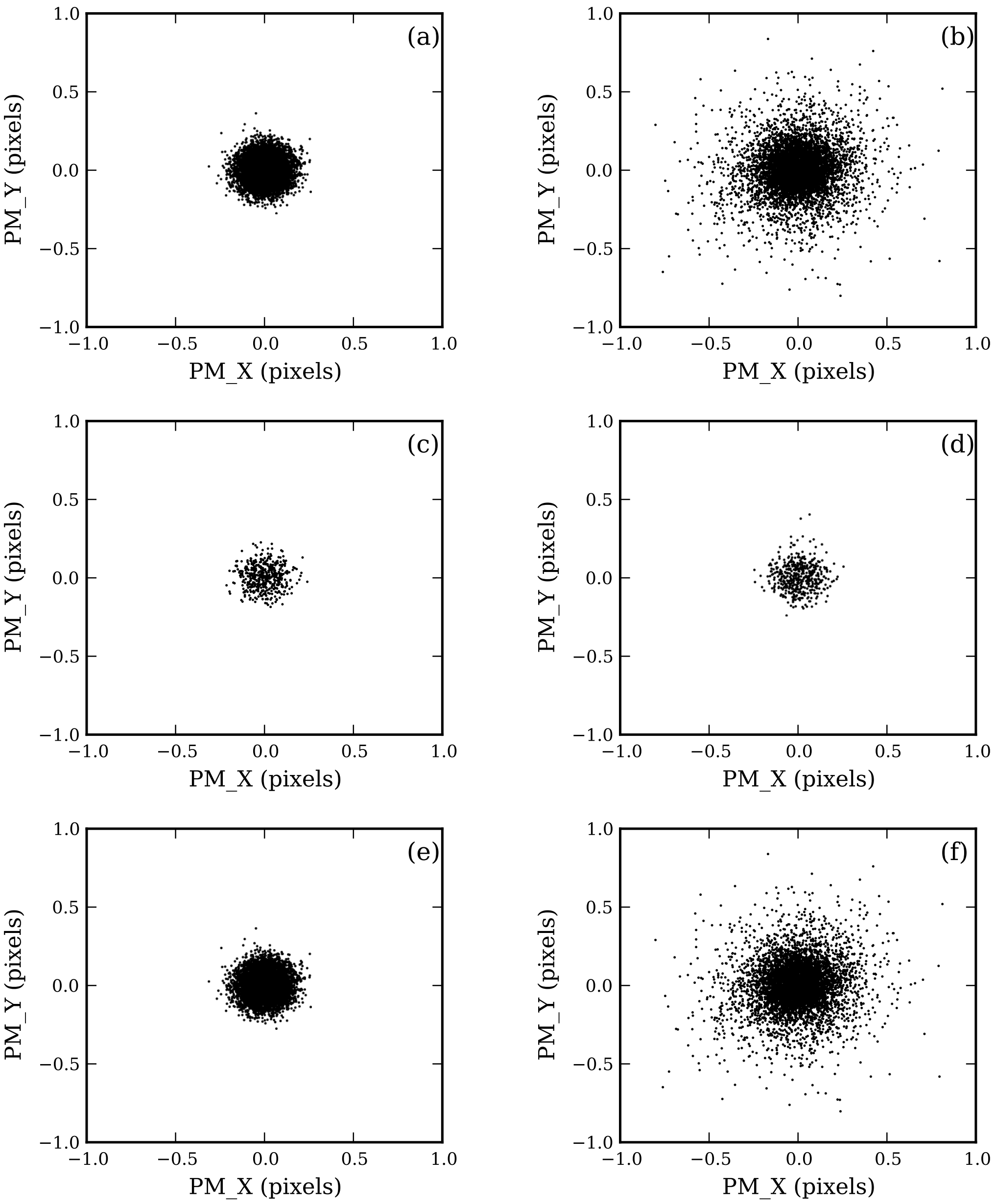

Figure 7.13: Proper motion plots. (a) & (b) Input and detected proper motion of all the cluster stars. (c) & (d) Input and detected proper motion of bright cluster stars (<= 21 mag). (e) & (f) Input and detected proper motion of faint cluster stars (> 21 mag). Higher dispersion is mostly introduced by the faint cluster stars .

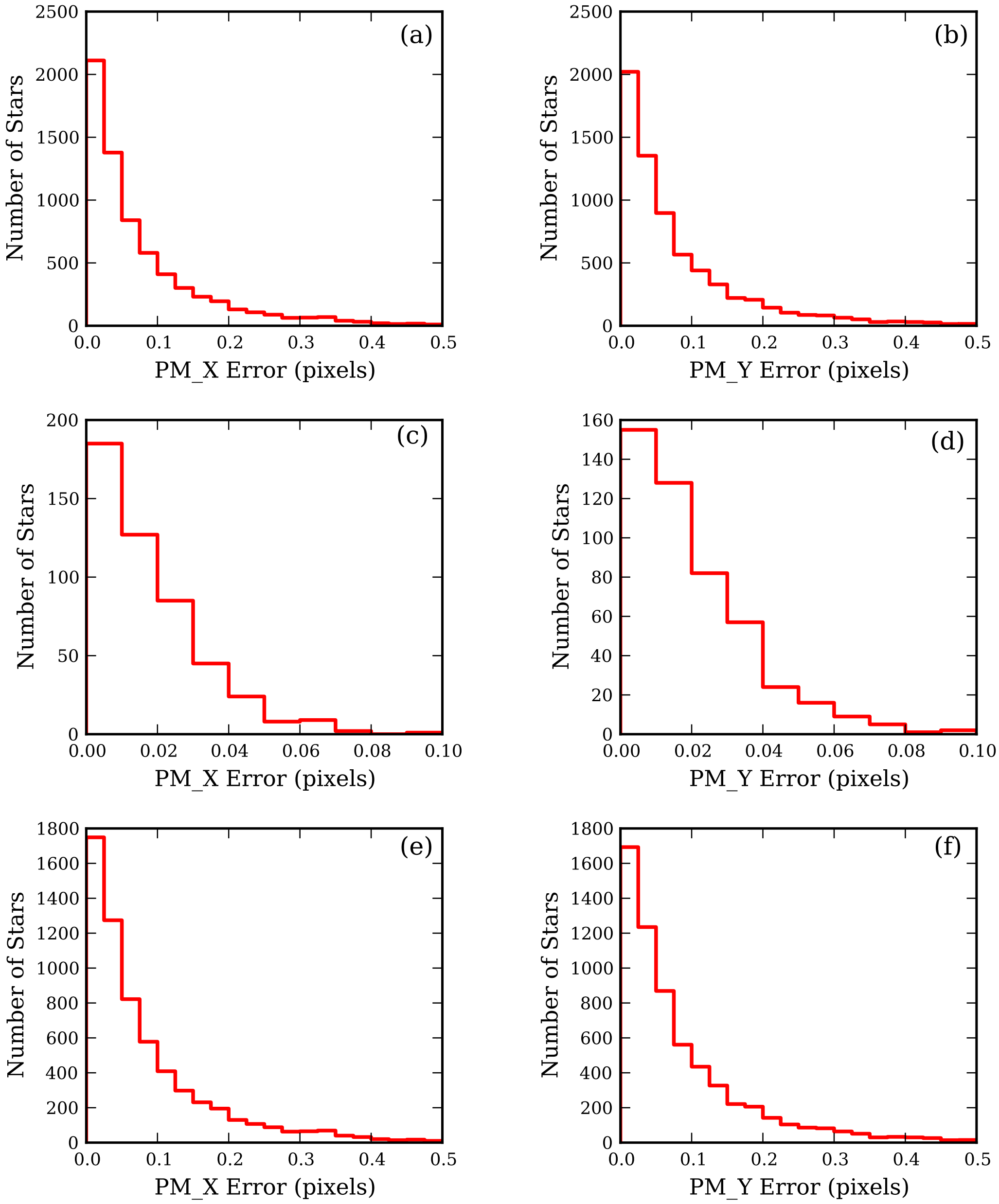

Figure 7.14: (a) & (b) Proper motion error histogram along the CCD x-axis and y-axis for all cluster stars. $\sim$ 92% of the stars have proper motion errors less then 0.2 pixels. Histogram bins are 0.02 pixels wide. (c) & (d) Proper motion error histogram along the CCD x-axis and y-axis for bright cluster stars ($<=$ 21 mag). (e) & (f) Proper motion error histogram along the CCD x-axis and y-axis for faint cluster stars (mag $>$ 21).

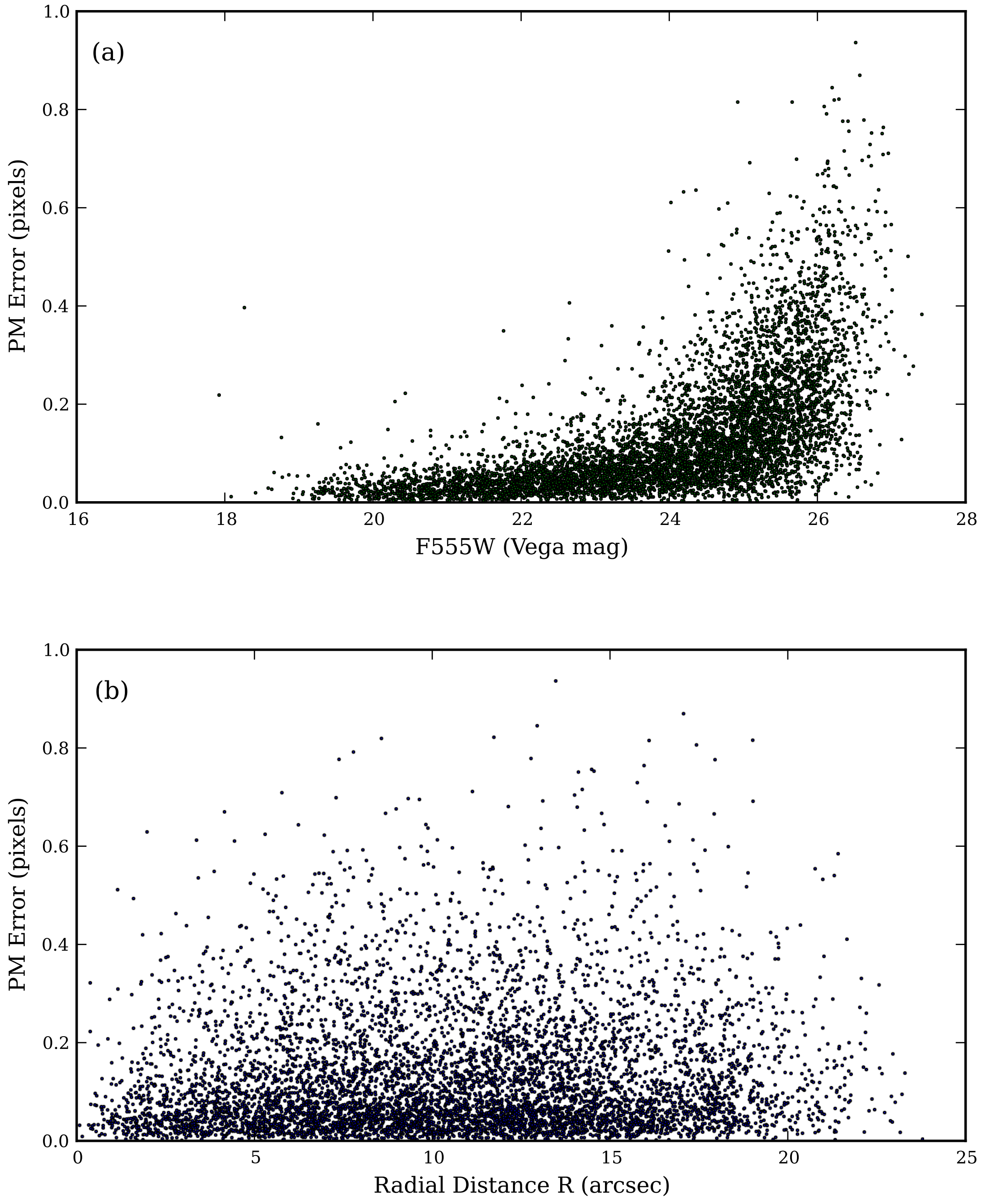

Figure 7.15: Absolute proper motion error as a function of stellar magnitude (a) and radial distance from the cluster centre (b). High magnitude stars show higher proper motion errors.

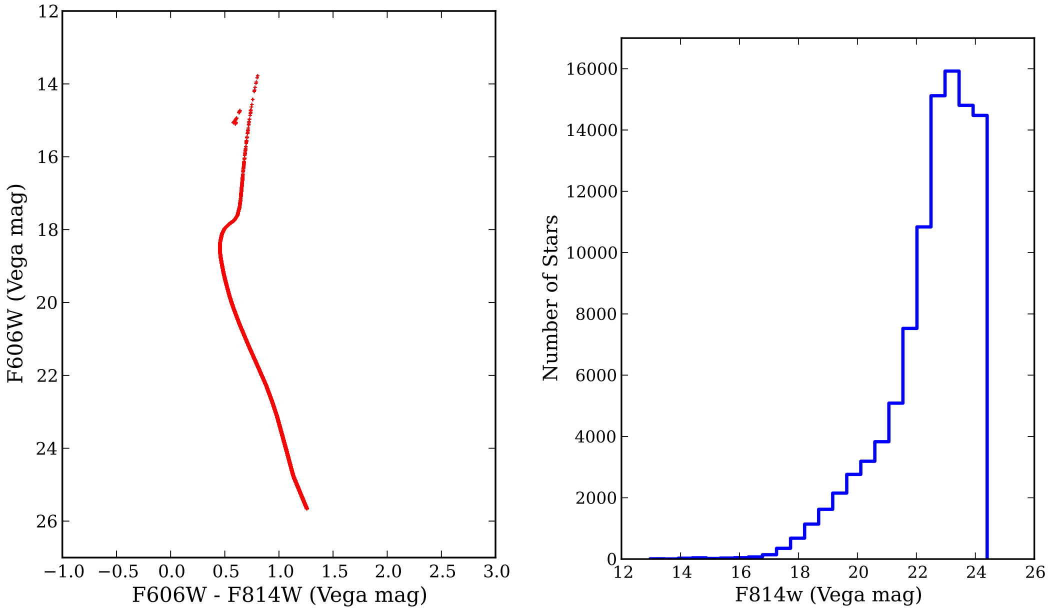

Figure 7.16: Input color magnitude diagram (left) and luminosity function (right) used to simulate M5 ACS WFC images.

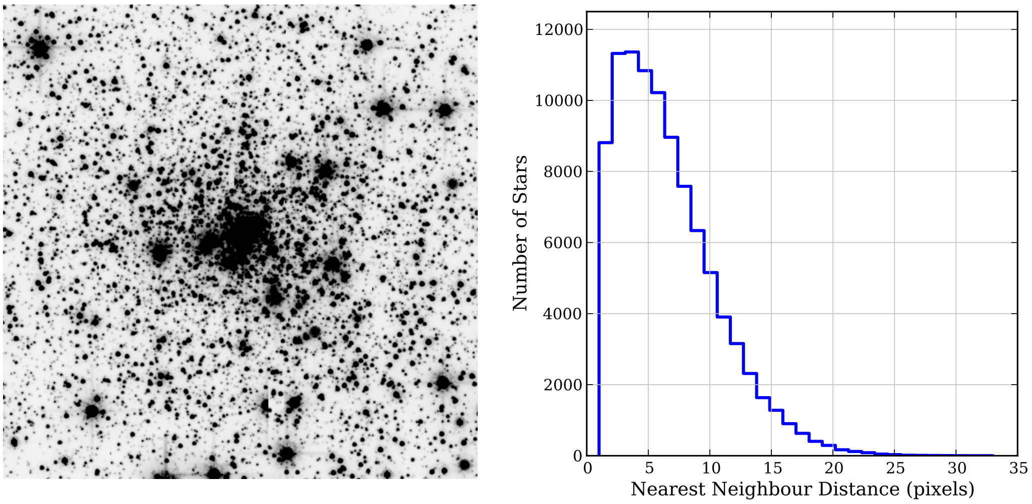

Figure 7.17: One of the simulated M5 images (left) and histogram of the nearest neighbour separation in pixels (right). The mean minimum separation between the stars is around 6 pixels.

The F606W and F814W filter deconvolved images were combined with statistical rejection of inconsistent high pixel values, and star detection was performed on the combined image. Both aperture photometry and PSF fitting photometry was performed on the detected stars. The next step was to improve upon the first guess TinyTIM-based PSF by modelling a new empirical PSF directly from a selection of bright stars in the image. Therefore, all of the stars fitted by the first PSF (except for stars used for psf modelling) were subtracted from the image and the *psf* task used to model the empirical point spread function with quadratic spatial variance. This second/refined point spread function was then used to fit the stars again, to give us both stellar position and magnitude.

The output star lists were matched to the input star lists and only stars within ±1.0 pixel and ±0.5 magnitude of an input star coordinate were kept in the final matched list. The total number of input stars and the matched stars are plotted as a function of star magnitude in Figure 7.18. As expected the detection efficiency decreases for high magnitude stars.

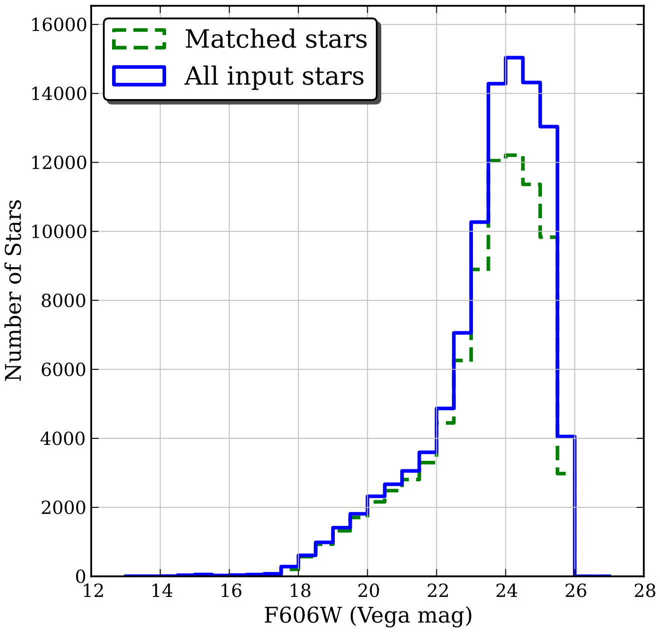

Figure 7.18: Total input stars and matched stars as a function of star magnitude. The efficiency decreases at high stellar magnitudes.

The most important result however is that our sub-sampled deconvolution technique shows better detection efficiency, especially for high magnitude stars and stars in the crowded core, compared to direct detection on the science images (see Figure 7.19).

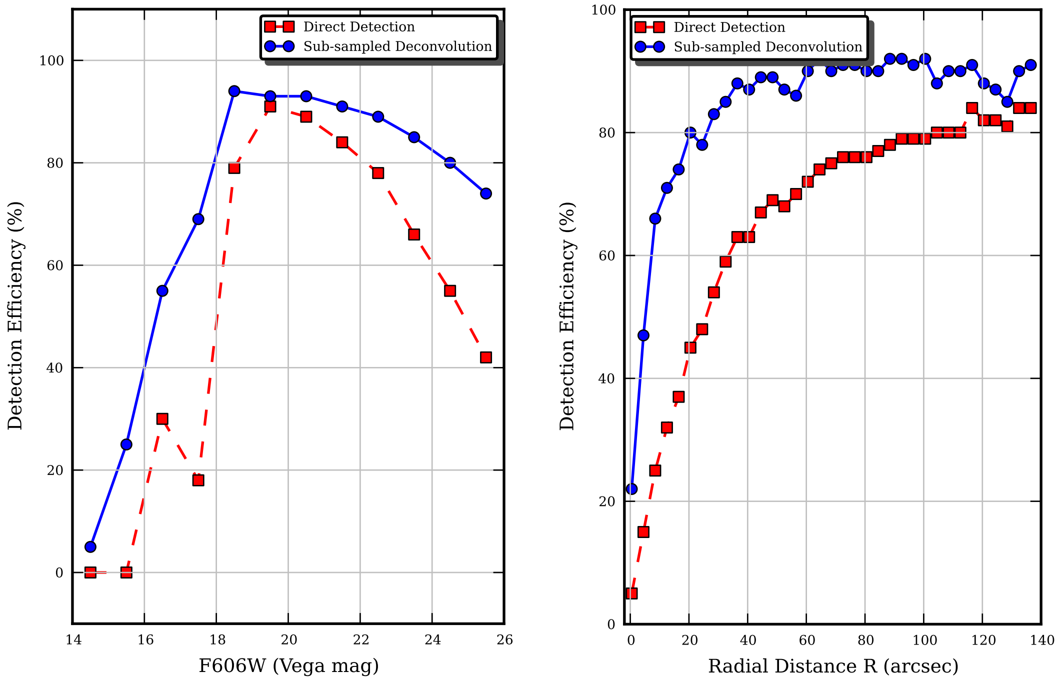

Figure 7.19: Comparison of star detection efficiency of the direct method and our sub-sampled deconvolution method. Left: detection efficiency as a function of stellar magnitude. Right: as a function of radial distance from the cluster centre. Our sub-sampled technique shows better detection efficiency, especially for the high magnitude stars and stars in the inner crowded core of the cluster. Crowding at the cluster core leads to positional errors of some stars to be above the mean value.

For proper motion studies, low positional errors are vital. A histogram of the positional difference between input and detected stellar positions is shown in Figure 7.20. Whether the first (TinyTIM) or second (empirical) PSF was used to fit the stars, we found comparable positional errors (see Figures 7.20 and 7.22). As was the case with WFPC2, higher positional errors are introduced by faint stars whereas $\sim 95\%$ of bright stars have absolute positional errors below 0.02 pixel.

To test if there are systematic positional errors, the x and y pixel errors were re-binned according to where, at the sub-pixel level, the peak of each star fell.

The integer part of each star's pixel coordinates were subtracted. A grid of 400 bins (0.05 pixel binwidth) was established over the remaining sub-pixel coordinates, and the error vectors inside each bin were averaged. The scaled positional errors are shown in Figures 7.20 and 7.22. The vectors are randomly pointed and have different magnitude, indicating no systematic error being introduced by our technique.

The positional errors do increase for high magnitude stars (see Figures 7.21 and 7.23). We also do see higher positional errors for some stars in the cluster core, which can be attributed to crowding at the center.

The positional errors estimated here are for an idealised simulated image. For a real image with variable sky, CCD chip defects, incompletely calibrated geometric distortion, zodiacal light, no cutoff of very high magnitude stars, and more extreme crowding in the central cluster core (e.g. M15 globular cluster), higher errors would be expected. Also, bleeding of the saturated pixels is more severe in real images, compared to the ones we simulated.

After getting the final star lists in both epochs, the lists were matched between the two epochs based on the star ID (same star IDs were used in both the epochs). The proper motion was simply calculated by subtracting stellar position in one epoch from the other. The scatter plot of the input and output proper motion is shown in Figure 7.24. Bright cluster stars depict less dispersion between input and detected proper motion vectors, compared to faint stars.

A histogram of the proper motion errors is shown in Figures 7.25 and 7.27. The proper motion errors are comparable whether we used the TinyTIM or the empirical PSF. Almost 98% of the stars have errors below 0.1 of a pixel (5 mas). But $\sim$ 98% bright stars ($<=$ 21 mag) have absolute proper motion errors below 0.02 pixel (1 mas). And these are the high quality proper motion stars that are used for determining internal proper motion dispersion in globular star clusters. As with WFPC2, high magnitude stars show higher proper motion errors (see Figures 7.26 and 7.28).

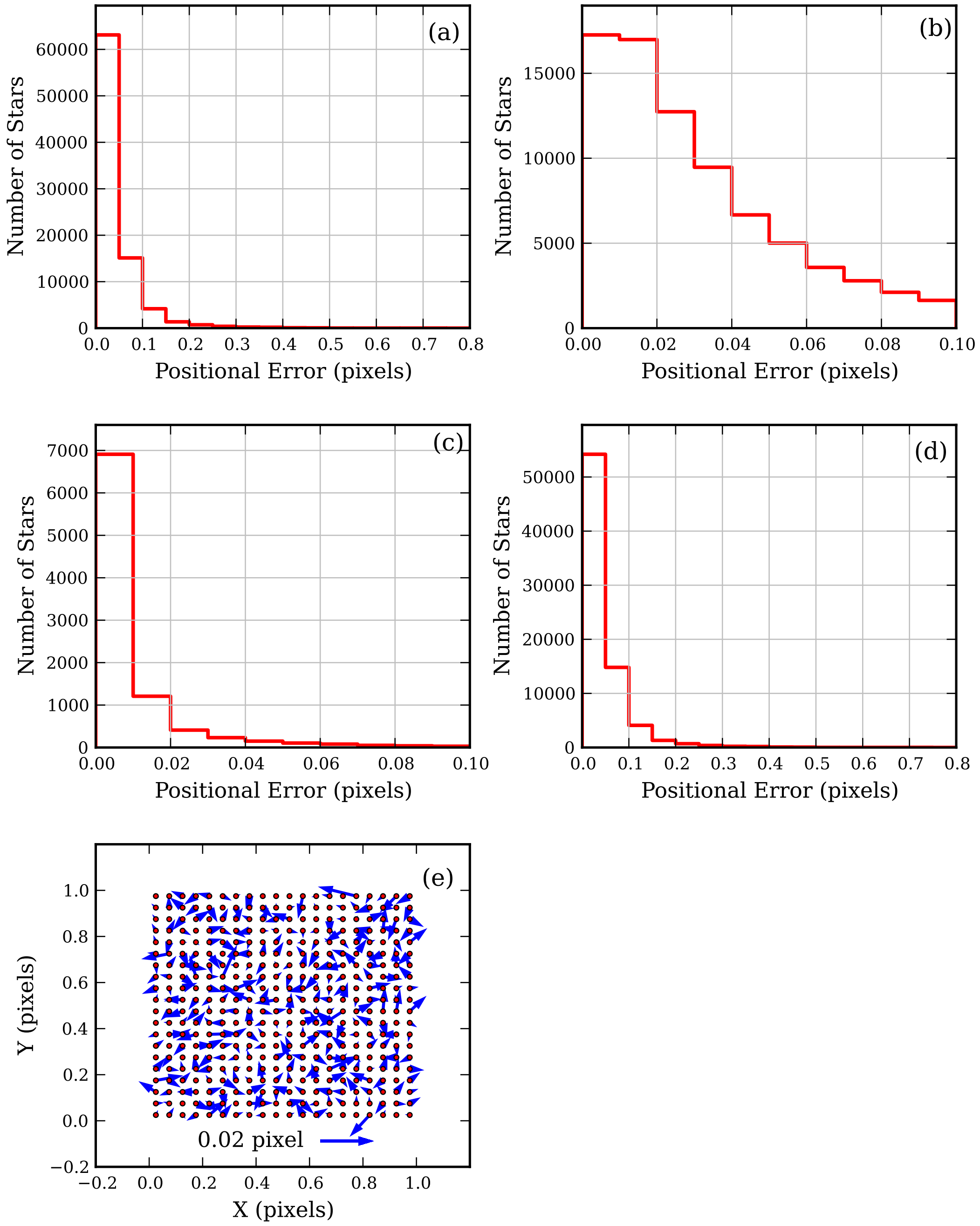

Figure 7.20: Positional error plots for the TinyTIM point spread function. (a) & (b) Histogram of the positional difference between input and detected stellar positions for all stars with different binning. (c) & (d) Histogram of absolute positional errors for bright ($<=$ 21 mag) and faint stars ($>$ 21) respectively. $\sim$ 95% of bright stars have errors $<$ 0.02 pixel. (e) A vector plot of the stellar positional errors, averaged into bins with respect to where each star's peak fell within the central pixel of its PSF. The vectors are 10× scaled up for clarity and do not show systematic errors.

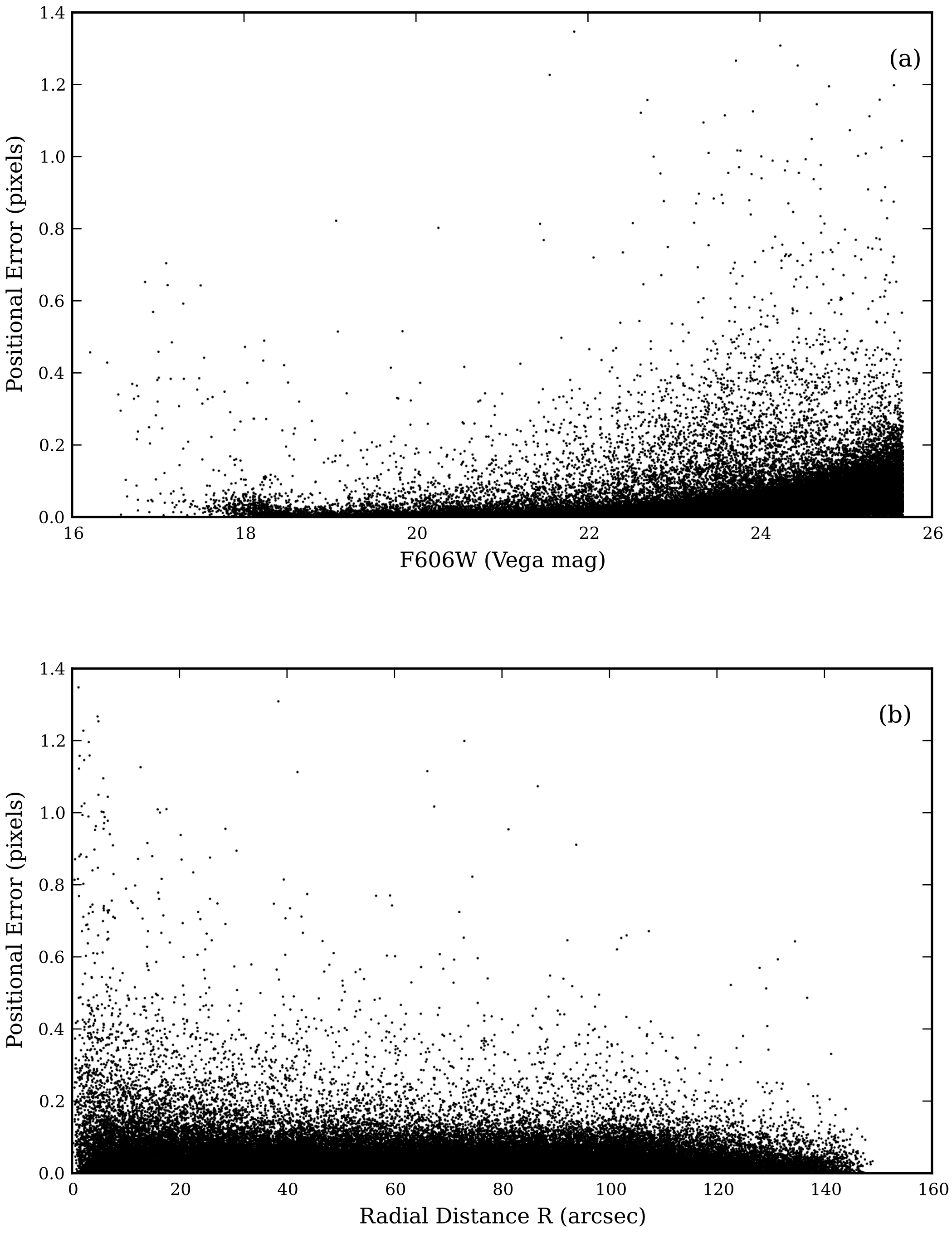

Figure 7.21: Positional error plots for the TinyTIM point spread function. Positional error for one simulated image as a function of magnitude (a) and radial distance from cluster centre (b). As expected, high magnitude stars show higher positional errors.

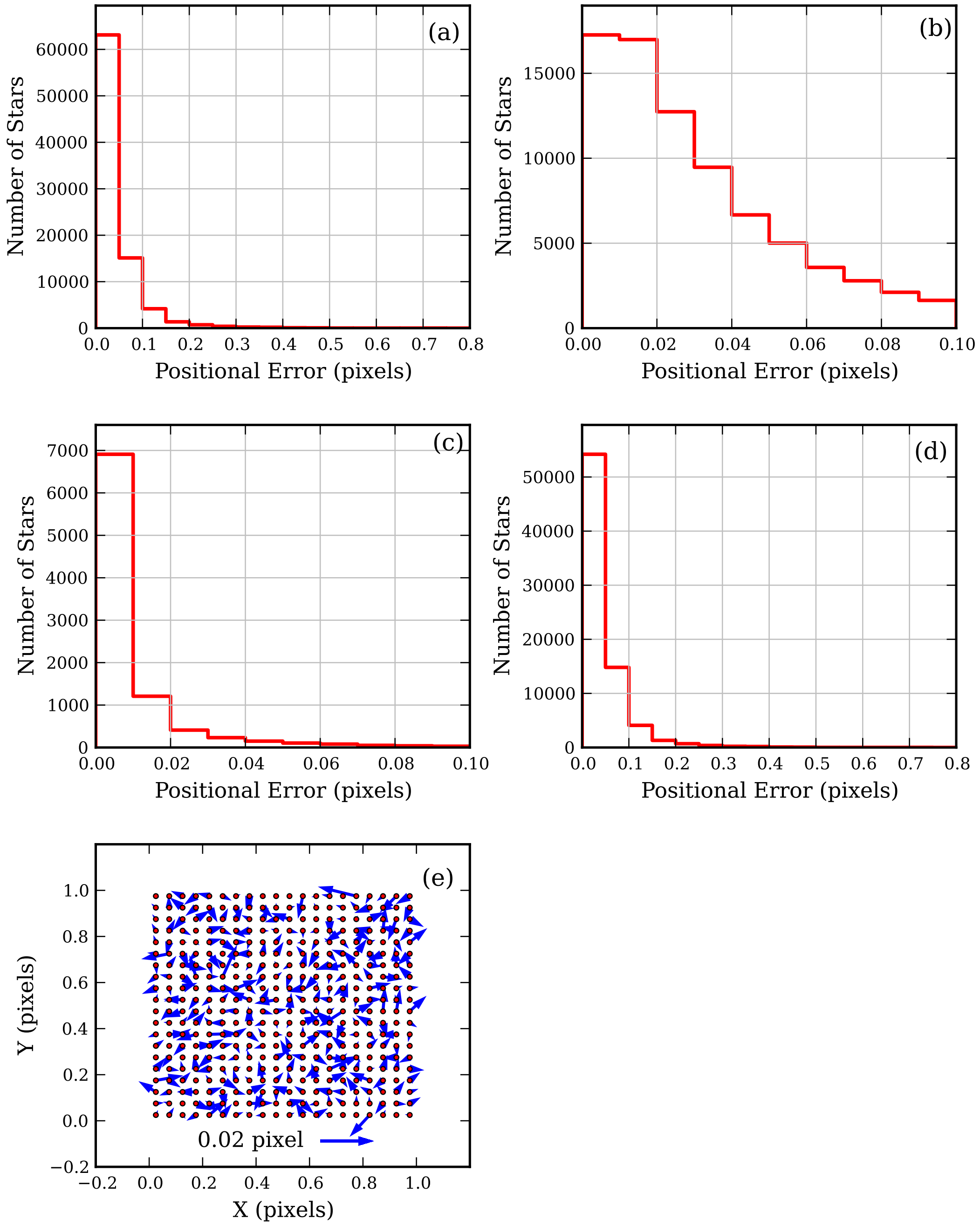

Figure 7.22: Positional error plots for the empirical point spread function. (a) & (b) Histogram of the positional difference between input and detected stellar positions with different binning. (c) & (d) Histogram of absolute positional errors for bright ($<=21$ mag) and faint stars (>21) respectively. $\sim 95\%$ of bright stars have errors < 0.02 pixel. (e) A vector plot of the stellar positional errors, averaged into bins with respect to where each star's peak fell within the central pixel of its PSF. The vectors are 10× scaled up for clarity and do not show systematic errors.

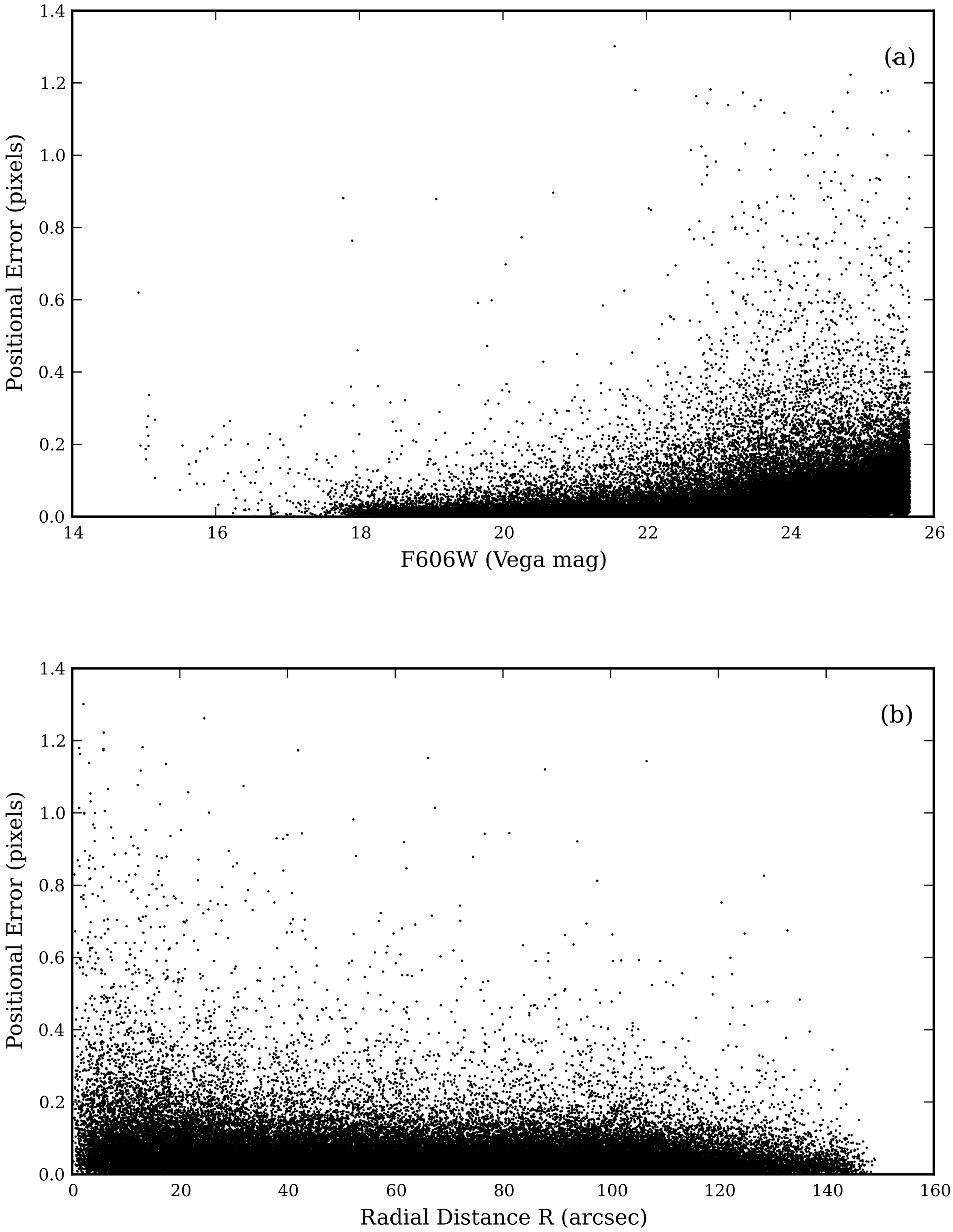

Figure 7.23: Positional error plots for the empirical point spread function. Positional error for one simulated image as a function of magnitude (a) and radial distance from cluster centre (b). As expected, high magnitude stars show higher positional errors.

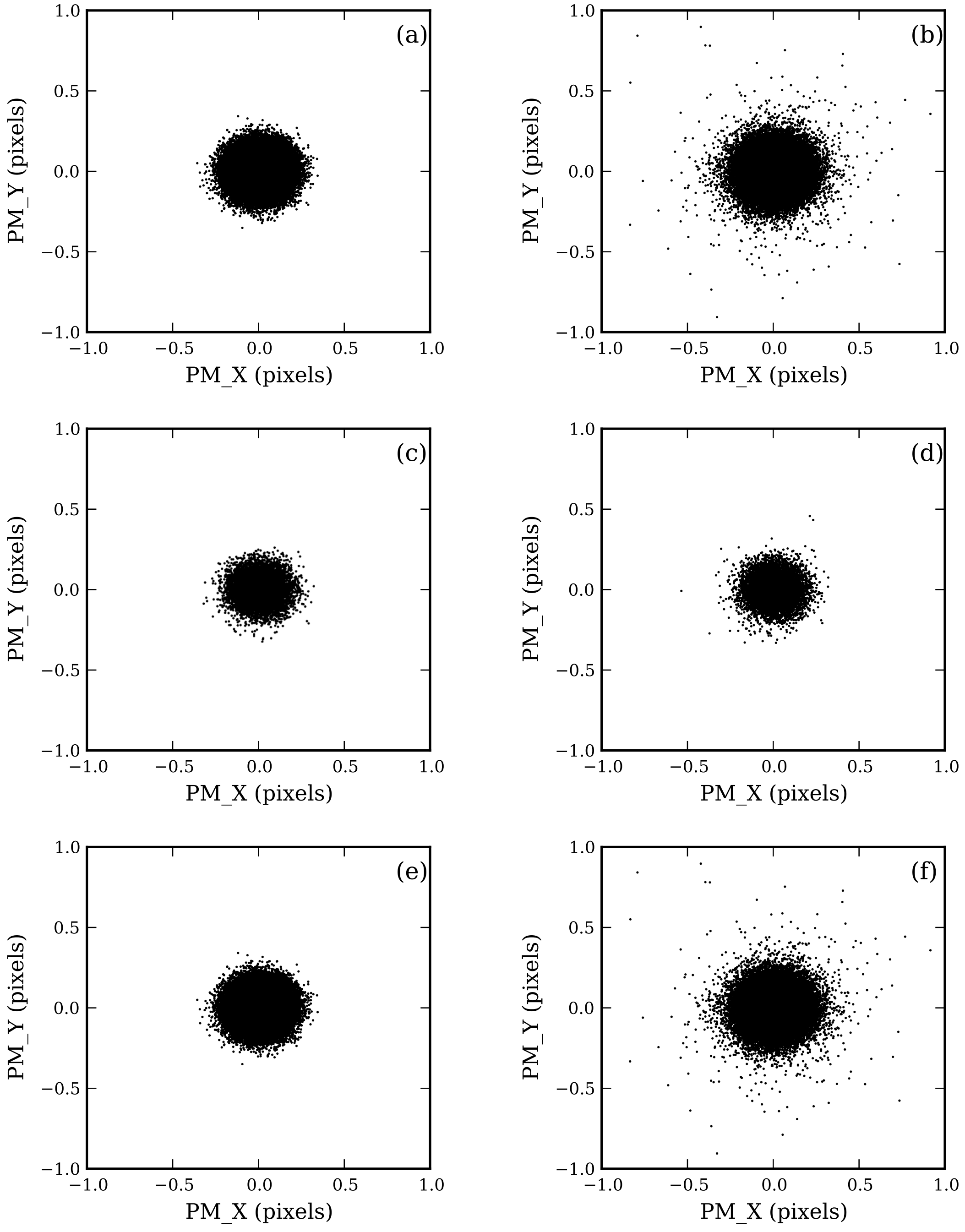

Figure 7.24: Proper motion scatter plot. (a) & (b) Input and detected proper motion of all the cluster stars. (c) & (d) Input and detected proper motion of bright cluster stars (<= 21 mag). (e) & (f) Input and detected proper motion of faint cluster stars (> 21 mag). Higher dispersion is mostly introduced by the faint cluster stars .

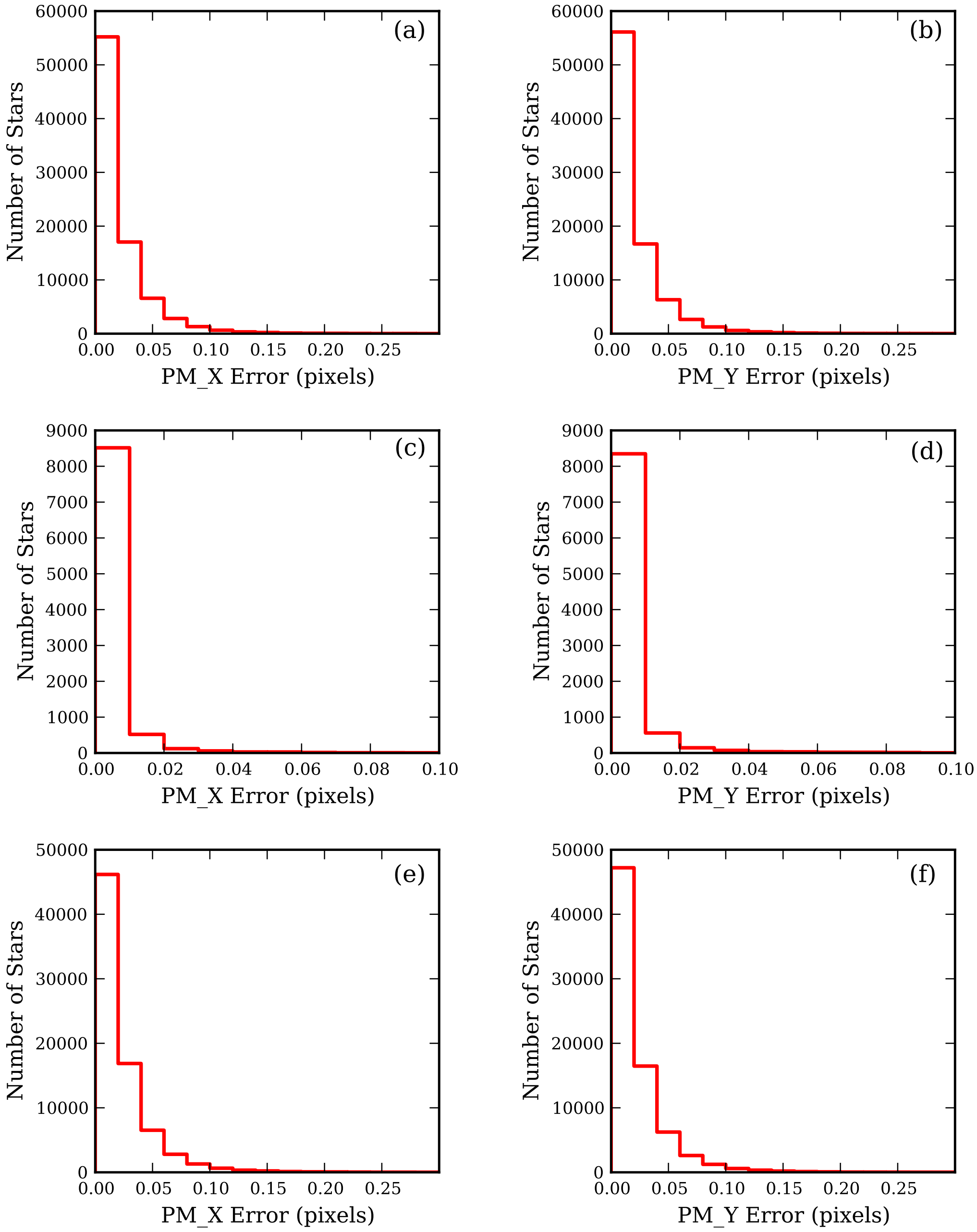

Figure 7.25: Proper motion errors for the TinyTIM PSF. Proper motion error histogram along CCD x-axis (a) and y-axis (b). ∼98% of the stars have errors less then 0.1 pixels. Histogram bins are 0.02 pixels wide. (c) & (d) Proper motion error histogram along the CCD x-axis and y-axis for bright cluster stars (<= 21 mag). (e) & (f) Proper motion error histogram along the CCD x-axis and y-axis for faint cluster stars (mag > 21).

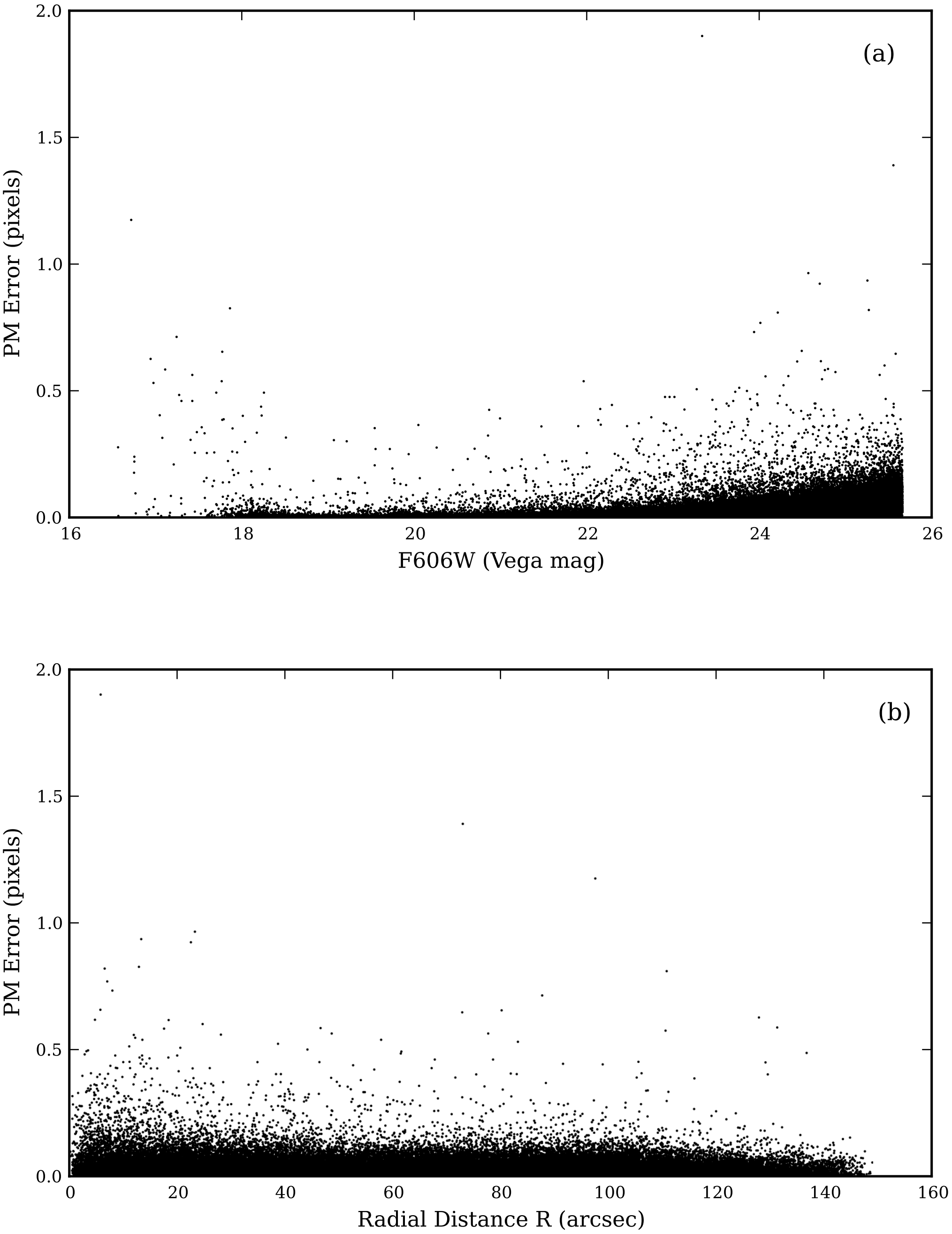

Figure 7.26: Proper motion errors for the TinyTIM PSF. Absolute proper motion errors as a function of stellar magnitude (a) and radial distance from the cluster centre (b). High magnitude stars show higher proper motion errors.

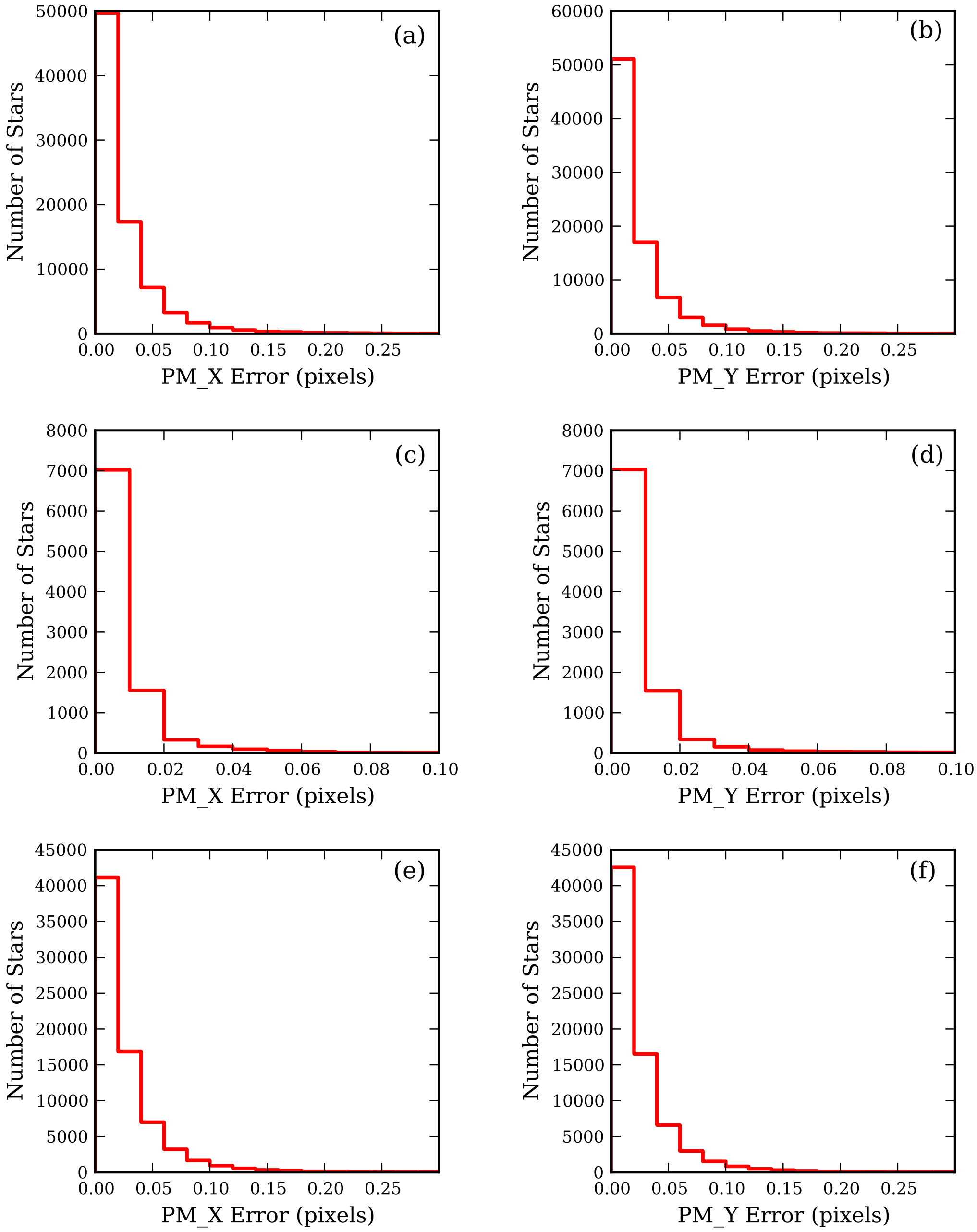

Figure 7.27: Proper motion errors for the empirical PSF. Proper motion error histogram along CCD x-axis (a) and y-axis (b). ∼98% of the stars have errors less then 0.1 pixels. Histogram bins are 0.02 pixels wide. (c) & (d) Proper motion error histogram along the CCD x-axis and y-axis for bright cluster stars (<= 21 mag). (e) & (f) Proper motion error histogram along the CCD x-axis and y-axis for faint cluster stars (mag > 21).

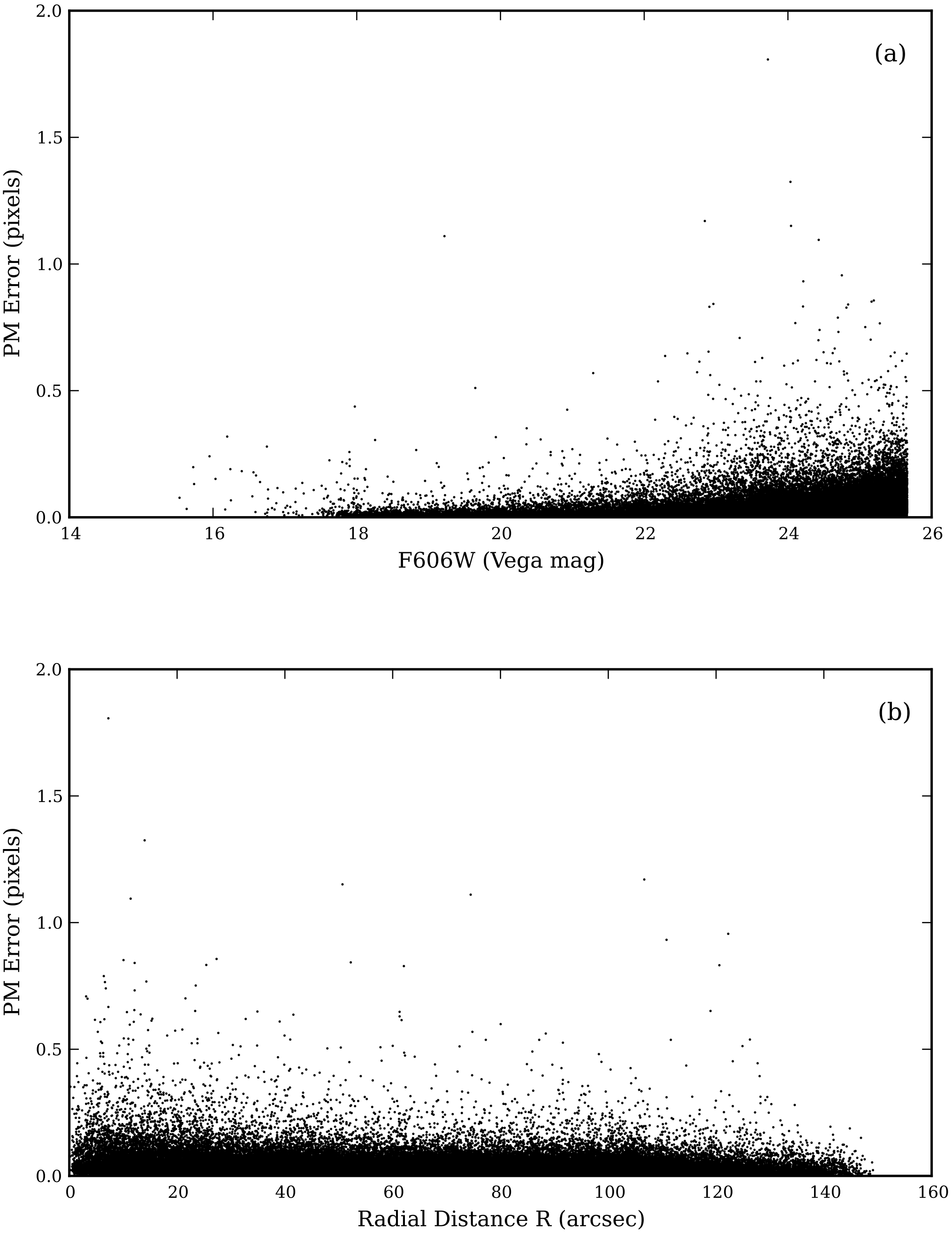

Figure 7.28: Proper motion errors for the empirical PSF. Absolute proper motion errors as a function of stellar magnitude (a) and radial distance from the cluster centre (b). High magnitude stars show higher proper motion errors.

Chapter 8

Stellar Proper Motion II: Real Cluster Images

Three galactic globular clusters were processed through our semi-automated pipeline to determine the stellar proper motion. These were chosen based on the HST data availability and the possibility of an IMBH at the core. [Baumgardt *et al.*, 2005] suggested that globular clusters with a larger core could harbour an intermediate mass black hole. As NGC 6838 (M71) has a bigger core radius than average, it could host a central black hole. Although, a recent study by a Samra *et al.* [2012] using the Gemini North telescope does not indicate that it does. As M71 has a small internal velocity dispersion, it also benchmarks the limiting accuracy of our technique. NGC 6293 is a southern hemisphere core collapsed cluster. Although at one time core collapsed clusters were believed to be the most likely to harbour an IMBH at their core, in recent years that picture has changed [Baumgardt *et al.*, 2005]. For both M71 and NGC 6293, multi epoch HST WFPC2 images were used. Another cluster which had been speculated to have a black hole at its core is NGC 7078 (M15). Although McNamara *et al.* [2003] were not able to find any concrete evidence for its presence using HST WFPC2 images, we selected M15 as a cluster to determine stellar proper motions. Instead of using only WFPC2 detector images, we took first epoch images from the WFPC2 and second epoch images from the ACS WFC detector. As the accuracy of proper motion suffers when using multi-epoch images from different detectors, this exercise helped to benchmark the technique when data is combined from different detectors.

8.1 Globular Cluster M71 (NGC 6838)

The globular cluster M71 (NGC 6838; $\alpha = 19^h 53^m 46^s.25, \delta = +18^o 46^{'} 46^{''}.7$) is a metal-rich cluster located at ∼4 kpc from us in the constellation Sagitta. It is sparsely crowded, at low galactic latitude ($b = -4^o.56$) with a $0.63'$ core radius. Basic properties of globular cluster M71 are listed in Table 8.1.

Right ascension	19:53:46.25
Declination	+18:46:46.7
Distance from Sun	4 kpc
Absolute Visual Magnitude	-5.61
Metallicity [Fe/H]	-0.78
Central velocity dispersion	2.3 km/sec
King concentration c	1.15
Core radius	0.63 arcmin
Half light radius	1.67 arcmin
Core relaxation time	34.67×10^7 years

Table 8.1: Globular cluster M71 properties. RA and DEC values are from Goldbury *et al.* [2010]; the rest of the values are from Harris [1996].

The first proper motion study of M71 was carried out by Cudworth [1985], and he estimated a low space velocity for the cluster. Cudworth [1985] calculated the proper motion dispersion within $100''$ radial distance of the centre to be $180 \pm 30\, \mu as/year$. Recently, in very close agreement, Samra *et al.* [2012] found the proper motion dispersion in the core to be $179 \pm 17\, \mu as/year$. They did not find a radial variation of the internal proper motion dispersion, and estimated an upper limit for the central black hole to be $\sim 150 M_{sun}$ at 90% confidence level.

8.1.1 Data

The first epoch observations were taken on May 21 2000 (HST Proposal ID 8118) with the HST WFPC2 detector in the F555W and F439W filters. The second epoch images were taken on April 25 2006 (HST Proposal ID 10524), but with a slightly different telescope orientation and using the F555W, F255W and F336W filters. The PC chip of the detector covered the same central core region of the cluster in both the epochs. The first epoch has 3 frames in both filters. The second epoch has two exposures in each filter. Only F555W filter images in the PC chip were used for proper motion determination, but the F439W frames from the first epoch were used to construct the colour magnitude diagram of the cluster. And the 1^{st} epoch F439W were used to reject spurious detections, also. For the present work, we used only the 30 second exposures in the F555W filter for 2000 epoch, and the 40 second exposures in F555W for the 2006 epoch. A journal of observations used for the present study is listed in Table 8.2.

Epoch	**Date**	**Filter**	**Datasets**	**Exptime** (sec)
First	21 May 2000	F555W	U5AQ4201R	3
			U5AQ4202R	30
			U5AQ4203R	30
		F439W	U5AQ4204R	40
			U5AQ4205R	100
			U5AQ4206R	100
Second	25 April 2006	F555W	U9BM0105M	40
			U9BM0106M	40
		F336W	U9BM0103M	400
			U9BM0104M	400

Table 8.2: HST WFPC2 observations of M71.

The 2000 and 2006 HST WFPC2 pointings are overlaid on the Digital Sky Survey (DSS)[1] image in Figure 8.1.

---

[1] The Digitized Sky Surveys were produced at the Space Telescope Science Institute under U.S. Government grant NAG W-2166. The images of these surveys are based on photographic data obtained using the Oschin Schmidt Telescope on Palomar Mountain and the UK Schmidt Telescope. The plates were processed into the present compressed digital form with the permission of these institutions.

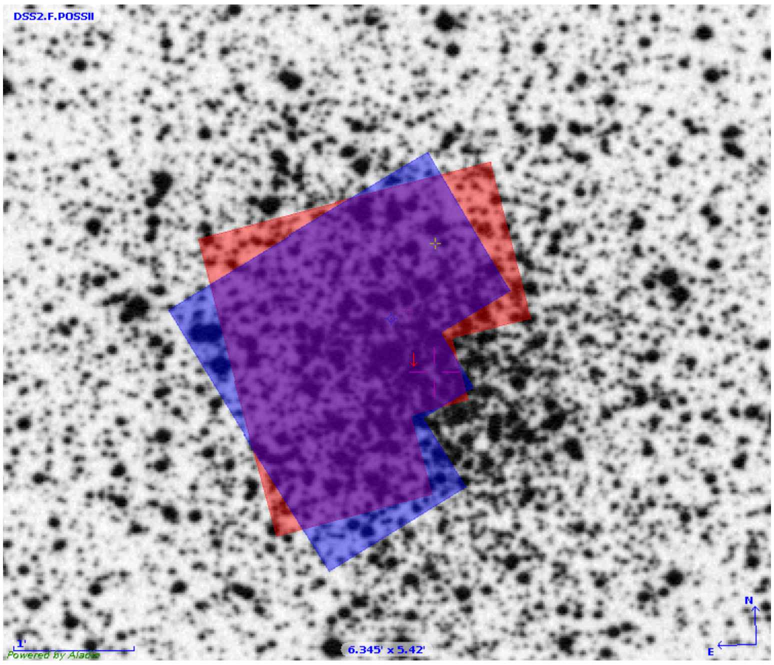

Figure 8.1: Multi epoch HST WFPC2 pointings on the core of M71 core. Red and blue mark the 2000 and 2006 epoch observations respectively. The HST WFPC2 FOV was overlaid on the DSS image using the ALADIN sky atlas [Bonnarel *et al.*, 2000].

8.1.2 Image Reduction, Star Detection, and PSF-Fitting Photometry

We followed the steps described in Section 5.3.1.1 to reduce and register the images in both epochs. Individual frames were cleaned of cosmic rays and saturated pixels using the data quality (DQ) masks generated from the imcombine step. A TinyTIM point spread function grid was created for each filter and a spatially varying first guess analytical PSF was generated using the IRAF *psf* task.

The high signal-to-noise combined image in each filter was deconvolved with the first guess analytical PSF. The sub-sampled deconvolved images for two filters (F555W and F439W in the 2000 epoch and F555W and F336W in the 2006 epoch) were co-added with cosmic ray rejection. It serves two purposes - increasing the SNR of the final combined image, and suppressing the spurious deconvolution artefacts. Deconvolution artifacts include deconvolution side-effects of noise bunching ("speckling" in the background), mismatches between model and actual structure in the PSF wings, and Gibbs oscillations (dark and bright rings around bright stars). They are low-intensity phenomena, which occur far from the intense core of the stars and are suppressed by coadding images with sigma-based outlier rejection. Rejection of PSF-related artefacts is particularly successful, because of the wavelength dependence of the approximately diffraction-limited PSF: star cores coincide and reinforce in different filter-band images, while other PSF structures do not coincide and are rejected. Star detection was performed on the combined deconvolved image with a threshold set to 10 sigma in *daofind*. The star list was refined manually by rejecting stars at the edge of the image and other spurious detections. The first set of star coordinates was generated by fitting the TinyTIM PSF (using the IRAF *allstar* task) on individual images in both filters.

The point spread function was improved in the second iteration by modelling it directly from the stars in the combined single filter images. Only unsaturated and bright, high SNR stars were used to model the spatially varying empirical point spread function after subtracting all other stars from the image. The first guess PSF is important as we would like to cleanly subtract the stars *not* used for PSF modelling in the second iteration. A second set of refined star coordinates was generated by fitting the empirical point spread function to individual images.

Deconvolved image sections from 2000 and 2006 frames are shown in Figure 8.2.

In total, four star lists were generated for the 2000 epoch (2 for the F555W filter and 2 for the F439W filter). How these lists were combined is described in the next subsection. Similarly, for the second epoch, the F555W star lists were combined with the F336W filter lists.

8.1.3 Starlist Merging and Proper Motion Determination

The errors in the star positions at each epoch were quantified by standard deviation. To be included in the final star list in each epoch, the star has to be within 0.2 pixels in each frame and its magnitude within ±0.5 mag. The final star list in the 2000 epoch had 213 stars whereas the 2006 star list had 215 stars (see Figure 8.3). Proper motion was determined using a pair of single uncombined exposures between the two epochs. This way we had 4 estimates of the proper motion for

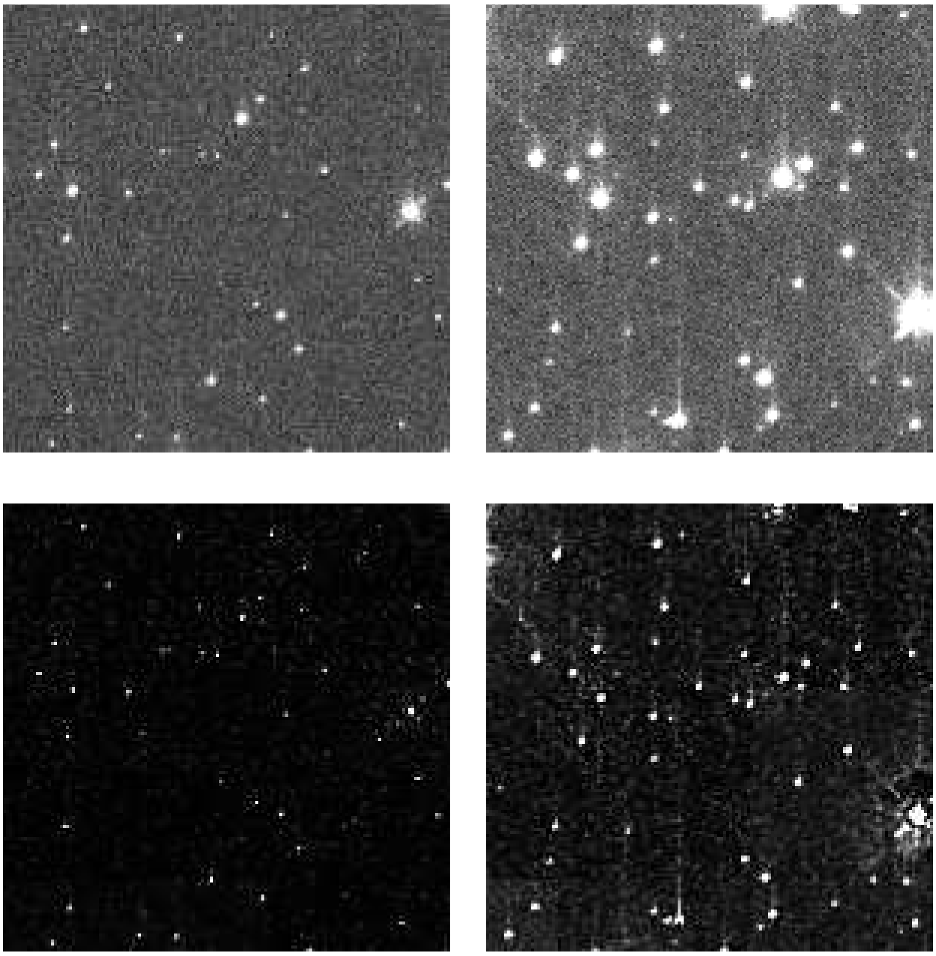

Figure 8.2: M71 deconvolved images. Image section of the F555W filter image from 2000 (top left) and 2006 (top right). The corresponding spatially varying empirical point spread function deconvolved image sections are shown below the image sections.

each matched star.

The first step in relative proper motion determination was to match the stars between the two epochs. To make the method robust, the first epoch image was transformed to the second epoch reference frame using the IRAF task *wcsmap*. The task uses the image header WCS information to transform from one coordinate to another. The output transformation database from *wcsmap* was then used to transform the star coordinates from the first to the second epoch reference frame. The transformed stars would not land exactly on their counterpart positions in the second epoch because of telescope pointing/WCS errors, cluster motion as a whole, and proper motion of cluster member stars. Using the average shift of the stars in the x and y image direction (which signify the average cluster motion as a whole), stars were matched using their pixel coordinates and magnitude. This avoided spurious matches in the crowded field of different stars lying in close proximity to each other. The final list had a total 175 matched stars between the two epochs.

Having a matched star list in hand, we now constructed a reference frame with cluster stars having zero proper motion. This allowed us to sift out the high proper motion stars relative to the zero mean proper motion frame of reference. The second step involved choosing reference stars to solve the geometric transformation equation between the two epochs. Apart from the linear terms, second order polynomial terms were also used in *geomap* to "map out" the residual instrumental distortions. A similar approach was taken by McNamara *et al.* [2003] with second order polynomial solution. The pointing accuracy of the HST is dependent on the guide star and therefore varies from one epoch to another. This is the reason that we develop a purely geometric transformation solution instead of using the image header WCS information for transforming the matched stars. The assumption here is that the mean proper motion of the cluster stars is zero. To get a good geometric transformation solution for transforming the coordinates from the first epoch to the reference coordinate system, the *geomap* task was run iteratively to include only the low proper motion stars. The choice of low proper motion stars for the transformation can be based on the colour magnitude diagram and/or iteratively running geomap.

Once we had the transformation solution, the 2000 epoch combined star list was transformed to the 2006 reference frame. This was repeated for the starlists from the inter-epoch image pairs. This gave us six estimates of proper motion for each star. The average of the six values was taken as the final proper motion value for the star. The standard deviation of the mean value is quoted as the proper motion error. The stellar proper motion vector plot for M71 is shown in Figure 8.4(a). Pixel values were converted to mas/year for the 6 year baseline. The red

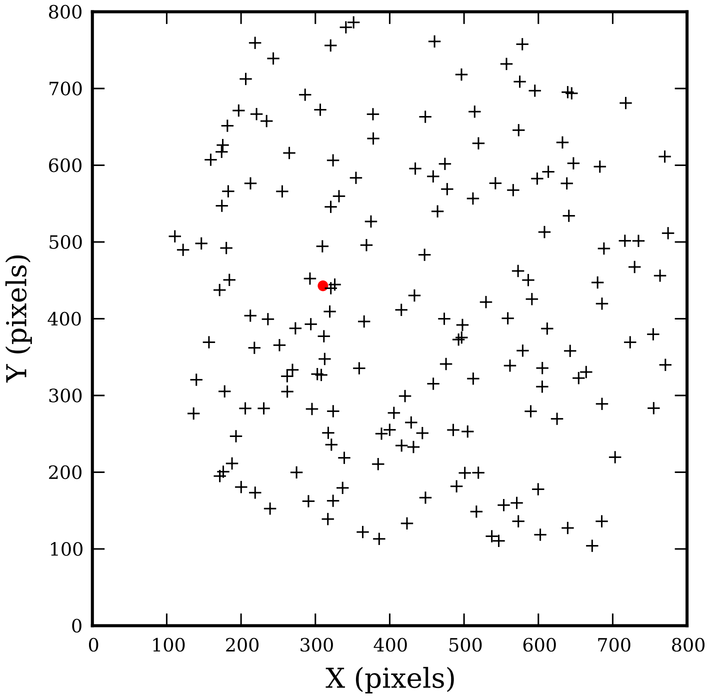

Figure 8.3: Location of the stars whose proper motion was measured in the 2006 epoch image. Stars in the first 100 vignetted/distorted rows + columns of the HST WFPC2 detector were not included in the final starlist. The cluster centre determined by Goldbury *et al.* [2010] is marked as a red dot.

circle corresponds to the escape velocity for M71 (0.88 mas/year) [Gnedin *et al.*, 2002; Samra *et al.*, 2012][1]. Corresponding proper motion histograms in the x and y directions (in the 2006 reference frame) are shown in Figure 8.4(b). Some apparently high velocity stars are seen - these will be discussed below.

The proper motion error estimate is equal to the standard deviation of the proper motion values. Proper motion and its corresponding errors as a function of star magnitude are shown in Figure 8.5. As expected, proper motion accuracy (as well as positional accuracy) decreases with increasing star magnitude. The magnitude is the HST WFPC2 instrumental magnitude in the F555W filter for the first epoch images.

The colour magnitude diagram of all the stars whose proper motion was de-

---

[1] Catalogue is available at http://dept.astro.lsa.umich.edu/∼ognedin/gc/vesc.dat

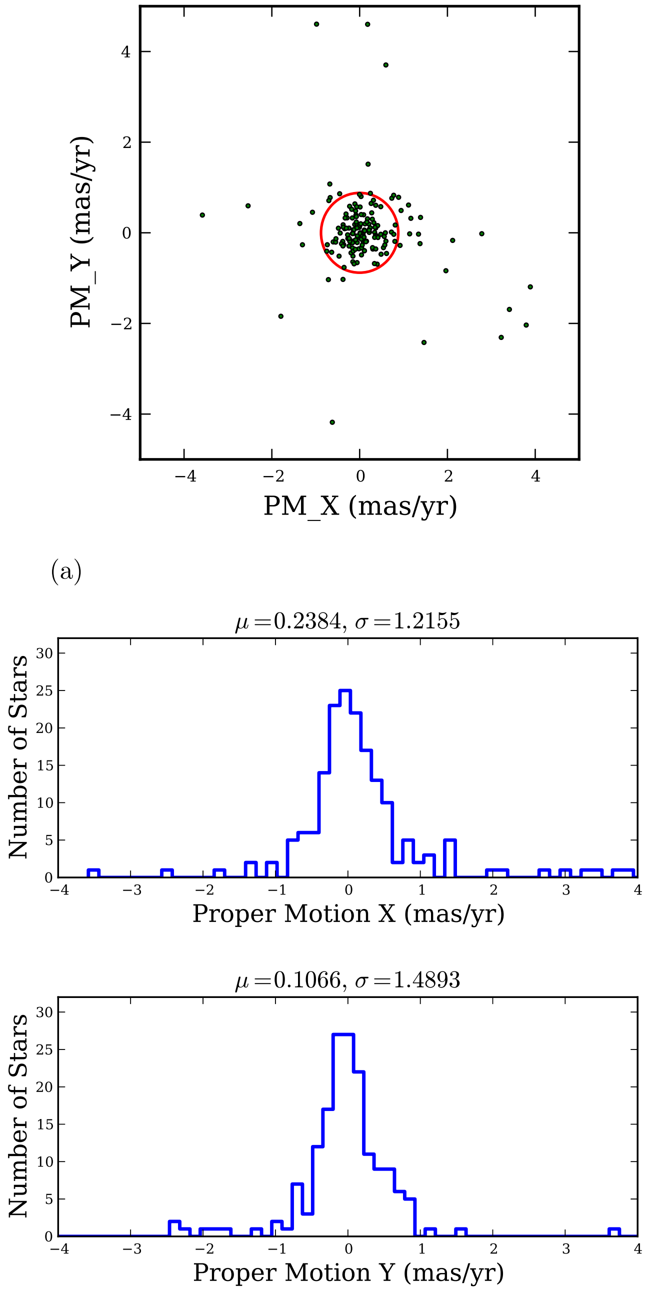

(a)

$\mu = 0.2384$, $\sigma = 1.2155$

$\mu = 0.1066$, $\sigma = 1.4893$

(b)

Figure 8.4: M71 stellar proper motion. (a) Stellar proper motion. Stars outside the 880 μas/year red circle are high velocity stars. (b) Histogram of these proper motions.

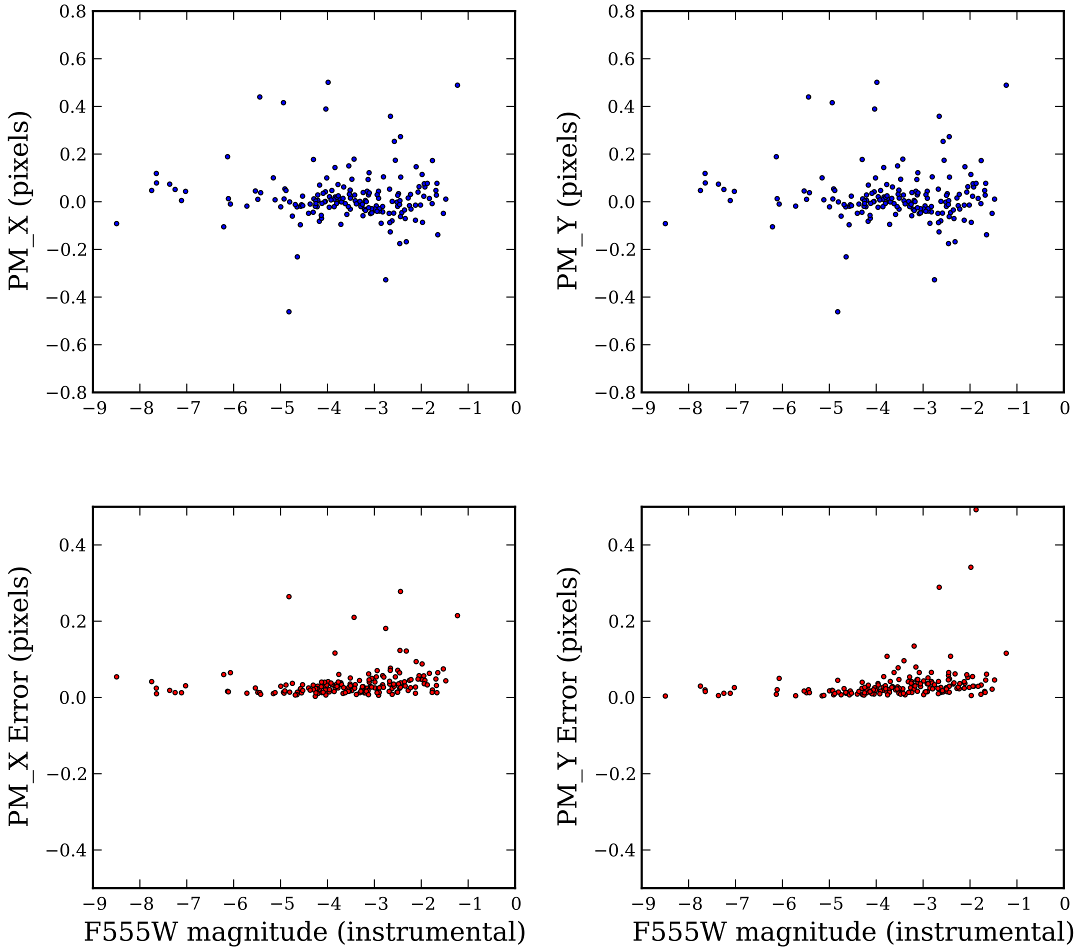

Figure 8.5: Proper motion, and proper motion error, as a function of star magnitude. As expected, proper motion accuracy decreases with increasing magnitude value.

termined is shown in Figure 8.6.

8.1.4 Internal Proper Motion Dispersion

The internal proper motion dispersion was calculated following the procedure described in Section 5.3.8. As internal velocity dispersion is sensitive to the quality of the proper motion measurements, we selected only the highest quality proper motion stars. The first criterion for selection was to include only the stars within the escape velocity envelope of the cluster ($\sim 0.8\,mas/year$). Out of 175 stars, 132

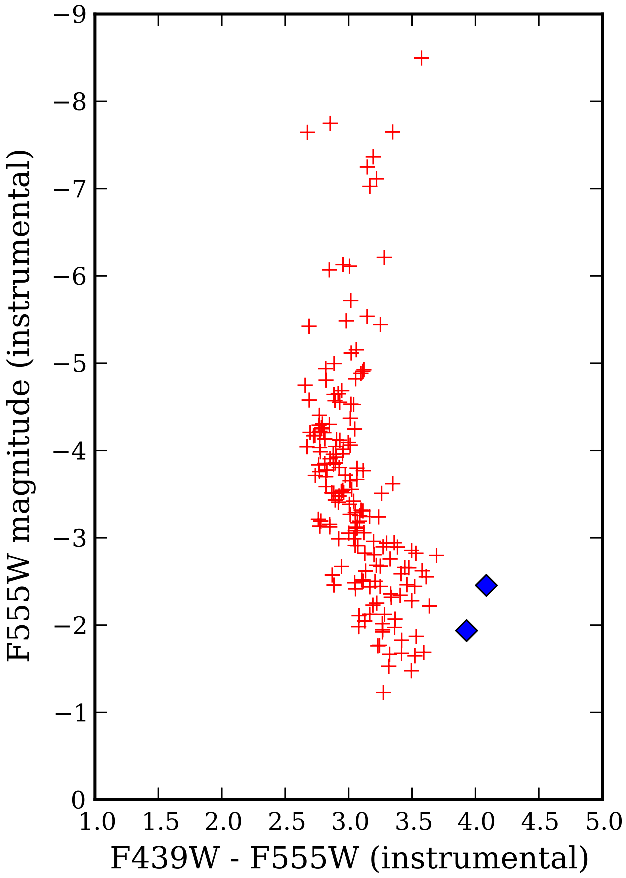

Figure 8.6: Colour magnitude diagram of 175 stars in M71, whose proper motion was measured. The magnitude and colour are in the HST WFPC2 instrumental magnitudes and are from the first epoch images. The two stars marked as blue diamonds in the CMD were removed from the starlist before determining the internal proper motion dispersion.

passed this criterion. Secondly, we removed two stars based on their anomalous position on the colour magnitude diagram (these are marked as blue diamonds in Figure 8.6). Thirdly, as the positional accuracy is poor for high magnitude stars, we selected only stars between -9.0 and -2.5 instrumental magnitude. This excluded the poorly measured stars as well as the 2 stars with anomalous CMD positions. Similar exclusion criteria were also used by McNamara *et al.* [2003] for M15, and McNamara *et al.* [2012] for NGC 6266. Finally, any star with proper motion error greater then 4 σ of the mean error was also excluded. The final star list used for internal proper motion analysis had 105 stars. Histograms of these stars, fitted with Gaussian profiles, are shown in Figure 8.7.

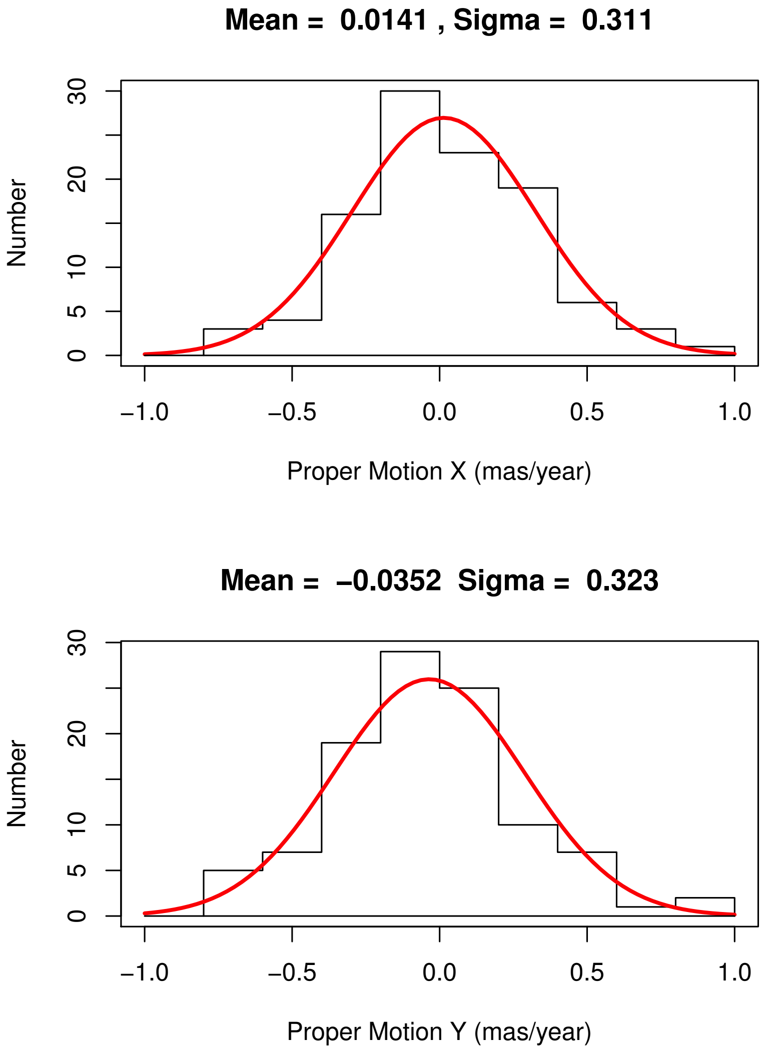

Figure 8.7: Proper motion histogram of M71 cluster stars with Gaussian profile fitted to it.

The **R** statistical package was used for fitting Gaussian distributions to the proper motion histograms. The maximum likelihood fitting method *fitdistr* in the package MASS was used to fit both the mean value and dispersion[1]. The

---

[1] Please refer to Appendix C for an example code.

cluster showed mean motion of 0.014 ± 0.030 mas/year in the x direction and -0.035 ± 0.031 mas/year in the y direction. These are far from the 0.180 mas/yr found by others. In fact, they are consistent with zero mean motion, because the way the epoch starlists were transformed to each other cancelled out any systematic shift. The uncorrected internal proper motion dispersion along the x and y direction was 0.311 ± 0.021 and 0.323 ± 0.022 mas/year respectively.

If an intermediate mass black hole is present at the cluster core, we would expect to see a steep rise in velocity dispersion at the centre of the cluster. To study the variation in proper motion dispersion, we created equally spaced radial bins from the cluster centre to $20''$ radius. To avoid small number statistics, the size of the bin was dictated by the number of stars in the first bin. Equally spaced $5''$ radial bins were found to be suitable. The radial variation of proper motion dispersion is also dependent on the exact cluster centre. We adopted the Goldbury *et al.* [2010] estimate of the cluster centre, which is accurate to within $\pm 0.5''$. The proper motion dispersion values are listed in Table 8.3. The table is visualised in Figure 8.8, both in terms of mas/year and km/sec. The distance to M71 was taken as 4 kpc for converting the dispersion value units from pixel to km/sec. The difference between σ_x and σ_y in the first radial bin could have been because of CTE imperfections but as we took care of that using Dolphin [2009] formulation, we anticipate it to be due to low number statistics.

Mean R (arsec)	N_{stars} (-)	σ_x (pixel)	ϵ_x (pixel)	σ_y (pixel)	ϵ_y (pixel)	σ_{avg} (pixel)	ϵ_{avg} (pixel)	σ_{avg} (μas/year)	ϵ_{avg} (μas/year)
3.10	11	0.027	0.006	0.061	0.013	0.033	0.005	256.12	38.81
7.68	31	0.028	0.004	0.030	0.004	0.029	0.003	225.07	23.28
12.50	41	0.031	0.003	0.027	0.003	0.029	0.002	225.07	15.52
17.18	17	0.031	0.005	0.022	0.004	0.026	0.003	201.79	23.28

Table 8.3: Internal proper motion dispersion of globular cluster M71. Mean R is the average radial distance of the stars in the bin. The mean value of the dispersion, σ_{avg}, is calculated by taking the weighted average of the dispersion in the x and y directions.

The velocity dispersion shows a slight increase from the second to the first bin but the values are within 1 σ error bars. The proper motion profile is almost flat

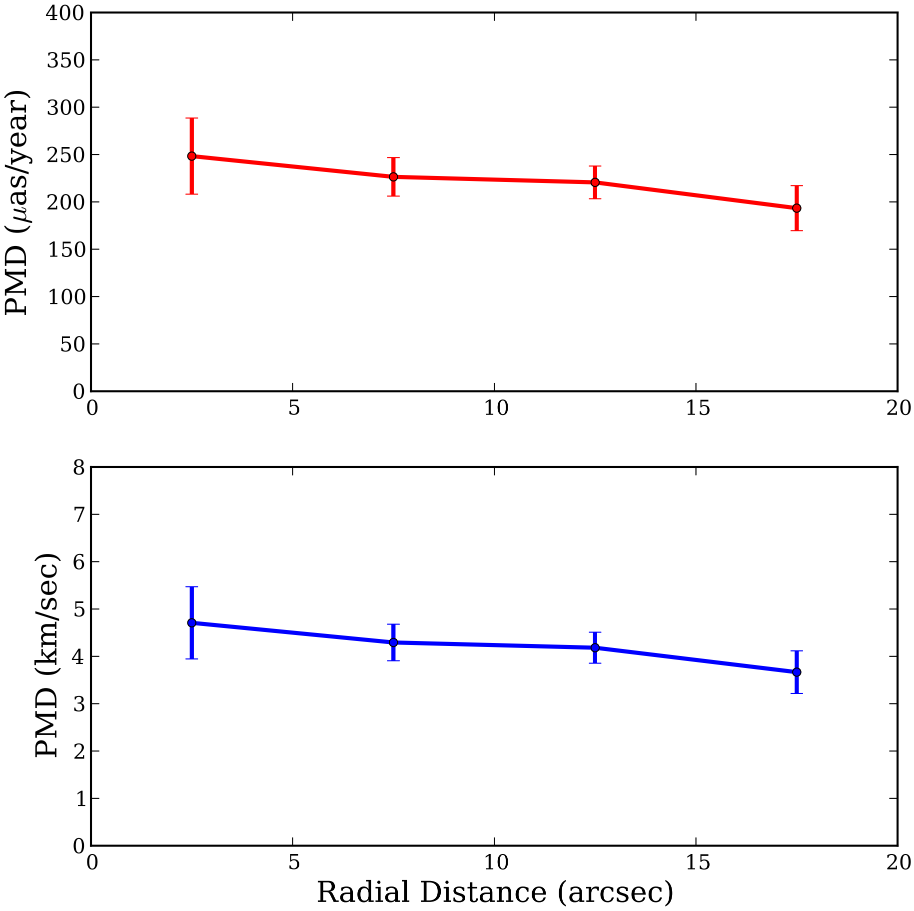

Figure 8.8: Internal proper motion dispersion of M71 as a function of radial distance from the cluster centre. (a) in units of mas/ year, (b) in units of km/sec. The conversion from μas/year to km/sec is based on a 4 kpc distance and a 6 year baseline.

between the second and the third bin and a slight drop occurs between the third and the fourth bin. The same result was also obtained by Samra *et al.* [2012], as they also did not observe a change in dispersion from the cluster centre to $22''$ radial distance. The dispersion values we got (201 - 256 μas/yr) are higher compared to the one quoted by both Cudworth [1985] and Samra *et al.* [2012] - respectively 180 ± 30 $\mu as\ yr^{-1}$ and 179 ± 14 $\mu as\ yr^{-1}$. We attribute this to the of higher positional errors in our case, and also to the choice of stars used for internal proper motion dispersion calculation. Nonetheless, the general profile of the velocity dispersion can give an indication of the presence of an intermediate mass black hole. Samra *et al.* [2012] estimated the mass of the black hole in M71 to be not more than 150 $M_\odot$.

8.2 Globular Cluster NGC 6293

The globular cluster NGC 6293 ($\alpha = 17^h 10^m 10^s.2, \delta = -26^o 34^{'} 55^{''}.5$) is a metal-poor globular cluster, situated nearly 10 kpc from us. It is a core collapsed cluster with a core radius of $\sim 0.05'$. As it is situated at 1.9 kpc distance from the galactic centre, it has high interstellar reddening of E(B-V) = 0.36 [Harris, 1996]. Table 8.4 lists the basic properties of NGC 6293.

Right ascension	17:10:10.20
Declination	-26:34:55.5
Distance from Sun	9.5 kpc
Absolute Visual Magnitude	-7.78
Metallicity [Fe/H]	-1.99
Central velocity dispersion	7.7 km/sec
King concentration c	2.5
Core radius	0.05 arcmin
Half light radius	0.89 arcmin
Core relaxation time	2.39×10^6 years

Table 8.4: Globular cluster NGC 6293 properties. Values are from Harris [1996].

8.2.1 Data

The first epoch observations were taken on March 23 1995 (HST Proposal ID 5366) with the HST WFPC2 detector in the F555W and F814W filters. The second epoch images were taken on April 20 2009 (HST Proposal ID 11975) but with a different telescope orientation and using the F555W and F336W filters. The PC chip of the detector covered the same central region of the cluster in both the observations. The first epoch has 7 frames in each filter. The second epoch has only three deep exposures in the F555W filter. Only the F555W filter images in the PC chip were used for proper motion determination, but the F814W frames from the first epoch were used for constructing colour magnitude diagram of the cluster. A journal of observations used for the present study is listed in Table 8.5.

Epoch	**Date**	**Filter**	**Datasets**	**Exptime** (sec)
First	23 March 1995	F555W	U28Q0201T	40
			U28Q0202T	40
			U28Q0203T	40
			U28Q0204T	500
			U28Q0205T	500
			U28Q0206T	500
			U28Q0207T	500
		F814W	U28Q0208T	60
			U28Q0209T	60
			U28Q020AT	60
			U28Q020BT	700
			U28Q020CT	700
			U28Q020DT	700
			U28Q020ET	700
Second	20 April 2009	F555W	UBAI3902M	100
			UBAI3903M	100
			UBAI3904M	100
		F336W	UBAI3905M	700
			UBAI3906M	700
			UBAI3907M	700

Table 8.5: HST WFPC2 observations of NGC 6293.

HST WFPC2 pointings for the two epochs are overlaid on the DSS image in Figure 8.9. The PC chip covers the $35'' \times 35''$ central region of the cluster.

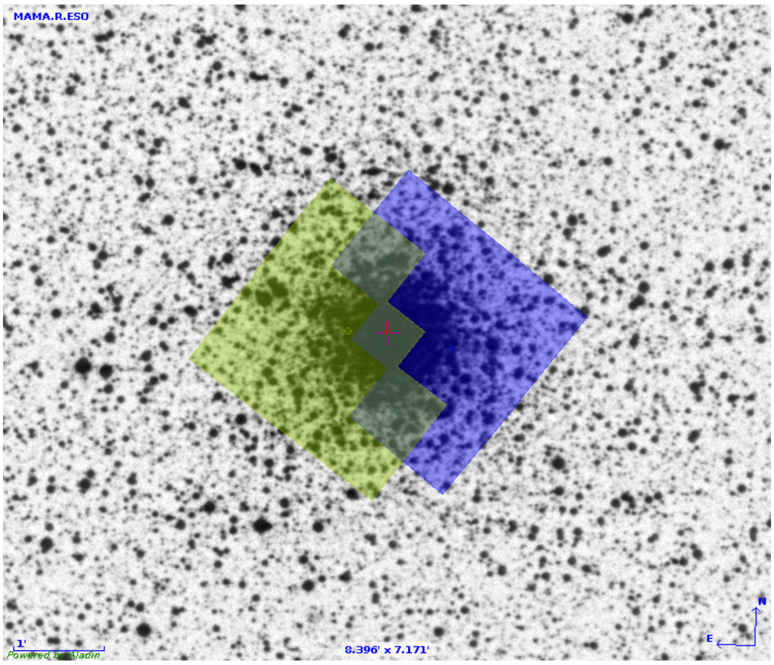

Figure 8.9: Multi epoch HST WFPC2 pointings on the core of NGC 6293. Blue and yellow mark the 1995 and 2009 epoch observations respectively. The WFPC2 FOV was overlaid on the DSS image using the ALADIN sky atlas.

8.2.2 Image Reduction, Star Detection, and PSF-Fitting Photometry

We followed the steps described in Section 5.3.1.1 to reduce and register the images in both epochs. Individual frames were cleaned of cosmic rays and saturated pixels using the data quality (DQ) masks generated from the imcombine step. A TinyTIM point spread function grid was created for each filter and a spatially varying first guess analytical PSF was generated using the IRAF *psf* task. The HST is affected by pointing jitter at the milli-arcsecond level. The jitter information is stored in JIT files during the observation. We used the epoch-averaged jitter value along the telescope's V3 axis in modelling the TinyTIM PSF. Slight point spread function variation due to telescope jitter and breathing are not included in modelling Anderson & King [2000] ePSF for WFPC2, which our technique takes into consideration. An example of the HST jitter for an observation in the F555W filter (2009 epoch) in shown in Figure 8.10.

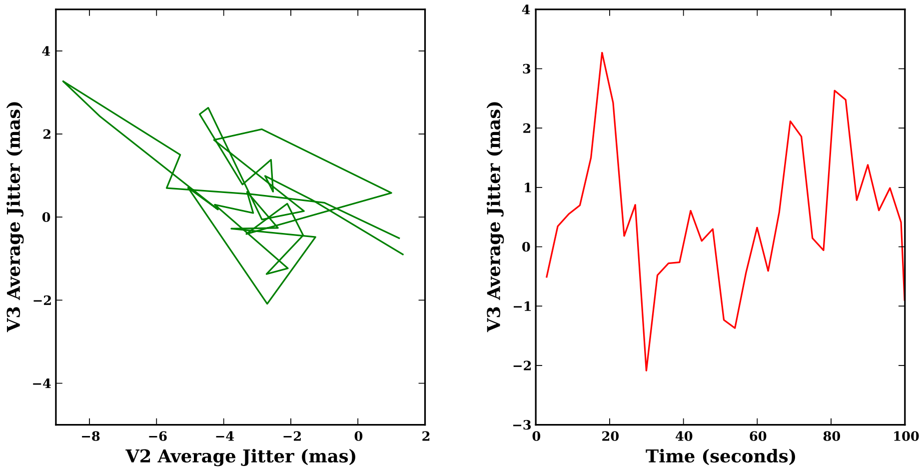

Figure 8.10: Hubble Space Telescope pointing jitter. The "jitter ball" is generated for the UBAI3903M dataset by plotting the pointing jitter along HST's V2 and V3 axis (left) and the average V3 jitter as a function of time (right). The pointing jitter is in milli-arcseconds. Jitter data was extracted from the JIT file for this observation.

The high signal-to-noise combined image in each filter was deconvolved with the first guess analytical PSF. Our parallel deconvolution routine specifically developed for this purpose was used. The sub-sampled deconvolved images for two filters (F555W and F814W in the 1995 epoch and F555W and F336W in the 2009 epoch) were then co-added with cosmic ray and artefact rejection as described in Section 8.1.2. Star detection was performed on the combined deconvolved image with a threshold set to 10 sigma in *daofind*. As the purpose of the study is not to catalog all the stars, but to measure highest quality stellar proper motion, 10 σ detection avoids detecting spurious deconvolution artefacts and low magnitude stars with higher positional errors. The star list was refined manually by rejecting stars at the edge of the image and other spurious objects, especially in the vicinity of saturated stars. The first set of star coordinates was generated by fitting the TinyTIM PSF (using the IRAF *allstar* task) to the the detected stars in the individual images in both filters.

The point spread function was improved in the second iteration by modelling it directly from the stars in the combined single filter images. Only unsaturated and bright, high SNR stars were used to model the spatially varying empirical point spread function. In order to avoid the light from the neighbouring stars influencing the point spread function, all the detected stars (apart from the stars used for PSF modelling) were subtracting from the image using the IRAF *substar* task. In this regard, the first guess PSF is important because a good model PSF can cleanly subtract the light of the neighbouring stars in the crowded field. A second set of refined star coordinates was generated by fitting the empirical point spread function to individual images.

Single band deconvolved image sections from 1995 and 2009 frames are shown in Figure 8.11.

In total fourteen star lists were generated for the 1995 epoch (7 each for the F555W and F814W filters). How these starlists were combined is described in the next subsection.

As the purpose of the study is not precise photometry, magnitudes were kept in the instrumental scale and aperture correction and/or reddening corrections were not made to the final stellar magnitudes.

8.2.3 Starlist Merging and Proper Motion Determination

Stellar positional errors in each epoch were calculated using the Anderson *et al.* [2006] formulation (see Section 5.3.7). The error in the mean position of a star was calculated using the intra-epoch displacement values. To be included in the final starlist in each epoch, the star has to be within ±0.3 pixels in each frame and its magnitude within ±0.5 mag. We choose stars within ±0.3 pixels instead of ±0.2 pixels (as was done for M17) as it turned up a much smaller starlist. This could be because of slight telescope pointing difference between different frames. Secondly, for both the 1995 and 2009 epochs, the star has to be detected in at least 3 frames to be included in the final list. The combined star list for the 1995 epoch had 1947 stars whereas the 2006 starlist had 3643 stars. Proper motion was determined using a pair of single uncombined exposures between the two epochs. This way we had at least 9 estimates of the stellar proper motion, and 21 estimates for most of the stars.

The first step in relative proper motion determination is to match the stars

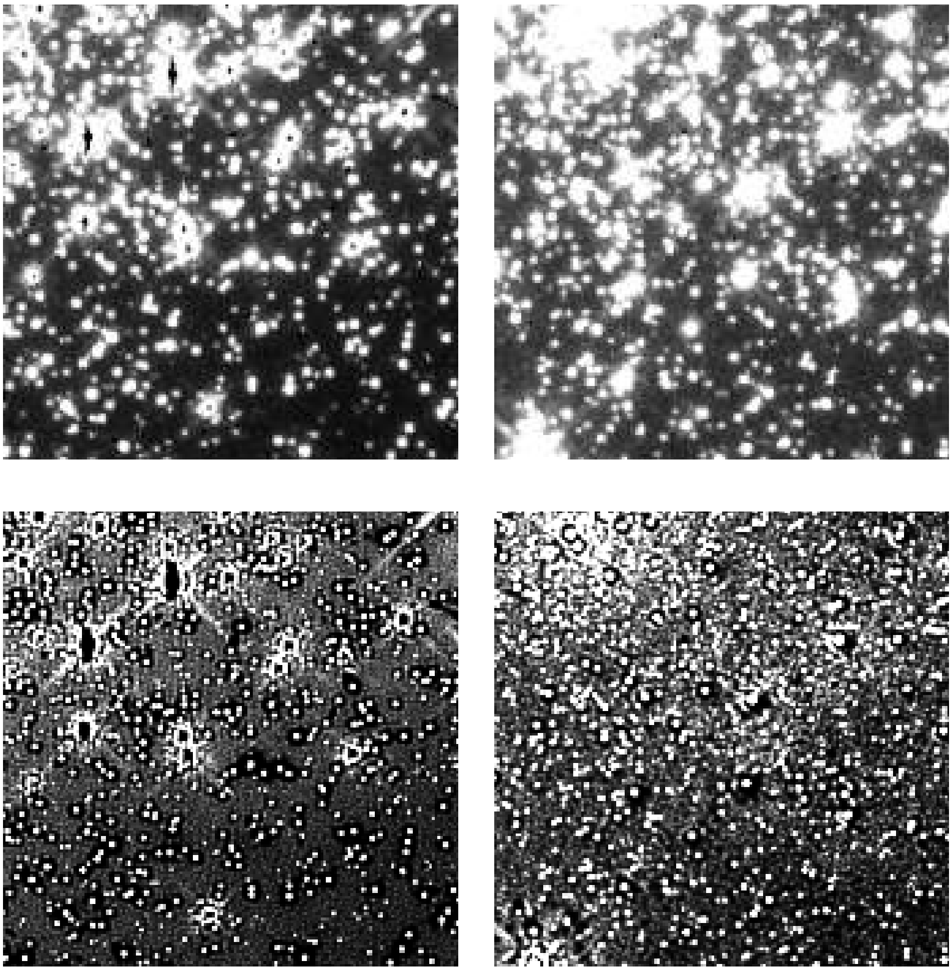

Figure 8.11: NGC 6293 deconvolved images. Image section of the F555W filter image from 1995 (top left) and 2009 (top right). The corresponding spatially varying empirical point spread function deconvolved image sections are shown below the image sections.

between the two epochs. This was done in exactly the same manner as for M71 (Section 8.1.3). A total of 1468 stars were matched between the two epochs. These are shown in Figure 8.12.

The second step involved choosing low proper motion cluster reference stars to be used to solve the geometric transformation equation between the two epochs. The assumption here is that the mean proper motion of the cluster stars is zero.

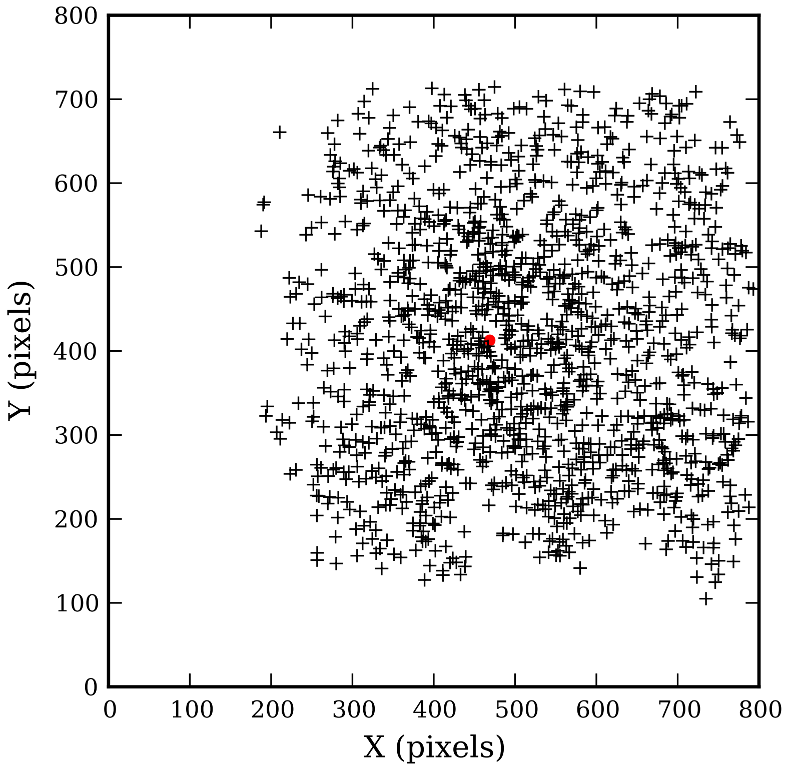

Figure 8.12: Location of stars whose proper motion was measured in the 2009 epoch images. Stars in the first 100 vignetted/distorted rows + columns of the HST WFPC2 detector were not included in the final star list. The cluster centre is marked as a red dot.

We took the second epoch frame as the reference coordinate system. To get a good geometric transformation solution for transforming the coordinates from the first epoch to the reference coordinate system, the *geomap* task was run iteratively to include only the low proper motion stars. In addition to the linear terms, quadratic polynomial terms were also included to "map out" the residual distortions (especially at the edges of the detector). The choice of low proper motion stars for the transformation can be based on the location of the star in the colour magnitude diagram and/or iteratively running the geomap task.

Once we had the transformation solution, the 1995 epoch combined star list was transformed to the 2009 reference frame. This was repeated for all the 21 inter-epoch image pairs. This gave us at least nine estimates of the proper motion for each star. The final stellar proper motion in the x and y directions (in the 2009 reference frame) was the mean of these multiple values. As described earlier, the Anderson *et al.* [2006] formula was used to estimate the proper motion errors. The NGC 6293 stellar proper motion scatter plot is shown in Figure 8.13(a). Pixel values were converted to mas/year for the 14 year baseline. The red circle corresponds to approximately 0.81 mas/year. This was set by visually examining the scatter diagram. Only stars within this circle were used for the internal proper motion dispersion calculation. The choice of the limiting proper motion was based also on the fact that the NGC 6293 image is contaminated by the field stars. The limiting proper motion values are subjective but the main idea is to include most of the cluster stars and exclude field star contamination. Corresponding proper motion histograms for all the matched stars is shown in Figure 8.13(b).

Proper motion and its corresponding errors as a function of star magnitude are shown in Figure 8.14. As expected, proper motion accuracy (as well as positional accuracy) decreases for low magnitude stars. The magnitude is the HST WFPC2 instrumental magnitude in the F555W filter for the first epoch images.

The colour magnitude diagram of all the stars whose proper motion was determined is shown in Figure 8.15.

8.2.4 Internal Proper Motion Dispersion

The internal proper motion dispersion was calculated following the procedure described in Section 5.3.8. As internal velocity dispersion is sensitive to the quality of proper motion measurements, we selected only the highest quality proper motion stars for this analysis. The first criterion for the selection was to include only the stars within the 0.81 mas/year envelope in the proper motion scatter diagram. Secondly, as the positional accuracy is poor for fainter stars, we selected only those stars with instrumental magnitude between -8.0 and -0.5 mag. This excluded any poorly measured stars. The first two selection criteria reduced the starlist to 1267 stars. Thirdly, any star with anomalous position on the CMD was also rejected. Although "anomalous" is subjective, it only affected six stars. Finally, any star with proper motion or proper motion errors greater than 4 σ of the mean in each bin was also excluded from the analysis. This affected only a

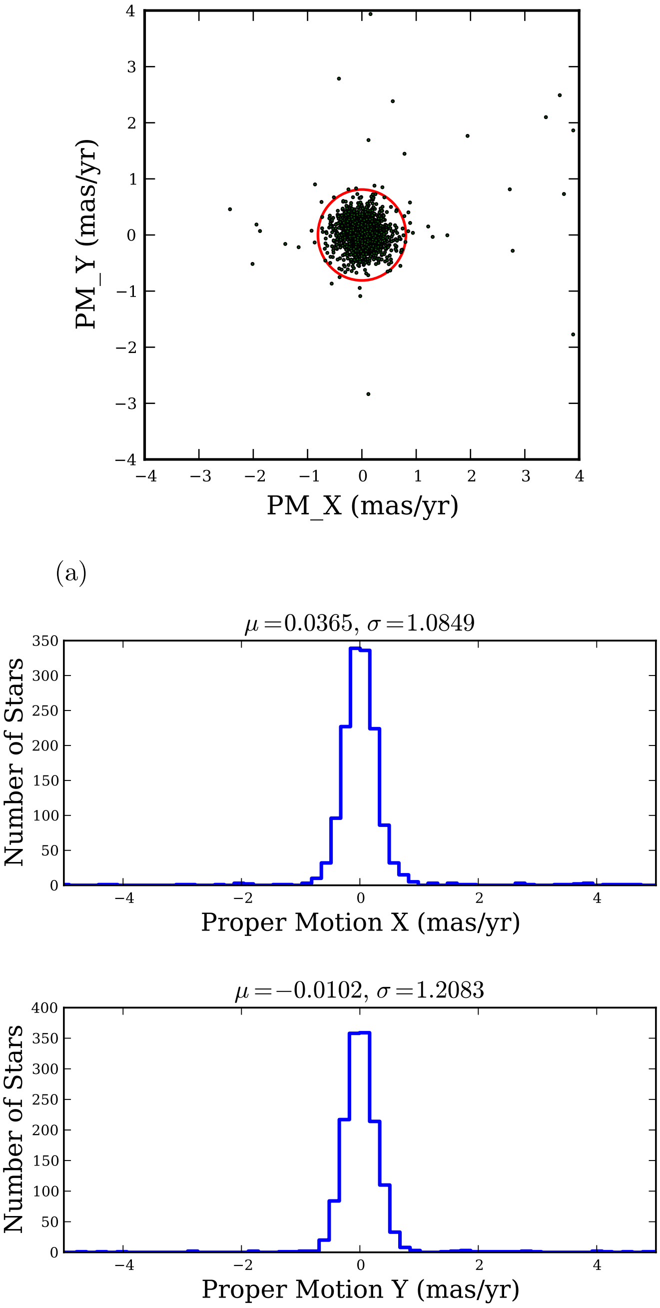

(a)

(b)

Figure 8.13: NGC 6293 stellar proper motion. (a) Stellar proper motion. (b) Histograms of these proper motions.

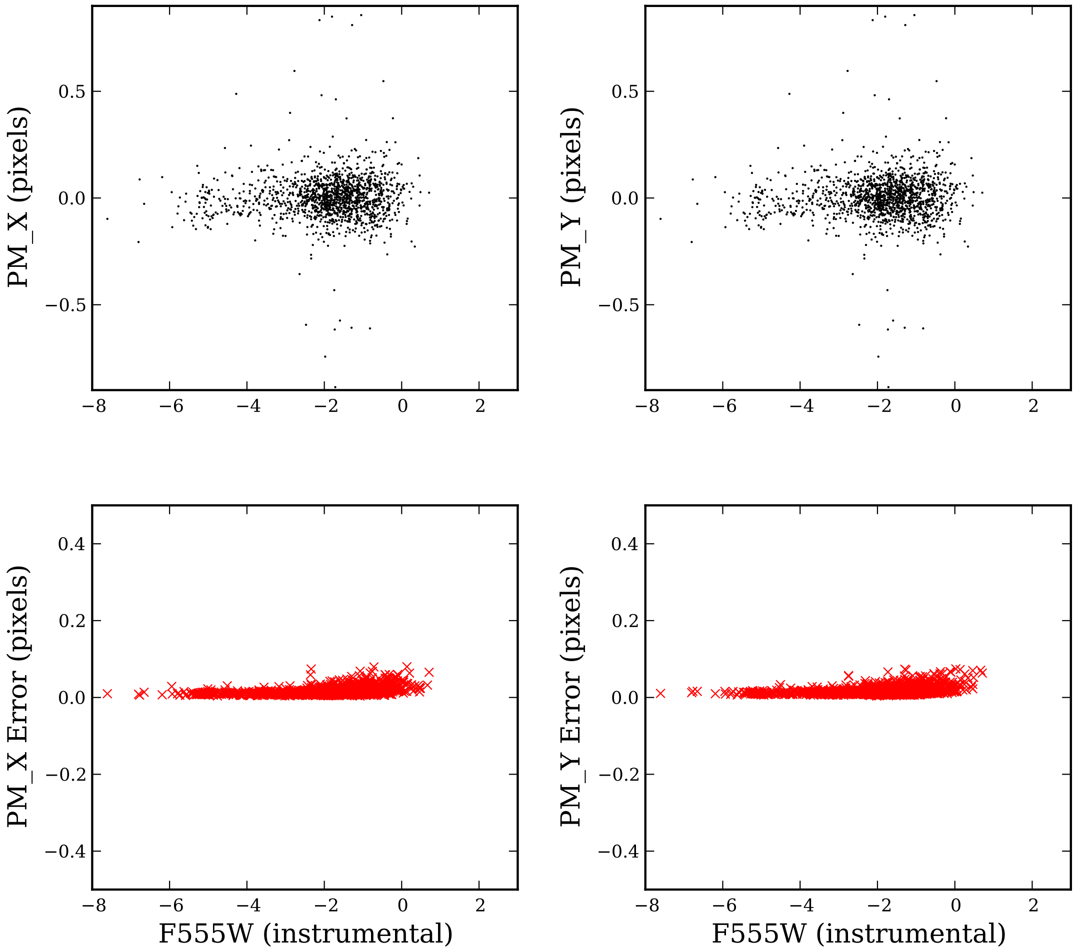

Figure 8.14: Proper motion, and proper motion error, as a function of star magnitude. As expected, proper motion accuracy decreases with increasing magnitude value.

few stars. The final star list used for the internal proper motion dispersion had 1245 stars. Histograms of these stars, with fitted Gaussian profiles are shown in Figure 8.16.

The **R** statistical package was used for fitting the Gaussian distributions to the proper motion histograms. The maximum likelihood fitting method *fitdistr* in the package MASS was used to fit both the mean value and the dispersion. The cluster showed mean motion of 0.000 ± 0.007 mas/year in the x direction and 0.002 ± 0.006 mas/year in the y direction. The uncorrected internal proper

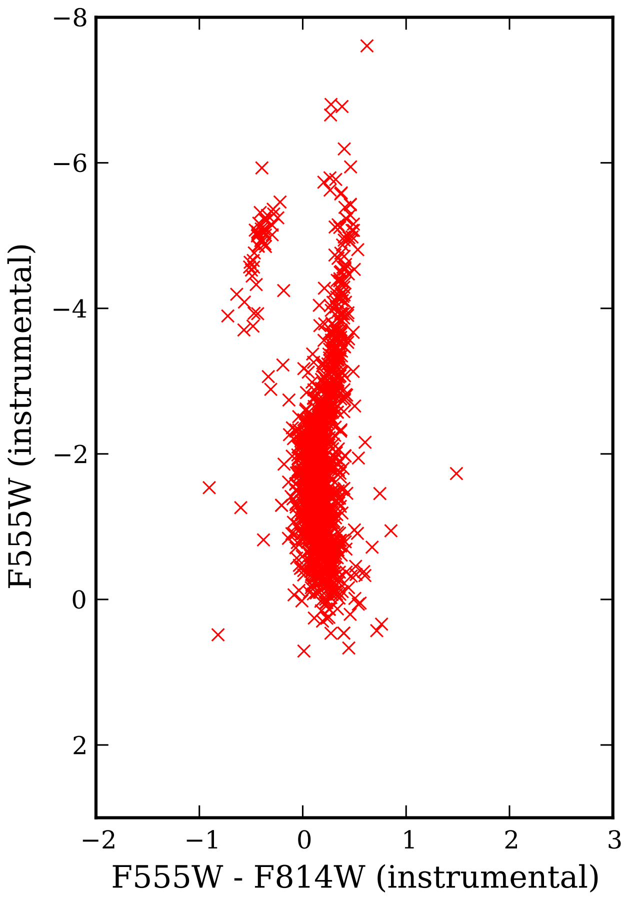

Figure 8.15: Colour magnitude diagram of 1468 stars in NGC 6293 whose proper motion was measured. The magnitude and colour are in HST WFPC2 instrumental magnitudes and are from the first epoch images.

motion dispersion along the x and y direction is 0.250 ± 0.004 and 0.243 ± 0.004 mas/year respectively.

If an intermediate mass black hole is present at the cluster core, we would expect to see a steep and gradual rise in velocity dispersion towards centre of the cluster. To study the variation in proper motion dispersion, we created equally spaced radial bins from the cluster centre to $20''$ radius. To avoid small number statistics, the size of the bins was dictated by the number of stars in the inner bin. Equally spaced $1.2''$ radial bins were found to be suitable (with the innermost bin having 15 stars). The radial variation of proper motion dispersion is also depen-

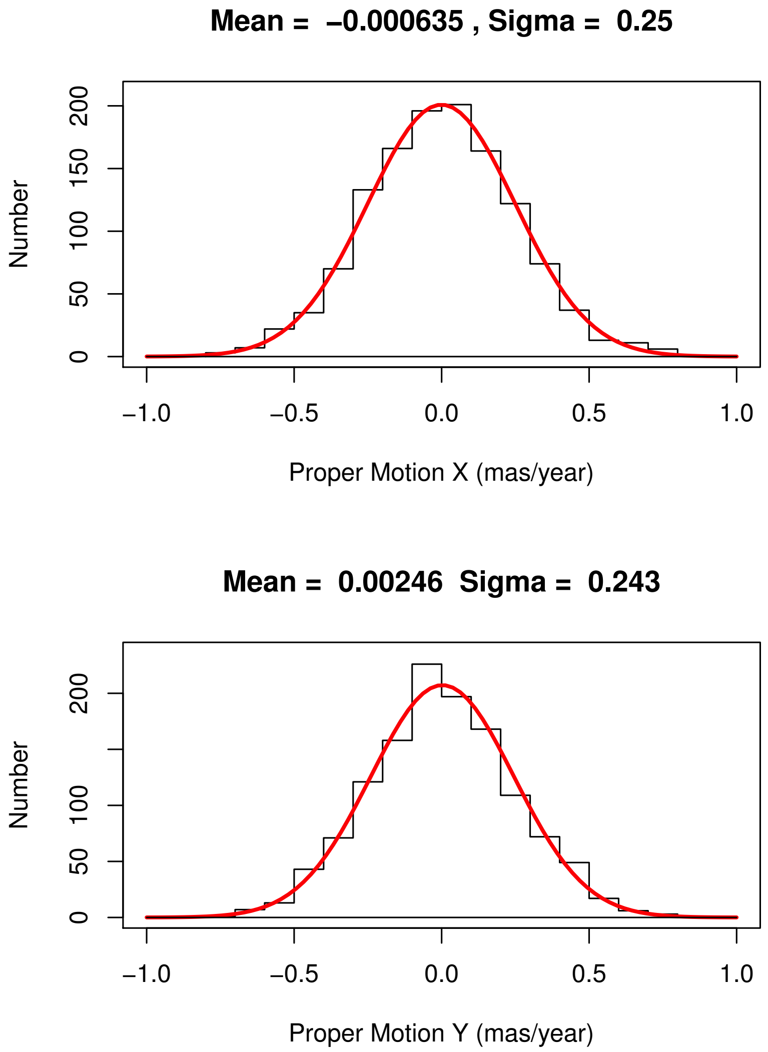

Figure 8.16: Proper motion histogram of NGC 6293 cluster stars with Gaussian profile fitted to it.

dent on the exact cluster centre. We found three different values of the cluster centre for NGC 6293 in the literature: $\alpha = 17^h 10^m 10^s.2, \delta = -26^o 34^{'} 55^{''}.5$ [Harris, 1996], $\alpha = 17^h 10^m 10^s.31, \delta = -26^o 34^{'} 57^{''}.77$ [Noyola & Gebhardt, 2006], and $\alpha = 17^h 10^m 10^s.42, \delta = -26^o 34^{'} 54^{''}.2$ [Lee & Carney, 2006]. We took the mean of the three cluster centre values for the proper motion dispersion estimation. The calculated proper motion dispersion values are listed in Table 8.6. The table is visualised in Figure 8.17, both in terms of mas/year and km/sec. The distance to NGC 6293 was taken as 9.5 kpc for converting the dispersion value units from pixel to km/sec. The proper motion dispersion value are higher than the radial velocity dispersion (7.7 ± 1.3 km/sec) quoted by Harris [1996].

Mean R (arsec)	N_{stars} (-)	σ_x (pixel)	ϵ_x (pixel)	σ_y (pixel)	ϵ_y (pixel)	σ_{avg} (pixel)	ϵ_{avg} (pixel)	σ_{avg} (mas/year)	ϵ_{avg} (mas/year)
0.79	16	0.061	0.011	0.088	0.016	0.070	0.009	0.229	0.030
1.89	53	0.085	0.008	0.076	0.007	0.080	0.005	0.261	0.016
3.07	75	0.069	0.006	0.075	0.006	0.072	0.004	0.235	0.013
4.19	97	0.080	0.006	0.072	0.005	0.075	0.004	0.245	0.013
5.43	122	0.072	0.005	0.073	0.005	0.073	0.004	0.238	0.013
6.52	96	0.069	0.005	0.078	0.006	0.073	0.004	0.238	0.013
7.81	125	0.081	0.005	0.078	0.005	0.080	0.004	0.261	0.013
8.95	116	0.070	0.005	0.069	0.005	0.070	0.004	0.229	0.013
10.34	156	0.074	0.004	0.066	0.004	0.070	0.003	0.229	0.010
11.62	127	0.080	0.005	0.062	0.004	0.069	0.003	0.225	0.010
12.72	104	0.076	0.005	0.067	0.005	0.072	0.004	0.235	0.013
13.92	80	0.067	0.005	0.085	0.007	0.073	0.004	0.238	0.013
15.05	48	0.085	0.009	0.066	0.007	0.073	0.006	0.238	0.020
16.32	22	0.076	0.011	0.054	0.008	0.062	0.006	0.203	0.020
17.64	8.0	0.076	0.019	0.079	0.020	0.077	0.014	0.252	0.046

Table 8.6: Internal proper motion dispersion of globular cluster NGC 6293. Mean R is the average radius of the stars in the bin. $\sigma_x, \epsilon_x, \sigma_y, \epsilon_y$ are the dispersion values and corresponding errors in the x and y directions respectively. The mean value of the dispersion, σ_{avg}, is calculated by taking the error-weighted average of the dispersion in the x and y directions.

The proper motion profile is almost flat from 0.8″ to 18″. The small deviations of the velocity dispersion value are within 1 σ error bars of each other. We did not observe any steep and gradual increase in the proper motion dispersion value near the core of the cluster. However, we cannot rule out the possibility of a central black hole just based on the proper motion dispersion values. Safonova & Shastri [2010] extrapolated the M_{BH}-σ relationship to estimate the mass of central IMBH in NGC 6293 to be ∼ 200,000 $M_\odot$. A detailed *N-body* modelling is required to reach any conclusion and to put an upper limit to the central intermediate mass black hole.

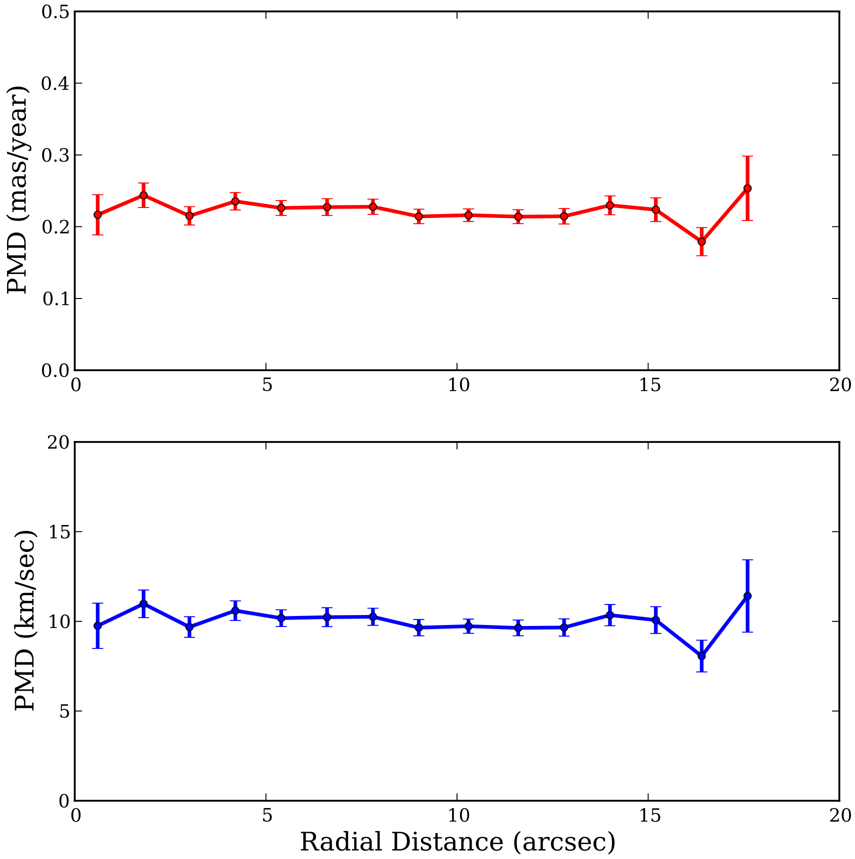

Figure 8.17: Internal proper motion dispersion of NGC 6293 as a function of radial distance from cluster centre. (a) in units of mas/ year, (b) in units of km/sec. The conversion from mas/year to km/sec is based on a 9.5 kpc distance and a 14 year baseline.

8.3 Globular Cluster M15 (NGC 7078)

The globular cluster M15 ($\alpha = 21^h29^m58^s.33, \delta = +12^o10^{'}01^{''}.2$) is a core-collapsed globular cluster in the constellation Pegasus. It is situated at $\sim 10kpc$ from us having an absolute visual magnitude of -9.19 mag. The core radius of the cluster is $\sim 0.14'$ and the half-light radius is $\sim 1.0'$. Table 8.7 lists the basic properties of M15.

Right ascension	21:29:58.33
Declination	+12:10:01.2
Distance from Sun	10.4 kpc
Absolute Visual Magnitude	-9.19
Metallicity [Fe/H]	-2.37
Central velocity dispersion	13.5 km/sec
King concentration c	2.29
Core radius	0.14 arcmin
Half light radius	1.00 arcmin
Core relaxation time	6.91×10^7 years

Table 8.7: Globular cluster M15 properties. The values are from Harris [1996]

8.3.1 Data

The first epoch observations were taken on April 7 1994 (HST Proposal ID 5324) with the HST WFPC2 detector in the F555W, F439W, and F336W filters. The second epoch images were taken on May 2 2006 (HST Proposal ID 10775) with the ACS WFC detector in the F606W and F814W filters. The WFPC2 pointing coincided with the central region of the WFC image. The first epoch has 4 frames in the F555W filter. The second epoch has five dithered frames in the F606W filter. Stars in the PC chip of the WFPC2 instrument in the F555W filter in the first epoch and the second epoch ACS WFC F606W frames were used for proper motion determination. The first epoch F439W filter images were used to reject spurious objects and for constructing the colour magnitude diagram. Similarly, F814W images in the second epoch were used to constrain genuine detections. A journal of observations used for the present study is listed in Table 8.8.

The telescope pointings for both epochs are overlaid on the DSS M15 image in Figure 8.18.

8.3.2 Image Reduction, Star Detection, and PSF-Fitting Photometry

The first epoch WFPC2 images were reduced and registered using the procedure described in Section 5.3.1.1. Individual frames were cleaned of cosmic rays and saturated pixels using the data quality (DQ) masks generated from the imcombine

Epoch	**Date**	**Filter**	**Datasets**	**Exptime** (sec)
First	07 April 1994	F555W	U2AS0201T	8
			U2AS0202T	8
			U2AS0203T	8
			U2AS0204T	8
		F439W	U2AS0205T	40
			U2AS0206T	40
Second	2 May 2006	F606W	J9L954F1Q	15
			J9L954F3Q	130
			J9L954F5Q	130
			J9L954F7Q	130
			J9L954F9Q	130
		F814W	J9L954FBQ	15
			J9L954FDQ	150
			J9L954FFQ	150
			J9L954FHQ	150
			J9L954FJQ	150

Table 8.8: HST observations of M15. Only the F555W and F606W filter images were used for proper motion determination.

step. The second epoch ACS WFC dithered images (in both the F555W and F814W filters) were combined using the IRAF task *multidrizzle* (see Section 5.3.1.4 for more details). The combined drizzled images were used for deconvolution and empirical point spread function modelling, but separate drizzled frames were used for proper motion determination.

A first guess point spread function was generated from a grid of TinyTIM PSFs for the WFPC2 detector (in the same way as for M71 and NGC 6293). For the ACS WFC detector, a single image having two separate TinyTIM grids (4096×2048 pixels) - for the WFC1 and WFC2 detectors - was constructed. The image was then drizzled with the same parameters as the science images (see Figure 8.19). The drizzled TinyTIM image was then used to generate the first guess spatially varying analytical point spread function (see Figure 8.19).

For the first epoch, the high signal-to-noise combined image in each filter was

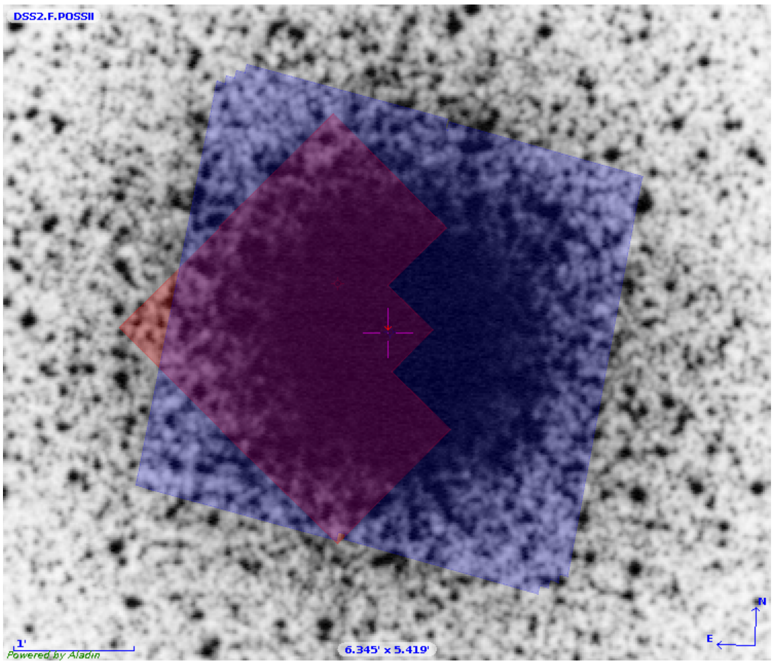

Figure 8.18: Multi epoch HST WFPC2 and ACS WFC pointings on the core of M15. Magenta and blue mark the 1994 WFPC2 and 2006 ACS WFC epoch observations respectively. The WFPC2 and ACS WFC FOVs were overlaid on the DSS image using the ALADIN sky atlas.

deconvolved with the first guess analytical PSF. Subsequently, the sub-sampled deconvolved F555W and F439W images were co-added with cosmic ray and artefact rejection. Star detection was performed on the combined deconvolved image with a threshold set to 10 σ of the sky value in *daofind*. The starlist was refined manually by rejecting stars at the edge of the image and other spurious detections, especially in the vicinity of the saturated stars. The first set of star coordinates was generated by fitting the TinyTIM PSF (using the IRAF *allstar* task) to individual images in both the filters.

The second epoch F606W and F814W drizzled images were deconvolved with the first guess TinyTIM point spread function. Similar to the first epoch images, the sub-sampled deconvolved images were co-added with cosmic ray and artefact rejection and stars were detected on the combined deconvolved image (using the *daofind* task with a 10 σ threshold). Starlists were generated for the individual drizzled images by fitting the TinyTIM PSF to the detected stars in the images.

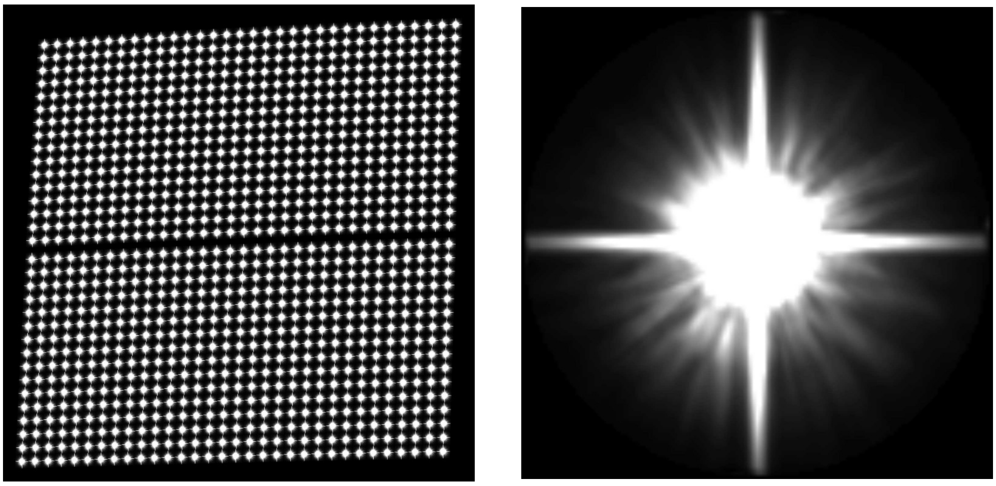

Figure 8.19: The drizzled image of the ACS WFC F606W TinyTIM point spread function star grid (left). It was drizzled with the same parameters as the science images. Spatially invariant point spread function generated for the spatially varying PSF for the the central chip position (right).

For the first epoch image, the point spread function was improved in the second iteration by modelling it directly from the stars in the combined single filter image. Only unsaturated and bright, high SNR stars were used to model the spatially varying empirical point spread function. The non-PSF modelling stars were subtracted from the image using the *substar* task. The psf task was then used to model the empirical PSF with quadratic spatial variation. A second set of refined star coordinates was generated using the empirical point spread function fitted to individual images. As demonstrated in Section 7.2.2, for the ACS WFC, astrometric and proper motion accuracy with the first guess TinyTIM PSF is comparable to the empirical PSF. Therefore we used the analytical TinyTIM PSF fitted stellar positions for the second epoch images[1].

The point spread function subtracted image section along with the corresponding original image section is shown in Figure 8.20.

In total six starlists were generated for the 1994 epoch (4 for the F555W filter and 2 for the F439W filter). The second epoch had 10 star lists in total (5 each

---

[1] The second guess point spread function is more important for WFPC2 images because of its under-sampled point spread function with extended "wings".

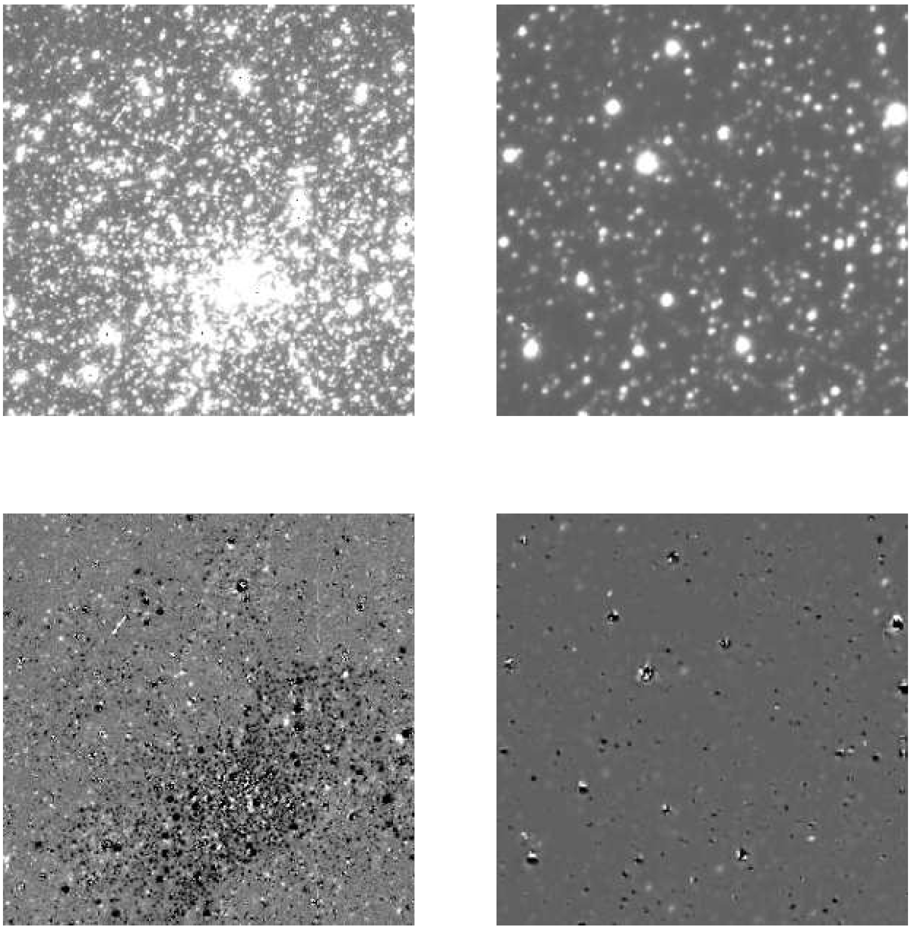

Figure 8.20: Globular cluster M15 image sections. Central image section in the F555W filter from the 1994 epoch (top left) and the F606W filter from the 2006 epoch (top right). The corresponding PSF fitted subtracted image sections are shown underneath.

for the F606W and F814W filters).

8.3.3 Starlist Merging and Proper Motion Determination

The errors in the star positions were calculated using the Anderson *et al.* [2006] formulation as detailed in Section 5.3.7. In the first epoch, for a star to be included in the final starlist (a) it has to detected in at least 3 frames, (b) it has to be within ±0.3 pixels in each frame, and (c) its magnitude has to be within

±0.5 mag. The final starlist for the 1994 epoch had 3456 stars. To have only highest quality proper motion stars, the selection criterion was more stringent for the 2006 epoch starlist. The stars had to be within ±0.2 pixels of each other. The 2006 starlist had 3988 stars in the central 1024×1024 pixels region. Proper motion was determined using the pairs of single, uncombined exposures between the two epochs (4 images from the first epoch and 5 from the second epoch). This way, we had a maximum of 20 estimates of the proper motion for a matched star.

The first step in relative proper motion determination was to match the stars between the two epochs. As the star lists were from two different detectors and filters, matching has to be robust, and the technique was somewhat different from the M71 and NGC 6293 cases. In the first step, a transformation solution was determined using only the WCS information in image header (using the IRAF *wcsmap* task). The transformation solution was then used to transform all the second epoch stars to the first epoch reference image. By visual inspection, three bright matching stars were then used to create a tiepoint file for the *xyxymatch* task. The IRAF task *xyxymatch* was used to match the two epoch starlists with 1.0 pixel tolerance and 2.0 pixels separation (with the above generated tiepoint file). Low tolerance was kept to avoid multiple matches in the crowded field. Inadvertently we may have also missed some genuine matches because of the stringent matching criteria. The matched stars in the 1994 reference frame are shown in Figure 8.21.

The second step involved choosing reference stars to solve the geometric transformation equation between the two epochs. The assumption here is that the mean proper motion of the cluster stars is zero. To get a good geometric transformation solution for transforming the coordinates from the second epoch to the reference coordinate system, the *geomap* task was run iteratively to include only the low proper motion stars. Apart from the linear terms, second order polynomial terms were also used in the *geomap* to “map out” the residual distortions. The choice of low proper motion stars for the transformation can be based on the colour magnitude diagram and/or iteratively running the geomap task.

Once we had the transformation solution, the 2006 epoch star positions were transformed to the 1994 reference frame. This was repeated for the 20 inter-epoch image pairs. This gave us at least nine estimates of proper motion for each

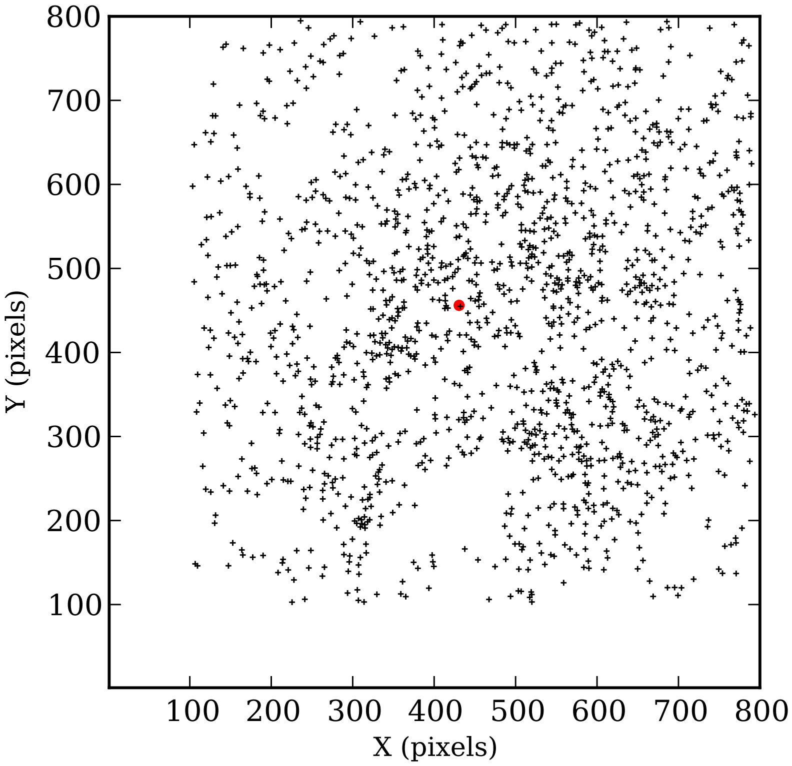

Figure 8.21: Location of stars whose proper motion was measured in the 1994 epoch image. Stars in the first 100 vignetted/distorted rows + columns of the HST WFPC2 detector were not included in the final star list. The cluster centre value from Harris [1996] is marked as a red dot. The gaps in the spatial distribution are in the vicinity of highly saturated stars in the ACS WFC images. Which were rejected because of higher positional errors.

star. The average of the these estimates was taken as the final proper motion value for the star. The stellar proper motion scatter plot for M15 is shown in Figure 8.22(a). Pixel values were converted to mas/year for the 12 year baseline. The red circle corresponds to 0.8 mas/year. This is close to the value chosen by McNamara *et al.* [2003] and includes most of the cluster member stars (see Figure 8.22(a)). Corresponding proper motion histograms in the x and y pixel directions (in the 1994 reference frame) are shown in Figure 8.22(b).

Proper motion and its corresponding errors as a function of star magnitude are shown in Figure 8.23. As expected, proper motion accuracy (as well as positional accuracy) decreases with increasing star magnitude. The stellar magnitude is

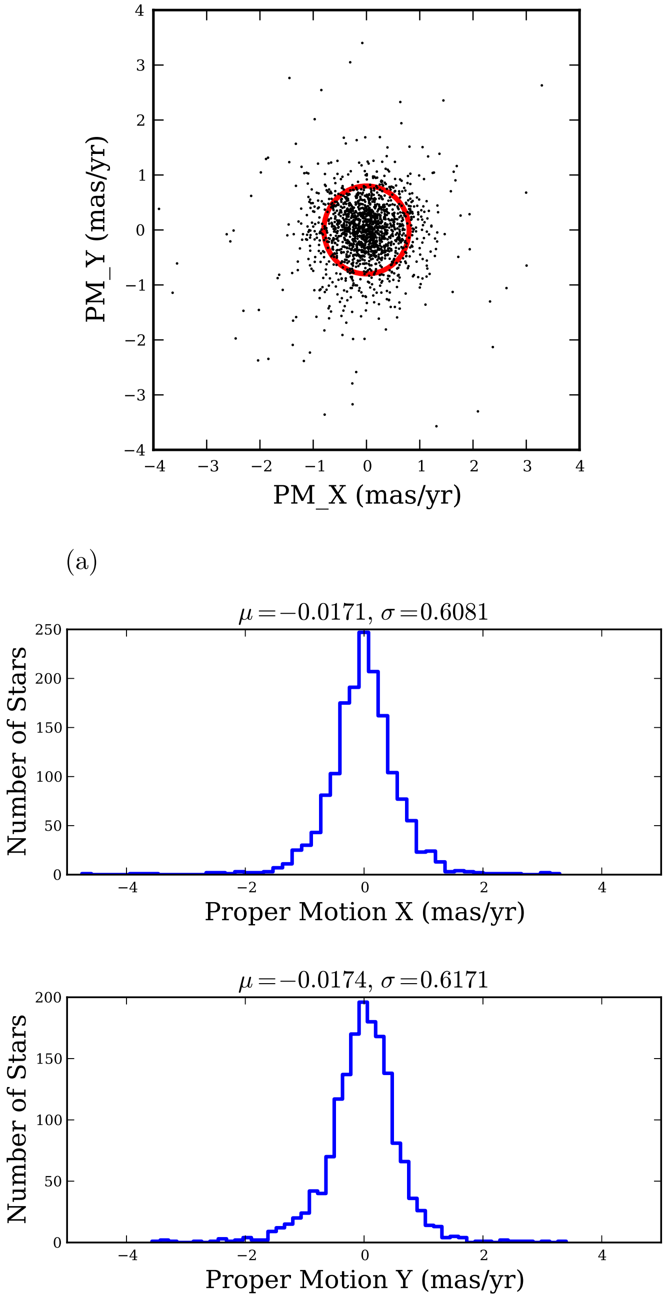

(a)

(b)

Figure 8.22: M15 proper motion scatter plot. (a) Stellar proper motion in mas/year in both the detector directions. The red circle corresponds to 0.8 mas/year, (b) Histograms of these proper motions in detector x and y direction.

in the ACS F606W instrumental magnitude (Vega mag) for the second epoch images.

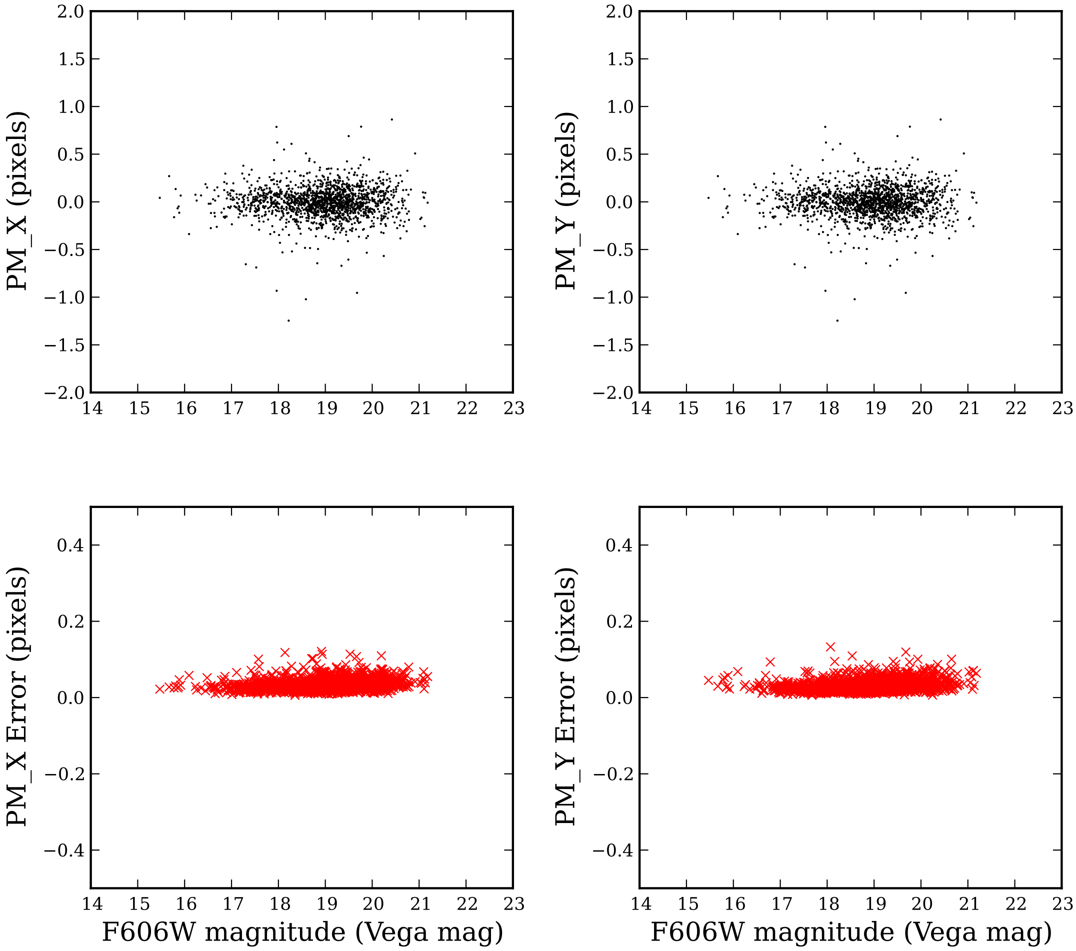

Figure 8.23: Proper motion, and proper motion error, as a function of star magnitude. As expected, proper motion accuracy decreases with increasing magnitude value.

The colour magnitude diagram of all the stars whose proper motion was determined is shown in Figure 8.24. It is plotted using the second epoch F606W magnitude and color (F606W - F814W) values. These values are in Vega mag.

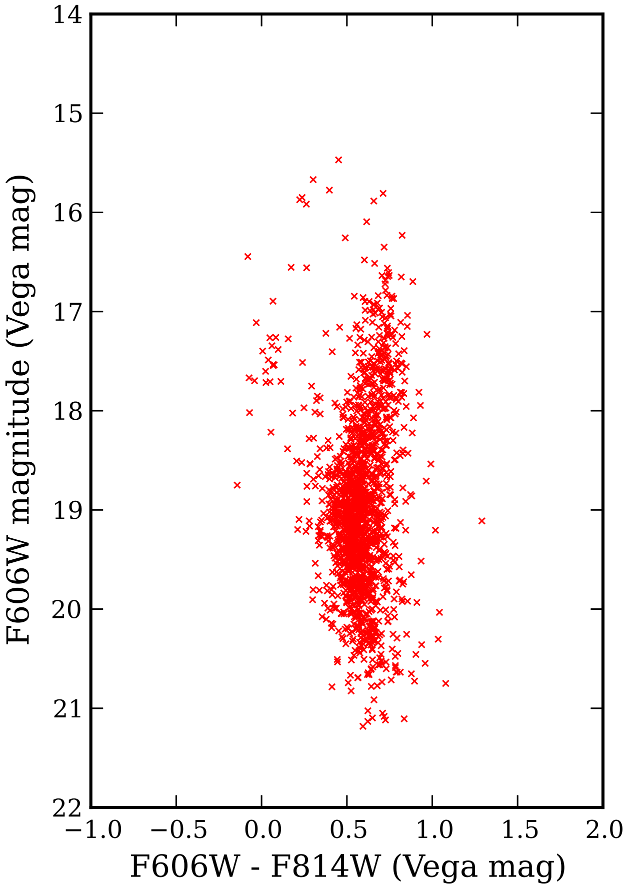

Figure 8.24: Colour magnitude diagram of 1994 stars in M15 whose proper motion was measured. The magnitude and colour are in HST ACS Vega mag and are from the second epoch images.

8.3.4 Internal Proper Motion Dispersion

The internal proper motion dispersion was calculated following the procedure described in Section 5.3.8. As internal velocity dispersion is sensitive to the quality of the proper motion measurements, we selected only the highest quality proper motion stars for this analysis. The first criterion for the selection was to include only the stars within the 0.8 mas/year envelope in the proper motion scatter diagram. Secondly, as the positional accuracy is poor for high magnitude stars, we selected stars between 15.0 and 19.0 F606W magnitude (Vega mag). This excluded any poorly measured stars. We did not remove any star based on its position in the color magnitude diagram. These two selection criteria reduced the starlist to 617 stars. Finally, any star deviating beyond 4 σ of the mean proper motion or proper motion error in each radial bin was also excluded from the analysis. This affected only a few stars. The final starlist used for internal proper motion dispersion had 598 stars. Histograms of these stars, with fitted Gaussian profiles are shown in Figure 8.25. Applying selection criteria result in only stars with low proper motion errors contributing to internal proper motion dispersion calculation. As shown in Section 7.2.2 on ACS WFC benchmarking, $\sim$ 98% of bright stars have absolute proper motion errors below 0.02 pixel.

The **R** statistical package was used for fitting Gaussian distributions to the proper motion histograms. The maximum likelihood fitting method *fitdistr* in the package MASS was used to fit both the mean value and dispersion. The cluster showed mean motion of 0.001 ± 0.0131 mas/year in the x direction and 0.027 ± 0.014 mas/year in the y direction. The uncorrected internal proper motion dispersion along the x and y direction was 0.319 ± 0.009 and 0.342 ± 0.010 mas/year respectively.

As mentioned before, a gradual rise in velocity dispersion towards the cluster centre could signify the presence of an intermediate mass black hole in the cluster core. To study the variation in proper motion dispersion, we created equally spaced radial bins from the cluster centre to $20''$ radius. To avoid small number statistics, the size of the bin was dictated by the number of stars in the inner most bin. Equally spaced $1.5''$ radial bins were found to be suitable. The radial variation of proper motion dispersion is also dependent on the exact cluster centre. We initially took the cluster centre value quoted in Harris [1996] as our estimate for the cluster centre. The proper motion dispersion values are listed in Table 8.9. The table is visualized in Figure 8.26, both in terms of mas/year and km/sec. The distance to M15 was taken as 10 kpc for converting the dispersion value units from pixel/year to km/sec.

The proper motion dispersion shows a gradual increase towards the cluster centre and flattening out after $5''$. As the radial profile is quite sensitive to the cluster centre, we also determined the velocity dispersion profile using the Noyola & Gebhardt [2006] cluster centre estimate (see Figure 8.27). The two centre are separated by 2 pixels in the x direction and 32 pixels in the y direction of the

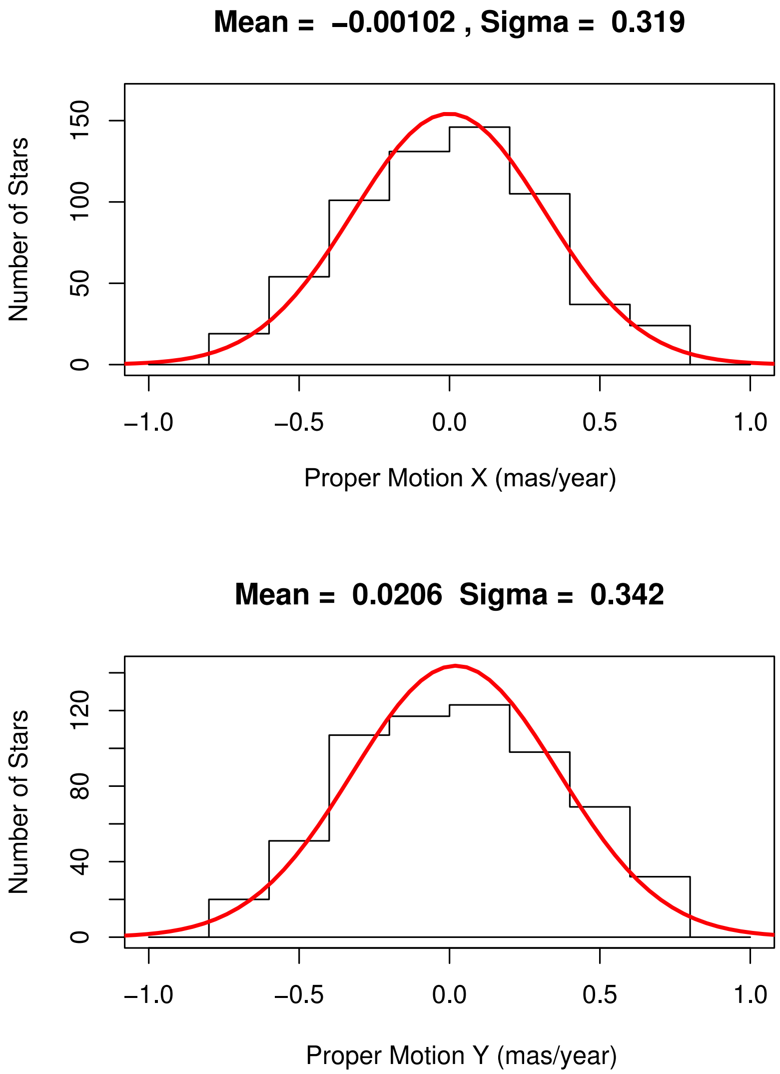

Figure 8.25: Proper motion histograms of M15 globular cluster stars with Gaussian profiles fitted to it.

PC chip. The two results were similar, but the more recent Noyola & Gebhardt [2006] centre lead to a somewhat smoother proper motion dispersion curve. The central dispersion values are $\sim 1.5\ \sigma$ above flatter dispersion profile above $5''$. This could be a bias and can be tested in simulation by focusing only on bright stars (with low random errors). Which in turn can reveal any systematic error or bias.

Identical results were also reached by McNamara *et al.* [2003], although they

Mean R (arsec)	N_{stars} (-)	σ_x (pixel)	ϵ_x (pixel)	σ_y (pixel)	ϵ_y (pixel)	σ_{avg} (pixel)	ϵ_{avg} (pixel)	σ_{avg} (mas/year)	ϵ_{avg} (mas/year)
0.97	8	0.105	0.026	0.114	0.028	0.109	0.019	0.416	0.072
2.16	31	0.094	0.012	0.088	0.011	0.091	0.008	0.347	0.030
3.63	35	0.089	0.011	0.079	0.009	0.083	0.007	0.316	0.027
5.27	41	0.081	0.009	0.105	0.012	0.090	0.007	0.343	0.027
6.75	56	0.068	0.006	0.090	0.008	0.076	0.005	0.290	0.019
8.25	69	0.072	0.006	0.083	0.007	0.077	0.005	0.293	0.019
9.77	68	0.075	0.006	0.093	0.008	0.081	0.005	0.309	0.019
11.29	55	0.084	0.008	0.085	0.008	0.085	0.006	0.324	0.023
12.73	58	0.074	0.007	0.072	0.007	0.073	0.005	0.278	0.019
14.25	63	0.080	0.007	0.086	0.008	0.083	0.005	0.316	0.019
15.75	58	0.081	0.008	0.086	0.008	0.084	0.006	0.320	0.023
17.10	44	0.065	0.007	0.068	0.007	0.067	0.005	0.255	0.019
18.70	12	0.076	0.016	0.085	0.017	0.080	0.012	0.305	0.046

Table 8.9: Internal proper motion dispersion of globular cluster M15. Mean R is the average radius of the stars in the bin. the mean value of the dispersion, σ_{avg}, is calculated by taking the weighted average of the dispersion in the x and y direction.

determined the proper motion dispersion within a 0.86 mas/yr proper motion envelope. They were able to fit the observed proper motion dispersion curve with an N-body modelling curve, having a population of neutron stars at the cluster centre. They did not rule out the presence of an intermediate mass black hole at the cluster centre but concluded that the central black hole mass has to be less than 500 $M_\odot$. Proper motion analysis yielding the internal velocity dispersion is an excellent tool to test the presence of a central black hole, but on its own it cannot confirm or reject the presence of an intermediate mass black hole. The velocity dispersion profile has to be used in conjunction with suitable *N-body* model to reach any definite conclusion.

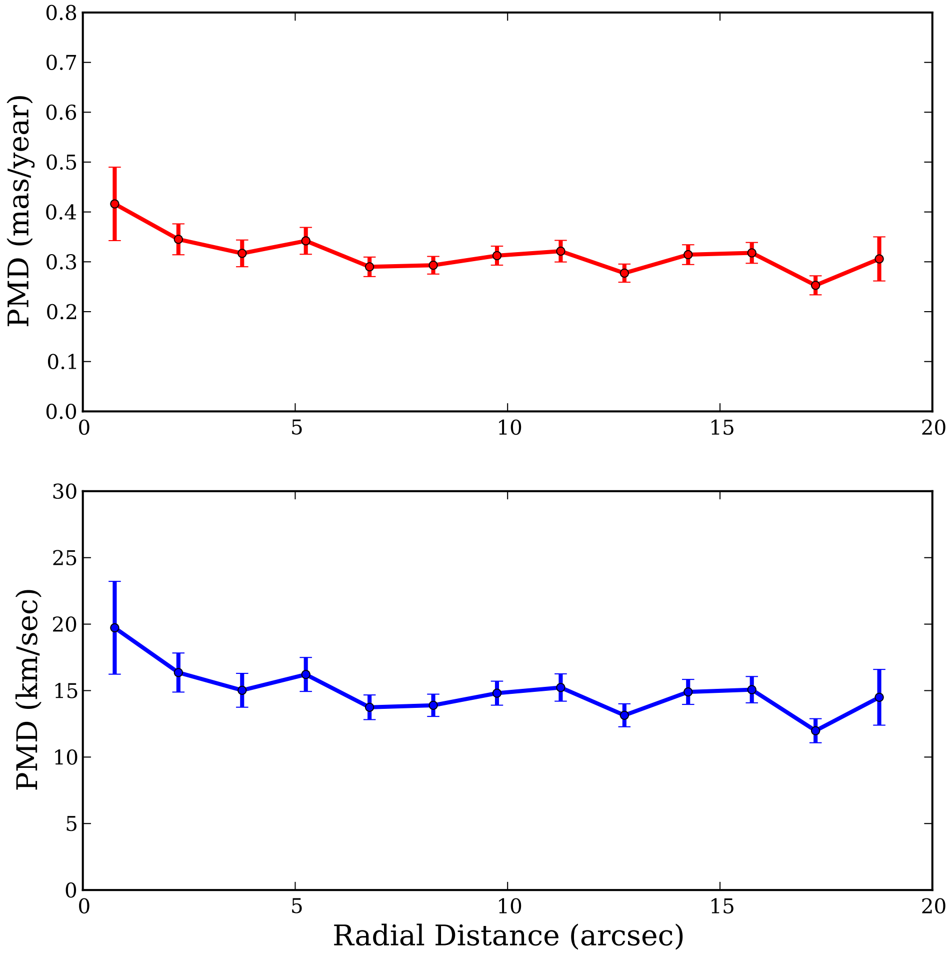

Figure 8.26: Internal proper motion dispersion of M15 as a function of radial distance from cluster centre. (a) in units of mas/ year, (b) in units of km/sec. The conversion from mas/year to km/sec is based on a 10 kpc distance and a 12 year baseline.

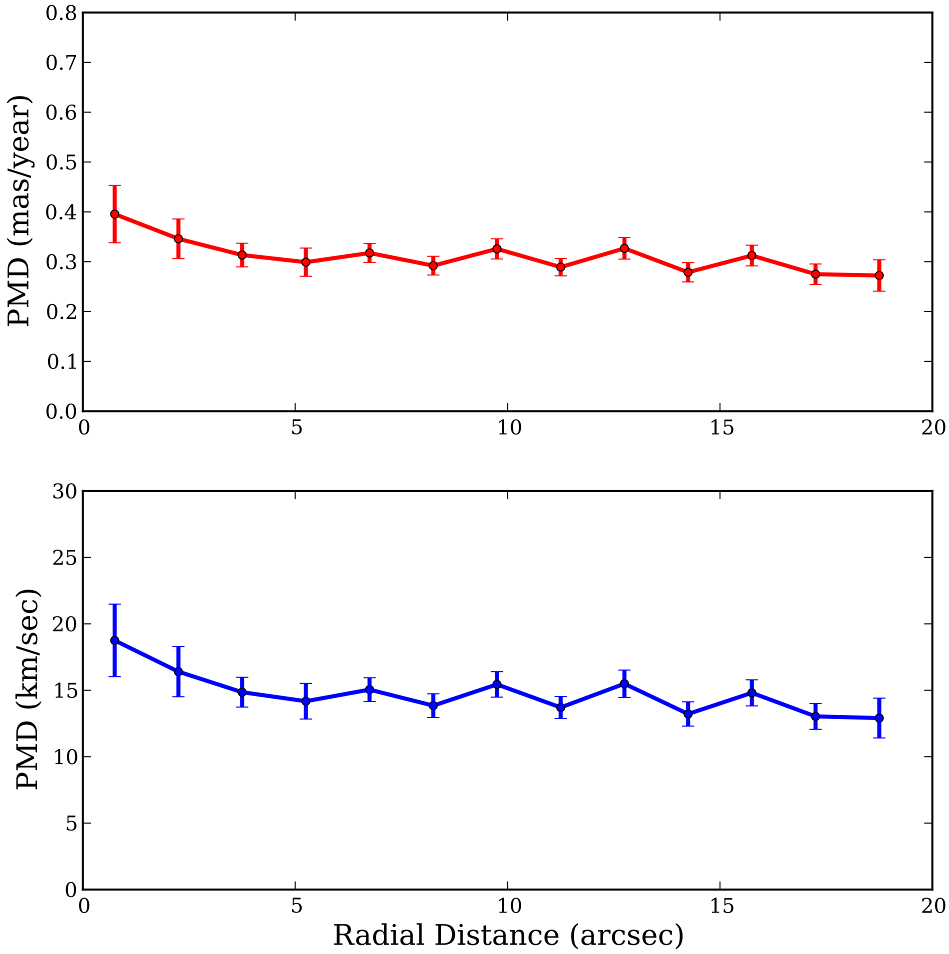

Figure 8.27: Internal proper motion dispersion of M15 using the Noyola & Gebhardt [2006] cluster centre estimate.

Chapter 9

Conclusions and Future Work

9.1 Conclusions

Here we summarise the results of the research under specific goal headings.

9.1.1 Cluster Simulation Pipeline and Data Processing Pipeline

An automated pipeline was developed to generate simulated multi-epoch globular cluster images. The pipeline uses accurate models for the surface brightness profile, theoretical isochrones, and detector point spread function (including its spatial variation) to generate simulated images. It is written in the *Python* programming language and uses PyRAF tasks.

To determine the stellar proper motion and internal proper motion dispersion, a semi-automated reduction pipeline was developed. The pipeline performs star detection on the combined sub-sampled deconvolved images, aperture and PSF-fitting photometry, star matching between two epochs, and proper motion determination. The highest quality proper motion stars, surviving range of various selection criteria, are then used to determine internal proper motion dispersion. The variation in velocity dispersion with the radial distance from the cluster centre is an indicator of the presence (or absence) of a central massive body or collection of massive bodies.

9.1.2 Sub-sampled Spatially-varying Deconvolution Technique

In the present study, we developed the sub-sampled deconvolution technique to resolve stars in the crowded globular cluster cores. It was applied to multi-epoch images from the Hubble Space Telescope WFPC2 and ACS WFC detectors. Our technique showed better star detection efficiency compared to the direct detection on the original science images. This is especially true for fainter stars in the crowded inner core of the globular cluster.

We benchmarked our sub-sampled deconvolution technique for the HST WFPC2 and ACS WFC detectors. The technique was benchmarked for astrometric and proper motion accuracy. For the WFPC2 detector, $\sim$92% of the matched stars had proper motion error < 0.2 pixel (9.2 mas). Whereas $\sim$98% of all matched stars had proper motion error < 0.1 pixel (5 mas) for the ACS WFC detector. These error values may be considered as the boundaries of the envelope; brighter stars have much lower errors than this. Because the true star positions are known exactly, these are absolute errors rather than uncertainty estimates.

9.1.3 Parallel Processing

Image deconvolution is an iterative process and an “embarrassingly” parallel problem. We parallelized the sub-sampled deconvolution to reduce the execution time drastically. The publically available code is written in the Python programming language and uses the PyRAF *mem* (Maximum Entropy Method) task. Two other requirements - World Coordinate transformations, and Monte Carlo completeness testing - were also parallelized. We used three different approaches to achieve parallelization on multicore machines. The Process/Queue approach performed better as a parallelizing scheme than both the Pool/Map and Parallel Python approaches. The cross-platform nature of Python makes the code portable on multiple computer platforms.

9.1.4 Measurement of Proper Motions and Determination of Internal Proper Motion Dispersion

The parallel sub-sampled deconvolution technique developed for precise astrometry was applied to determine the stellar proper motions and internal proper motion dispersion in three Galactic globular clusters. Relative proper motions were determined for stars in the globular cluster M71, using HST WFPC2 images separated by 6 years. We found the internal proper motion dispersion for M71 to be 0.311 ± 0.021 and 0.323 ± 0.022 mas/year along the x and y directions, in agreement with previous work. The central velocity dispersion profile is almost flat from $3''$ to $18''$ from the cluster centre. This could be interpreted as the absence of a central black hole in M71. Stellar proper motions were determined for the first time for stars in NGC 6293, using HST WFPC2 images on a 14 year baseline. We found the internal proper motion dispersion values to be 0.250 ± 0.004 and 0.243 ± 0.004 mas/year along the x and y directions, for the entire star sample. The proper motion dispersion profile with radial distance from $0.8''$ to $18''$ is flat and thus not giving an indication of a central intermediate mass black hole or collection of low mass black holes.

We used multi-epoch images from two different detectors over a 12 year baseline to determine the stellar proper motions in the core of globular cluster M15. We determined the proper motion dispersion value to be 0.319 ± 0.009 and 0.342 ± 0.010 mas/year along the x and y directions. The proper motion dispersion radial profile showed a gradual increase towards the cluster centre, as was observed by McNamara *et al.* [2003], who estimated an upper limit of 500 $M_\odot$ for any central intermediate mass black hole in M15.

9.2 Future Work

We have demonstrated that the techniques are successful and can, without further modification, be applied to a larger sample of globular clusters.

The present study developed the sub-sampled deconvolution technique to determine precise internal proper motions in HST images of globular star clusters.

Only the workhorse WFPC2 and ACS WFC instruments were considered. But the technique can also be extended to the latest Wide Field Camera 3 (WFC3) on the Hubble Space Telescope. Images from more than two epochs can be used to get a better estimate of the proper motion vectors and internal proper motion dispersion. Although challenging, we have shown by our WFPC2 and ACS work that multi epoch images from *different* HST instruments can be used in the search for black holes in globular clusters and the many other uses of proper motion information [Bellini *et al.*, 2013].

As the stellar proper motion inside a globular cluster is small, we need longer baselines to determine the precise internal proper motion dispersion. The next logical step could be to use images from both HST and ground based AO systems for this type of analysis. The 8-10 meter class telescopes in Hawaii (Keck I and II, Gemini North, Subaru) and Chile (VLT, Gemini south) can be used for this purpose. There may not be sufficient archival data for this but newer observations at the current epoch can be acquired. This is a challenging task for the following reasons -

1. Precise matching of the stars in the crowded central core of the globular clusters is always difficult between two epoch images
2. Modelling the first guess point spread function for the AO system. Although the PSF may not be undersampled for the current AO systems, it is both spatially and temporally varying with atmospheric seeing conditions. This is different to the situation with HST observations, where there is a temporally stable PSF that can be predictably modelled using TinyTIM. Even for *empirical* PSF extraction, the spatial variation of an AO PSF may be more than the quadratic DAOPHOT model can handle.
3. As with all analyses utilising 2 different instruments, residual geometric distortions could cause higher errors in proper motion and thus in internal velocity dispersion

Determining internal proper motion dispersion is by itself not conclusive evidence in the search for intermediate mass black holes. Velocity profiles generated by N-Body simulations - with and without a central black hole - have to be compared with the observational result. Even a gradual rising velocity dispersion profile in M15 does not necessarily translate to an intermediate mass black hole in the core [McNamara *et al.*, 2012]. N-Body modelling can also be used to constrain the mass of the central black hole.

The *simulated* globular star cluster image generation pipeline can be easily extended to include ground based telescope detectors, in addition to HST. In addition to proper motion studies, these images can be used to test photometric and/or astrometric accuracy of the image processing techniques. We are going to make the standalone pipeline publicly available for the astronomy community to use.

Last but not the least, stellar proper motions can be combined with the N-Body simulations and other multi-wavelength studies to get a better insight into the problem at hand. For example - a follow up proper motion study can be conducted to confirm the 2 low mass black hole candidates detected in M22 using the JVLA radio interferometer [Strader *et al.*, 2012a]. This will involve determining proper motions of a small sample of stars in a specific region of the globular star cluster.

Appendix A

All the steps in *Multidrizzle* run automatically one after another and can be switched on or off using input parameter flags. Please refer to the *Multidrizzle Handbook* for an in-depth treatment of drizzling and Multidrizzle task [Fruchter & Sosey, 2009]. A simplified flowchart of the *Multidrizzle* steps is shown in Figure A-1 and a brief description is given below.

Step 1: Static Mask. The first step in the processing involves creating a bad pixel mask for the succeeding steps. It uses the data quality (DQ) mask in the input image and also contains pixels with values below a set threshold. Users can also specify additional masks to be added to it.

Step 2: Sky Subtraction. Sky subtraction in *multidrizzle* is done iteratively by taking the median value as the sky value for the image and rejecting the deviating pixels above a certain threshold value. For multi-chip instruments such as the WFPC2 and ACS WFC, the lower of the detector sky values is taken. However, it has been recommended [Pavlovsky *et al.*, 2006] that sky background should not be subtracted from the images if they are to be used for crowded field photometry using DAOPHOT because it changes the Poisson component of error estimates. Therefore we have kept the sky background in the final drizzled ACS images.

Step 3: Drizzle Separate Images and Determine Shifts. In the first iteration, each of the input images is drizzled separately onto the output pixel grid. The type of drizzling kernel, pixfrac and the scale can be set for this step in multidrizzle. The distortion corrected intermediate single drizzled images are then used to determine accurate shifts between the input

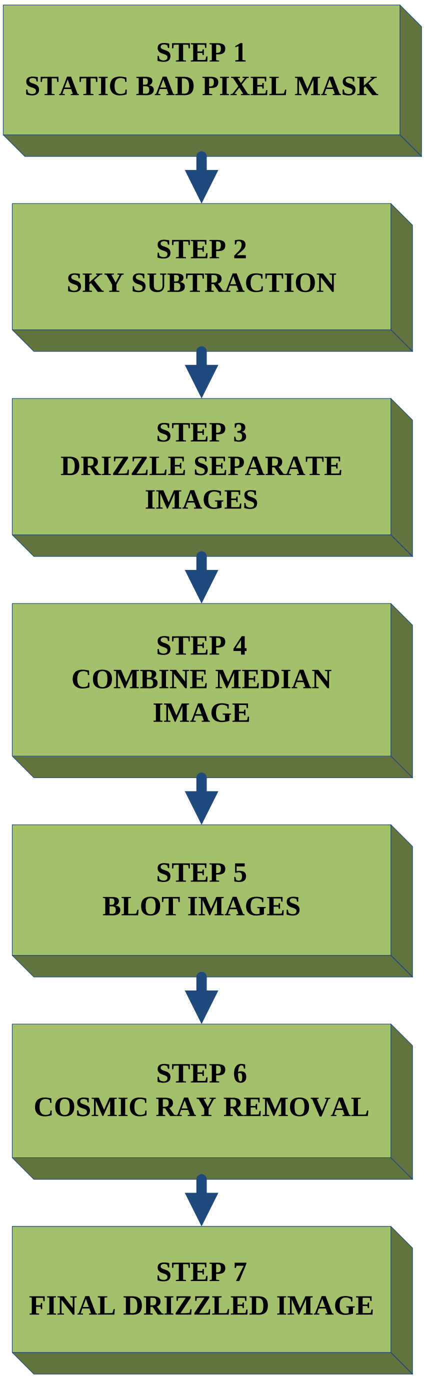

Figure A-1: A simplified flowchart of steps involved in the Multidrizzle task.

dithered frames. Multidrizzle uses the image header keywords to determine the shift between the images. These shifts may not be exact because of pointing jitter, guide star position and acquisition, telescope breathing etc. We used the *tweakshift* task interactively to determine the accurate shift. This involves selecting 3 common stars in the input frames, and then tweakshift uses object matching and cross-correlation methods to calculate the shifts. Both methods can be run one after another to validate the results. The residual shifts are written to an output *shifts* file, which can be given as input to the next iteration of the multidrizzle task.

Step 4: Combined Median Image. The distortion corrected intermediate drizzled images are combined with shift correction to create an intermediate median image. This combined image is the first estimation of the cosmic ray free image.

Step 5. Blot . The median combined image created above is then mapped back to the individual input images in the distorted reference frame (taking care of the shifts). This process is know as *blot*, which is basically the reverse of the drizzling process and involves interpolating the median image. The output blotted images should now have cosmic rays removed, at least to the first approximation.

Step 6: Remove Cosmic Rays. Input dithered images in conjunction with the blotted images are now used to create the final cosmic ray mask. Cosmic ray and the static pixel masks are used in the next step.

Step 7: Final Drizzled Image. Single drizzled images are combined into a final drizzled image with improved cosmicray/bad pixel rejection. The two main parameters governing this task are the *pixfrac* and the *scale*.

Appendix B

Code implementation of the three python multiprocessing approaches is discussed in detail below.

1. **The Pool/Map Approach**. Out of the two *multiprocessing* approaches, this is the simplest to implement. The *Pool/Map* approach spawns a pool of worker processes and returns a list of results. In Python functional programming, a function can be applied to every item iterable using the built-in *map* function. For example, instead of running an iterative loop, the *map* function can be used:

Listing 1: Example Python iterative function

```
# Iterative function
def worker( indata ):
  ...
  return result

# Input dataset divided into chunks
lst = [ in1, in2, ... ]

# Loop over lst items and append results
results = []
for item in lst:
```

```
    results.append( worker( item ) )
```

Listing 2: Python map function

```
# Iterative function
def worker( indata ):
  ...
  return result

# Input dataset divided into chunks
lst = [ in1, in2, ... ]

# Iteratively run func in serial mode
results = map( worker, lst )
```

The *map* function is extended to the *multiprocessing* module and can be used with the *Pool* class to execute worker processes in parallel, as depicted in Listing 3.

Listing 3: Pool/Map multiprocessing implementation

```
# Import multiprocessing module
import multiprocessing as mp

# Get number of processors on the machine
# or manually enter required number of processes
```

```
ncpus = mp.count_cpus()

# Define pool of ncpus worker processes
pool = mp.Pool( ncpus )

# Start ncpus pool of worker processes in parallel
# output is appended to results python list
results = pool.map( worker, lst )
```

The *import* command includes the *multiprocessing* module in the routine, the *count_cpus* method gets the number of processors or cores on the machine, the *Pool* class creates a pool of *ncpus* processes, and *Pool's map* method iterates over the input element list in parallel, and maps each element to the *worker* function. The number of worker processes spawned can be more than the number of cores on the machine but as we will see in Section 6.4, best performance is achieved when the number of processes is equal to the number of physical processor cores or the total number of concurrent threads.

2. **The Process/Queue Approach**. The Pool/Map approach allows only one argument as an input parameter to the calling function. There are two ways to send multiple arguments: pack arguments in a python list or a tuple, or use the *process* class in conjunction with a *queue* or *pipe*. Although a process can be used without queues and pipes, it is good programming practice to use them[1]. Two FIFO (First In, First Out) queues are created - one for sending input data elements and another for receiving output data. Parallel worker processes are started using the *Process* class and smaller chunks of input data are put on the send queue for processing. Each worker process picks the next data chunk in the queue after processing the previous

---

[1] Python documentation suggests to avoid synchronisation locks and instead use the queue or the pipe (http://docs.python.org/library/multiprocessing.html#programming-guidelines/)

chunk. The output result is put on the receive queue, and then read at the end for post-processing.

An example Python code listing for the Process/Queue approach is shown below:

Listing 4: Process/Queue multiprocessing implementation

```
# Import multiprocessing module
import multiprocessing as mp

# Worker function
# iter is standard python built-in function
def worker( s_q, r_q, arg1, arg2, ... ):
  for value in iter( s_q.get, ‘STOP‘ ):
    ...
    r_q.put( result )

# Get number of cores on the machine
ncpus = mp.count_cpus()

# Create send and receive queues
send_q = mp.Queue()
recv_q = mp.Queue()

# Start ncpus number of processes
for i in range( ncpus ):
  mp.Process( target = worker, args = ( send_q, recv_q, arg1, arg2,
... ) )

# Put input data chunks on send queue
```

```
# indata is python list of input data set,
# which is already divided into smaller chunks
for chunk in indata:
  send_q.put( chunk )

# Get output from receive queue
results = []
for i in range( len( indata ) ):
  results.append( recv_q.get() )

# Stop all the running processes
for i in  range( ncpus ):
  send_q.put( ‘STOP‘ )
```

The code is self-explanatory but the main point to notice is the code related to stopping the running processes. *STOP* or any other value can be put in the send queue to stop the processes, as the worker function reads from the queue until it encounters *STOP*. We have found that in certain conditions, the Process/Queue approach performs better than the Pool/Map approach, as shown in Section 6.4.

3. **Parallel Python Approach**. Parallel Python is an open source cross-platform module for parallelising python code. It provides dynamic computation resource allocation as well as dynamic load balancing at runtime. In addition to executing programs in parallel on Symmetric multiprocessing (SMP) machines, it can also be used on clusters of heterogeneous multi-platform machines [Vanovschi, 2013].

   Processes in Parallel Python run under a job server. The job server is started locally (or remotely if running on a cluster of machines) with the desired number of processes (ideally equal to the number of processor cores). A very basic code template is shown below:

Listing 5: Parallel Python implementation

```
# Import Parallel Python module
import pp

# Parallel Python worker function
def worker( indata ):
  ...
  return result

# Create an empty tuple
ppservers = ()

# Either manually set the number of processes or
# default to the number of cores on the machine
if ncpus:
  job_server = pp.Server( int(ncpus), ppservers = ppservers )
else:
  job_server = pp.Server( ppservers = ppservers )

# Divide data into smaller chunks for better
# performance (based on the scheduler type)
chunks = getchunks( infile, job_server.get_ncpus(), scheduler )

# Start the worker processes in parallel
jobs = []
for value in chunks:
  indata = ( arg1, arg2, ...  )
  jobs.append( job_server.submit( worker, (indata,), (func1,func2
```

```
,...), (mod1,mod2,...) ) )


# Append the results
results = []
for job in jobs:
  results.append( job())
```

The number of processes (*ncpus*) is passed to the program as user input, or defaulted to the number of cores on the machine. The input data is divided into smaller chunks for better load balancing. The *Parallel Python* job server starts the worker processes for parallel execution. At the end of the execution, results are retrieved from the processes. The parameters to the job server's submit method are the worker function, its arguments, and any other function or module used by the worker function.

Appendix C

An example ‘R’ code to fit and plot Gaussian distribution to proper motion histograms.

```
# Weighted Non-Linear Least Square Fitting of Gaussian data
# @author: Navtej, Date: 15 Feb 2013
#
#   Analysis based on ’Fitting Distributions with R’ by Vitol Ricci
#

# >>>> Enter the name of the datafile - it should have two columns <<<<
#               PM_X PM_Y
#
#=========================================================================

# Read the input proper motion file
pmtab = ’data/output/results/N6293_pm_mas.txt’


# Load the Libraries
library(nlstools)
library(fBasics)
library(robustbase)
```

```
# Load the proper motion data in R dataframe
pm <- read.table( pmtab, header = F )

total_counts = length( pm$V1 )

# Proper motion data in x and y directions
pm_x <- pm$V1
pm_x_err <- pm$V2
pm_y <- pm$V3
pm_y_err <- pm$V4


# Summarize basic descriptive statistics
summary( pm_x )
summary( pm_y )


# Visualize data using histograms
postscript(paste(pmtab, ".pm_x.hist.eps",sep=""), width=300, height=300)
hist( pm_x, breaks = ’sturges’, main = ’Histogram of NGC 6293 Proper
Motion (X)’, prob = TRUE )
dev.off()

postscript(paste(pmtab, ".pm_y.hist.eps",sep=""), width=300, height=300)
hist( pm_y, breaks = ’sturges’, main = ’Histogram of NGC 6293 Proper
Motion (Y)’, prob = TRUE )
dev.off()
```

```
# Plot frequency density of the proper motion
plot( density(pm_x), main = ’Density estmate of proper motion x’ )

plot( density(pm_y), main = ’Density estmate of proper motion y’ )



# Plot empirical cummulative distribution function (ecdf)
plot( ecdf(pm_x), main = ’Empirical cumulative distribution function’ )

plot( ecdf(pm_y), main = ’Empirical cumulative distribution function’ )

# Determine skewness and kurtosis of the proper motion
skewness( pm_x )
kurtosis( pm_x )

skewness( pm_y )
kurtosis( pm_y )



# Comparing fitted and observed values (Assuming gaussian profile fit)
# abline plots 45 degree reference line
pm_x.norm <- (pm_x - mean(pm_x)) / sd(pm_x)

postscript(paste(pmtab, ".pm_x.qqplot.eps",sep=""), width=300, height=300)
qqnorm( pm_x.norm )
abline( 0, 1, lwd = 2.5 )
dev.off()

pm_y.norm <- (pm_y - mean(pm_y)) / sd(pm_y)
```

```
postscript(paste(pmtab, ".pm_y.qqplot.eps",sep=""), width=300, height=300)
qqnorm( pm_y.norm )
abline( 0, 1, lwd = 2.5 )
dev.off()



# Estimate mean and sigma for the normal distibution along with
# standard errors. Use these estimates for goodness of fit.
pm_x_est = fitdistr( pm_x, 'normal' )
pm_x_mean <- pm_x_est$estimate[1]
pm_x_mean_sd <-  pm_x_est$sd[1]
pm_x_sigma <- pm_x_est$estimate[2]
pm_x_sigma_sd <- pm_x_est$sd[2]

pm_y_est = fitdistr( pm_y, 'normal' )
pm_y_mean <- pm_y_est$estimate[1]
pm_y_mean_sd <- pm_y_est$sd[1]
pm_y_sigma <- pm_y_est$estimate[2]
pm_y_sigma_sd <- pm_y_est$sd[2]

print( paste( 'PM X mean = ', format(pm_x_mean,digits=3), '+/-', format(pm
_x_mean_sd,digits=3)))
print( paste( 'PM X sigma = ', format(pm_x_sigma,digits=3), '+/-', format(
pm_x_sigma_sd,digits=3)))

print( paste( 'PM Y mean = ', format(pm_y_mean,digits=3), '+/-', format(pm
_y_mean_sd,digits=3)))
print( paste( 'PM Y sigma = ', format(pm_y_sigma,digits=3), '+/-', format(
pm_y_sigma_sd,digits=3)))
```

```
## True dispersion value
print( paste( ’PM X dispersion =’, format(pm_x_sigma - sum(pm_x_err**2)/
length(pm_x),digits=3) ) )
print( paste( ’PM Y dispersion =’, format(pm_y_sigma - sum(pm_y_err**2)/
length(pm_x),digits=3) ) )


# Estimate dispersion using Qn parameter rather than standard dispersion
#
Qn( pm_x, finite.corr = T )
Qn( pm_y, finite.corr = T )


# Goodness of fit. Use graphical method to display the proper motion
# histogram and overlay fitted gaussian PDF
h <- hist( pm_x, breaks = ’sturges’, plot = FALSE )
bin_size = h$breaks[2] - h$breaks[1]
xhist <- c( min(h$breaks), h$breaks )
yhist <- c(0, h$density  * bin_size * total_counts, 0 )
xfit <- seq(-1, 1, length = 80 )
yfit <- dnorm( xfit, mean = pm_x_mean, sd = pm_x_sigma )

postscript(paste(pmtab, ".pm.fit.eps",sep=""), width=5.5, height=7.5,
horizontal = FALSE )
layout(matrix(c(1,2), 2, 1, byrow = TRUE))

plot( xhist, yhist, type = "s", xlim = c(-1, 1), ylim = c(0, max(yhist,
yfit)+10), main = paste( ’Mean = ’,    format(pm_x_mean,digits = 3), ’,
Sigma = ’, format(pm_x_sigma,digits = 3) ), xlab = ’’, ylab = ’Number’,
pch = 4, col =’black’ )
```

```
lines( xfit, yfit * bin_size * total_counts, col = ’red’, lwd = 2.5 )
lines( seq(-1,1,length=40), seq(0,0,length=40))

h <- hist( pm_y, breaks = ’sturges’, plot = FALSE )
bin_size = h$breaks[2] - h$breaks[1]
xhist <- c( min(h$breaks), h$breaks )
yhist <- c(0, h$density * bin_size * total_counts, 0 )
xfit <- seq(-1, 1, length = 80 )
yfit <- dnorm( xfit, mean = pm_y_mean, sd = pm_y_sigma )

plot( xhist, yhist, type = "s", xlim = c(-1, 1), ylim = c(0, max(yhist,
yfit)+10), main = paste( ’Mean = ’, format(pm_y_mean,digits=3), ’ Sigma =
’, format(pm_y_sigma,digits = 3) ), xlab = ’Proper Motion (mas/year)’,
ylab = ’Number’, pch = 4, col =’black’ )
lines( xfit, yfit * bin_size * total_counts, col = ’red’, lwd = 2.5 )
lines( seq(-1,1,length=40), seq(0,0,length=40))
dev.off()
```

References

Aarseth, S. (1999). From NBODY1 to NBODY6: The Growth of an Industry. *The Publications of the Astronomical Society of the Pacific*, **111**, 1333–1346. 26, 27

Aarseth, S. (2003). *Gravitational N-Body Simulations*. Cambridge University Press, illustrated edn. 27

Amdahl, G.M. (1967). Validity of the Single-Processor Approach to Achieving Large-Scale Computing Capabilities. 532–533, AFIPS Press. 98

Anderson, J. & King, I.R. (1999). Astrometric and Photometric Corrections for the 34th Row Error in HST's WFPC2 Camera. *The Publications of the Astronomical Society of the Pacific*, **111**, 1095–1098. 58

Anderson, J. & King, I.R. (2000). Toward High-Precision Astrometry with WFPC2. I. Deriving an Accurate Point-Spread Function. *Publications of the Astronomical Society of the Pacific*, **112**, 1360–1382. 87, 164

Anderson, J. & King, I.R. (2003). An Improved Distortion Solution for the Hubble Space Telescope's WFPC2. *The Publications of the Astronomical Society of the Pacific*, **115**, 113–131. 57, 58

Anderson, J. & King, I.R. (2004). Multi-filter PSFs and distortion corrections for the HRC. Instrument Science Report ACS 2004-15, STScI. 66

Anderson, J. & van der Marel, R.P. (2010). New Limits on an Intermediate-Mass Black Hole in Omega Centauri. I. Hubble Space Telescope

Photometry and Proper Motions. *The Astrophysical Journal*, **710**, 1032–1062. 40

Anderson, J., Bedin, L.R., Piotto, G., Yadav, R.S. & Bellini, A. (2006). Ground-based CCD astrometry with wide field imagers. *Astronomy & Astrophysics*, **454**, 1029–1045. 92, 93, 166, 169, 180

Archinal, B.A. & Hynes, S.J. (2003). *Star Clusters*. Willmann-Bell, Inc. 5

Ashman, K.M. & Zepf, S.E. (1998). *Globular Cluster Systems*. Cambridge University Press, illustrated edn. 5

Bahcall, J.N. & Wolf, R.A. (1976). Star distribution around a massive black hole in a globular cluster. *The Astrophysical Journal*, **209**, 214–232. 34

Baumgardt, H., Hut, P., Makino, J., McMillan, S.L. & Zwart, S.F.P. (2003a). On the Central Structure of M15. *The Astrophysical Journal*, **582**, L21–L24. 38

Baumgardt, H., Makino, J., Hut, P., McMillan, S.L.W. & Zwart, S.F.P. (2003b). A Dynamical Model for the Globular Cluster G1. *The Astrophysical Journal*, **589**, L25–L28. 38

Baumgardt, H., Makino, J. & Hut, P. (2005). Which Globular Clusters Contain Intermediate-Mass Black Holes? *The Astrophysical Journal*, **620**, 238–243. 30, 33, 34, 40, 148

Beazley, D.M. (2006). *Python Essential Reference*. Sam Publishing, 3rd edn. 99

Bedin, L.R., Anderson, J., King, I.R. & Piotto, G. (2001). Color-magnitude diagram and luminosity function of m4 near the hydrogen-burning limit. *The Astrophysical Journal*, **560**, L75–L78. 87

Bedin, L.R., Piotto, G., Anderson, J., Cassisi, S., King, I.R., Momany, Y. & Carraro, G. (2004). ω Centauri: The Population Puzzle Goes Deeper. *The Astrophysical Journal*, **605**, L125–L128. 1

Belleman, R.G., Bedorf, J. & Portegies Zwart, S.F. (2008). High performance direct gravitational N-body simulations on graphics processing units II: An implementation in CUDA. *New Astronomy*, **13**, 103–112. 96

Bellini, A., van der Marel, R.P. & Anderson, J. (2013). HST proper motions of stars within globular clusters. *ArXiv e-prints*, **1301**, 2338. 194

Bennett, C.L., Larson, D., Weiland, J.L., Jarosik, N., Hinshaw, G., Odegard, N., Smith, K.M., Hill, R.S., Gold, B., Halpern, M., Komatsu, E., Nolta, M.R., Page, L., Spergel, D.N., Wollack, E., Dunkley, J., Kogut, A., Limon, M., Meyer, S.S., Tucker, G.S. & Wright, E.L. (2012). Nine-Year Wilkinson Microwave Anisotropy Probe (WMAP) Observations: Final Maps and Results. *ArXiv e-prints*, **1212**, 5225. 11

Bertin, E. & Arnouts, S. (1996). SExtractor: software for source extraction. *Astronomy & Astrophysics Supplement*, **317**, 393–404. 86

Bessell, M.S. (2005). Standard Photometric Systems. *Annual Review of Astronomy and Astrophysics*, **43**, 293–336. 54

Binney, J. & Merrifield, M. (1998). *Galactic Astronomy*. Princeton University Press. 7, 11, 12, 91

Bonnarel, F., Fernique, P., Bienaymé, O., Egret, D., Genova, F., Louys, M., Ochsenbein, F., Wenger, M. & Bartlett, J.G. (2000). The ALADIN interactive sky atlas. a reference tool for identification of astronomical sources. *Astronomy and Astrophysics Supplement Series*, **143**, 33–40. 151

Bradt, H. (2008). *Astrophysics Processes: The Physics of Astronomical Phenomena*. Cambridge University Press. 35

Bromer, R., Hantho, F. & Vinter, B. (2011). pupyMPI - MPI implemented in pure python. EuroMPI'11, 130–139, Springer-Verlag, Berlin, Heidelberg. 100

Butler, R. (2000). Deconvolution as a tool for improved crowded-field photometry with HST. vol. 216, 595–598, Astronomical Society of the Pacific. 70, 74, 75, 107, 116

CALDWELL, N., HARDING, P., MORRISON, H., ROSE, J.A., SCHIAVON, R. & KRIESSLER, J. (2009). Star Clusters in M31. I. A Catalog and a Study of the Young Clusters. *The Astronomical Journal*, **137**, 94–110. 17

CARR, B.J. & HAWKING, S.W. (1974). Black holes in the early Universe. *Monthly Notices of the Royal Astronomical Society*, **168**, 399–416. 30

CHANDRA, R., DAGUM, L., KOHR, D., MAYDAN, D., MCDONALD, J. & MENON, R. (2001). *Parallel Programming in OpenMP*. Morgan Kaufmann Publishers. 109

COLES, J. (2008). A New Estimate of the Hubble Time with Improved Modeling of Gravitational Lenses. *The Astrophysical Journal*, **679**, 17–24. 14

COTE, P. (1999). Kinematics of the Galactic Globular Cluster System: New Radial Velocities for Clusters in the Direction of the Inner Galaxy. *The Astronomical Journal*, **118**, 406. 5

CSEH, D., KAARET, P., CORBEL, S., KORDING, E., CORIAT, M., TZIOUMIS, A. & LANZONI, B. (2010). Radio observations of NGC 6388: an upper limit on the mass of its central black hole. *Monthly Notices of the Royal Astronomical Society*, **406**, 1049–1054. 39

CUDWORTH, K.M. (1985). Photometry, proper motion, and membership in the globular cluster m71. *The Astronomical Journal*, **90**, 65–73. 149, 161

DALCIN, L., RODRIGO, P., STORTI, M. & D'ELIA, J. (2008). MPI for python: Performance improvements and MPI-2 extensions. *Journal of Parallel and Distributed Computing*, **68**, 655–662. 100

D'ERCOLE, A., VESPERINI, E., D'ANTONA, F., MCMILLAN, S.L. & RECCHI, S. (2008). Formation and dynamical evolution of multiple stellar generations in globular clusters. *Monthly Notices of the Royal Astronomical Society*, **391**, 825–843. 1

DOLPHIN, A.E. (2009). A revised characterization of the WFPC2 CTE loss. *Publications of the Astronomical Society of the Pacific*, **121**, 655–667. 56, 88, 160

Drukier, G.A. & Bailyn, C.D. (2003). Can High-Velocity Stars Reveal Black Holes in Globular Clusters? *The Astrophysical Journal*, **597**, L125–L128. 39

Elson, R.A.W. (1999). Stellar Dynamics in Globular Clusters. In *Globular Clusters: X Canary Islands Winter School of Astrophysics*, 209–250, Cambridge University Press. 16

Fabbiano, G. (2005). The Hunt for Intermediate-Mass Black Holes. *Science*, **307**, 533–534. 30, 36

Farrell, S.A., Webb, N.A., Barret, D., Godet, O. & Rodrigues, J.M. (2009). An intermediate-mass black hole of over 500 solar masses in the galaxy ESO 243-49. *Nature*, **460**, 73–75. 30, 37

Ferrarese, L. & Merritt, D. (2000). A Fundamental Relation between Supermassive Black Holes and Their Host Galaxies. *The Astrophysical Journal*, **539**, L9–L12. 31

Foundation, P.S. (2012). *Python/C API Reference Manual*. Python Software Foundation. 99

Freedman, W.L., Madore, B.F., Gibson, B.K., Ferrarese, L., Kelson, D.D., Sakai, S., Mould, J.R., Kennicutt, R.C., Ford, H.C., Graham, J.A., Huchra, J.P., Hughes, S.M.G., Illingworth, G.D., Macri, L.M. & Stetson, P.B. (2001). Final Results from the Hubble Space Telescope Key Project to Measure the Hubble Constant. *The Astrophysical Journal*, **553**, 47–72. 14

Fruchter, A. & Hook, R. (1997). A novel image reconstruction method applied to deep Hubble Space Telescope Images. vol. 3164. 80, 82

Fruchter, A. & Sosey, M. (2009). The MultiDrizzle handbook. 79, 80, 81, 82, 196

Garver, S.L. & Crepps, B. (2009). The new era of tera-scale computing. http://software.intel.com/en-us/articles/the-new-era-of-tera-scale-computing/. 95

GEBHARDT, C., BENDER, R., BOWER, G., DRESSLER, A., FABER, S.M., FILIPPENKO, A.V., GREEN, R., GRILLMAIR, C., HO, L.C., KORMENDY, J., LAUER, T.R., MAGORRIAN, J., PINKNEY, J., RICHSTONE, D. & TREMAINE, S. (2000). A Relationship between Nuclear Black Hole Mass and Galaxy Velocity Dispersion. *The Astrophysical Journal*, **539**, L13–L16. 31

GEBHARDT, C., ADAMS, J., RICHSTONE, D., LAUER, T.R., FABER, S.M., GULTEKIN, K., MURPHY, J. & TREMAINE, S. (2011). The Black Hole Mass in M87 from Gemini/NIFS Adaptive Optics Observations. *The Astrophysical Journal*, **729**, 1–13. 30

GEBHARDT, K., RICH, R.M. & HO, L.C. (2002). A 20,000 Msolar Black Hole in the Stellar Cluster G1. *The Astrophysical Journal*, **578**, L41–L45. 2, 31

GEBHARDT, K., RICH, R.M. & HO, L.C. (2005). An Intermediate-Mass Black Hole in the Globular Cluster G1: Improved Significance from Keck and Hubble Space Telescope Observations. *The Astrophysical Journal*, **634**, 1093–1102. 30, 37

GERSSEN, J., VAN DER MAREL, R.P., GEBHARDT, K., GUHATHAKURTA, P., PETERSON, R.C. & PRYOR, C. (2002). Hubble Space Telescope Evidence for an Intermediate-Mass Black Hole in the Globular Cluster M15. II. Kinematic Analysis and Dynamical Modeling. *The Astronomical Journal*, **124**, 3270–3288. 30, 37, 87

GHEZ, A.M., KLEIN, B.L., MORRIS, M. & BECKLIN, E.E. (1998). High Proper-Motion Stars in the Vicinity of Sagittarius A*: Evidence for a Supermassive Black Hole at the Center of Our Galaxy. *The Astrophysical Journal*, **509**, 678–686. 30

GILMOZZI, R., KINNEY, E.K., EWALD, S.P., PANAGIA, N. & ROMANIELLO, M. (1994). WFPC2 observations of the double cluster NGC 1850 in the Large Magellanic Cloud. *Astrophysical Journal, Part 2 - Letters*, **435**, L43–L46. 17

GIRARDI, L., WILLIAMS, B.F., GILBERT, K.M., ROSENFIELD, P., DALCANTON, J.J., MARIGO, P., BOYER, M.L., DOLPHIN, A.E., WEISZ, D.R., Melbourne, J., Olsen, K.A.G., Seth, A.C. & Skillman, E. (2010). The ACS Nearby Galaxy Survey Treasury. IX. Constraining Asymptotic Giant Branch Evolution with Old Metal-poor Galaxies. *The Astrophysical Journal*, **724**, 1030–1043. 117

Gnedin, O.Y., Zhao, H., Pringle, J.E., Fall, S.M., Livio, M. & Meylan, G. (2002). The Unique History of the Globular Cluster ω Centauri. *The Astrophysical Journal Letters*, **568**, L23–L26. 155

Goldbury, R., Richer, H.B., Anderson, J., Dotter, A., Sarajedini, A. & Woodley, K.A. (2010). The ACS Survey of Galactic Globular Clusters. X. New Determinations of Centers for 65 Clusters. *The Astronomical Journal*, **140**, 1830–1837. 149, 155, 160

Gonzaga, S. (2002). WFPC2 data analysis: A tutorial. 77

Gonzaga, S. & Birreta, J. (2010). HST WFPC2 Data Handbook, v. 5.0. 55, 56, 58

Goodwin, S.P. (1997). The initial conditions of young globular clusters in the Large Magellanic Cloud. *Monthly Notices of the Royal Astronomical Society*, **286**, 669–680. 17

Goodwin, S.P. & Bastian, N. (2006). Gas expulsion and the destruction of massive young clusters. *Monthly Notices of the Royal Astronomical Society*, **373**, 752–758. 17

Goudfrooij, P., Puzia, T.H., Kozhurina-Platais, V. & Chandar, R. (2011). Population Parameters of Intermediate-age Star Clusters in the Large Magellanic Cloud. II. New Insights from Extended Main-sequence Turnoffs in Seven Star Clusters. *The Astrophysical Journal*, **737**. 17

Gove, D. (2010). *Multicore Application Programming : For Windows, Linux, and Oracle Solaris*. Addison-Wesley Professional, illustrated edn. 98

Gultekin, K., Miller, M.C. & Hamilton, D.P. (2004). Growth of Intermediate-Mass Black Holes in Globular Clusters. *The Astrophysical Journal*, **616**, 221–230. 30

HACK, W. & COX, C. (2000). Geometric distortion table: IDCTAB. Instrument Science Report ACS 2000-11, STScI. 65, 66

HARRIS, W.E. (1996). A Catalog of Parameters for Globular Clusters in the Milky Way. *The Astronomical Journal*, **112**, 1487–1488. 4, 5, 6, 13, 117, 119, 121, 131, 149, 162, 173, 174, 176, 182, 186

HARRIS, W.E. (2001). Globular Cluster Systems. In *Star Clusters*, Springer, Berlin. 5

HAWKING, S.W. (1974). Black Hole explosions? *Nature*, **248**, 30–31. 30

HEGGIE, D.C. & HUT, P. (2003). *The Gravitational Million-Body Problem*. Cambridge University Press, illustrated edn. 19, 22, 23, 24, 25, 26, 123

HILS, D. & BENDER, P.L. (1995). Gradual approach to coalescence for compact stars orbiting massive black holes. *Astrophysical Journal Letters*, **445**, L7–L10. 38

HOLLEY-BOCKELMANN, K., GULTEKIN, K., SHOEMAKER, D. & YUNES, N. (2008). Gravitational Wave Recoil and the Retention of Intermediate-Mass Black Holes. *The Astrophysical Journal*, **686**, 829–837. 31

HOLTZMAN, J.A., BURROWS, C.J., CASERTANO, S., HESTER, J., TRAUGER, J.T., WATSON, A.M. & WORTHEY, G. (1995). The photometric performance and calibration of WFPC2. *Publications of the Astronomical Society of the Pacific*, **107**, 1065–1093. 57, 88, 117

HOWELL, S.B. (2006). *Handbook of CCD Astronomy*. Cambridge University Press, 2nd edn. 43, 44, 48

HURLEY, J.R. (2007). Ratios of star cluster core and half-mass radii: a cautionary note on intermediate-mass black holes in star clusters. *Monthly Notices of the Royal Astronomical Society*, **379**, 93–99. 34

HUT, P. (2003). The Starlab Environment for Dense Stellar Systems. In *Astrophysical Supercomputing using Particle Simulations*, vol. 208 of *IAU Symposium*, 331. 27

Irwin, J.A., Brink, T.G., Bregman, J.N. & Roberts, T.P. (2010). Evidence for a Stellar Disruption by an Intermediate-mass Black Hole in an Extragalactic Globular Cluster. *The Astrophysical Journal Letters*, **712**, L1–L4. 36

Jones, B.F. (1970). Internal motions in the pleiades. *The Astronomical Journal*, **75**, 563–574. 94

Kalirai, J.S. & Richer, H.B. (2010). Star clusters as laboratories for stellar and dynamical evolution. *Philosophical Transactions of the Royal Society A: Mathematical, Physical and Engineering Sciences*, **368**, 755–782. 1

Kalirai, J.S., Anderson, J., Richer, H.B., King, I.R., Brewer, J.P., Carraro, G., Davis, S.D., Fahlman, G.G., Hansen, B.M.S., Hurley, J.R., Lepine, S., Reitzel, D.B., Rich, R.M., Shara, M.M. & Stetson, P.B. (2007). The Space Motion of the Globular Cluster NGC 6397. *The Astrophysical Journal*, **657**, L93–L96. 41

Karakla, D. & Rose, S. (2010). HST primer for cycle 16. 51, 52

Karttunen, H., Kröger, P., Oja, H., Poutanen, M. & Donner, K.J. (2000). *Fundamental Astronomy*. Springer-Verlag, 3rd edn. 12, 29

King, I.R. (1962). The structure of star clusters. i. an empirical density law. *Astronomical Journal*, **67**, 471. 20

King, I.R. (1966). The structure of star clusters. III. some simple dynamical models. *Astronomical Journal*, **71**, 64. 12, 20, 23

Kirsten, F. & Vlemmings, W.H.T. (2012). No evidence for a central IMBH in M15. *Astronomy & Astrophysics*, **542**. 39

Kong, A.K.H., Heinke, C.O., di Stefano, R., Cohn, H.N., Lugger, P.M., Barmby, P., Lewin, W.H.G. & Primini, F.A. (2010). Localization of the X-ray source in the globular cluster G1 with Chandra. *Monthly Notices of the Royal Astronomical Society: Letters*, **407**, L84–L88. 36

KOOPMANS, L.V.E. & FASSNACHT, C.D. (1999). A Determination of H_0 with the CLASS Gravitational Lens B1608+656. II. Mass Models and the Hubble Constant from Lensing. *The Astrophysical Journal*, **527**, 513–524. 14

KRAUSS, L.M. & CHABOYER, B. (2003). Age Estimates of Globular Clusters in the Milky Way: Constraints on Cosmology. *Science*, **299**, 65–69. 11

KRIST, J. (2003). ACS WFC & HRC field-dependent PSF variations due to optical and charge diffusion effects. Instrument Science Report ACS 2003-06, Space Telescope Science Institute. 66

KRIST, J.E., HOOK, R.N. & STOEHR, F. (2011). 20 years of Hubble Space Telescope optical modeling using Tiny Tim. In *Society of Photo-Optical Instrumentation Engineers (SPIE) Conference Series*, vol. 8127 of *Society of Photo-Optical Instrumentation Engineers (SPIE) Conference Series*. 59, 83

KROUPA, P. & BOILY, C.M. (2002). On the mass function of star clusters. *Monthly Notices of the Royal Astronomical Society*, **336**, 1188–1194. 19

KULKARNI, S.R., HUT, P. & MCMILLAN, S. (1993). Stellar black holes in globular clusters. *Nature*, **364**, 421–423. 2, 31

LAIDLER, V., BOFFI, F., BARLOW, T., BROWN, T., FRIEDMAN, S., JESTER, S., APELLANIZ, J.M. & PROFFITT, C. (2008). Synphot Data User's Guide (Baltimore, STScI). 54

LANZONI, B., DALESSANDRO, E., FERRARO, F.R., MIOCCHI, P., VALENTI, E. & ROOD, R.T. (2007). The Surface Density Profile of NGC 6388: A Good Candidate for Harboring an Intermediate-Mass Black Hole. *The Astrophysical Journal Letters*, **668**, L139–L142. 34, 35, 38

LEE, J.W. & CARNEY, B.W. (2006). VI photometry of globular clusters NGC 6293 and NGC 6541: The formation of the metal-poor inner halo globular clusters. *The Astronomical Journal*, **132**, 2171–2186. 125, 173

LÜTZGENDORF, N., KISSLER-PATIG, M., NOYOLA, E., JALALI, B., DE ZEEUW, P.T., GEBHARDT, K. & BAUMGARDT, H. (2011). Kinematic signature of an intermediate-mass black hole in the globular cluster NGC 6388. *Astronomy & Astrophysics*, **533**. 38

Maccarone, T.J. (2004). Radio emission as a test of the existence of intermediate-mass black holes in globular clusters and dwarf spheroidal galaxies. *Monthly Notices of the Royal Astronomical Society*, **351**, 1043–1059. 38

Maccarone, T.J. & Servillate, M. (2008). Radio observations of NGC 2808 and other globular clusters: constraints on intermediate-mass black holes. *Monthly Notices of the Royal Astronomical Society*, **389**, 379–384. 39

Maccarone, T.J., Kundu, A., Zepf, S.E. & Rhode, K.L. (2007). A Black Hole in a globular cluster. *Nature*, **445**, 183–185. 35, 36

Mackey, A.D. & Gilmore, G.F. (2003a). Surface brightness profiles and structural parameters for 10 rich stellar clusters in the Small Magellanic Cloud. *Monthly Notices of the Royal Astronomical Society*, **338**, 120–130. 31

Mackey, A.D. & Gilmore, G.F. (2003b). Surface brightness profiles and structural parameters for 53 rich stellar clusters in the large magellanic cloud. *Monthly Notices of the Royal Astronomical Society*, **338**, 85–119. 31

Mackey, A.D., Wilkinson, M.I., Davies, M.B. & Gilmore, G.F. (2008). Black holes and core expansion in massive star clusters. *Monthly Notices of the Royal Astronomical Society*, **386**, 65–95. 30

Madau, P. & Rees, M.J. (2001). Massive Black Holes as Population III Remnants. *The Astrophysical Journal*, **551**, L27–L30. 33

Makino, J., Taiji, M., Ebisuzaki, T. & Sugimoto, D. (1997). GRAPE-4: A Massively Parallel Special-Purpose Computer for Collisional N-Body Simulations. *Astrophysical Journal*, **480**, 432–446. 26, 27, 96

Makino, J., Fukushige, T., Koga, M. & Namura, K. (2003). GRAPE-6: Massively-Parallel Special-Purpose Computer for Astrophysical Particle Simulations. *Publications of the Astronomical Society of Japan*, **55**, 1163–1187. 27

Mapelli, M., Huwyler, C., Mayer, L., Jetzer, P. & Vecchio, A. (2010). Gravitational Waves from Intermediate-mass Black Holes in Young Clusters. *The Astrophysical Journal*, **719**, 987–995. 38

Marigo, P., Girardi, L., Bressan, A., Groenewegen, M.A.T., Silva, L. & Granato, G.L. (2008). Evolution of asymptotic giant branch stars. II. Optical to far-infrared isochrones with improved TP-AGB models. *Astronomy and Astrophysics*, **482**, 883–905. 117

Marín-Franch, A., Aparicio, A., Piotto, G., Rosenberg, A., Chaboyer, B., Sarajedini, A., Siegel, M., Anderson, J., Bedin, L.R., Dotter, A., Hempel, M., King, I., Majewski, S., Milone, A.P., Paust, N. & Reid, I.N. (2009). The ACS Survey of Galactic Globular Clusters. VII. Relative Ages. *The Astrophysical Journal*, **694**, 1498–1516. 11

Massey, P. & Hunter, D.A. (1998). Star Formation in R136: A Cluster of O3 Stars Revealed by Hubble Space Telescope Spectroscopy. *The Astrophysical Journal*, **493**, 180. 17

Maybhate, A. (2010). ACS instrument handbook version 10.0 (baltimore: STScI). 61, 62, 63, 79

McLaughlin, D.E., Anderson, J., Meylan, G., Gebhardt, K., Pryor, C., Minniti, D. & Phinney, S. (2006). Hubble Space Telescope Proper Motions and Stellar Dynamics in the core of the globular cluster 47 Tucane. *The Astrophysical Journal Supplement Series*, **166**, 249–297. 40, 87, 91, 121

McMaster, M. & Biretta, J. (2008). WFPC2 Instrument Handbook, Version 10.0 (Baltimore: STScI). 50, 53, 59

McNamara, B.J., Harrison, T.E. & Anderson, J. (2003). Does M15 Possess an Intermediate-Mass Black Hole in its Core? *The Astrophysical Journal*, **595**, 187–194. 40, 148, 154, 158, 182, 187, 193

McNamara, B.J., Harrison, T.E., Baumgardt, H. & Khalaj, P. (2012). A search for an intermediate-mass black hole in the core of the globular cluster NGC 6266. *The Astrophysical Journal*, **745**. 40, 158, 195

Merritt, D., Piatek, S., Zwart, S.P. & Hemsendorf, M. (2004). Core Formation by a Population of Massive Remnants. *The Astrophysical Journal*, **608**, L25–L28. 31

Meylan, G. & Mayor, M. (1991). Studies of dynamical properties of globular clusters VI. the high-concentration cluster NGC 6397. *Astronomy & Astrophysics*, **250**, 113–126. 94

Mighell, K.J. (2010). CRBLASTER: a parallel-processing computational framework for embarrassingly parallel image-analysis algorithm. *Publications of the Astronomical Society of the Pacific*, **122**, 1236–1245. 96

Miller, J.M., Fabbiano, G., Miller, M.C. & Fabian, A.C. (2003). X-Ray Spectroscopic Evidence for Intermediate-Mass Black Holes: Cool Accretion Disks in Two Ultraluminous X-Ray Sources. *The Astrophysical Journal*, **585**, L37–L40. 37

Miller, M.C. (2002). Gravitational Radiation from Intermediate-Mass Black Holes. *The Astrophysical Journal*, **581**, 438–450. 38

Miller, M.C. & Hamilton, D.P. (2002). Production of intermediate-mass black holes in globular clusters. *Monthly Notices of the Royal Astronomical Society*, **330**, 232–240. 33

Miller-Jones, J.C.A., Wrobel, J.M., Sivakoff, G.R., Heinke, C.O., Miller, R.E., Plotkin, R.M., Di Stefano, R., Greene, J.E., Ho, L.C., Joseph, T.D., Kong, A.K.H. & Maccarone, T.J. (2012). The Absence of Radio Emission from the Globular Cluster G1. *The Astrophysical Journal Letters*, **755**. 38

Milone, A.P., Piotto, G., Bedin, L.R., Anderson, J., Marino, A.F., Bellini, A., Gratton, R., Renzini, A., Stetson, P.B., Cassisi, S., Aparicio, A., Bragaglia, A., Carretta, E., D'Antona, F., Di Criscienzo, M., Lucatello, S., Monelli, M. & Pietrinferni, A. (2012). Multiple Stellar Populations in 47 Tucanae. *The Astrophysical Journal*, **744**. 1

MOORE, G.E. (1965). Cramming more components into integrated circuits. *Electronics Magazine*, **38**. 95

NARAYAN, R. & NITYANANDA, R. (1986). Maximum Entropy Image Restoration in Astronomy. *Annual Review of Astronomy & Astrophysics*, **24**, 127–170. 74

NIELSEN, O. (2003). *Pypar software package*. Published: http://datamining.anu.edu.au/ ole/pypar. 100

NITADORI, K. & AARSETH, S. (2012). Accelerating NBODY6 with graphics processing units. *Monthly Notices of the Royal Astronomical Society*, **424**, 545–552. 27

NOYOLA, E. & BAUMGARDT, H. (2011). Testing Photometric Diagnostics for the Dynamical State and Possible Intermediate-mass Black Hole Presence in Globular Clusters. *The Astrophysical Journal*, **743**. 34

NOYOLA, E. & GEBHARDT, K. (2006). Surface Brightness Profiles of Galactic Globular Clusters from Hubble Space Telescope Images. *The Astronomical Journal*, **132**, 447–466. xvii, 34, 118, 119, 173, 186, 187, 190

NOYOLA, E. & GEBHARDT, K. (2008). Gemini and Hubble Space Telescope Evidence for an Intermediate-Mass Black Hole in ω Centauri. *The Astrophysical Journal*, **676**, 1008–1015. 30, 32, 37

NOYOLA, E., GEBHARDT, K., KISSLER-PATIG, M., LÜTZGENDORF, N., JALALI, B., DE ZEEUW, P.T. & BAUMGARDT, H. (2010). Very Large Telescope Kinematics for Omega Centauri: Further Support for a Central Black Hole. *The Astrophysical Journal Letters*, **719**, L60–L64. 37

PARMENTIER, G., GOODWIN, S.P., KROUPA, P. & BAUMGARDT, H. (2008). The Shape of the Initial Cluster Mass Function: What It Tells Us about the Local Star Formation Efficiency. *The Astrophysical Journal*, **678**, 347–352. 19

PAVLOVSKY, C., KOEKEMOER, A. & MACK, J. (2006). ACS data handbook, version 5.0, (baltimore: STScI). 64, 65, 79, 80, 196

Piatek, S., Pryor, C. & Olszewski, E.W. (2008). Proper motions of the Large Magellanic Cloud and Small Magellanic Cloud: re-analysis of Hubble space telescope data. *The Astronomical Journal*, **135**, 1024–1038. 87

Pooley, D. & Rappaport, S. (2006). X-Rays from the Globular Cluster G1: Intermediate-Mass Black Hole or Low-Mass X-Ray Binary? *The Astrophysical Journal*, **644**, L45–L48. 36

Prialnik, D. (2000). *An Introduction to the Theory of Stellar Structure and Evolution*. Cambridge University Press. 7, 28

Rich, R.M., Shara, M.M. & Zurek, D. (2001). New Photometry for the Intermediate-Age Large Magellanic Cloud Globular Cluster NGC 2121 and the Nature of the LMC Age Gap. *The Astronomical Journal*, **122**, 842–848. 17

Richstone, D., Ajhar, E.A., Bender, R., Bower, G., Dressler, A., Faber, S.M., Filippenko, A.V., Gebhardt, K., Green, R., Ho, L.C., Kormendy, R., Lauer, T.R., Magorrian, J. & Tremaine, S. (1998). Supermassive black holes and the evolution of galaxies. *Nature*, **385**, A14. 30

Riess, A. & Mack, J. (2004). Time dependence of ACS WFC CTE corrections for photometry and future predictions. Instrument Science Report ACS 2004-006, STScI. 64, 65, 88

Riess, A.G., Macri, L., Casertano, S., Lampeitl, H., Ferguson, H.C., Filippenko, A.V., Jha, S.W., Li, W. & Chornock, R. (2011). A 3% Solution: Determination of the Hubble Constant with the Hubble Space Telescope and Wide Field Camera 3. *The Astrophysical Journal*, **730**, 119. 14

Robitaille, T.P. (2011). HYPERION: an open-source parallelized three-dimensional dust continuum radiative transfer code. *Astronomy & Astrophysics*, **536**. 96

Safonova, M. & Shastri, P. (2010). Extrapolating SMBH correlations down the mass scale: the case for IMBHs in globular clusters. *Astrophysics and Space Science*, **325**, 47–58. 174

Samra, R.S., Richer, H.B., Heyl, J.S., Goldsbury, R., Thanjavur, K., Walker, G. & Woodley, K.A. (2012). Proper Motions and Internal Dynamics in the Core of the Globular Cluster M71. *The Astrophysical Journal Letters*, **751**. 40, 148, 149, 155, 161, 162

Sarajedini, A., Bedin, L.R., Chaboyer, B., Dotter, A., Siegel, M., Anderson, J., Aparicio, A., King, I., Majewski, S., Marin-Franch, A., Piotto, G., Reid, I.N. & Rosenberg, A. (2007). The ACS survey of galactic globular clusters. i. overview and clusters without previous hubble space telescope photometry. *The Astronomical Journal*, **133**, 1658–1672. 8

Sariya, D.P. & Yadav, R.K.S. (2012). Proper motions and membership probabilities of stars in the region of globular cluster NGC 6809. *Astronomy & Astrophysics*, **543**. 40

Sigurdsson, S. & Hernquist, L. (1993). Primordial black holes in globular clusters. *Nature*, **364**, 423–425. 31

Sirianni, M., Jee, M.J., Benitez, N., Blakeslee, J.P., Martel, A.R., Meurer, G., Clampin, M., Marchi, G.D., Ford, H.C., Gilliland, R., Hartig, G.F., Illingworth, G.D., Mack, J. & McCann, W.J. (2005). The photometric performance and calibration of the hubble space telescope advanced camera for surveys. *Publications of the Astronomical Society of the Pacific*, **117**, 1049–1112. 88, 117

Sparke, L.S. & Gallagher, J.S. (2007). *Galaxies in the Universe: An Introduction*. Cambridge University Press, 2nd edn. 13, 15, 16, 17

Spitzer, L. (1987). *Dynamical Evolution of Globular Clusters*. Princeton University Press, illustrated edn. 12, 13, 15

Starck, J.L. & Murtagh, F. (1994). Image restoration with noise suppression using the wavelet transform. *Astronomy and Astrophysics*, **288**, 342–348. 71

Starck, J.L., Pantin, E. & Murtagh, F. (2002). Deconvolution in Astronomy: A Review. *Publications of the Astronomical Society of the Pacific*, **114**, 1051–1069. 70, 71, 73

Stetson, P.B. (1987). DAOPHOT - a computer program for crowded-field stellar photometry. *The Publications of the Astronomical Society of the Pacific*, **99**, 191–222. 75, 87

Strader, J., Chomiuk, L., Maccarone, T.J., Miller-Jones, J.C.A. & Seth, A.C. (2012). Two stellar-mass black holes in the globular cluster M22. *Nature*, **490**, 71–73. 2

Strader, J., Chomiuk, L., Maccarone, T.J., Miller-Jones, J.C.A. & Seth, A.C. (2012a). Two stellar-mass black holes in the globular cluster M22. *Nature*, **490**, 71–73. 195

Strader, J., Chomiuk, L., Maccarone, T.J., Miller-Jones, J.C.A., Seth, A.C., Heinke, C. & Sivakoff, G.R. (2012b). No Evidence for Intermediate-mass Black Holes in Globular Clusters: Strong Constraints from the JVLA. *The Astrophysical Journal Letters*, **750**, L27. 39

Strzodka, R., Doggett, M. & Kolb, A. (2005). Scientific computation for simulations on programmable graphics hardware. *Simulation Modelling Practice and Theory, Special Issue: Programmable Graphics Hardware*, **13**, 667–680. 96

Sutton, A.D., Roberts, T.P., Walton, D.J., Gladstone, J.C. & Scott, A.E. (2012). The most extreme ultraluminous X-ray sources: evidence for intermediate-mass black holes? *Monthly Notices of the Royal Astronomical Society*, **423**, 1154–1177. 37

Szalay, A. (2011). Extreme Data-Intensive Scientific Computing. *Computing in Science & Engineering*, **13**, 34–41. 96

Thorne, K.S. & Braginskii, V. (1976). Gravitational-wave bursts from the nuclei of distant galaxies and quasars - Proposal for detection using Doppler tracking of interplanetary spacecraft. *The Astrophysical Journal*, **204**, L1–L6. 38

Togneri, R. & deSilva, C.J. (2002). *Fundamentals of Information Theory and Coding Design*. discrete mathematics and its applications, Chapman & Hall/CRC. 72

Trager, S.C., King, I.R. & Djorgovski, S. (1995). Catalogue of Galactic globular-cluster surface-brightness profiles. *The Astronomical Journal*, **109**, 218–241. 119

Ulvestad, J.S., Greene, J.E. & Ho, L.C. (2007). Radio Emission from the Intermediate-Mass Black Hole in the Globular Cluster G1. *The Astrophysical Journal*, **661**, L151–L154. 36, 38, 39

Vanovschi, V. (2013). Parallel python software. 203

Vesperini, E. & Trenti, M. (2010). Widespread Presence of Shallow Cusps in the Surface-brightness Profile of Globular Clusters. *The Astrophysical Journal Letters*, **720**, L179–L184. 34

Vesperini, E., McMillan, S.L.W., D'Ercole, A. & D'Antona, F. (2010). Intermediate-mass Black Holes in Early Globular Clusters. *The Astrophysical Journal Letters*, **713**, L41–L44. 33

Vinter, B., Bj$Ø$rndalen, J.M. & Friborg, R.M. (2009). PyCSP revisited. 277–292, IOS Press. 100

Wiley, K., Connolly, A., Gardner, J., Krughoff, S., Balazinska, M., Howe, B., Kwon, Y. & Bu, Y. (2011). Astronomy in the cloud: Using MapReduce for image co-addition. *Publications of the Astronomical Society of the Pacific*, **123**, 366–380. 96

Zloczewski, K., Kaluzny, J. & Thompson, I.B. (2011). A proper motion study of the globular cluster M55. *Monthly Notices of the Royal Astronomical Society*, **414**, 3711–3718. 41

Zwart, S.F.P., Baumgardt, H., Hut, P., Makino, J. & McMillan, S.L.W. (2004). Formation of massive black holes through runaway collisions in dense young star clusters. *Nature*, **428**, 724–726. 32, 36

ZWART, S.F.P., MCMILLAN, S.L.W. & GIELES, M. (2010). Young Massive Star Clusters. *Annual Review of Astronomy and Astrophysics*, **48**, 431–493. 4, 17, 19

ZWART, S.P. & MCMILLAN, S.L. (2002). The Runaway Growth of Intermediate-Mass Black Holes in Dense Star Clusters. *The Astrophysical Journal*, **576**, 899–907. 33